Development and Application of Fractional Calculus-based Mathematical Models and Soft Computing Techniques

THESIS

Submitted in partial fulfillment of the requirements for the degree of

DOCTOR OF PHILOSOPHY

by

SUGANDHA
(ID No. 2018PHXF0024P)

Under the Supervision of

Prof. Trilok Mathur

and Co-Supervision of

Prof. Kamlesh Tiwari

BITS Pilani
Pilani | Dubai | Goa | Hyderabad | Mumbai

BIRLA INSTITUTE OF TECHNOLOGY AND SCIENCE

PILANI-333031 (RAJASTHAN) INDIA

2023

"***As for the future, your task is not to foresee it, but to enable it.***"

- Antoine de Saint-Exupéry

BIRLA INSTITUTE OF TECHNOLOGY & SCIENCE, PILANI

CERTIFICATE

This is to certify that the thesis entitled, **"Development and Application of Fractional Calculus-based Mathematical Models and Soft Computing Techniques"** submitted by **Ms. Sugandha** ID No. **2018PHXF0024P** for the award of Ph.D. degree of the institute embodies original work done by her under my supervision.

_____

Signature of the Supervisor

Name : **PROF. TRILOK MATHUR**

Designation : **Associate Professor,**

Department of Mathematics,

BITS Pilani, Pilani Campus

Date: __/__/____

_____

Signature of the Co-Supervisor

Name : **PROF. KAMLESH TIWARI**

Designation: **Associate Professor,**

Department of Computer Science and Information Systems,

BITS Pilani, Pilani Campus

Date: __/__/____

Dedicated to My Beloved Family

Acknowledgements

Completing the research and writing this thesis would not have been possible without the support and guidance of numerous individuals who have played a crucial role in this academic journey. It's a great perk with the grace of God that I now have the opportunity to thank them all.

First, I express my deep appreciation and sincere gratitude to my thesis supervisors Prof. Trilok Mathur and Prof. Kamlesh Tiwari, for their valuable guidance and continuous encouragement throughout my Ph.D. duration. Under their motivating mentorship, my cognitive process and creative thinking got matured. Their profound knowledge, insightful guidance, and rigorous feedback have shaped my research methodology, refined my analytical skills, and expanded my intellectual horizons. I am also grateful for the opportunities they have provided me, whether attending conferences, workshops, presenting my work, or collaborating on research projects. These experiences have enriched my academic journey and expanded my network, opening doors to new possibilities and fostering a deeper understanding of the academic community.

I am also thankful to all the professors of the Department of Mathematics of BITS Pilani, Pilani Campus for their guidance and valuable suggestions in my research work. I feel fortunate to have my Doctoral Advisory Committee (DAC) members as Prof. Surekha Bhanot and Prof. Shivi Agarwal whose constant encouragement and support made my work focused. Their constructive comments, suggestions, and feedback have greatly contributed to the development of this research and helped me refine my ideas and arguments.

I am obliged to Prof. Balram Dubey, Prof. Bhupendra Kumar Sharma (Ex. HoDs) and Prof. Devendra Kumar, HoD, Department of Mathematics for their support. I would like to acknowledge all the faculty members and research scholars for their valuable support and cooperation during my research work. The memories that have been established hold a significant place in my heart and will be valued indefinitely. I express my gratitude for your significant contribution to my academic journey

I would like to thank the Vice-Chancellor, Director, Dean Academic (AGSRD), and Registrar of BITS Pilani for providing me an opportunity to achieve a challenging position in the respective field pertinent to my qualification, which allowed me to use my skills to prove myself worthy. I am deeply grateful to the institution for providing me with a stimulating academic environment, state-of-the-art facilities, and access to resources necessary for conducting this research.

I want to express my deepest gratitude to my parents (Mr. Narender Kumar Arora and Mrs. Veena Arora) for believing in me more than myself. Their constant support and tremendous understanding kept me motivated throughout my Ph.D. and my life in general.

I would also like to thank my sister Parnika Arora and brother Divyam Arora for being a sympathetic ear and encouraging me. I would also like to give my affection to my little dog Smokey for being a delightful diversion from monotony and frustration. I am deeply indebted to my entire family for their trust in me which made me confident enough to accomplish this journey.

Not to forget, I could not have completed this thesis without my friends Abhishek, Kunal, Pallav, Barkha, Komal, Deepak, Umesh, Sonali, Chandan, Little Komal, Himanshu, Meghana, Parveen, Amit, Babli, Satpal and Geetika who provided stimulating discussions and happy distractions to rest my mind outside my research. My appreciation also goes to my cousins Ankit, Jagriti and Shivam who have always accompanied and supported me outside the academic world. I am really grateful to all my friends and cousins for cheering me up when I was down. Their unwavering support and encouragement have kept me motivated and focused, and I am truly grateful for their presence in my life.

Place: BITS Pilani, Pilani Campus

Date: __/__/____ **(Sugandha)**

Abstract

Fractional calculus is an abstract idea exploring interpretations of differentiation having non-integer order. For a very long time, it was considered a topic of merely theoretical interest. However, introducing several useful definitions of fractional derivatives has extended its application domain. Fractional calculus has emerged as a multifarious domain supported by computational power and algorithmic representations. It has been found that the fractional derivatives are capable of incorporating memory into the system and thereby are suitable to improve the performance of history-dependent tasks, such as the prediction of time series data, capturing the viscoelastic behavior of complex fluids, describing anomalous diffusion processes, modeling the transmission of diseases, or some biological phenomena, and locality-aware tasks such as image processing and computer vision in general. Fractional calculus is one of the fastest-growing topics in the field of mathematics. Although there is tremendous growth in fractional calculus applications, we are still at the beginning of applying this powerful tool in many research fields. The potential applications of this field of research are vast and far-reaching, making it an area of significant interest and importance to researchers.

The thesis explores the synergy between fractional calculus and artificial intelligence, specifically in time series forecasting, computer vision, and biometrics. It also investigates the significance of fractional calculus-based techniques in crime transmission modeling. Chapter 1 begins with an introduction to fractional calculus, highlighting the advantages of applying fractional derivatives to solve real-world problems. The next section of the chapter highlights the addressed research gaps to formulate the objectives for the proposed work. The methodology to achieve research goals is devised, and fundamental concepts of fractional calculus, criminology, computer vision, biometrics, time-series forecasting, and mathematical approaches have been introduced. A thorough literature survey is conducted in Chapter 2 to establish the research gaps.

Fractional calculus is applied in criminology due to the dependency of the current situation of crime prevalent in society on the past behavior of the citizens. A criminally active individual's contact may impact the behavior of others adversely. Therefore, the future state highly correlates to an individual's criminal history in the transmission phase. Various integer-order differential models have been proposed to capture the spread of crime. Most of these dynamic systems haven't considered the criminal's history and the crime's

impact on society. To incorporate history, a fractional-order crime transmission model is proposed in Chapter 3 considering five classes viz law-abiding citizens, non-incarcerated criminals, incarcerated criminals, prison-released, and recidivists. The primary focus of the proposed model is to study the effect of recidivism in society and decide the adequate imprisonment for repeat offenders. The existence, uniqueness, non-negativity and boundedness of the solution of the proposed model are examined. The local stability of the equilibrium points is also analyzed using Routh-Hurwitz Criteria with Matignon conditions. Further, the threshold condition for the uniform asymptotic stability of the system is evaluated using the Lyapunov stability method. Moreover, the current study also examines the long-term impact of the imprisonment of criminals on society. The numerical simulations of the model for a range of fractional orders are obtained using the power series expansion method to strengthen the theoretical results.

Another application of fractional calculus is examined on time-series forecasting. In Chapter 4, the Air Quality Index (AQI) of Indian cities of different tiers is predicted using Vanilla Recurrent Neural Network (RNN). AQI is used to measure the air quality of any region which is calculated based on the concentration of ground-level Ozone, particle pollution, Carbon Monoxide, and Sulphur Dioxide in the air. The air quality of an area depends on current weather conditions, vehicle traffic in that area, or anything that increases air pollution. But the current air quality also depends on the climate conditions and growth of industrialization in that area, making AQI a history-dependent parameter. To capture this dependency, the memory property of fractional derivatives is exploited in this algorithm. The fractional gradient descent algorithm involving Caputo's derivative is used in the backpropagation algorithm to train RNNs. Due to the availability of a large amount of data and high computation support, deep neural networks are capable of giving state-of-the-art results in time series prediction. But in this study, basic Vanilla RNN is chosen to check the effectiveness of fractional derivatives.

One of the important applications of fractional calculus in the past decade is in the field of computer vision. Deep CNNs are being applied in computer vision tasks such as image classification, image denoising, object detection, etc. Their ability to learn complex and non-linear relationships between the features leads to higher accuracies. The performance of any deep learning algorithm is dependent on the quality of features that are being extracted. Thus for effective feature extraction, long-term memory is incorporated into deep neural networks with the help of fractional derivatives. This methodology is applied to three computer vision tasks: road segmentation, salient object detection, and palmprint

image recognition in Chapter 5, Chapter 6, and Chapter 7 respectively.

Segmentation of a road portion from a satellite image is challenging due to its complex background, occlusion, shadows, clouds, and other optical artifacts. One must combine local and global cues for an accurate and continuous/connected road network extraction. Chapter 5 proposes a model using fractional derivative-based weighted skip connections on a dense convolutional neural network for road segmentation. Weights corresponding to the skip connections are determined using Grunwald-Letnikov fractional derivative. Fractional derivatives being non-local incorporates memory into the system, combining local and global features. Experiments have been performed on two open-source, widely-used benchmark databases $viz.$ Massachusetts Road Database (MRD) and Ottawa Road Database (ORD). These datasets represent different road topography and network structure, including varying road widths and complexities.

The application of fractional calculus to salient object detection is discussed in Chapter 6. Detecting multiple salient objects of varying scales, from a cluttered background and without sharp boundaries is still challenging. An accurate saliency map production requires low-level appearance and high-level semantic features. Thus an optimal combination of local and global cues is required to extract effective and comprehensive features. This chapter proposes a salient object detection network with a densely connected encoder having fractional derivative-based weighted skip connections and a decoder with multiple modules for improving the quality of features. The weightage for the skip connections is determined using Grunwald–Letnikov's version of fractional derivative. Due to the non-locality of fractional derivatives, memory is incorporated into the system, thereby preventing the dilution of features due to the increasing network depth. The decoder has multiple modules to refine the extracted features, aggregate the multi-level features and remove redundant information. The weighted skip connections and multiple decoder modules assist in obtaining the discriminative features required for learning the relationship between multiple salient objects. The proposed technique is tested on six widely-used, publicly available databases: ECSSD, HKU-IS, PASCAL-S, DUT-OMRON, DUTS-TE and SOD.

Chapter 7 analyzes the effectiveness of fractional calculus in palmprint-based human authentication systems. Palmprint identification attempts to determine a person's identity by matching a palmprint image sample to all of the templates in the database and identifying the most similar. A palmprint recognition system based on ResNet34 integrated with the attention mechanism is developed. For higher recognition accuracy, the

memory is incorporated into the network by densely connecting the layers of the networks with fractional weighted skip connections. These fractional weights are derived from the Grunwald-Letnikov version of the fractional derivative. The non-locality of fractional derivatives enhances the feature extraction performance of the network by combining the local and global features, thereby improving the matching accuracy of the authentication system. The features are further improved by using attention modules at each level and large-margin cosine loss and focal loss to optimize the network parameters. Experiments are performed on three open-source, widely-used palmprint databases: IIT-D Touchless, CASIA, and Tongji-Contactless.

Chapter 8 consolidates the work by comprehensively summarizing the critical research findings and highlighting the potential areas for future exploration.

Contents

List of Abbreviations

AQI:	Air Quality Index
ARIMA:	Autoregressive Integrated Moving Average
AUC :	Area Under the Curve
BCE:	Binary Cross Entropy
CAM:	Channel Attention Module
CLAHE:	Contrast Limited Adaptive Histogram Equalization
CO:	Carbon Monoxide
CRR:	Correct Recognition Rate
DCNNs:	Deep Convolutional Neural Networks
DCFB:	Densely Connected Fractional Block
DCL:	Dice Coefficient Loss
DI:	Discriminative Index
DL :	Deep Learning
EER:	Equal Error Rate
FAR:	False Acceptance Rate
FCNN:	Fully Convolutional Neural Networks
FI:	Feature Integration
FNNs:	Feed-Forward Neural Networks
FOCNet:	Fractional Optimal Control Network
FODE:	Fractional Order Differential Equations
FL:	Focal Loss
FRR :	False Rejection Rate
GFF:	Global Feature Flow
G-L:	Grunwald Letnikov
GT:	Ground Truth
HA:	Head Attention
LBP :	Local Binary Pattern
LLDP :	Local binary pattern-based feature descriptor
LMCL:	Large Margin Cosine Loss
LSTM:	Long Short-Term Memory
MAE:	Mean Absolute Error

MAPE:	Mean Absolute Percentage Error
mIoU:	Mean Intersection over Union
MRD:	Massachusetts Road Database
NO_2:	Nitrogen Dioxide
NO_x:	Nitrogen oxides
O_3:	Ozone
ODE:	Ordinary Differential Equations
ORD:	Ottawa Road Database
PAM:	Position Attention Module
PM:	Particulate Matter
P-R:	Precision-Recall
PSO:	Particle Swarm Optimization
R-L:	Riemann-Liouville
RMSE:	Root Mean Squared Error
RNN:	Recurrent Neural Network
ROC :	Receiver Operating Characteristic Curve
ROI :	Region of Interest
SIFT :	Scale Invariant Feature Transform
SGD:	Stochastic Gradient Descent
SOTA:	State-Of-The-Art
SO_2:	Sulphur Dioxide
SR:	Self Refinement
SSIM:	Structural Similarity
TU:	Transition Up
TD:	Transition Down
VOCs:	Volatile Organic Compounds

List of Symbols

α : Fractional order of differentiation

ν_1 : Crime indulgence rate due to social interactions

η_1 : Rate of assimilating back in society from criminal class O_1

λ_1 : Law-enforcement rate

r : prison-release rate

ν_{20} : Rate of crime indulgence of prison-released people

η_2 : Rate at which recidivists become criminally inactive

λ_2 : Law-enforcement rate on recidivists

ξ : Rate of moving back to society after releasing from prison

$\mathcal{R}_0$: Reproduction Number for crime model

E^* : High crime equilibrium

E^0 : Crime free equilibrium

$\mathbb{N}$: Natural numbers

$\mathbb{R}$: Real numbers

Γ : Gamma function

TP : True Positive

TN : True Negative

FP : False Positive

FN : False Negative

F_β : F-measure

List of Tables

List of Figures

Chapter 1

Introduction

The idea of fractional calculus is fundamental that refers to obtaining functional derivatives and integrals when order is not strictly an integer. Developing empirical interpretations of these mathematical representations remained a puzzle for a long time. Some early works indicate that the notion incorporates the sense of locality and thus encompasses history. This seemingly strange concept can be correlated to common real-life applications such as crime spread, epidemics, time series, and images. For example, a pixel in an image is associated with its neighborhood and cannot be arbitrarily different from its surrounding. Fractional calculus can inherently model these relations and become helpful in various applications. In the past two decades, fractional order-based systems are performing better in various science and engineering applications where non-locality or history has an important role to play [21–26]. This thesis aims to highlight the advantages of using fractional calculus to overcome the challenges in the existing literature. A brief introduction to fractional calculus, mathematical modeling, and soft computing techniques, specifically neural networks & computer vision, is done in this chapter. It also accommodates the description of useful definitions, theorems, and evaluation parameters required to develop and analyze the proposed fractional calculus-based models.

1.1 Fractional Calculus

Issac Newton and Leibniz invented differential calculus around three centuries ago. In basic calculus, for an integer m, the m-th order derivative of a function means differentiating a function $'m'$ times successively. The expression $\frac{d^m g}{dt^m}$ can also be interpreted as an operator whose action on the function $g(t)$ is determined by the parameter m. Fractional calculus was originated in 1695 when L'hopital asked Leibniz about the behavior of this general

operator for n being a non-integer. After that, the search for an operator that transforms g into its m-th derivative or anti-derivative starts. Fractional calculus is an area which deals with differentiation and integration of arbitrary order. Many different ways has been proposed to generalize differentiation and integration for non-integer orders that preserve the several standard differential properties.

Initially, this field was not utilized for practical applications, and due to this, fractional calculus was considered an abstract area containing only rigorous and complicated mathematical manipulations. The pertinence of the subject stands lacking to date. However, due to the advent of multiple tools and software, a significant resurgence of interest has developed in it. Fractional calculus is emerging and has been applied to several fields of Science, Engineering, and Economics [21–31]. Abel was the first one to apply fractional derivatives to solve the tautochrone problem. The leading edge of applying fractional derivative over ordinary derivative is that the piece-wise continuity of a function is sufficient to be fractionally differentiable. Another useful property is that fractional derivatives (and integrals) are global. Thereby these consider the history and non-local distributed effects [32]. Hence it is beneficial to use fractional derivatives where history dependency exists, including viscoelasticity [33], biology [34], stock market [35], anomalous diffusion [36], bacterial chemotaxis [37], signal and image processing [38] and complex networks [39]. Arbitrary order α of differentiation/integration in fractional-order-based methods also contribute to an additional degree of freedom in the process of optimization. Differentiation and integration of arbitrary order have been defined in various ways, including Riemann-Liouville, Grunwald-Letnikov, Caputo, Weyl, Jumarie, Riesz, Hadamard and Erdelyi-Kober. Each definition has its own distinct characteristics. There are pros and cons of using any version of fractional derivative. To overcome cons of definitions, several new versions of fractional derivatives are being introduced. Most commonly used fractional differential and integral versions are mentioned as follows:

1.1.1 Riemann-Liouville (R-L) Fractional Integral Operator

The R-L generalization of integration is the most frequently used version of fractional integration [21]. If $\alpha > 0$ and g is a piece wise continuous function on $J' = [0, \infty)$ and integrable on any finite subinterval of $J = (0, \infty)$, then for $t > a$ and $t, a \in \mathbb{R}$ the following equation

$$ {}_aD_t^{-\alpha} g(t) = \frac{1}{\Gamma(\alpha)} \int_a^t (t-\eta)^{\alpha-1} g(\eta)\, d\eta \tag{1.1.1} $$

represents the R-L fractional integral of order α and the function $\Gamma(\cdot)$ is the Gamma function. This definition cannot be treated as a generalization of differentiation. As if $-\alpha$ is replaced by some $\beta > 0$, then

$$ {}_aD_t^{\beta} g(t) = \frac{1}{\Gamma(-\beta)} \int_a^t (t-\eta)^{-\beta-1} g(\eta)\, d\eta \tag{1.1.2} $$

The above expression have $\Gamma(-\beta)$ in the denominator which is not defined for negative integers and zero. Hence the R-L fractional integral operator in Equation (1.1.1) doesn't work for regular differentiation and thus cannot be generalized to the fractional differential operator, which led to the development of different operators for generalized differentiation [40]. The three most frequently used definitions are the following:

1.1.2 Riemann-Liouville (R-L) Fractional Derivative

The R-L fractional derivative definition is a natural generalization of the ordinary derivative. As in the integer-order case, the R-L fractional derivative is left inverse of the fractional integral,

$$ {}_a^{RL}D_t^{\alpha} D^{-\alpha} g(t) = D^0 g(t) = g(t). \tag{1.1.3} $$

If $t > a$, $\alpha > 0$ and $m \in \mathbb{N}$, such that $m-1 < \alpha < m$, then for evaluating the derivative of order α , the $m-\alpha$ order R-L integral of function $g(t)$ is differentiated m-times,

$$ {}_a^{RL}D_t^{\alpha} g(t) = D^m \left[{}_aD_t^{-(m-\alpha)} g(t) \right], $$

i.e.

$$ {}_a^{RL}D_t^{\alpha} g(t) = \begin{cases} \dfrac{1}{\Gamma(m-\alpha)} \dfrac{d^m}{dt^m} \displaystyle\int_a^t \frac{g(\eta)}{(t-\eta)^{\alpha+1-m}}\, d\eta, & m-1 < \alpha < m \\ \dfrac{d^m}{dt^m} g(t), & \alpha = m \end{cases} \tag{1.1.4} $$

is called the R-L fractional derivative of order α [21]. But this definition has some disadvantages as well. Firstly the R-L derivative of order $\alpha, (< 1)$ of a constant is not zero.

$$ {}_0^{RL}D_t^{\alpha} k = \frac{k}{\Gamma(1-\alpha)} t^{-\alpha} \neq 0 \tag{1.1.5} $$

Secondly, the Laplace transform of this R-L derivative of order $\alpha > 0,\ m-1 \leq \alpha < m$ defined by

$$\mathscr{L}\{{}_0^{RL}D_t^{\alpha}g(t);s\} = s^{\alpha}G(s) - \sum_{k=0}^{n-1} s^k [{}_0^{RL}D_t^{\alpha-k-1}g(t)]_{t=0}. \tag{1.1.6}$$

involves the usage of initial values for fractional order derivatives, which don't have any physical interpretations.

1.1.3 Caputo Fractional Derivative

If $t > a$, $\alpha > 0$ and $m \in \mathbb{N}$, such that $m-1 < \alpha < m$, then for evaluating the derivative of order α , the $m-\alpha$ order R-L integral of m^{th} order differentiation of function $g(t)$ is computed,

$${}_a^C D_t^{\alpha}g(t) = {}_aD_t^{-(m-\alpha)}\left[D^m g(t)\right],$$

i.e.

$${}_a^C D_t^{\alpha}g(t) = \begin{cases} \dfrac{1}{\Gamma(m-\alpha)}\displaystyle\int_a^t \frac{g^{(m)}(\eta)}{(t-\eta)^{\alpha+1-m}}\,d\eta, & m-1 < \alpha < m \\ \dfrac{d^m}{dt^m}g(t), & \alpha = m \end{cases} \tag{1.1.7}$$

which is called the Caputo fractional derivative of order α. This definition of fractional derivative was given by Caputo in 1967 to overcome the limitations of R-L derivative as explained above [41]. The Caputo's derivative of order $\alpha > 0,\ m-1 \leq \alpha < m$ for a constant k is zero,

$${}_0^C D_t^{\alpha}k = \frac{1}{\Gamma(n-\alpha)}\int_0^t \frac{k^{(m)}}{(t-\eta)^{\alpha+1-m}}\,d\eta = 0 \ \ , m-1 < \alpha < m \tag{1.1.8}$$

and Laplace transforms of Caputo fractional derivative of order $\alpha > 0,\ m-1 \leq \alpha < m$ defined as

$$\mathscr{L}\{{}_0^C D_t^{\alpha}g(t);s\} = s^{\alpha}G(s) - \sum_{k=0}^{n-1} s^{\alpha-k-1} [{}_0^C D_t^k g(t)]_{t=0}. \tag{1.1.9}$$

involves the usage of initial values of ordinary derivative, which makes this definition more applicable to real-world problems.

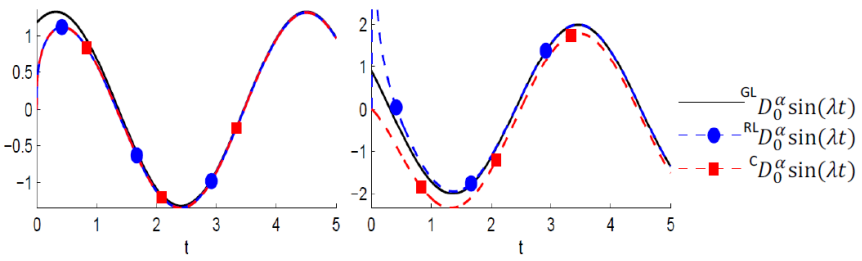

a) $\alpha = 0.7$ b) $\alpha = 1.7$

Figure 1.1: Comparing Grunwald–Letnikov, Riemann-Liouville, and Caputo fractional derivative of a function $\sin(\lambda t)$ for $\lambda = 1.5$

1.1.4 Grünwald-Letnikov (G-L) Fractional Derivative

This is the discrete version of fractional derivative, which was introduced by Anton Karl Grünwald and Aleksey Vasilievich Letnikov in 1867 and 1868 respectively. In the expression (1.1.10), derivative of order α is expressed as limit of a sum and it is very intriguing that it makes no assumption other than that the function should be defined.

$$ {}_aD_t^\alpha g(t) = \lim_{\substack{h\to 0 \\ nh=t-a}} h^{-\alpha} \sum_{r=0}^{n} (-1)^r \binom{\alpha}{r} g(t-bh) \tag{1.1.10} $$

$$ {}_aD_t^\alpha g(t) = \sum_{k=0}^{m-1} \frac{g^{(k)}(a)(t-a)^{-\alpha+k}}{\Gamma(-\alpha+m)} + \frac{1}{\Gamma(m-\alpha)} \int_a^t \frac{g^{(m)}(\eta)}{(t-\eta)^{-m-1+\alpha}}\, d\eta, \tag{1.1.11} $$

If the function is continuously differentiable m times, then for positive real number α, $m-1 < \alpha < m$, (1.1.10) can be written as (1.1.11). The above two expressions represent G-L derivative of order α and the function $\Gamma(\cdot)$ is the Gamma function. The equation (1.1.10) can be written as

$$ \frac{\delta^\alpha g(t)}{\delta t^\alpha} = g(t) + (-\alpha) g(t-1) + \frac{(-\alpha)(-\alpha+1)}{2} g(t-2) + \frac{(-\alpha)(-\alpha+1)(-\alpha+2)}{6} g(t-3) + \cdots + \frac{\Gamma(-\alpha+1)}{m!\Gamma(-\alpha+m+1)} g(t-m) + \cdots \tag{1.1.12} $$

Similarly, for the two dimensional signal $g(r,t)$, α order differentiation w.r.t r can be

expressed as

$$\frac{\delta^{\alpha} g(r,t)}{\delta r^{\alpha}} = g(r,t) + (-\alpha) g(r-1,t) + \frac{(-\alpha)(-\alpha+1)}{2} g(r-2,t) + \frac{(-\alpha)(-\alpha+1)(-\alpha+2)}{6} g(r-3,t) + \cdots + \frac{\Gamma(-\alpha+1)}{m!\Gamma(-\alpha+m+1)} g(r-m,t) + \cdots \quad (1.1.13)$$

where r, t can have only discrete values, that is $r = 1, 2, \cdots$, $t = 1, 2, \cdots$. The Grünwald-Letnikov fractional derivative formulation is widely used in several branches of study to solve fractional differential equations numerically. Based on the properties of different definitions, R-L derivative is generally used to evaluate theoretical results, the Caputo derivative is used for solving engineering problems, involving fractional differential equations, and the G-L derivative is mainly used in signal processing. Figure 1.1 shows the asymptotic behavior of all three derivative versions, and it can be observed that as $t \to \infty$, all the definitions are equivalent, *i.e.*, ${}_{a}D_{t}^{\alpha} g(t) \sim {}_{a}^{C}D_{t}^{\alpha} g(t) \sim {}_{a}^{RL}D_{t}^{\alpha} g(t)$.

1.1.5 Memory Property

The attractive property of fractional derivatives is non-locality. When the integer-order derivative is computed at a point b, the value obtained depends only on b and $b+h$ or $b-h$. This property is called a locality. But the fractional derivative is derived by integrating over an entire range of values, which can be seen from the above two definitions (1.1.3) and (1.1.4). While evaluating the G-L derivative, it considers all the past values of the function, which is clear from (1.1.10). This non-locality is one of the main drivers of interest in fractional calculus applications. Many physical phenomena have memory effects, meaning their present state also depends on previous states. Such systems are difficult to model and analyze using integer-order differential equations (IODE), but non-locality makes integer-order differential equations (FODE) capable of incorporating memory effects. It can be seen from the expression (1.1.10) that the values of the function at all past points are taken into account while calculating the fractional derivative at a point t. The memory of a dynamic system follows the power law, in which while defining the present state of the system at time t, the weight of the previous state at time t_j is proportional to $(t - t_j)^{\alpha-1}$, where $0 < \alpha < 1$ is the order of the derivative [42, 43]. Figure 1.2 depicts the short-term memory of IODE and the long-term memory of FODE.

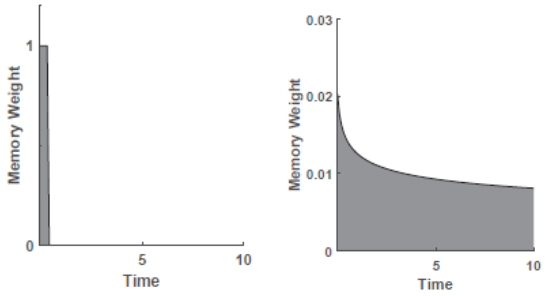

Figure 1.2: Memory weights corresponding to IODE and FODE [5]

1.2 Mathematical Modeling

Mathematical modeling represents real-world phenomena or systems using mathematical equations and structures. Its process involves problem formulation, assumptions, mathematical model development, parameter estimation, model analysis, simulations for validating it, and refinement of the model as needed. Mathematical models help to understand complex systems, make predictions, optimize processes, and test hypotheses. It is a powerful tool for analyzing real-life problems in various fields, including engineering [32], sociology [44], biology [45], economics [46], and epidemiology [47]. A few common approaches to mathematical modeling are deterministic modeling, stochastic modeling, optimization, and data-driven modeling [48]. This thesis has explored deterministic and optimization modeling approaches. The optimization modeling approach is discussed in the next section. The deterministic models assume that the system's behavior is predictable and does not incorporate randomness or uncertainty. The change in variables of these models is generally described using differential equations. Several approaches have been developed in the existing literature to analyze the deterministic models. The standard approaches used to investigate the stability of the proposed fractional-order model are explained in this section after describing a few useful definitions related to this study.

Definition 1.2.1. ***(Dynamical System)*** *If an object's state varies over time, that system is termed a dynamical system. Mathematically, it is a system in which the trajectory of an object is represented with the help of a function dependent on time that describes the relation of future states with the current state.*

Definition 1.2.2. ***(Deterministic System)*** *A dynamical system is called deterministic if it leads to the unique final state for each initial state. Such a system can be expressed*

through the following mapping

$$\zeta(x,t) \equiv \zeta_t(x) : \Omega \to \Omega \tag{1.2.1}$$

for each continuous time variable $t \in \mathbb{R}$ and phase space Ω. The position of the system started from x_0 at time t is given by $x(t) = \zeta_t(x_0)$. Moreover, it is assumed that $t \geq 0$ and at $t = 0,\ \zeta_t(x_0) = x_0$.

Definition 1.2.3. ***(Fractional-order Autonomous System)*** *Consider the following fractional-order system*

$$_0^C D_t^\alpha x(t) = f(x),\ x(0) = x_0 \tag{1.2.2}$$

where $0 < \alpha \leq 1$, $x \in \mathbb{R}^n$ is a vector and $f : E(\subset \mathbb{R}^n) \to \mathbb{R}^n$ is a continuously differentiable function. It is said to be autonomous if f does not depend on t explicitly.

Definition 1.2.4. ***(Stability)*** *The solution $x(t)$ of system (1.2.2) with $x(0) = x_0$, is called locally stable if for any $\epsilon > 0$ there exist a $\delta(\epsilon) > 0$ and t_0 such that for a solution $\hat{x(t)}$, the inequality $||\hat{x}_0 - x_0|| < \delta$ implies $||\hat{x}(t) - x(t)|| < \epsilon$ for each $t > t_0$, In other words, the solution x(t) is locally stable if any solution initiated from δ-neighborhood of x_0 always remains in ϵ-neighborhood of $x(t)$ after a considerable time.*

Definition 1.2.5. ***(Asymptotic Stability)*** *The solution $x(t)$ of the system (1.2.2) with initial data $x(0) = x_0$, is said to be locally asymptotically stable if there exists a $\delta > 0$ such that the inequality $||\hat{x}_0 - x_0|| < \delta$ implies $\lim_{t\to\infty} ||\hat{x}(t) - x(t)|| \to 0$. In other words the solution $x(t)$ is locally asymptotically stable if any solution initiated from δ-neighborhood of x_0 converges to the solution $x(t)$.*

Definition 1.2.6. ***(Instability)*** *The solution $x(t)$ of the system (1.2.2) is known as unstable if it is not locally stable.*

Definition 1.2.7. ***(Equilibrium Point)*** *Equilibrium point is a solution $\hat{x}$ of system (1.2.2) that does not change with time and it satisfies $f(\hat{x}) = 0$.*

Definition 1.2.8. ***(Global Stability)*** *An equilibrium point is called globally asymptotically stable if the solutions initiated from a point in a finite region, converge to the equilibrium point.*

Definition 1.2.9. ***(Invariant Set)*** *) A set $\Omega \in \mathbb{R}^n$ is said to be invariant if for every solution $x(t)$, $x(t_0) \in \Omega$ implies $x(t) \in \Omega$ for all $t > t_0$. In other words, if a solution is started from a point in Ω remains in Ω all the time.*

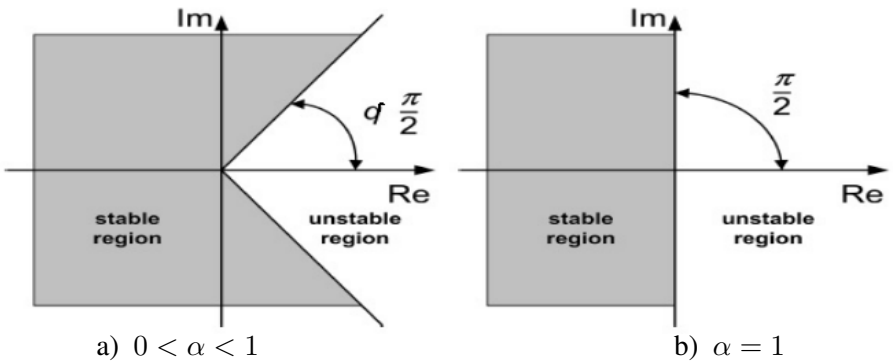

a) $0 < \alpha < 1$ b) $\alpha = 1$

Figure 1.3: Stability region for fractional-order system (a) and integer-order system (b)

Theorem 1.2.1. ***(Existence and Uniqueness Theorem)***[49] *Consider the following initial value problem*

$$ {}_0^C D_t^\alpha x(t) = g(t, x(t)), \qquad x^{(k)}(a) = x_k \tag{1.2.3} $$

where $k = 0, 1, \cdots, \lceil \alpha \rceil - 1$ *for some* $\alpha > 0$ *on the interval* $[a, T]$ *and* ${}_0^C D_t^\alpha$ *denotes the Caputo fractional differential operator of order* α*, and if* $g : [a, T] \times \mathbb{R} \to \mathbb{R}$ *be a continuous and bounded function which satisfies the Lipschitz condition* (1.2.4) *with respect to the second variable, i.e.,*

$$ |g(y, x_1) - g(y, x_2)| \leq l|x_1 - x_2| \tag{1.2.4} $$

for some constant $l > 0$*. Then, the fractional order initial value problem has a unique continuous solution on* $[a, T]$*.*

Theorem 1.2.2. ***(Matignon Criteria for Local Asymptotic Stability)*** [50] *The fractional-order system* (1.2.2) *is said to be locally asymptotically stable at the equilibrium point* $\hat{x} \in E(\subset \mathbb{R}^n)$ *if all the eigenvalues* λ_i *of the Jacobian matrix* $J = \frac{\partial f}{\partial x}$*,* $x \in \mathbb{R}^n$ *evaluated at the equilibrium point* $\hat{x}$ *satisfy*

$$ |arg(\lambda_i)| > \frac{\alpha\pi}{2}, \quad i = 1, 2, \cdots, n, \quad 0 < \alpha < 1 \tag{1.2.5} $$

where $arg(\lambda_i)$ *is the principal value of the argument of the eigenvalue* λ_i *of the Jacobian matrix* J*. If* $arg(\lambda_i)$ *does not satisfy* (1.2.5)*, then the system is unstable around that point.*

These conditions of the Theorem 1.2.2 are presented graphically in Figure 1.3. It can be observed that the stability region of the fractional order system is more than that of the integer order system.

Theorem 1.2.3. ***(Routh-Hurwitz Criteria for Fractional-order System)*** [51, 52] *Let* $P(\lambda) = 0$ *be the characteristic equation of the Jacobian matrix* $J = \frac{\partial f}{\partial x}$, $x \in \mathbb{R}^n$ *for the fractional order system* (1.2.2)

$$P(\lambda) = \lambda^n + A_1\lambda^{n-1} + A_2\lambda^{n-2} + ...A_n = 0, \tag{1.2.6}$$

with real coefficients $A_1, A_2, \cdots A_n$. *The conditions in which all the roots of expression (1.2.6) satisfy (1.2.5) are known as fractional order Routh-Hurwitz conditions. A sufficient condition for all the solutions of the inequality* (1.2.5) *is the positivity of all principal diagonals of minors of the Hurwitz matrix*

$$H_n = \begin{bmatrix} A_1 & 1 & 0 & 0 & 0 & 0 & \dots & 0 \\ A_3 & A_2 & A_1 & 1 & 0 & 0 & \dots & 0 \\ A_5 & A_4 & A_3 & A_2 & A_1 & 1 & \dots & 0 \\ \dots & \dots & \dots & \dots & \dots & \dots & \dots & \dots \\ 0 & 0 & 0 & 0 & 0 & 0 & 0 & A_n \end{bmatrix}.$$

It can be observed that the entries in H_n *on the principal diagonal are the coefficients of* (1.2.6), *and the alternating columns of* H_n *consist of either the coefficients with only even or with only odd indices. Thus,* $H_n = (h_{ij})$, *where* $h_{ij} = A_{2i-k}$, *with missing coefficients being replaced with zero. The conditions for negative real parts of the solutions of* (1.2.6) *for some values of* $n = 2,\ 3$ *and* 4 *are given below. However, the use of this theorem becomes impractical for large* n.

- $n = 2:\ A_1 > 0,\ A_2 > 0$ or $A_1 < 0, 4A_2 > (A_1)^2, \left|\tan^{-1}(\sqrt{4A_2 - A_1^2}/A_1\right| > \dfrac{\alpha\pi}{2}$
- $n = 3:\ A_1 > 0,\ A_3 > 0,\ A_1A_2 > A_3$ if discriminant of polynomial (1.2.6) is positive.

Theorem 1.2.4. ***(Extended Lyapunov Approach for Uniform Asymptotic Stability)*** [49, 53] *Let* x_0 *be an equilibrium point of the non-autonomous fractional-order dynamical system (1.2.3) where* x_0 *belongs to domain* $\Phi \subset \mathbb{R}$. *Then if for any continuously differentiable function* $F(x,t) : \Phi \times [\,0, \infty) \to \mathbb{R}$, *there exists continuous positive definite functions* $F_1(x), F_2(x), F_3(x)$ *defined on domain* Φ *such that* $F_1(x) \leq F(x,t) \leq F_2(x)$ *and* ${}_0^C D_t^\alpha F(x,t) \leq -F_3(x)$ *for every* $\alpha \in (0,1)$. *Then the equilibrium point* x_0 *is uniformly asymptotically stable.*

1.3 Soft Computing

Soft computing originated in the mid-1980s as a response to the limitations of traditional computing methods in dealing with real-world problems that involve uncertainty, imprecision, and complexity. Traditional computing methods based on precise mathematical models are not always sufficient to deal with real-world problems involving ambiguity and uncertainty. Researchers realized there was a need for a new approach that could handle imprecise and uncertain information, and thus the field of soft computing was born. The origins of soft computing can be traced back to the work of several pioneers in the field, including Lotfi A. Zadeh, who introduced the concept of fuzzy sets and fuzzy logic in 1965 [54]. Soft computing originated as a response to the limitations of traditional computing methods in dealing with real-world problems that involved uncertainty, imprecision, and complexity. It emerged from the convergence of several fields, including fuzzy logic, neural networks, and genetic algorithms, and has since grown to encompass other techniques such as machine learning, evolutionary computation, and swarm intelligence. The interdisciplinary nature of soft computing has made it a powerful tool for tackling a wide range of challenging problems in diverse domains. The proposed work is based on the soft computing techniques briefly described below.

1.3.1 Artificial Neural Networks

Artificial Neural Networks (ANNs) are computational models inspired by the structure and functioning of the human brain. They are designed to process the data and learn complex patterns from it. ANNs consist of interconnected artificial neurons (nodes or units) organized in layers, which receive input signals, perform calculations, and produce output signals. It involves machine learning that makes the system capable of learning and improving from experience without being explicitly programmed [55–58]. The learning process commences with the observation of data like examples, instructions, patterns, or direct experiences. This develops criteria that help the machine make decisions in the future. Training an ANN involves a learning process where the network adjusts the weights and biases associated with its connections to minimize the error between the predicted and desired outputs. This is typically done using optimization algorithms, such as gradient descent, which iteratively updates the weights based on the calculated error. The training aims to optimize the network's ability to generalize and make accurate predictions on unseen data.

Backpropagation is one of the ways of training multi-layer ANN. It has a mathematical foundation that is strong although not highly practical. Rumelhart $etal.$ [59] first introduced a backpropagation neural network in 1986. The backpropagation algorithm is used to efficiently train ANNs following a gradient-based optimization algorithm that uses the chain rule. The main feature of backpropagation is its iterative, recursive, and efficient method for calculating the weights updates to improve the network until it can perform the task for which it is being trained. The update rule it uses is

$$\Delta w = -\eta \frac{\delta E}{\delta w} \tag{1.3.1}$$

where η is the learning rate.

ANNs can be applied to various tasks, including classification, regression, pattern recognition, and time series analysis. They have been successfully used in diverse fields such as image and speech recognition, natural language processing, recommendation systems, and financial forecasting. With the advancements in deep learning, which involves using ANNs with many hidden layers (known as deep neural networks), ANNs have achieved remarkable performance in complex tasks and have become prominent techniques in machine learning and artificial intelligence. This thesis explores the application of fractional calculus in the backpropagation algorithm for time-series forecasting through RNNs. Some popular variants of ANNs are briefly described below:

1. **Feed Forward Neural Network [60]:** This was the first and the simplest ANN, in which information just passes in the forward direction, i.e., from the input layer through the hidden layer to the output layer. No loops or cycle exists in the network connections.

2. **Recurrent Neural Network (RNN) [61]:** Recurrent Neural Networks (RNNs) is a type of Neural Network where the output from the previous step is fed as input to the current step. Such networks are developed to handle sequential data. Basic RNNs face difficulty in learning long-term dependencies.

3. **Autoencoders [62]:** The structure of these networks has two components: encoder network, and decoder network. Encoder learns a compressed representation of the input data and then decoder decompresses the encoding of the input data by reconstructing it and generating the desired output. These networks are majorly used for image reconstruction, such as for denoising, captioning, and segmenting.

4. **Long Short-Term Memory (LSTM) [63]:** It is a variant of RNN developed for learning long-term dependencies using dedicated circuits . An LSTM unit has a cell, an input gate, a forget cate and an output gate. The cell remembers values over arbitrary time intervals and the gates control the flow of information to the cell. The information which is not required from the previous cell state is removed by the forget gate. The input gate controls the information to be added to the current cell state. Lastly, the extraction of useful information from the current cell state to generate output is managed by the output gate. This design of the network addresses the problem of vanishing gradient problem. The comparison of the structures of RNN and LSTM is shown with the help of a figure in Chapter 4, where these networks are leveraged for AQI prediction.

5. **Convolutional Neural Network (CNN):** These networks are developed for dealing with image, speech, or audio signal inputs. A CNN has three components: 1) Convolutional layer, 2) Pooling layers, and 3) Fully connected layer. The first layer of a CNN is a convolutional layer and the last layer is the fully connected layer. In between these layers, several convolutional and pooling layers are stacked. The complexity of the network increases with an increase in the number of convolutional layers. The convolutional layers are the main building blocks of the CNNs. It applies the filter to the input image and generates a feature map. A filter is a 2-dimensional array of weights. It is applied to a section of the image and the dot product between pixel values of the images and these weights is computed to generate the corresponding output. This filter is repeatedly swept by a stride and applied over the whole image to generate the final output feature map. A ReLu activation function[1] is generally added after the convolution layer to introduce non-linearity to the network. The pooling layer reduces the dimension of the input by applying a filter over it, reducing the complexity of the network. Unlike convolutional layers, the filters of pooling layers do not have any weights. The output feature map corresponding to a particular position is computed by taking the max of the pixel values (max-pooling) or the average of the pixel values (average pooling). As the name depicts, the fully connected layer is the last layer of the network connected to each node of its previous layer. The feature extracted through this layer is fed to the softmax activation function to obtain the probabilities from 0 to 1. This helps in the classification of the input data. Some popular CNN architectures

[1] $f(x) = \max\{0, x\}$

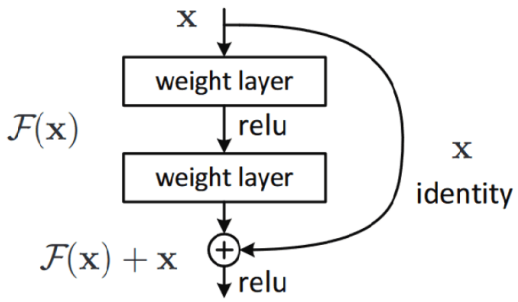

Figure 1.4: Skip Connection [6]

are LeNet-5 [64], AlexNet [65], VGG-16 [66] and ResNet [6].

6. **Residual Neural Network (ResNet) [6]:** It is the most frequently used deep convolutional neural network that uses a technique called skip connections to solve the problem of vanishing/exploding gradients. These skip connections connect activations of a layer to further layers by skipping some layers in between. This forms a residual block. ResNets are made by stacking these residual blocks together. Layers connected via skip connections are shown in Figure 1.4. The weight of the skip connection is equal to one in ResNet. If the weightage is not unity, then that skip is termed as a **weighted skip connection**.

1.3.2 Computer Vision

Computer vision is an important application of artificial intelligence, that originated around 60 years ago. Computer vision aims to develop machines that can see. Recent events incited a transformed curiosity in how machines see and how computer vision can be used. Computer vision is an interdisciplinary area dealing with developing vision-related capabilities for a computer. It aims to extract meaning from the image pixel values. Computer vision aims to build a system that performs the same task as the human visual system. Specifically, describing images and videos by recognizing objects, providing annotation, performing segmentation and analyzing the motion of image frames [67]. All these tasks involve pre-processing, feature extraction, matching, and decision.

It all started in 1966, when Seymour Papert and Marvin Minsky started a summer vision project in the AI group of MIT. The project aimed to build a system that can analyze a scene and then detect objects in the scene. The project continued for two months, opening the door to an important research area. David Marr, a neuroscientist at MIT, started working in computer vision in the 70s and contributed significantly to it [68]. He is known as the father of the current computer vision. Subdomains of computer vision comprise

edge detection, object detection, video tracking, motion analysis, image denoising, scene reconstruction, image segmentation, $etc.$ This thesis explores the application of fractional calculus in the domains $viz.$ image segmentation, object detection and image recognition. This section describes the mathematical approach employed in the study for memory incorporation into the architecture of DCNNs that improves the quality of feature extraction.

1.3.2.1 Modeling the Underlying Dynamics and Architecture of DCNN as Fractional Optimal Control Problem

This section explains the approach for dynamic system modeling of the forward propagation of Deep Convolutional Neural Networks (DCNNs) [69]. The output of any layer of a CNN depends on that layer's input and the convolution kernel's parameters. Thus the propagation of a simple DCNN with T number of layers can be represented by the following mathematical expression:

$$z_{t+1} = \sigma(\theta_t * z_t) \quad t = 1, 2, \cdots T \tag{1.3.2}$$

where $z_t \in \mathbb{R}^n$ is the input of the t^{th} layer, $z_{t+1} \in \mathbb{R}^n$ is the output of the t^{th} layer of the network and $\theta_t \in \mathbb{R}^m$ is the matrix of parameters of the convolution kernel and $\sigma : \mathbb{R}^n \to \mathbb{R}^n$ is a non-linear activation function dependent on the input z_t and convolution parameters θ_t. The optimal parameters of the neural network are obtained by minimizing the sum of the loss function and the regularization function of the parameters over all layers. Mathematically, the optimal solution $\theta(t)$ is evaluated by solving the following expression

$$\min_{\{\theta_t\}_{t=1}^{T}} \sum_{t=1}^{T} R(\theta_t) + L(\Phi(z_T), u), \tag{1.3.3}$$

where $R(\cdot)$ is the regularization function dependent on convolution parameters, $\Phi(z_T) : \mathbb{R}^n \to \mathbb{R}^d$ is the output of the final layer, u is the expected output of the network and $L(\cdot, \cdot) : \mathbb{R}^d \to \mathbb{R}$ is the loss function.

The forward propagation of a DCNN is equivalent to a dynamical system and a dynamic system can be described by an ODE [69, 70]. If $z(t)$ is the corresponding trajectory of the system, then the dynamics of the deep neural network can be represented by the following ODE:

$$\dot{z}(t) = f(z(t), \theta(t)), \qquad z(0) = z_0, \;\; t \in [0, T] \tag{1.3.4}$$

where z_0 is the initial condition of the dynamic system and $\theta(t)$ is the control parameter [71], and that system can be solved by the optimal control method. The target is to find the best control $\theta(t)$ for the system at time t. Thus for that the payoff P has to be maximized which is shown in the following equation :

$$P(\theta) = \int_0^T H(z(t), \theta(t)) + J(\Phi(\theta(t)))d\theta \tag{1.3.5}$$

where $H(\cdot)$ and $J(\cdot)$ are the running payoff and the terminal payoff respectively [71], which act like the loss and regularization function in (1.3.3).

In this thesis, the proposed computer vision algorithms design the architecture of the networks by solving a fractional optimal control problem. The propagation of features through layers of DCNN is treated as a dynamic system and is represented with the help of a fractional differential system with optimal controls. Consider the following fractional differential system [72] describing the propagation of deep CNN in which the feature trajectory $z(t, s)$ is assumed to be continuous in time and space:

$$\min_{\theta(t)} \int_\Omega L(\Phi(z(T, s)), u(s))\ ds$$

s.t.

$$ {}_0D_t^\alpha z(t, s) = f(z(t, s), \theta(t)),\ \ z(0, s) = \Psi(I(s)),\ \ t \in [0, T] \tag{1.3.6}$$

where $s \in \Omega$ is the two dimensional spatial position, $I(s)$ is the input image, $u(s)$ is the ground truth image and Φ, Ψ are linear transformation , $e.g.$ convolution. The proposed networks are designed by solving the corresponding fractional optimal control problem as the fractional-order differential equation has long-term memory. The problem (1.3.6) aims to find the optimal control $\theta(t)$ such that the objective loss is minimized [73].

The architectures of the proposed computer vision models are designed by discretizing the fractional differential system of equations. Analysis in [74], justifies that the discretizations correspond to the forward propagation of these networks. In each transition, all the features given by the output of the historical states are being used at each state, and thus the features are being used for a long time. Due to the application of fractional derivatives in the evolution process, the network gets embedded with weighted skip connections. Those weights depend on the fractional order of differentiation and the current state. The order α is positive and less than 1, so the weighted sum remains positive and doesn't explode. For discretization, the step size, h is set to be 1. Then definition (1.1.10) takes the following

form for order $0 < \alpha < 1$:

$$ {}_0D_t^{\alpha} z(t,s) \approx \sum_{k=0}^{t} (-1)^k \binom{\alpha}{k} z(t-k,s) \tag{1.3.7} $$

Thus, after combining the above expression (1.3.7) with ${}_0D_t^{\alpha} z(t,s) = f(z(t,s),\theta(t))$ of the system (1.3.6), we get expression (1.3.8) that clearly shows the incorporation of memory into the network.

$$ z(t,s) = f(z(t,s),\theta(t)) - \sum_{k=1}^{t} (-1)^k \binom{\alpha}{k} z(t-k,s) \tag{1.3.8} $$

$$ z_{t+1} = f(z_t,\theta_t) + \sum_{k=1}^{t} (-1)^{(t-k+1)} \binom{\alpha}{t-k+1} z_k \tag{1.3.9} $$

Pontryagin's maximum principle [73] further justifies the long-term memory incorporation into the network. The long-term memory in the network helps prevent the dilution of features, after propagation through multiple layers. Subsequently, this improves the performance of the network. and accuracy of the predictions.

1.3.3 Evaluation Parameters

This section defines the evaluation parameters adopted for measuring the performance of the proposed networks. This thesis analyses the performance of algorithms developed for time series and image data. To measure the performance of computer vision algorithms, the pixels of the predicted images are divided into four categories concerning the ground truth of the saliency map: true positive (TP), true negative (TN), false positive (FP), and false negative (FN). Here, TP denotes the number of correctly detected pixels, FN denotes the number of missed pixels, TN denotes the correctly excluded pixels, and FP is the number of pixels falsely detected. The effectiveness of the proposed methods is evaluated using standard metrics, described below.

Definition 1.3.1. ***(Mean Squared Error (MSE))*** *It gives the average of the squared difference between the actual value and output value which can be expressed as*

$$ MSE = \frac{1}{N} \sum_{i=1}^{N} (x_i - y_i)^2 \tag{1.3.10} $$

where x_i, y_i are output and actual values. It is always positive, and lower values of MSE indicate the good performance of the model.

Definition 1.3.2. ***(Root Mean Squared Error (RMSE))*** *It gives the square root of the average of the squared difference between the actual value and output value. Mathematically, it can be expressed as*

$$RMSE = \sqrt{\frac{1}{N}\sum_{i=1}^{N}(x_i - y_i)^2} \tag{1.3.11}$$

where x_i, and y_i are predicted and actual values, which are observed for N times.

Definition 1.3.3. ***(Mean Absolute Percentage Error (MAPE))*** *is the average percentage of the absolute difference between the actual and predicted value divided by the actual values for each period [75]. The following expression can express MAPE*

$$MAPE = \frac{100}{N}\sum_{i=1}^{N}\frac{|x_i - y_i|}{|y_i|} \tag{1.3.12}$$

where x_i is the predicted value and y_i is the expected output for iteration i, which are observed for N times. This is a form of percentage error, which helps analyze the different models in varying situations.

Definition 1.3.4. ***(Structural Similarity (SSIM))*** *It estimates the level of similarity between two images. Its values lie in $[-1, 1]$. The higher the absolute value of SSIM, the more the similarity. The negative structural similarity scores correspond to inverted local image structures. For two images I_1, I_2 can be computed as*

$$SSIM = \frac{(2\mu_{I_1}\mu_{I_2} + a)(2\sigma_{I_1 I_2} + b)}{(\mu_{I_2}^2 + \mu_{I_2}^2 + a)(\sigma_{I_2}^2 + \sigma_{I_2}^2 + b)} \tag{1.3.13}$$

where μ_i, σ_i are mean and standard deviation of image i, and $\sigma_{I_1 I_2}$ is co-variance of I_1 and I_2.

Definition 1.3.5. ***(Recall (R))*** *It is the ratio of successfully retrieved relevant pixels to the total relevant pixels which can be expressed as*

$$Recall = TP/(TP + FN) \tag{1.3.14}$$

Definition 1.3.6. ***(Precision (P))*** *This metric is also based on relevance, which is given by*

the ratio of successfully retrieved relevant pixels to the total retrieved pixels. Thus it can be expressed as

$$Precision = TP/(TP + FP) \tag{1.3.15}$$

Definition 1.3.7. ***(Mean Intersection over Union (mIoU))*** *It measures the percentage of overlap between the ground truth and the predicted output. It can be evaluated by the following expression* (1.3.16)*. In other words, it is the ratio of the common number of pixels between the expected and predicted output, and the total pixels across both images.*

$$IoU = (target \cap prediction)/(target \cup prediction) \tag{1.3.16}$$

Definition 1.3.8. ***(Pixel Level Mean Absolute Error (MAE))*** *The average pixel-wise absolute difference between the predicted image and the ground truth is termed MAE. It is expressed as*

$$MAE = \frac{1}{XY}\sum_{x=1}^{X}\sum_{y=1}^{Y}|GT(x,y) - PI(x,y)| \tag{1.3.17}$$

where GT is the ground truth, PI is the predicted image, X, and Y is the width and height of predicted image. The smaller the value of MAE, the better the system.

Definition 1.3.9. ***(Precision-Recall (P-R) Curve)*** *The values of precision and recall are computed at different thresholds, and the curve plotted using these precision-recall pairs is called as* ***P-R curve****. A high area implies high precision and recall, equivalent to having low FP and low FN, respectively, thus, the system with the higher area is considered better.*

Definition 1.3.10. ***(F-measure (F_β))*** *This metric is chosen for gauging the similarities between the predicted image and the ground truth. Precision (P) and recall (R) are taken into account in F_β evaluation, which is expressed as*

$$F_\beta = \frac{(1+\beta^2)P \cdot R}{\beta^2 \cdot P + R}. \tag{1.3.18}$$

where β^2 is chosen to be less than 1 for emphasizing more on the precision. More be the F_β score, better be the system. For $\beta = 1$, this score is called the F1-score/ dice coefficient. It is used for testing the efficiency of object/activity detection algorithms. It ranges between 0 and 1. The higher be the value of the F-measure, the more is the efficiency of the algorithm. The F-measure score is determined for each pair of precision-recall data and uses the highest value as the dataset's evaluation score denoted as F_β^{max}. An adaptive threshold

that is twice the mean value of the prediction is used to calculate F_β^{avg}. It reflects the spatial consistency of the predictions. The values of precision and recall are computed at different thresholds and the curve plotted using the values of F-measure corresponding to these precision-recall pairs is called ***F-measure curve****.*

The performance of an authentication system depending on any **biometric modality** is evaluated using the five standard evaluation metrics $viz.$ Correct Recognition Rate (CRR), Equal Error Rate (EER), Accuracy (Acc), Discriminative Index (DI) and Reciever Operating Characteristic (ROC) curve. A comparison of two biometric samples is referred to as genuine if they belong to the same individuals. However, if the comparison is made between two samples belonging to different individuals, it is known as an imposter comparison. All these evaluation metrics are described below.

Definition 1.3.11. ***(Correct Recognition Rate (CRR))*** *The percentage of the test set that gets its actual match at rank-1 is rank-1 recognition accuracy, also known as CRR. Mathematically, it can be expressed as equal to $\frac{C}{T} \times 100$, where C is the number of samples correctly matched at rank-1 and T is the total number of samples matched.*

Definition 1.3.12. ***(Equal Error Rate (EER))*** *The number of imposter matches accepted by the system out of the total number of samples provided is known as the false acceptance rate (FAR). The False Rejection Rate (FRR) is the proportion of genuine samples the system rejects. When the value of FAR and FRR coincides, then that value is referred as the equal error rate (EER).*

Definition 1.3.13. ***(Accuracy (Acc))*** *The accuracy of a recognition system is the ratio of the correctly recognized samples to the total number of samples matched. Mathematically, it is $max\left(100 - \frac{FAR+FRR}{2}\right)$.*

Definition 1.3.14. ***(Discriminative Index (DI))*** *It measures how effectively genuine and imposter matching scores are isolated. It can be mathematically expressed as $\frac{\mu_g - \mu_i}{{\sigma_g}^2 - {\sigma_i}^2}$, where μ_g/ μ_i and σ_g / σ_i are mean and standard deviation of genuine/imposter scores.*

Definition 1.3.15. ***(Reciever Operating Characteristic (ROC) Curve)*** *The parametric plot of FAR against FRR for different decision threshold values refers to the ROC curve. It evaluates the classification performance comprehensively at different threshold values. The area under the ROC curve depicts the error in distinguishing between the classes, therefore it is also called as Error Under Curve (EUC). The system with the lesser area is considered better.*

1.4 Research Gaps

Based on a thorough review[2] of the existing literature, the following gaps were identified:

1. Fractional-order differential models for designing the policies and law enforcement on recidivists have not been researched upon.

2. Effectiveness of Fractional order gradient-based learning algorithm for training ANNs is not yet investigated much.

3. Fractional calculus-based deep learning algorithms have not been explored for computer vision applications such as object detection, image segmentation, and image matching.

4. Real-time robust vision system is still a challenge in matching features of different biometric modalities.

1.5 Thesis Objectives

Based on the identified research gaps, the thesis aims to perceive the applications and possible postulates of fractional calculus in three different areas: criminology, time-series forecasting, and computer vision. To achieve this primary objective, three sub-objectives are framed as follows:

1. To analyze the effectiveness of fractional differential equations methods in modeling crime transmission.

2. Investigate the importance of fractional gradient-based learning in improving the training of Artificial Neural Networks (ANNs).

3. Apply Fractional Calculus based approaches to solve image segmentation, object detection and image matching problems in Computer Vision domain.

The first objective is addressed in Chapter 3, the second is discussed in Chapter 4 and the third objective is addressed in Chapter 5-Chapter 7.

[2]Detailed review of the existing literature is presented in Chapter 2.

1.6 Thesis Contribution

In this thesis, some history-dependent processes are modeled using fractional calculus-based techniques to characterize them accurately. The main contribution of the thesis can be categorized based on the domain, in which fractional calculus is applied.

1. **Criminology:** The primary purpose of crime transmission modeling here is to help understand the facts and analyze, based on the past behavior of criminals and judiciary that how crime rates are expected to vary when specific parameters are modified in the presence of recidivists. The population comprises five compartments: criminal, non-criminal, imprisoned, prison-released, and recidivist. A fractional-order crime dissemination model with the aforementioned compartments is developed to comprehend the complexity of criminal activity and societal behaviors. The historical dependencies of crime transmission in society are modeled by exploiting the memory property of fractional derivatives. The ablation study is performed to obtain adequate imprisonment, especially for repeat offenders.

2. **AQI Prediction:** With sufficient data and computational support, AQI forecasting is being done with deep neural networks. But these methods require learning a large number of parameters. Thus, a simpler and more accurate method is developed in this thesis using a Vanilla RNN. The current level of air pollution in any area also depends on the AQI status in the past. The architecture of vanilla RNN is much simpler than the structure/functioning of an LSTM, but the predictions made by RNNs with fractional gradient-based backpropagation are comparable and sometimes even better than LSTM with the integer-order gradient descent algorithm. With simpler architecture, achieving better results shows the effectiveness of fractional gradient over integer-order gradient descent on time series data.

3. **Sattelite Image Road Segmentation:** The complex backgrounds and occlusion due to buildings, cars, trees , $etc.$, overlapping, interlacing, and shadowing of the clouds, trees $etc.$ in satellite images affect the accuracy of road network extraction. Long-term feature interactions are required to extract roads from the images with complex backgrounds since such interactions can preserve semantic/appearance information. Thus to improve the forward propagation of the features, it is better to reuse the feature extracted at preceding states. A U-shaped densely connected network with fractional-weighted skip connections for satellite image road segmentation is

proposed in this thesis. This work has exploited the memory property of fractional derivatives to prevent the dilution of features after propagation through multiple layers. Experiments show that extracted road networks are continuous and the edge information is preserved even in the presence of occlusions like trees and buildings. The effectiveness of non-local fractional derivatives in the proposed network can be observed from the segmented outputs as there is less loss of information.

4. **Salient Object Detection:** Detecting multiple salient objects of varying scales, from a cluttered background and with sharp boundaries is still challenging. An accurate saliency map production requires low-level appearance and high-level semantic features. Thus an optimal combination of local and global cues is required to extract features effectively. A salient object detection network with a densely connected encoder having fractional derivative-based weighted skip connections and a decoder with multiple modules is proposed in this thesis to improve the quality of features. The network predictions for each fractional α are aggregated using a weighted average ensemble method based on the system's F-measure, to diversify the predictions. The proposed model performs better even in challenging scenarios such as cluttered background, multiple salient objects, low contrast difference between salient objects and background, and foreground/background disturbances. Moreover, it chooses the correct salient objects and produces more complete salient maps due to the simultaneous aggregation of local and local features.

5. **Palmprint Image Recognition:** The non-uniformity in the features of the palm, due to the significant variations in the shape and texture of the palm from person to person, makes it challenging to develop a universal and robust model that can accurately identify all individuals. This paper proposes a palmprint-based authentication system that extracts features from FrDPalmNet, a novel fractional-derivative-based residual network embedded with dual attention modules. The trainable weights of FrDPalmNet are optimized by using large-margin cosine loss with focal loss. This increases the inter-class variations with intra-class similarities. This feature extraction process generates more expressive and discriminative features. The predictions of FrDPalmNet for each fractional α are aggregated using a weighted average ensemble method based on the system's error rate. The effectiveness of adopting the proposed palmprint recognition system is evaluated on unconstrained databases. Results show that the proposed system achieves state-of-the-art performance with uniform accuracy over heterogeneous databases.

1.7 Thesis Organisation

Having discussed the main objectives and contribution of the thesis, this section provides a brief thematic overview of the chapter-wise road map. The thesis organizes the research effort into seven chapters. **Chapter 2** is dedicated to a detailed literature survey of the application of fractional calculus in considered problems. The next five chapters, $i.e.$, Chapter 3 - Chapter 7, address the application of fractional derivatives in criminology, AQI forecasting, road segmentation, salient object detection, and palmprint recognition.

Chapter 3 proposes a five-compartment fractional-order model to analyze the dynamics of crime transmission. The analysis is focused on designing the policies and law enforcement on the recidivists. Subsequently, the stability of the equilibrium points and threshold conditions for the system are determined. Numerical simulations are also performed to validate the theoretical results.

Chapter 4 analyzes the effectiveness of using a fractional gradient descent algorithm in training neural networks for time-series forecasting. The algorithm's efficacy is demonstrated in the data on air quality. In this chapter, five cities of different tiers are considered for AQI prediction. Bengaluru, Kolkata, and Hyderabad are Tier I cities, while Patna and Talcher are Tier II and Tier III cities, respectively.

Chapter 5 proposes a U-shaped densely connected network with fractional-weighted skip connections for satellite image road segmentation. This work has exploited the memory property of fractional derivatives to prevent the dilution of features after propagation through multiple layers. Experiments are carried out on two open-source databases MRD and ORD, with different road structures and backgrounds.

Chapter 6 proposes a salient object detection network with a densely connected encoder having fractional derivative-based weighted skip connections and a decoder with multiple modules for improving the quality of features. Experiments are performed on six benchmark databases with different complexities: ECSSD, HKU-IS, PASCAL-S, DUT-OMRON, DUTS-TE and SOD.

Chapter 7 proposes a palmprint-based human authentication system that uses a metric-based deep learning network, called FrDPalmNet, for feature extraction. The long-term memory of fractional derivatives and the dual attention mechanism is exploited to extract highly discriminative features. The proposed technique is tested on four popular publicly available palmprint databases viz. CASIA, IIT-D Touchless and Tongji-Contactless.

Subsequently, **Chapter 8** provides the overall summary and discusses the potential future scope of the work.

Chapter 2

Literature Review

This chapter presents a detailed review of fractional-order derivative-based techniques in the existing literature. The discussion highlights the advantages of fractional calculus-based algorithms over conventional algorithms. It has been observed that the memory property of fractional derivatives is being exploited in the considered domains. This study shows the successful implementations of fractional calculus and brings out the challenges and future scopes. Application of fractional derivatives is discussed in six different domains $viz.$ crime modeling, backpropagation training algorithm for ANNs and computer vision in Section 2.1, Section 2.2 and Section 2.3 respectively. A summary of the survey is presented at the end of the chapter.

2.1 Fractional Calculus in Crime Tansmission Modeling

Criminologists examined various reasons in the twenty-first century to understand why an individual would commit crimes. Throughout history, individuals have sought to understand why a person will commit crimes in terms of biological, psychological, social, and economic aspects. Greed, anger, jealousy, retribution, or vanity may contribute to a crime being committed. Some individuals tend to commit organized crimes. In the transmission phase, the future condition is strongly linked to a person's criminal history. The likelihood of having a criminal conviction is two times higher in the children of criminal parents than in non-criminal parents [76, 77]. To reduce crime dissemination, the history and experience of the judiciary are also very relevant [78]. Further, to strengthen the proper functioning of jurisdictional agencies, several mathematical models were introduced [3, 79–81]. The previous experiments were conceived as a preliminary investigation based on the ordinary differential equation (integer-order) compartmental crime models.

Conventional mathematical models cannot obtain the higher degree of accuracy necessary to explain the transmission process. Since fractional calculus can better represent and handle the retention and transmission characteristics of different materials than integer-order models [82], fractional differential equations are being used to address this issue. In light of this, two fractional-order crime transmission models are developed to include the history of crime [7, 8].

The model shown in Figure 2.1 is a fractional-order three-compartment model partitioned into three sections: non-offenders (A) indulged in crime/offenders (O) and the imprisoned population (P).

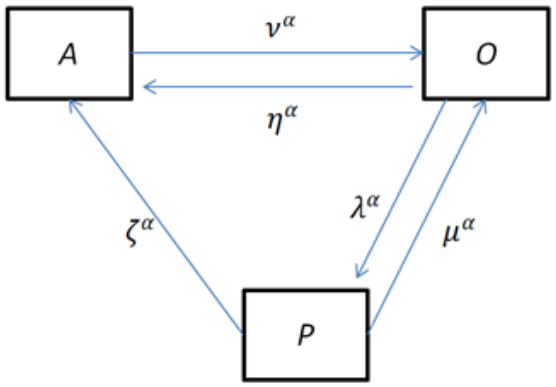

Figure 2.1: Flowchart of the three-compartment fractional crime transmission model [7]

The above fractional-order model is three-compartment, and the equilibrium points are determined using the phase plane method. Further, equilibrium points are classified into low and high-crime equilibriums. The tipping point classifying low and high equilibrium points in the crime transmission fractional model is identified to be the threshold value. The obtained equilibria points help to analyze the impact of criminal activity in the community by altering crucial parameters such as people's incarceration and the release of criminals. One of the critical conclusions of the study is to show that a minute growth in the imprisonment rate tends to lower the spread of crime. Adopting this model by jurisdiction departments and allies may help tackle crime transmission effectively.

In the above model, the behavior of prison-released individuals is not analyzed. Hence, a fractional-order crime propagation four-compartment mathematical model is proposed for analyzing the dynamics of the spread of crime by categorizing the extant population into four subgroups based on their criminal histories. These clusters include law-abiding citizens (non-criminals (X)), criminally active individuals (who have not been imprisoned

(C)), prisoners (P), and prisoners who completed the prison tenure (recovered (R)), shown in Figure 2.2.

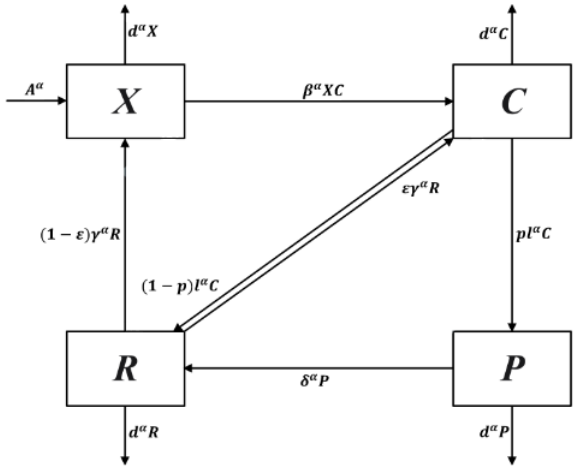

Figure 2.2: Schematic Diagram of the four-compartment Crime Transmission Model [8]

It is assumed that crime can be optimized with proper law enforcement and subsequent treatment. Individuals from the recovered class are believed to transfer to the criminal or non-criminal populations as certain offenders do not change their minds even after rehabilitation. The delay coefficient (τ) is also included in this four-compartment model to investigate the time difference between an individual's crime and judgment. The results of the delayed version of this model suggest that once the delay reaches a certain threshold, the model oscillates periodically. If the order of derivative increases from 0 to 1, the delay decreases, indicating that the model's stability region expands. Further, to consider the role of recidivists in crime transmission, a five-dimensional fractional-order model is developed in this thesis, shown in Chapter 3.

2.2 Fractional Calculus in Training of ANN

This section discusses the application of fractional calculus in improving the training of neural networks. Fractional Calculus has been applied to ANNs due to the long-term memory, or non-locality of fractional derivatives [39, 83–85]. While training of neural networks using the backpropagation algorithm, instead of integer order derivative, the fractional-order derivative is used in the fractional-order gradient-based algorithm, and the update rule becomes

$$\Delta w = -\eta \frac{\delta^\alpha E}{\delta w^\alpha} \tag{2.2.1}$$

where η is the learning rate, and α is the fractional order of differentiation. The fractional derivative was used for the backpropagation algorithm for feed-forward neural networks(FNNs) by Chen $etal.$ [86] in 2013. The simulation results demonstrated that the convergence speed based on fractional-order FNNs was much faster than integer-order FNNs. In 2015, Pu [87] paid attention to the fractional order gradient method. It was observed that this method might not lead to the actual extreme point. Chen [88, 89] rectified this defect using truncation and short memory principle in the fractional-order gradient method. In 2017, Wang $etal.$ [84] used the fractional steepest descent algorithm for training three-layered neural networks and proved its monotonicity and convergence.

Also, Khan $etal.$ [85], proposed fractional-order backpropagation through a time algorithm for Recurrent Neural Networks (RNNs). Year after, Khan $etal.$ [90] proposed a fractional gradient descent-based learning algorithm (FGD) for the radial basis function neural networks. The proposed FGD amalgamates the conventional and the modified Riemann–Liouville derivative-based fractional gradient descent method. In 2018, Bao $etal.$ [91], proposed a deep fractional-order BP neural network with L_2 regularisation term, and the order α can be any positive real number. Caputo's derivative-based fractional gradient method for backpropagation of Convolutional Neural Networks (CNNs) has been introduced, successfully converging to real extreme points [92]. Memory or history plays a significant role in the training of neural networks. Hence, applying fractional derivatives that inherently incorporate history in computation seems meaningful and beneficial for training these neural networks. For dealing with the complexity of history-dependent data, fractional-order neural networks can be used for rigorous analysis.

2.3 Fractional Calculus in Computer Vision

Fractional calculus has been applied in various computer vision domains [93–96], but still, there are many areas where this technique needs to be involved and evaluated for improvement. In 1991, Oustaloup $et\ al.$ laid a cornerstone for the application of fractional calculus in computer vision. They used fractional derivatives for edge detection [97, 98], and since then, it has been applied in various domains of computer vision. Fractional calculus is used in computer vision for enhancement, better detection selectivity, developing robust denoising models, and dealing with discontinuities. Unlike integer-order derivatives, fractional derivatives' non-local nature helps gather past and surrounding information. This section highlights the usage of fractional calculus in three domains $viz.$ image segmentation, image recognition, and object detection, along with a summarization

of the advantages of fractional-order methods for computer vision and image processing which have been used till now.

2.3.1 Image Segmentation

Image segmentation is the process of partitioning an image into multiple segments or sets of pixels. This is typically used to locate objects and their boundaries in images. The segmentation process converts an image into a more meaningful version that is easier to analyze. In an image, there are regions that don't contain any useful information. So processing the whole image is not efficient. By dividing the image into segments, the important segments can be used for processing the image. Image segmentation techniques have made a massive impact on the analysis of medical images and remote sensing images. These techniques help to approach problems in a more granular manner and get more meaningful results. There are several techniques for segmenting an image, such as the threshold methods [99, 117, 118], clustering method, PDE-based methods [119], variational methods and hybrid techniques [120]. The image segmentation techniques, which are based on differential calculus, are being generalized using fractional derivatives.

The most commonly used are optimal threshold methods which segment an image into two or more clusters. These methods search for the optimal threshold values, making the thresholded classes based on suitable characteristics. This is done by optimizing an objective function. Otsu's thresholding method [117] automatically determines an optimal threshold value to separate the pixels of an image into two classes: foreground and background. This threshold is determined by minimizing intra-class intensity variance, or, equivalently, by maximizing inter-class variance. Some other thresholding methods adopt several biological-inspired algorithms when the function that is to be optimized is not continuous, non-differentiable, and contains multiple non-linearly related parameters.

Particle Swarm Optimization (PSO) is a method of optimization inspired by birds flocking in search of food. It consists of several particles that iteratively move in the search space seeking the global optimum. In image processing, pixels of an image act as search space. The objective is to evaluate the threshold value that maximizes the between-class variance of the distribution of intensity levels in the given image. However, PSO and other optimization algorithms have a problem getting trapped on a local optimum so that the algorithm can fail. Fractional derivatives exhibit memory property, so they are more suitable for describing phenomena like irreversibility and chaos. Thus, the dynamic phenomena of the trajectory of a particle build a case where fractional derivatives can be utilized.

Table 2.1: Some benchmarking fractional-order image segmentation methods

S No.	Authors	Methods	Database	Results	Outperformed
1	Ghamisi *et al.* . [99] (2012)	FODPSO	Hyperspectral ROSIS dataset (Pavia)	Average & STD fitness value at level 12 = 3002.73±5.14	Otsu, PSO and DPSO
2	Ghamisi *et al.* . [100] (2013)	FODPSO + SVM	**a)**Hyperspectral ROSIS dataset (Pavia) **b)** Multispectral Worldview images (Australia)	Acc = 96%	PSO+SVM and DPSO+SVM
3.	Ghamisi *et al.* . [101] (2013)	FODPSO + SVM + Mean Shift Segmentation (MSS)	**a)** Hyperspectral ROSIS dataset (Pavia) **b)** Hyperspectral AVIRIS dataset (Salinas)	Accuracy= 98.04% Acc= 96.27%	FODPSO+SVM, MSS+SVM and SVM
4.	Lahmiri *et al.* . [9] (2017)	(PSO, DPSO and FODPSO) + Directional Spectral Distribution (DSD)	Glioma images	Acc = 99.18%	PSO+DSD and DPSO+DSD
5.	Yousri *et al.* . [102] (2020)	FO-FPA + fuzzy entropy	Natural grayscale images	PSNR = 22.93 Average SSIM= 0.806	traditional FPA, Cuckoo Search [103], PSO, GWO [104] and SSA [105]
6.	Perez *et al.* . [106] (2019)	ABC-fractional Gaussian kernel + Cuckoo search [103]	HRF [107] STARE [108] DRIVE [109]	Acc = 95.12% Acc =94.39% Acc =95.97%	nOtsu, Gabor filter and fractional Gaussian derivative method [110]
7.	Shukla *et al.* . [93] (2020)	Weighted fractional derivative mask + local PCA	STARE[108] DRIVE[109]	Acc= 95.73% Acc= 94.74 %	Several traditional methods
8.	Ren *et al.* . [111] (2015)	fractional active contour model	real and synthetic images	visual comparison	C-V model [112], local binary fitting energy model [113] and a level set approach [114]
9.	Chen *et al.* . [115] (2019)	adaptive-weighting fractional active contour model	real ultrasound and synthetic images	dice similarity coefficient metric value = 0.9686 (gaussian noise with SD = 0.1)	CV model [112], local binary fitting energy model [113], a level set approach [114] and a global level set approach [116]

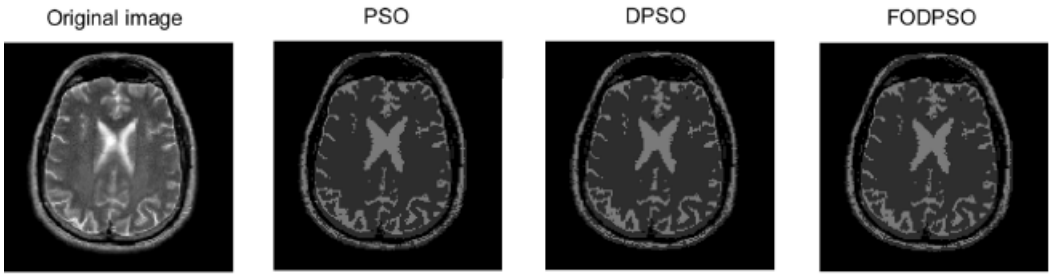

Figure 2.3: Segmentation results on brain MRIs for Glioma detection [9]

One of the best performing PSO variants named Darwinian PSO [121] was extended using fractional calculus to control the convergence rate of the algorithm, denoted as FODPSO [122]. Search methods based on Otsu's thresholding method are simple but are computationally expensive and can get trapped on local optima. To overcome these problems, the two algorithms, DPSO and FODPSO, have been applied to multi-level segmentation [99, 118]. Results showed that FODPSO is more efficient than DPSO, particularly during the increased level of segmentation, making it possible to achieve a better threshold, more stability, and less processing time due to less computational complexity.

As hyperspectral and multispectral images have high dimensions, it is not easy to design algorithms for image segmentation with high accuracy and efficiency. FODPSO has been used to segment such remote sensing images [100]. Moreover, a classification approach based on FODPSO and Support Vector Machine (SVM) has been proposed to show the efficiency of segmentation carried out by FODPSO. It has been observed that SVM classification accuracy is more while using FODPSO for segmentation. Also, as a preprocessing step to the classification of remote sensing images, FODPSO has been integrated with the mean shift variance method of segmentation to overcome drawbacks of both methods, resulting in an increase of accuracy in classification [101]. Glioma detection system based on segmented brain MRIs by FODPSO outperformed other systems based on PSO and DPSO [9]. The results have been validated on brain MRI data obtained from the webpage of Harvard Medical School[1]. So FODPSO has been proven successful in segmenting medical images as well, which can be seen in Figure 2.3. FODPSO has also been used in the preprocessing step of recognizing handwritten polynomials [123]. Firstly, the input image was segmented using the FODPSO technique, and then this segmented image was further used as an input to these CNNs for character recognition. The results

[1]http://med.harvard.edu/AANLIB/

obtained from this recognition method were significant, with an average accuracy of 99 $\%$.

Flower Pollination Algorithm (FPA) is another biologically inspired algorithm recently integrated with fractional calculus to benefit from the memory properties of fractional derivatives [102]. The search abilities of FPA were enhanced, and the algorithm became adaptive in terms of FPA exploration and exploitation chores. This FO-FPA has been used for multi-level image segmentation by evaluating thresholds that divide the image into a set of classes. FO-FPA outperforms the other meta-heuristic methods such as PSO, Cuckoo Search, and traditional FPA.

Fractional calculus is being leveraged in the pre-processing step before the image segmentation. A method to detect blood vessels in retinal images based on the Atangana–Baleanu fractional derivative with fractional Gaussian kernel has been presented [106]. In this method, a fractional derivative-based Gaussian mask has been proposed to denoise the image. The enhanced image has been segmented manually and by using other segmentation methods. This method provided two degrees of freedom due to different derivative orders while evaluating the gradient and Gaussian kernel. This segmentation method performed well for various kinds of images, whether noisy or with other lighting conditions. The technique has been tested on two databases. The STARE [108] database consists of 400 raw fundus images collected by the Shiley eye center at the University of California and the Veterans Administration Medical Center in San Diego. The database has a list of diagnoses along with the diagnosis code and results of blood vessel segmentation for 40 hand-labeled images. The DRIVE database [109] contains images of diabetic retinopathy collected from diabetic retinopathy screening programs in the Netherlands. A Canon CR5 non-mydriatic 3CCD camera with a 45-degree field of vision was used to collect data from 400 diabetic participants aged 25 to 90. The proposed technique has obtained The average accuracy of 95.58% and 95.97% was attained for vessel segmentation on STARE [108] and DRIVE [109] databases. Another fractional filter-based efficient algorithm has been presented for retinal blood vessel segmentation in [93]. Saving thin retinal vessels and noise removal simultaneously in the segmentation process is a challenging task. Firstly, the fractional filter is applied to the gray image of the input retinal image to overcome this problem. This fractional mask removed the noise and preserved the fine details and edges simultaneously. The rest of the processing steps' performance, like Principal Component Analysis (PCA), is enhanced by using this noise immune fractional mask. The average accuracy of 95.73% and 94.76% on STARE and DRIVE databases was attained for vessel segmentation. This algorithm was

computationally efficient and relatively better than the other state-of-the-art methods of retinal image segmentation. Being non-adaptive is the only limitation of this algorithm. This limitation can be further overcome, and the technique can be improved by introducing an adaptive function corresponding to the fractional filter.

Besides these, the other method for image segmentation is by means of active contour models using level sets. The basic idea of such models is detecting objects in an image by developing a curve, subject to some constraints derived from the input image. The curve evolution equation is derived from the minimization problem for the energy function defined on the level set function. The Chan-Vese (CV) [119] model is a popular region-based level set model for image segmentation. The model is robust to initial contours and noise, and here regions are assumed to have piece-wise constant intensity. But real-world images have intensity inhomogeneity. For such images, the CV model is not efficient for segmentation. To deal with this problem, various other models have been proposed. A generalized CV model with a fractional-order derivative term has been introduced to the energy function as a regularisation term. This fractional-order gradient term helps preserve low-frequency features and texture, which leads to better extraction of image details when intensity inhomogeneity exists [124].

Another active contour model based on fractional-order differentiation consisting of the energy functional with the global fitting term and fractional-order derivative term as regularization term has also been introduced [111]. The model captured details of intensity inhomogeneous images more accurately. For segmentation of inhomogeneous images, a Fourier domain fractional differentiation based adaptive-weighting active contour model has also been proposed [115]. The energy function is the sum of the regularization term for smooth curve evolution, with the local term and global information term having corresponding weights that are automatically adjusted. This model's energy fitting term is the amalgamation of the fractional order differentiation, the fractional-order gradient magnitude, and the difference image into the CV model. As fractional-order derivative preserves and enhances the low-frequency features in an excellent manner [124], thus this helps in the segmentation of intensity inhomogeneous images. The magnitude of the fractional gradient also has the memory property of fractional differentiation. This property makes the process immune to noise. Similarly, when the image with fractional order gradient magnitude image is subtracted from the actual image, the image becomes smoother than the true image. Also, the contrast of this difference image is better than the contrast of the difference image obtained while using integer-order differentiation

Table 2.2: Some benchmarking fractional-order object detection methods

S No.	Authors	Methods	Database	Results	Outperformed
1	Guan *et al.* . [128] (2012)	FrFT based ALE	Sea clutter data (recorded by the McMaster University IPIX radar)	SCR = - 6db	traditional amplitude detector and CA-CFAR detector [129]
2.	Yu *et al.* . [130] (2018)	SFrFT	Radar target	SNR = -3db	DFrFT
3.	Ratre *et al.* . [131] (2018)	FKSOM	UCSD AD [2]	MOTP = 0.989 Av Acc = 0.934 Sensitivity = 0.929 Specificity=1.	SOM and Deep Belief Network [132]
4.	Lingaswamy *et al.* . [133] (2020)	Gaussian denoising filters + fractional derivatives for forward and backward tracking + Otsu,	Human motion videos	Acc $\in [93.6, 97.3]$	Traditional object tracking methods
5.	Takeda *et al.* . [12] (2019)	Fractional anisotropic filter	Real videos like Drone, gun and 4 synthetic ball videos	PSNR=46.5	Acceleration[10] and Jerk [11]
6.	Chen *et al.* . [89] (2018)	FrQZM	FAU [134] GRIP [135]	F-measure = 0.953 F-measure = 0.939	Forgery detection methods [135–138]

[3]The UCSD image database is available at the following link: http://www.svcl.ucsd.edu/projects/anomaly/dataset.htm

magnitude [115]. The segmentation results were satisfactory for inhomogeneous intensity images, but the model didn't perform well for unevenly illuminated images. The order of differentiation was still chosen manually between 0 and 1. Some benchmarking works mentioned above are summarized in Table 2.1.

The state-of-the-art image segmentation networks involve, Transformers [125] such as BEiT [126], and OneFormer [127], which are deep neural networks. Fractional calculus can be integrated with deep learning architectures for image segmentation like in FOCNet [5]. Fractional calculus-based image denoising techniques can also be adopted to improve the pixel classification accuracy during segmentation.

2.3.2 Object Detection

One of the most exciting problems of computer vision and image processing is *object detection*. It is the technique of classifying and detecting multiple objects of a specific class in an image or a video. Feature extraction can be performed using various techniques,

including: 1) Handcrafted feature extractors like Histogram of Oriented Gradients (HOG), Scale-Invariant Feature Transform (SIFT), Speeded-Up Robust Features (SURF), and Local Binary Patterns (LBP); 2) Dimensionality reduction techniques like PCA, Linear and Discriminant Analysis (LDA); 3) Deep learning algorithms like CNNs. Due to the non-locality of fractional differentiation, as mentioned before, fractional calculus-based techniques have been used in pre-processing steps of object detection algorithms for more accurate feature extraction, and significant results are obtained. This section describes the fractional calculus-based pre-processing steps for detecting objects in different areas such as moving object detection, object tracking, and subtle change detection in the videos etc.

Fractional Fourier Transform (FrFT) transforms a function defined in the time/frequency domain into a domain between frequency and time. Thus it provides a way of measuring the angular distribution in the time-frequency plane. It offers an extra degree of freedom of choosing any rotation angle, further improving results compared to when ordinary Fourier transform is used. High dimensional echo data of radar can be sparsely represented in the Fourier domain to reduce the computational complexity. On the same grounds, sparse Fractional Fourier Transform (SFrFT) was proposed and used for Moving Target Detection in radar images [130, 139]. The SFrFT-based method was found to be computationally less complicated and had significant clutter suppression ability, thus producing the desired output.

Anomaly detection in video surveillance is not an easy task. A three-step hybrid model has been presented in [131], starting with object identification and tracking, then followed by feature extraction. A Fractional Kohonen Self-Organizing Map (FKSOM) has been proposed for localizing anomalies in video surveillance. FKSOM is developed by using fractional calculus in the weight update process of SOM (an ANN developed by Kohonen). It organizes the features extracted by the tracking model to check for any abnormal behavior in the video. The performance of pattern matching and filtering gets enhanced by the application of fractional derivatives. This algorithm performs better than SOM and Deep Belief Network [132]. Desired values of evaluation parameters- accuracy, sensitivity, and specificity- were obtained.

Fractional calculus has been successfully applied to license plate recognition [140]. The license plate quality is generally low due to various factors such as improper illumination conditions, weather conditions, and background. So to improve detection accuracy, there is a need for edge enhancement in plate images. Image enhancement studies the sudden changes in pixel values to enhance image quality. Evaluation of derivatives is

well-known for measuring such abrupt changes. Fractional derivatives have long memory properties, so they are expected to portray such changes better. A mathematical model for text detection involving Reisz fractional operator for enhancement has been developed. It is based on the idea that the real and complex number power of derivatives can be used to examine the rapid changes in license plate images caused by several factors. Experiments on benchmark license plate image databases showed that the model performed better than the existing enhancement techniques. The edges on license plate images are enhanced even in different distortions, thus improving license plate detection and recognition performance. The best character recognition rate of 77.38% was obtained for ICDAR 2015-SR dataset [141] after enhancement by this Reisz fractional operator.

The properties of fractional derivatives have been exploited for improving the results for moving object detection and object tracking involving forward and backward tracking [133]. In this approach, the input video is divided into different frames, and then each frame is first denoised by Gaussian filters. After denoising, fractional derivatives are evaluated for forward and backward tracking, and the absolute difference is figured out. The results from forward and backward tracking are pooled together to get the final product. The resultant image is then segmented using Otsu's thresholding method, and the object is detected on each frame. The performance of this method was found to be significantly better than the traditional strategies.

Fractional calculus has been applied to video magnification as well. Video magnification is a technique to observe the subtle changes in the video, invisible to the naked eye. While capturing, these subtle changes get mixed up with the noise. Traditional methods also consider non-meaningful subtle changes occur due to photographic noise and thus give misleading results. Also, the temporal distribution of meaningful subtle changes is regarded as anisotropic diffusion. Based on these observations, a fractional anisotropic filter has been proposed for detecting only significant subtle changes [12] as in Figure 2.4. The filter produced remarkable magnification results and was much better than those obtained with state-of-the-art methods. But still, the process had some limitations. Firstly, the estimation of co-variance in fractional anisotropy was not immune to outliers. Secondly, it performed slowly for large-sized videos. Most importantly, it assumed the distribution of noise to be having isotropic diffusion, and this assumption can also result in misleading results. Fractional calculus has been applied to copy-move forgery and its automatic detection as well [89]. Fractional Quaternion Zernike Moments (FrQZM)'s results were found to be superior to various existing algorithms, but better results can be

expected using a deep learning approach in this model.

State-of-the-art deep learning algorithms for real-time object detection include YOLOv4 [142] in terms of time estimation and quality of results on the MS Coco dataset [143]. At the same time, the best pedestrian detection results are obtained by Beta R-CNN [144]. YOLO [145], RetinaNet [146] and Fast RCNN [147] are some of the milestones in the cutting edge of object detection. The architecture of the above state-of-the-art model can be used with fractional derivatives for feature extraction. like in FOCNet [5], the network layers are connected via fractional-weighted skips. The weights are obtained from the definition of the G-L fractional derivative. Some benchmarking object detection methods mentioned in this section are summarized in Table 2.2.

2.3.3 Image Recognition

Image recognition is a classical computer vision problem of pattern recognition. It determines whether a particular object, activity, or feature is contained in the image or not. It is a combined task of first detecting and then classifying the object or activity. There are numerous methods of image recognition. Generally, a feature vector is extracted for image recognition. For feature extraction, dimensionality reduction is the most popular machine learning method. The image is decomposed into a composition of a set of base images. The dimensionality reduction methods like PCA, Linear Discriminant Analysis (LDA), and some kernel-based non-linear feature extractors like SVM, kernel-PCA, and kernel discriminant analysis have caught much attention. Such methods may lead to poor classification performance in case of significant variations, say, variations in illumination, facial expressions, age, facial hair, and poses. The image gray value matrices are very sensitive to such variations. For instance, in face recognition, prominent facial variations such as occlusion, lighting, expressions, and so on affect these ML methods' performance [148, 149]. To address these problems, fractional calculus has been used for the dimension reduction of an image.

For instance, the Fractional-order Embedding Canonical Correlation analysis (FECCA) method is built for multi-view dimensionality reduction and recognition [150]. Between-set and within-set samples, covariance matrices are used in dimensionality reduction, which helps in recognition. But these matrices suffer from noise disturbance. Due to less availability of training samples, matrices deviate from true ones. During canonical correlation analysis, these biased estimates deteriorate the learning for dimensionality reduction. To reduce the adverse effects of biased estimates, fractional calculus is employed to correct eigenvalues and singular values of covariance matrices and then reconstruct the covariance

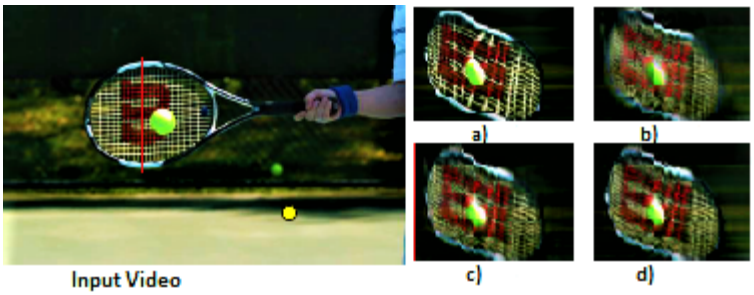

Figure 2.4: Comparison of magnification results. a) Original b) Acceleration [10] of and c) Jerk [11] d) Fractional method in [12]

matrices. This method outperformed the existing Canonical Correlation Analysis (CCA) methods and joint dimensionality reduction techniques pertaining to classification accuracy. Another successful development of the fractional calculus-based dimensionality reduction method is seen in digital holograms. A digital hologram encapsulates the complete information of a three-dimensional object into a two-dimensional complex fringe pattern. Under the aegis of digital Fresnel holography, three-dimensional objects are recognized using fractional Fourier transform-based correlators: Joint Fractional Correlator(JFC) and Non-linear Joint Fractional Correlator (NJFC) [151]. On comparing the recognition performance, the non-linear fractional correlator distinguished similar objects more easily than the linear fractional correlator.

Furthermore, in image recognition, some techniques have been developed that produce the intermediate representation between the original grayscale image and the dimensionality reduction methods. Singular Value Decomposition (SVD) is the most well-known technique to obtain such image representation. Every image matrix can be decomposed into a set of base images by SVD. On these grounds, the image matrix can be viewed as a composition of a set of base images. Among these base images, some leading images correspond to high singular values. These leading images, which represent the original image matrix, are more prone to sensitivity. Thus great variations affect the process of feature extraction. To overcome this, the fractional parameter α has been introduced to SVD for developing the intermediate representation of the image in [152]. With this parameter's help, the weights of variations in the leading base images are deflated to reduce the effects of variations. The fractional parameter α is chosen based on the database and methods to be implemented for the recognition. The effectiveness of using this fractional-order SVD representation has been analyzed for many facial recognition methods, such as PCA and LDA. The results showed significant improvement in the classification performance in the presence of high facial variations.

Gabor filter is another way of extracting features, that employs a linear filter for texture analysis, which essentially means that it analyzes whether there is any specific frequency content in the image in specific directions in a localized region around the point or region of analysis. Gabor filter has been integrated with fractional power polynomial and fractional Fourier transform to improve its feature extraction capability. The fractional Power Polynomial (FPP) model and Gabor filter have been used with kernel discriminant analysis and kernel PCA for reducing the dimension of features [153, 154]. By combining fractional Fourier transform with the discrimination analysis technique of dimension reduction, a face recognition approach has been developed [155]. This Gabor filter can also be integrated with fractional-order SVD to obtain better intermediate representations of the image matrix.

Recently, feature extractors based on moments are catching attention. The moment is a type of image transform that projects an image into the frequency domain using orthogonal or non-orthogonal polynomials, either in cartesian or polar coordinates. Image reconstruction using non-orthogonal moments is challenging to carry out. Moreover, these moments make the process noisy. On the other hand, orthogonal moments are obtained from a set of orthogonal polynomials that can represent images with the minimum amount of information redundancy and high noise robustness. Orthogonal moments defined in polar coordinates have the advantage of being rotation invariant. Zernike Moments (ZM) radially shifted Legendre polynomials and Chebyshev–Fourier moments are familiar orthogonal moments in polar form. The fractional framework of above mentioned moments has also been presented, and experiments show that while extracting features, fractional-order orthogonal moments reconstruct the image with high accuracy and recognize the image robustly [167]. A leaf disease classifying model has been developed based on Fractional-order Zernike Moments (FZM) [165]. Features are extracted using FZM, and then further SVM has been used for classifying the disease. The results show that the FZM-SVM algorithm outperforms other state-of-the-art methods, including integer-order ZM, SIFT, HOG, and SURF, with 97.4% accuracy at moment order 30 and differential order 2.5. Another fractional-order moment presented for image analysis is Chebyshev moments [163]. This fractional-order Chebyshev moment performed significantly well in image representation and pattern recognition with high robustness to noise. In the future, other fractional-order moments can be derived and used for feature extraction.

The fractional differential theory has been used in designing the PCA-SVM coupling algorithm. In [166], a fractional differential mask operator has been developed for edge

Table 2.3: Some benchmarking fractional-order image recognition methods

S No.	Authors	Methods	Database	Accuracy	Outperformed
1	Liu *et al.* . [153] (2004)	Gabor based Kernel PCA + FPP	FERET [156] CMU PIE [157]	99.5% 95.3%	PCA, kernel PCA, Kernel PCA with FPP, Gabor based PCA and Gabor based Kernel PCA with polynomial kernel
2	Jing *et al.* . [155] (2006)	FrFT + discriminant analysis technique	ORL [158] FERET [156]	97.5% 82.63%	Eigen-face, fisher face, DLDA and Fourier LDA
3.	Liu *et al.* . [152] (2008)	Fractional SVD	FERET [156], AR [159] and YALE [160]	80.92%	OGVM and SV
4.	Li *et al.* . [154] (2012)	Gabor filter + FPP based kernel discriminant locality preserving projection	ORL [158]	96.7%	PCA, kernel PCA, LDA and KDA
5.	Yuan *et al.* . [150] (2014)	FECCA	CENPARMI, UCI, AR [159], AT&T [161] and COIL-20 [162]	93.4%, 98.1%, 98.4%, 96.35% and 98.17% resp.	CCA, generalized CCA, Regularized CCA and locality preserving CCA
6.	Kumar *et al.* . [151] (2015)	NJFC with digital fresnel holography	-	(Peak to side lobe) 78.25	JFC
7.	Benouini *et al.* . [163] (2019)	Fractional-order chebyshev moment (FCM) and Moment Invariants(MI)	MPEG-7 [164] COIL-20 [162] Butterfly	90.1% 86.22 57.05%	Legendre MI, Gegenbauer MI, Discrete Tchebichef MI, Discrete Krawtchouk MI and Geometric MI
8.	Kaur *et al.* . [165] (2019)	FZM + SVM	Grape leaf database (from plant village website)	97.4%	SIFT, SURF and HOG
9.	Hu *et al.* . [166] (2019)	Fractional-order-PCA-SVM	ORL [158]	99.24%	PCA-NN, Sobel-SVM, Sobel-PCA-NN, fractional-order PCA-NN and fractional-order-SVM

detection in highly self-similar images. PCA is applied for feature extraction, and then these images are recognized using the SVM algorithm. The fractional differential mask helped fast extract facial features, even in variable illumination and expressions. Signifi-

cant improvement in speed and accuracy of recognition was observed on account of the fractional-order-PCA-SVM coupling algorithm. All the methods mentioned in this section are also shown in Table 2.3.

The above-mentioned methods are mostly machine learning-based algorithms, but currently, deep learning methods are outperforming other recognition methods. ViT-G/14[168] and FixEfficientNet-L2[169] are state-of-the-art deep learning models for classification. But even these deep learning models don't perform well while recognizing objects in a noisy image and small size objects in a large image. Therefore to improve recognition abilities, these deep learning techniques can be integrated with fractional calculus.

2.4 Summary

This chapter presents a thorough review of existing literature related to the application of fractional calculus in criminology, training algorithms of ANNs, and computer vision domains $viz.$ image segmentation, object detection, and image recognition. Based on the survey of fractional-order crime transmission models, it has been observed that the role of recidivists is not analyzed with historical consideration. The policies and rehabilitation programs can be designed separately for such criminals by developing fractional-order models. In the case of neural network training algorithms based on fractional calculus, it is noted that it is beneficial to use those algorithms in the cases of history-dependent data. Moreover, it is observed that the applications of these algorithms are not investigated much. In computer vision domains, it is observed that the synergy of deep learning and fractional calculus is not explored. The memory property of fractional calculus can be utilized for enhancing the memory of deep neural networks and preventing information loss. Therefore, fractional calculus can be used to improve the feature extraction capability of the deep neural networks from the images and develop state-of-the-art models. All these identified gaps are addressed in this thesis chapter-wise.

A part of this chapter is published in the following referred publication:

Sugandha Arora, Trilok Mathur, Shivi Agarwal, Kamlesh Tiwari, and Phalguni Gupta. "Applications of fractional calculus in computer vision: A survey." Neurocomputing 489 (2022): 407-428 (I.F- 6, SCI-Q1, Elsevier)

Chapter 3

Crime Transmission Modeling

There is no such simple or universal definition of crime. For various purposes, legitimate definitions of crime have been stipulated. The most widely held belief is that crime is a legal category, that is, some act is a crime if it is proclaimed as such by the relevant and applicable legislation. Human trafficking, theft, fraud, kidnapping, rape, conspiracy, first-degree murder, domestic abuse, child abuse are major crimes. It has been analyzed that inequality in society and the lack of employment also lead to increased materialistic crimes like vehicle theft, robbery *etc.* [170]. Modeling the prevalence of crime is a multidisciplinary task as crime is a social issue. Thus it necessitates a comprehension of the social structure and economic factors promoting the dissemination of crime.

The theories behind the development of crime transmission models for increasing the efficiency of law enforcement and criminal justice have been discussed in [171]. 'Broken window theory' is the most widely adopted criminological theory, introduced by Wilson and Kelling [172]. It states that multiple broken windows are likely due to a single damaged window. The theory has linked the broken window to the insufficient monitoring of the target population, leading to a rise in the crime rate. The notion is demonstrated by using a variety of examples and anecdotes. The effect of minor features concerning urban chaos is illustrated in spreading anti-social behavior and perilous crimes. Blumstein's work is focused on modeling the recidivism process with the help of criminal data [173]. He has proposed the modification of the deployment of police forces and accordingly advised policymakers on incarceration to reduce crime. In general, it is believed that the increase in prison length leads to a decrease in the rate of crime spread. But it has been reviewed and concluded that length of imprisonment deters crime but weakly [174]. This means that a specific optimal value of the length of the prison exists, which can reduce the

crime spread. Thus models are now developed to obtain an optimal prison length [79].

Over the past few years, several mathematical models have been introduced to control and comprehend criminal activities [175–178]. For example, the evolution of regional heterogeneity in criminal behavior was studied using innovative reaction-diffusion systems [179, 180]; approaches based on game theory have been applied to better understand criminal behavior [81, 181, 182]; and differential systems have been developed to model the dynamics of the spread of crime in a society [1, 3, 183]. Extensive use of statistical tools has also been seen in the analysis of criminal data [184, 185].

Although numerous factors influence crime transmission in society, this is evident that it is propagating like an infectious disease. There is a spike in the number of criminal activities, thus motivating the jurisdiction's design of several new policies. To control the spread of crime, it is required to analyze the factors leading to its propagation including the several past stages of criminal behavior. A criminally active individual's contact may impact the behavior of others adversely. Therefore, the future state highly correlates to an individual's criminal history in the transmission phase. Very few models [7, 8] have considered the history of criminals and criminal justice, one of the significant factors that decide the future state of crime transmission in society. In these works, fractional differential equation-based systems have been developed to model crime propagation. The memory property and non-local behavior of fractional derivatives assist in effectively modeling the history-dependent dynamic systems [44, 47]. Non-locality means that the current and past behavior of the function determines the future state of the function. In addition, the models based on fractional differentiation provide an additional degree of freedom due to different fractional orders. Further, it is noteworthy that fractional-order derivatives model the physical engineering processes superior to that of ordinary derivatives [32].

Pritam *et al.* [7] proposed an essential fractional-order crime transmission model with three states of criminal activity. Based on crime involvement and imprisonment, along with considering the criminal history of any member of the population, they divided the population into three compartments, $viz.$ non-criminal population, criminal population, and imprisoned population. They used phase-plane analysis to evaluate the equilibria of the model and employed the Lyapunov function to determine the threshold conditions. Bansal *et al*. [8] proposed a four-compartment fractional-order model for analyzing the spread of crime with an additional factor of time delay between the occurrence of criminal activity by an individual and their imprisonment. In addition to criminal, non-criminal,

and imprisoned, they considered the population released separately. They have analyzed the stability of equilibria of the delayed model. The existing crime transmission fractional-order differential models have not considered the possibility of recidivism in society. It has been observed that past offenders are relapsing into crime either due to ineffective or severe punishments [186]. Hence, it is essential to evaluate the adequate subjection amount of 'stick' and 'carrot' on criminals [187]. Specifically, in addition to imprisoning criminals with appropriate prison length, there is a need to rehabilitate and integrate past offenders into society. Therefore, a five-compartment fractional-order crime transmission model is developed in this chapter to analyze crime spread in the presence of recidivists. The contributions of the chapter are highlighted below:

1. In this work, a 5-D fractional-order crime dissemination model is developed to comprehend the complexity of criminal activity and behaviors in society. The history dependencies of crime transmission in society are modeled by exploiting the memory property of fractional derivatives. The population is divided into criminal, non-criminal, imprisoned, prison-released, and recidivist.

2. Routh–Hurwitz criteria [51, 52] with Matignon conditions [50] are employed to analyze the model's equilibrium points and evaluate the threshold conditions. The extended Lyapunov function approach is also used to determine the global stability of the fractional-order system and the corresponding threshold condition for a crime-free society. Results show that the fractional-order crime dissemination model is uniformly asymptotic stable.

3. The primary purpose of crime transmission modeling here is to help understand the facts and analyze how crime rates are expected to vary when specific parameters are modified in the presence of recidivists. The ablation study is performed to obtain adequate imprisonment, especially for repeat offenders.

4. Numerical simulations are also carried out for the stability analysis of the model with different fractional orders α. The memory effect due to different orders is observed in the spread of crime and thus on the population of criminals. Numerical results show that the derivative order α can be used to avoid ineffective punishments.

The chapter is structured as follows: Section 3.1 describes the proposed fractional-order crime dissemination model; The existence, uniqueness, non-negativity, and boundedness of the solution are proved in Section 3.2; Section 3.3 explains the theoretical results

related to the stability of crime-free and endemic equilibrium of the proposed model; The stability analysis of endemic equilibrium is done with the help of numerical simulations in Section 3.4; The ablation study is discussed in Section 3.5 accompanied by the concluding remarks.

3.1 Proposed Fractional-order Crime Transmission Model

Crime spreads in society like a communicable disease. A person with a criminal background may affect or influence someone with no criminal background. Thus it is required to imprison the criminals to control the spread of crime for some period of time. But after imprisonment, they get released and then can assimilate back into society or can again indulge in criminal activities due to ineffective or severe punishments. Hence, it is required to keep a check on the criminals released from prison and then further on the recidivists. For modeling the dynamics of the crime spread in society, these five sub-populations are needed to be focused and the policies are to be designed for each set of populations separately such as different rehabilitation programs, different prison lengths $etc.$ Unlike existing crime transmission differential models, the developed fractional dynamic system (3.1.1) helps investigate historic and simultaneous effects of imprisonment, length of prison, recidivism, contagion, history of criminals, and jurisdiction on crime transmission.

The conventional integer-order crime transmission model is taken from [79], and the fractionalizing procedure given by Dokoumetzidis *et al.* [188] is adopted for developing the proposed crime transmission fractional differential model and for analyzing the dynamical aspects of the final fractionalized differential system. The proposed fractional-order differential system demonstrates crime propagation in society based on an individual's criminal record and imprisonment by classifying the total population into the following classes:

- A : Law abiding people
- O_1 : Non-Incarcerated criminals
- P : Incarcerated criminals
- O_2 : Repeat offenders
- R : Released people

Figure 3.1 displays the population flow between the bifurcated classes. Five sub-populations *viz.* non-criminals, non-incarcerated criminals, prisoners, recidivists, and

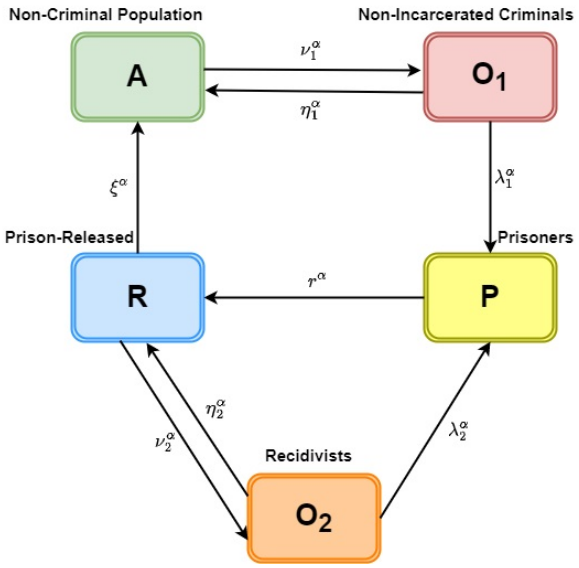

Figure 3.1: Schematic diagram of the fractional-order crime transmission model

prison-released are shown in green, red, yellow, orange, and blue colored boxes respectively. Arrows with the flow rate over it show the flow of the population to other compartments. The system (3.1.1) represents Caputo's version-based fractional-order crime transmission model with five classes where α is the fractional order which lies in $(0, 1]$. The dimension of all the population-based parameters A, O_1, P, O_2, R, and N used in the proposed fractional crime transmission model is aligned with the conventional integer-order crime transmission model [79]. Therefore, the incoming and outgoing flux for a class is not violating the population balance. It can also be seen from the L.H.S. of the system that the fractionalized system satisfies the power-law kind of system dynamics and the population of the classes is in fractional time with dimension $t^{-\alpha}$. Further, every parameter in the R.H.S. of the system has power α to keep the system dimensionally balanced because the rate of change of any population concerning time has dimension t^{-1}.

The first equation of the system (3.1.1) depicts the flux of non-criminal class A. Law-abiding citizens can indulge in criminal activities due to social interaction with other criminals at the rate ν_1. The term $\nu_1^\alpha \frac{A(O_1+O_2)}{(N-P)}$ captures the change in population due to contact of innocent citizens with other criminals. People indulging in criminal activity for the first time can return to the non-criminal class without punishment, at rate η_1, and the term $\eta_1^\alpha O_1$ captures this flux. The first-time offenders are caught at the incarceration rate λ_1. The second equation of the system (3.1.1) is the sum of terms relating to a contagion effect, non-contagion effect, resistance, and incarceration, which depicts the flux of the criminal population/ offenders.

$$
\begin{aligned}
{}_0^C D_t^\alpha A(t) &= \eta_1^\alpha O_1 - \nu_1^\alpha \frac{A(O_1+O_2)}{(N-P)} + \xi^\alpha R \\
{}_0^C D_t^\alpha O_1(t) &= -\eta_1^\alpha O_1 + \nu_1^\alpha \frac{A(O_1+O_2)}{(N-P)} - \lambda_1^\alpha O_1 \\
{}_0^C D_t^\alpha P(t) &= \lambda_1^\alpha O_1 + \lambda_2^\alpha O_2 - r^\alpha P \\
{}_0^C D_t^\alpha R(t) &= r^\alpha P + \eta_2^\alpha O_2 - \nu_2^\alpha R - \xi^\alpha R \\
{}_0^C D_t^\alpha O_2(t) &= \nu_2^\alpha R - \lambda_2^\alpha O_2 - \eta_2^\alpha O_2 \\
N &= A + O_1 + O_2 + P + R
\end{aligned}
\tag{3.1.1}
$$

The third equation of the system (3.1.1) captures the change in the prison population occurring due to the imprisonment of first-time and repeat offenders and the release of prisoners after punishment at a rate r. The fourth equation of the system (3.1.1) captures the change in the current prison-released population. The prison-released people can indulge in criminal activities again at rate ν_2 due to their natural tendency, independent of interactions with other criminals. The term $\nu_2^\alpha A$ captures the change in population due to the non-contagion effects. The prison-released people move back to society at the rate η_2 after punishment and rehabilitation programs, the term $\eta_2^\alpha O_2$ captures this flux. The repeat offenders are caught at the incarceration rate λ_2. The last equation of the system shows the assumption that the total population remains constant. It can be observed that all the equations of the system are dimensionally balanced and thus, the model is well-posed.

Table 3.1: Parameter elucidation: Parameterization of the population flows

Parameter	**Elucidation**
ν_1	Crime indulgence rate due to social interactions
η_1	Rate of assimilating back into society from criminal class O_1
λ_1	Law-enforcement rate
r	Prison-release rate
ν_2	Rate of crime indulgence of prison-released people
η_2	Rate at which recidivists become criminally inactive
λ_2	Law-enforcement rate on recidivists
ξ	Rate of moving back to society after releasing from prison

3.2 Analysis of Solution

This section shows that the solutions of the system (3.1.1) are not only existent but also unique, non-negative and bounded. Let $X(t) = (A(t), O_1(t), P(t), R(t), O_2(t))$ and $\Omega_+ = \{X(t) \in \Omega \subseteq \mathbb{R}^5 : X(t) \geq 0\}$.

3.2.1 Existence and Uniqueness of Solution

Theorem 3.2.1. *If $X(t) = (A(t), O_1(t), P(t), R(t), O_2(t))$ there exists a unique solution of system (3.1.1) with initial condition $X(t_0 = 0)$.*

Proof. Consider the following system with each equation assumed to be represented by a function $f_i(t, A(t), O_1(t), P(t), R(t), O_2(t))$.

$$\begin{aligned}
{}_0^C D_t^\alpha A(t) &= \eta_1^\alpha O_1 - \nu_1^\alpha \frac{A(O_1+O_2)}{(N-P)} + \xi^\alpha R = f_1(t, A, O_1, P, R, O_2) \\
{}_0^C D_t^\alpha O_1(t) &= -\eta_1^\alpha O_1 + \nu_1^\alpha \frac{A(O_1+O_2)}{(N-P)} - \lambda_1^\alpha O_1 = f_2(t, A, O_1, P, R(t), O_2) \\
{}_0^C D_t^\alpha P(t) &= \lambda_1^\alpha O_1 + \lambda_2^\alpha O_2 - r^\alpha P = f_3(t, A, O_1, P, R, O_2) \\
{}_0^C D_t^\alpha R(t) &= r^\alpha P + \eta_2^\alpha O_2 - \nu_2^\alpha R - \xi^\alpha R = f_4(t, A, O_1, P, R, O_2) \\
{}_0^C D_t^\alpha O_2(t) &= \nu_2^\alpha R - \lambda_2^\alpha O_2 - \eta_2^\alpha O_2 = f_5(t, A, O_1, P, R(t), O_2)
\end{aligned} \tag{3.2.1}$$

To prove the Lipschitz continuity, consider the function f_1

$$\begin{aligned}
&|f_1(t, A, O_1, P, R, O_2) - f_1(t, A', O_1', P', R', O_2')| \\
&= \left| \left(\eta_1^\alpha (O_1 - O_1') - \nu_1^\alpha \left[\frac{A(N-P-R)}{(N-P)} - \frac{A'(N-P'-R')}{(N-P')} \right] + \xi^\alpha (R - R') \right) \right| \\
&\leq \max\{\eta_1^\alpha, \nu_1^\alpha, \xi^\alpha\} \left(|A - A'| + |R - R'| + |O_1 - O_1'| \right) \\
&\leq L||X - X'||
\end{aligned} \tag{3.2.2}$$

where $||\cdot||$ is the L_1 -norm defined on $\mathbb{R}^5$. Hence, $f_1(t, A, O_1, P, R, O_2)$ satisfies the Lipschitz condition and the other $f_i(t, A, O_1, P, R, O_2)$ also satisfy Lipschitz condition in a similar manner. Being the total population to be constant, the sub-population $A(t), O_1(t), P(t), R(t), O_2(t)$ are bounded and clearly, $f_i(t, A, O_1, P, R, O_2)$ are continuous on $(0, \infty)$. Thus $f_i(t, A, O_1, P, R, O_2)$ are bounded on $(0, \infty)$. Using Theorem 1.2.1, it can be easily concluded that the system (3.1.1) has unique continuous solution on $(0, \infty)$.

This completes the proof of Theorem 3.2.1. □

3.2.2 Non-Negativity and Boundedness of Solution

The solution of the system (3.1.1) denotes the population of non-criminal population, criminal population, prisoners, recidivists, and recovered population. In real-life scenarios, the number of persons can not be negative. So, the solution of the system is shown as non-negative. Boundedness refers to the restriction on the growth of a particular population class.

Theorem 3.2.2. *The solutions of system* (3.1.1) *are non-negative and bounded, if they initiate in* Ω_+.

Proof. From the model (3.1.1), we find that

$$\begin{aligned} {}_0^C D_t^\alpha A(t)|_{A=0} &= \eta_1^\alpha O_1 + \xi^\alpha R \geq 0 \\ {}_0^C D_t^\alpha O_1(t)|_{O_1=0} &= \nu_1^\alpha \frac{AO_2}{(N-P)} \geq 0 \\ {}_0^C D_t^\alpha P(t)|_{P=0} &= \lambda_1^\alpha O_1 + \lambda_2^\alpha O_2 \geq 0 \\ {}_0^C D_t^\alpha R(t)|_{R=0} &= r^\alpha P + \eta_2^\alpha O_2 \geq 0 \\ {}_0^C D_t^\alpha O_2(t)|_{O_2=0} &= \nu_2^\alpha R \geq 0 \end{aligned} \tag{3.2.3}$$

Thus the sub-populations $A(t), O_1(t), P(t), R(t)$ and $O_2(t)$ are non-negative. As $A(t) + O_1(t)+P(t)+R(t)+O_2(t) = N$, where the total population N is considered to be constant, each sub-population lies in $[0, N]$. Hence the sub-populations $A(t), O_1(t), P(t), R(t)$ and $O_2(t)$ are bounded as well. This completes the proof of Theorem 3.2.2. □

3.3 Equilibrium Points and their Stability

In this section, the equilibrium points for the system (3.1.1) are determined and their asymptotic stability is analyzed. The equilibrium points are classified into crime-free equilibrium E_0 and positive equilibrium E^*. The crime-free equilibrium point E_0 for the system denotes the steady state solution when there is no criminal population and it is given by

$$O_1 = P = O_2 = R = 0. \tag{3.3.1}$$

The endemic equilibrium point $E^* = (O_1^*, P^*, R^*, O_2^*)$ is steady state solution of system (3.3.2) which is obtained when $O_1 > 0$. The total population is assumed to be constant,

thus the system (3.1.1) is reduced to a four-dimensional fractional-order system by putting $A = N - (O_1 + O_2 + P + R)$. After replacing A in the system (3.2.1), the following system (3.3.2) is obtained. This system is equivalent to the proposed model represented by the system (3.1.1).

$$\begin{aligned}
{}_0^C D_t^\alpha O_1(t) &= -\eta_1^\alpha O_1 + \nu_1^\alpha \frac{A(O_1+O_2)}{(N-P)} - \lambda_1^\alpha O_1 = f_2(t, A, O_1, P, R, O_2) \\
{}_0^C D_t^\alpha P(t) &= \lambda_1^\alpha O_1 + \lambda_2^\alpha O_2 - r^\alpha P = f_3(t, A, O_1, P, R, O_2) \\
{}_0^C D_t^\alpha R(t) &= r^\alpha P + \eta_2^\alpha O_2 - \nu_2^\alpha R - \xi^\alpha R = f_4(t, A, O_1, P, R, O_2) \\
{}_0^C D_t^\alpha O_2(t) &= \nu_2^\alpha R - \lambda_2^\alpha O_2 - \eta_2^\alpha O_2 = f_5(t, A, O_1, P, R, O_2)
\end{aligned} \tag{3.3.2}$$

The reduced system with four equations is examined in place of the proposed model which has a set of five equations. Firstly, the stability of E_0 and E^* are analyzed using Routh–Hurwitz criteria [51, 52] with Matignon conditions [50]. Further, the extended Lyapunov function approach [49, 53] is employed on the obtained four-dimensional fractional system for verifying the threshold conditions.

3.3.1 Crime Free Equilibrium

In this section, threshold conditions is derived for the global asymptotic stability of the crime-free equilibrium of the system using Routh-Hurwitz criteria [51] with Matignon conditions [50, 52] and then verified by using extended Lyapunov function approach [49, 53].

3.3.1.1 Stability Analysis of E_0 using Matignon Criteria

To evaluate the stability of the steady-state E_0, the Jacobian matrix $J(E_0)$ is computed as below

$$J^0 = \begin{bmatrix} \frac{\partial f_2}{\partial O_1} & \frac{\partial f_2}{\partial P} & \frac{\partial f_2}{\partial R} & \frac{\partial f_2}{\partial O_2} \\ \frac{\partial f_3}{\partial O_1} & \frac{\partial f_3}{\partial P} & \frac{\partial f_3}{\partial R} & \frac{\partial f_3}{\partial O_2} \\ \frac{\partial f_4}{\partial O_1} & \frac{\partial f_4}{\partial P} & \frac{\partial f_4}{\partial R} & \frac{\partial f_4}{\partial O_2} \\ \frac{\partial f_5}{\partial O_1} & \frac{\partial f_5}{\partial P} & \frac{\partial f_5}{\partial R} & \frac{\partial f_5}{\partial O_2} \end{bmatrix}_{E_0} = \begin{bmatrix} -{\eta_1}^\alpha - {\lambda_1}^\alpha + {\nu_1}^\alpha & 0 & 0 & {\nu_1}^\alpha \\ {\lambda_1}^\alpha & -r^\alpha & 0 & {\lambda_2}^\alpha \\ 0 & r^\alpha & -{\nu_2}^\alpha - \xi^\alpha & {\eta_2}^\alpha \\ 0 & 0 & {\nu_2}^\alpha & -{\lambda_2}^\alpha - {\eta_2}^\alpha \end{bmatrix}$$

From row 1, first eigen value of J^0, $e_1 = -{\eta_1}^\alpha - {\lambda_1}^\alpha + {\nu_1}^\alpha$. For other eigen values, consider the following reduced forms of J^0 as follows:

$$\begin{bmatrix} -r^{\alpha} & 0 & {\lambda_2}^{\alpha} - \frac{{\lambda_1}^{\alpha}{\nu_1}^{\alpha}}{-{\eta_1}^{\alpha}-{\lambda_1}^{\alpha}+{\nu_1}^{\alpha}} \\ r^{\alpha} & -{\nu_2}^{\alpha} - \xi^{\alpha} & {\eta_2}^{\alpha} \\ 0 & {\nu_2}^{\alpha} & -{\lambda_2}^{\alpha} - {\eta_2}^{\alpha} \end{bmatrix} \rightarrow \begin{bmatrix} -r^{\alpha} & 0 & {\lambda_2}^{\alpha} - \frac{{\lambda_1}^{\alpha}{\nu_1}^{\alpha}}{-{\eta_1}^{\alpha}-{\lambda_1}^{\alpha}+{\nu_1}^{\alpha}} \\ 0 & -{\nu_2}^{\alpha} - \xi^{\alpha} & {\eta_2}^{\alpha} + {\lambda_2}^{\alpha} - \frac{{\lambda_1}^{\alpha}{\nu_1}^{\alpha}}{-{\eta_1}^{\alpha}-{\lambda_1}^{\alpha}+{\nu_1}^{\alpha}} \\ 0 & {\nu_2}^{\alpha} & -{\lambda_2}^{\alpha} - {\eta_2}^{\alpha} \end{bmatrix}$$

Here it can be seen that the second eigenvalue, $e_2 = -r^{\alpha} < 0$. Now, consider the trace and determinant of the following reduced matrix

$$V = \begin{bmatrix} -{\nu_2}^{\alpha} - \xi^{\alpha} & {\eta_2}^{\alpha} + {\lambda_2}^{\alpha} - \frac{{\lambda_1}^{\alpha}{\nu_1}^{\alpha}}{-{\eta_1}^{\alpha}-{\lambda_1}^{\alpha}+{\nu_1}^{\alpha}} \\ {\nu_2}^{\alpha} & -{\lambda_2}^{\alpha} - {\eta_2}^{\alpha} \end{bmatrix}$$

$$e_3 + e_4 = \text{Trace}(V) = -{\nu_2}^{\alpha} - \xi^{\alpha} - {\lambda_2}^{\alpha} - {\eta_2}^{\alpha} < 0$$

$$\text{Det}(V) = ({\nu_2}^{\alpha} + \xi^{\alpha})({\lambda_2}^{\alpha} + {\eta_2}^{\alpha}) - {\nu_2}^{\alpha}\left({\eta_2}^{\alpha} + {\lambda_2}^{\alpha} - \frac{{\lambda_1}^{\alpha}{\nu_1}^{\alpha}}{-{\eta_1}^{\alpha} - {\lambda_1}^{\alpha} + {\nu_1}^{\alpha}}\right) \tag{3.3.3}$$

For the eigenvalues with negative real parts, their product will be positive, thus $e_3 \cdot e_4 = \text{Det}(V) > 0$. Therefore from (3.3.3), we get the following:

$$({\nu_2}^{\alpha} + \xi^{\alpha})({\lambda_2}^{\alpha} + {\eta_2}^{\alpha}) > {\nu_2}^{\alpha}\left({\eta_2}^{\alpha} + {\lambda_2}^{\alpha} - \frac{{\lambda_1}^{\alpha}{\nu_1}^{\alpha}}{-{\eta_1}^{\alpha} - {\lambda_1}^{\alpha} + {\nu_1}^{\alpha}}\right)$$

$$\implies \frac{{\nu_2}^{\alpha}{\lambda_1}^{\alpha}{\nu_1}^{\alpha}}{\xi^{\alpha}({\lambda_2}^{\alpha} + {\eta_2}^{\alpha})({\eta_1}^{\alpha} + {\lambda_1}^{\alpha} - {\nu_1}^{\alpha})} < 1 \implies \frac{\nu_1^{\alpha}}{\lambda_1^{\alpha} + \eta_1^{\alpha}} + \frac{\nu_1^{\alpha}\lambda_1^{\alpha}(\nu_2^{\alpha})}{(\lambda_2^{\alpha} + \eta_2^{\alpha})(\lambda_1^{\alpha} + \eta_1^{\alpha})\xi^{\alpha}} < 1 \tag{3.3.4}$$

From the above equation, we get $\frac{\nu_1^{\alpha}}{(\lambda_1^{\alpha} + \eta_1^{\alpha})} < 1 \implies \nu_1^{\alpha} < \lambda_1^{\alpha} + \eta_1^{\alpha} \implies \text{Re}\{e_1\} < 0$. The expression in the above equation represents the threshold condition for the fractional-order system (3.3.2), which can be denoted by $\mathcal{R}_0$ as follows:

$$\mathcal{R}_0 = \left(\frac{\nu_1^{\alpha}}{\lambda_1^{\alpha} + \eta_1^{\alpha}}\right) + \frac{\nu_1^{\alpha}\lambda_1^{\alpha}(\nu_2^{\alpha})}{(\lambda_2^{\alpha} + \eta_2^{\alpha})(\lambda_1^{\alpha} + \eta_1^{\alpha})\xi^{\alpha}} < 1 \tag{3.3.5}$$

All the eigen values have negative real parts, *i.e.*, $|arg(e_i)| > \frac{\alpha\pi}{2}$ for $0 < \alpha < 1$ when $\mathcal{R}_0 < 1$. So the system satisfies Matignon conditions [50] and by Routh-Hurwitz criteria [51, 52] it can be concluded that $E_0 = (0, 0, 0, 0)$ of the system (3.3.2) is locally asymptotically stable when $\mathcal{R}_0 < 1$. $(O_1^0, P^0, R^0, O_2^0) \rightarrow (0, 0, 0, 0)$ as $t \rightarrow \infty$. So the crime-free equilibrium point E_0 is globally asymptotically stable for $\mathcal{R}_0 < 1$. Thus, we have the following theorem.

Theorem 3.3.1. *If $\mathcal{R}_0 < 1$, equilibrium point $E_0 = (0, 0, 0, 0)$ of the system (3.3.2) is globally asymptotically stable, else it is unstable.*

3.3.1.2 Threshold using Lyapunov Method

Extended Lyapunov function approach [49, 53] is employed on four-dimensional fractional dynamical system (3.3.2) obtained by putting $A = N - (O_1 + O_2 + P + R)$ in (3.1.1). Consider the following Lyapunov function for the fractional-order system (3.3.2)

$$L = O_1 + C_1 P + C_2 R + C_3 O_2 \tag{3.3.6}$$

where C_1, C_2, C_3 are positive constants and they will be chosen later such that the solutions of the fractional system propagate to lower level sets and hence the solution of the system tends to the origin.

$$\begin{aligned}
{}_0^C D_t^\alpha L &= {}_0^C D_t^\alpha O_1 + C_1 {}_0^C D_t^\alpha P + C_2 {}_0^C D_t^\alpha R + C_3 {}_0^C D_t^\alpha O_2 \\
&= \nu_1^\alpha \frac{A(O_1 + O_2)}{(N - P)} - \lambda_1^\alpha O_1 - \eta_1^\alpha O_1 \\
&\quad + C_1 \lambda_1^\alpha O_1 + C_1 \lambda_2^\alpha O_2 - C_1 r^\alpha P \\
&\quad + C_2 r^\alpha P + C_2 \eta_2^\alpha O_2 - C_2 \nu_2^\alpha R - C_2 \xi^\alpha R \\
&\quad - C_3 \lambda_2^\alpha O_2 + C_3 \nu_2^\alpha R - C_3 \eta_2^\alpha O_2 \\
&= O_1 \left[\nu_1^\alpha \left(\frac{A}{N - P} \right) - (\lambda_1^\alpha + \eta_1^\alpha) + C_1 \lambda_1^\alpha \right] \\
&\quad + P \left[(C_2 - C_1) r^\alpha \right] + R \left[-C_2 (\nu_{20}^\alpha + \xi^\alpha) + C_3 \nu_2^\alpha \right] \\
&\quad + O_2 \left[\nu_1^\alpha \left(\frac{A}{N - P} \right) + (C_1 - C_3) \lambda_2^\alpha + (C_2 - C_3) \eta_2^\alpha \right]
\end{aligned} \tag{3.3.7}$$

We look for the positive constants C_1, C_2, C_3 in such a way that the values in all the square brackets of equation (3.3.7) remain negative, i.e., ${}_0^C D_t^\alpha L < 0$. Thus for the term in the first pair of square brackets in (3.3.7):

$$\nu_1^\alpha \left(\frac{A}{N - P} \right) - (\lambda_1^\alpha + \eta_1^\alpha) + C_1 \lambda_1^\alpha \leq \nu_1^\alpha - (\lambda_1^\alpha + \eta_1^\alpha) + C_1 \lambda_1^\alpha \leq 0$$

requiring

$$0 < C_1 \leq \frac{\lambda_1^\alpha + \eta_1^\alpha - \nu_1^\alpha}{\lambda_1^\alpha} \implies \nu_1^\alpha < \lambda_1^\alpha + \eta_1^\alpha \tag{3.3.8}$$

For the term in the second pair of square brackets in (3.3.7) to be negative requires the following:

$$C_2 < C_1 \tag{3.3.9}$$

For the negativity of the term in the third pair of square brackets in (3.3.7), the following should hold:

$$\begin{aligned} -C_2(\nu_2^\alpha + \xi^\alpha) + C_3\nu_2^\alpha &< -C_2(\nu_{20}^\alpha + \xi^\alpha) + C_3\nu_{20}^\alpha \\ &= C_3(\nu_2^\alpha) - C_2(\nu_2^\alpha + \xi^\alpha) < 0 \end{aligned}$$

$$\implies C_3 < C_2\left(\frac{\nu_2^\alpha + \xi^\alpha}{\nu_2^\alpha}\right) \tag{3.3.10}$$

And using (3.3.9), for the negativity of the term in the last pair of square brackets in (3.3.7):

$$\begin{aligned} \nu_1^\alpha\left(\frac{A}{N-P}\right) + (C_1 - C_3)\lambda_2^\alpha + (C_2 - C_3)\eta_2^\alpha &\leq \nu_1^\alpha - (C_1 - C_3)\lambda_2^\alpha + (C_2 - C_3)\eta_2^\alpha \\ &< \nu_1^\alpha + (C_1 - C_3)(\lambda_2^\alpha + \eta_2^\alpha) < 0 \end{aligned}$$

$$\implies C_1 + \frac{\nu_1^\alpha}{\lambda_2^\alpha + \eta_2^\alpha} < C_3 \tag{3.3.11}$$

Now, combining (3.3.9), (3.3.10) and (3.3.11), we get:

$$\begin{aligned} C_1 + \frac{\nu_1^\alpha}{\lambda_2^\alpha + \eta_2^\alpha} < C_3 < C_2\left(\frac{\nu_2^\alpha + \xi^\alpha}{\nu_2^\alpha}\right) &< C_1\left(\frac{\nu_2^\alpha + \xi^\alpha}{\nu_2^\alpha}\right) \\ \implies \frac{\nu_1^\alpha}{\lambda_2^\alpha + \eta_2^\alpha} &< C_1 \cdot \frac{\xi^\alpha}{\nu_2^\alpha} \\ \implies \frac{\nu_1^\alpha(\nu_2^\alpha)}{\xi^\alpha(\lambda_2^\alpha + \eta_2^\alpha)} &< C_1 \end{aligned} \tag{3.3.12}$$

Combining (3.3.8) and (3.3.12), we get:

$$\frac{\nu_1^\alpha(\nu_2^\alpha)}{\xi^\alpha(\lambda_2^\alpha + \eta_2^\alpha)} < C_1 < \frac{\lambda_1^\alpha + \eta_1^\alpha - \nu_1^\alpha}{\lambda_1^\alpha} \tag{3.3.13}$$

There exists a positive constants C_1 which satisfy (3.3.13) and suitable C_2, C_3, if and only if the following holds:

$$\frac{\nu_1^\alpha(\nu_2^\alpha)}{\xi^\alpha(\lambda_2^\alpha+\eta_2^\alpha)} < \frac{\lambda_1^\alpha+\eta_1^\alpha-\nu_1^\alpha}{\lambda_1^\alpha}$$

$$\implies \frac{\nu_1^\alpha}{\lambda_1^\alpha+\eta_1^\alpha} + \frac{\nu_1^\alpha\lambda_1^\alpha(\nu_2^\alpha)}{(\lambda_2^\alpha+\eta_2^\alpha)(\lambda_1^\alpha+\eta_1^\alpha)\xi^\alpha} < 1 \tag{3.3.14}$$

The expression (3.3.14) is same as the threshold condition (3.3.5) obtained from the Routh-Hurwitz criteria with Matignon conditions. For $\mathcal{R}_0 < 1$, the Lyapunov function L with suitable $C_1,\ C_2$ and C_3 is bounded for the constant population N and the Caputo's fractional derivative of L is negative *i.e.,* ${}_0^C D_t^\alpha L < 0$ with ${}_0^C D_t^\alpha L = 0$ if and only if $O_1 = P = O_2 = R = 0$. Thus this makes the function L suitable as a Lyapunov candidate for the model. It can be concluded from Theorem 1.2.4 that the proposed fractional-order crime transmission model is uniformly asymptotic stable [49, 53]. Thus we have the following theorem.

Theorem 3.3.2. *If $\mathcal{R}_0 < 1$, equilibrium point $E_0 = (0,0,0,0)$ of the system (3.3.2) is uniformly asymptotically stable, else it is unstable.*

Reproduction Number ($\mathcal{R}_0$). The expression in the equation (3.3.14) represents the threshold condition for the fractional-order system (3.3.2), which is denoted by $\mathcal{R}_0$. The inequality $\mathcal{R}_0 < 1$ behaves as a separating border for the crime-free equilibrium cases and cases where the solution tends to the endemic equilibrium point depicting the high crime state. The $\mathcal{R}_0$ is the reproduction number, representing the number of citizens a criminal can influence to indulge in crime. The first term of the expression (3.3.5) is dedicated to first-time offenders O_1. The numerator is the crime indulgence rate and the denominator comprises the sum of the law-enforcement rate and desistance rate. The numerator in the second term of the expression (3.3.5), is the product of the crime indulgence rate of first-time offenders, the crime indulgence rate of repeat offenders and the law-enforcement rate on first-time offenders. The second term of the expression (3.3.5) is dedicated to repeat-offenders O_2. The denominator of the second term of the expression (3.3.5) is the product of three terms responsible for leaving the repeat-offender class O_2. It is the combination (sum/product) of the law-enforcement rate and desistance rate of repeat-offenders and the redemption rate of prison-released criminals. Hence for crime-free equilibrium, *i.e.*, for $\mathcal{R}_0 < 1$, the numerator of $\mathcal{R}_0$ should be less than the denominator.

3.3.2 Endemic Equilibrium in the System

The endemic equilibrium point $E^* = (O_1^*, P^*, R^*, O_2^*)$ is steady state solution of system (3.3.2) which is obtained when $O_1 > 0$ and, it yields the following equations:

$$\begin{aligned} -\eta_1^\alpha O_1 + \nu_1^\alpha \frac{A(O_1+O_2)}{(N-P)} - \lambda_1^\alpha O_1 &= 0 \\ \lambda_1^\alpha O_1 + \lambda_2^\alpha O_2 - r^\alpha P &= 0 \\ r^\alpha P + \eta_2^\alpha O_2 - \nu_2^\alpha R - \xi^\alpha R &= 0 \\ \nu_2^\alpha R - \lambda_2^\alpha O_2 - \eta_2^\alpha O_2 &= 0 \end{aligned} \tag{3.3.15}$$

The above system can be simplified as :

$$\begin{aligned} \frac{A}{(N-P)} &= \frac{\eta_1^\alpha + \lambda_1^\alpha}{\nu_1^\alpha} \frac{O_1}{(O_1+O_2)} \\ r^\alpha P &= \lambda_1^\alpha O_1 + \lambda_2^\alpha O_2 \\ r^\alpha P + \eta_2^\alpha O_2 &= (\nu_2^\alpha + \xi^\alpha) R \\ \nu_2^\alpha R &= (\lambda_2^\alpha + \eta_2^\alpha) O_2 \end{aligned} \tag{3.3.16}$$

From the last three equations of the above simplified system, we obtain $O_1 = \dfrac{\xi^\alpha}{\lambda_1^\alpha} R$ and $O_2 = \dfrac{\nu_2^\alpha}{(\lambda_2^\alpha + \eta_2^\alpha)} R$. Putting this in equation first of system (3.3.15), we get

$$\frac{A}{(N-P)} = \frac{\eta_1^\alpha + \lambda_1^\alpha}{\nu_1^\alpha} \frac{1}{1 + \dfrac{\nu_2^\alpha \lambda_1^\alpha}{(\eta_2^\alpha + \lambda_2^\alpha)\xi^\alpha}} \tag{3.3.17}$$

Now, using equation (3.3.5), we get

$$\mathcal{R}_0 = \frac{\nu_1^\alpha}{\eta_1^\alpha + \lambda_1^\alpha} \left(1 + \frac{\nu_2^\alpha \lambda_1^\alpha}{(\eta_2^\alpha + \lambda_2^\alpha)\xi^\alpha} \right) = \frac{(N-P)}{A} \tag{3.3.18}$$

Thus at the endemic equilibrium of the system, we have

$$\frac{A}{(N-P)} = \frac{1}{\mathcal{R}_0} \tag{3.3.19}$$

$$\implies O_1 + O_2 + A + R = N - P = A \cdot \mathcal{R}_0 \implies O_1 + O_2 + R = A(\mathcal{R}_0 - 1) \quad (3.3.20)$$

As $O_1 > 0,\ O_2 > 0, A > 0$ and $R > 0$, therefore $\mathcal{R}_0 > 1$. Moreover, the prevalence of equilibrium $\frac{1}{\mathcal{R}_0}$ of non-criminals can be interpreted as the the ratio of the rate of discontinuing criminal activities and the rate of involvement in illegal activities. Thus E^* equilibrium occurs if $\mathcal{R}_0 > 1$. The endemic equilibrium $E^* = (O_1^*, P^*, R^*, O_2^*)$ where

$$O_1^* = \frac{\xi^\alpha}{\lambda_1^\alpha} R^*, \quad O_2^* = \frac{\nu_2^\alpha}{(\lambda_2^\alpha + \eta_2^\alpha)} R^*, \quad P^* = N - \left(\frac{\mathcal{R}_0}{\mathcal{R}_0 - 1}\right)\left[\frac{\xi^\alpha}{\lambda_1^\alpha} + \frac{\nu_2^\alpha}{\lambda_2^\alpha + \eta_2^\alpha} + 1\right] R^*,$$

$$R^* = \frac{\lambda_1^\alpha \xi^\alpha (\lambda_2^\alpha + \eta_2^\alpha)(\mathcal{R}_0 - 1)\, N}{(\mathcal{R}_0 - 1)\left[\lambda_1^\alpha(\nu_2^\alpha \lambda_2^\alpha + \xi^\alpha(\eta_2 \alpha + \lambda_2^\alpha))\right] + \mathcal{R}_0(\xi^\alpha((\lambda_2^\alpha + \eta_2^\alpha)\xi^\alpha + \nu_2^\alpha \lambda_1^\alpha + \lambda_1^\alpha(\lambda_2^\alpha + \eta_2^\alpha))}.$$

3.3.2.1 Stability Analysis of E^* using Routh-Hurwitz Criteria

To evaluate the stability of the endemic equilibrium E^*, we compute the Jacobian matrix $J(E^*)$ as below

$$J^* = \begin{bmatrix} \frac{\partial f_2}{\partial O_1} & \frac{\partial f_2}{\partial P} & \frac{\partial f_2}{\partial R} & \frac{\partial f_2}{\partial O_2} \\ \frac{\partial f_3}{\partial O_1} & \frac{\partial f_3}{\partial P} & \frac{\partial f_3}{\partial R} & \frac{\partial f_3}{\partial O_2} \\ \frac{\partial f_4}{\partial O_1} & \frac{\partial f_4}{\partial P} & \frac{\partial f_4}{\partial R} & \frac{\partial f_4}{\partial O_2} \\ \frac{\partial f_5}{\partial O_1} & \frac{\partial f_5}{\partial P} & \frac{\partial f_5}{\partial R} & \frac{\partial f_5}{\partial O_2} \end{bmatrix}_{E^*} = \begin{bmatrix} a & b & c & d \\ e & f & 0 & h \\ 0 & j & k & l \\ 0 & 0 & n & o \end{bmatrix}$$

where $a = -\eta_1^\alpha - \lambda_1^\alpha + \frac{\nu_1^\alpha}{\mathcal{R}_0} + c,\ b = -c\left[\frac{1}{\mathcal{R}_0} - 1\right],\ c = -\nu_1^\alpha\left[\frac{\xi^\alpha}{\lambda_1^\alpha} + \frac{\nu_2^\alpha}{(\lambda_2^\alpha + \eta_2^\alpha)}\right]\frac{R^*}{N - P^*}$,

$d = \frac{\nu_1^\alpha}{\mathcal{R}_0} + c\ ,\ e = {\lambda_1}^\alpha, f = -r^\alpha\ ,\ h = {\lambda_2}^\alpha\ , j = r^\alpha, k = -{\nu_2}^\alpha - \xi^\alpha\ ,\ l = {\eta_2}^\alpha,$
$n = {\nu_2}^\alpha\ ,\ o = -{\lambda_2}^\alpha - {\eta_2}^\alpha\ .$

The characteristic polynomial of the above Jacobian matrix is $m^4 + K_1 m^3 + K_2 m^2 + K_3 m + K_4 = 0$, where

$$K_1 = -a - f - k - o$$

$$K_2 = af - be + ak + ao + fk + fo + ko - ln$$

$$K_3 = bek - afk - cej - afo + beo - ako + aln - fko + fln - hjn$$

$$K_4 = afko - afln + ahjn - beko + beln + cejo - dejn$$

Hence, by using the Routh-Hurwitz criterion [51, 52], the endemic equilibrium $E^* = (O_1^*, P^*, R^*, O_2^*)$ is locally asymptotically stable.if and only if the following conditions are met:

$$K_1 > 0;\ K_4 > 0;\ K_1K_2 - K_3 > 0;\ K_1K_2K_3 - K_3^2 - K_4K_1^2 > 0 \tag{3.3.21}$$

Thus, the following theorem can be stated.

Theorem 3.3.3. *The endemic equilibrium point $E^* = (O_1^*, P^*, R^*, O_2^*)$ for the system (3.3.2) exists and is locally asymptotically stable if and only if the inequalities in (3.3.21) hold.*

3.4 Stability Analysis of Endemic Equilibrium using Numerical Simulations

In this section, the stability of endemic equilibrium points of the model (3.1.1) for different fractional orders α is shown with the help of numerical simulations. Most of the values of parameters in S_2 are fetched from [1–3] to illustrate the dynamics of crime, which are also shown in Table 3.2. For evaluating the numerical solution of the proposed fractional model, we used the Power Series Expansion (PSE) approach described in [189, 190]. In this approach, Caputo's fractional derivative is approximated with the help of Grünwald–Letnikov's definition of fractional derivative in (1.1.10) because for a broad class of functions and for $t \to \infty$, these two definitions of fractional derivatives are equivalent [72]. The Adams–Bashforth–Moulton and PSE methods are the most frequently used methods for evaluating numerical solutions of fractional models. Both methods have approximately the same accuracy in terms of solutions [189]. In this work, the PSE method is used which gives a more straightforward numerical solution for the system ${}_0^C D_t^\alpha X(t) = f(X(t), t)$ of the form

$$X(t_k) = h^\alpha \left(f(X(t_k), t_k)\right) - \sum_{j=1}^{k} c_j^{(\alpha)} X(t_{k-j}) \tag{3.4.1}$$

where $t_k = kh$, h is the time step of calculation and $c_j^{(\alpha)} = (-1)^j \binom{\alpha}{j} = \frac{\Gamma(\alpha+1)}{\Gamma(\alpha-j+1).\Gamma(j+1)}$ are binomial coefficients for $j = 0, 1, \cdots$, computed using expression (3.4.2) given in

Algorithm 1 Numerical approximation of the true solution of the proposed model

Input Variables

$\alpha \leftarrow$ fractional order of the differential equation $(0 < \alpha \leq 1)$

$X_0 \leftarrow$ array of the initial conditions $(A(1), O_1(1), P(1), R(1), O_2(1))$

TSim $\leftarrow$ simulation time

h $\leftarrow$ time step size $(0 < h \leq 1)$

n = round(TSim/h); % time step:

% parameters of the proposed model:

$\nu_1 = 0.005;\ \eta_1 = 0.045;\ \lambda_1 = 0.6;\ r = 0.01;\ \nu_2 = 0.3;\ \eta_2 = 0.03;\ \lambda_2 = 0.7;\ \xi = 0.1;$

```
function [yo] = mem(r, c, p) % Memory Function
hist = 0;
for ii=1:p-1
   memory = memory + c(ii)*r(p-i);
end
yo = memory;
```

Discretization of Proposed Model using Power Series Expansion Method of Approximation:

% binomial coefficients calculation:

cp1 = 1; cp2 = 1; cp3 = 1; cp4 = 1; cp5 = 1;

for j=1:n

c1(j) = (1 − (1 + α)/j) ∗ cp1;

c2(j) = (1 − (1 + α)/j) ∗ cp2;

c3(j) = (1 − (1 + α)/j) ∗ cp3;

c4(j) = (1 − (1 + α)/j) ∗ cp4;

c5(j) = (1 − (1 + α)/j) ∗ cp5;

cp1 = c1(j); cp2 = c2(j); cp3 = c3(j); cp4 = c4(j); cp5 = c5(j);

end

% initial conditions:

A(1) = X0(1); O1(1) = X0(2); P(1) = X0(3); R(1) = X0(4); O2(1) = X0(5);

% calculation of numerical solution of proposed model:

for i=2:n

$A(i) = (\eta_1{}^{\alpha} * O_1(i-1) - \nu_1^{\alpha} * (O_1(i-1) + O_2(i-1)) * \left(\frac{A(i-1)}{N-P(i-1)}\right) + \xi^{\alpha} * R(i-1)) * h^{\alpha} -$ mem(A, c1, i);

$O_1(i) = (-\eta_1{}^{\alpha} * O_1(i-1) + \nu_1^{\alpha} * (O_1(i-1) + O_2(i-1)) * \left(\frac{A(i-1)}{N-P(i-1)}\right) - \lambda_1^{\alpha} * O_1(i-1)) * h^{\alpha} -$ mem(O_1, c2, i);

$P(i) = (\lambda_1^{\alpha} * O_1(i) + \lambda_2^{\alpha} * O_2(i-1) - r^{\alpha} * P(i-1)) * h^{\alpha} - mem(P, c3, i);$

$R(i) = (r^{\alpha} * P(i) + \eta_2{}^{\alpha} * O_2(i-1) - \nu_2^{\alpha} * R(i-1) - \xi^{\alpha} * R(i-1)) * h^{\alpha} - mem(R, c4, i);$

$O_2(i) = (\nu_2^{\alpha} * R(i) - \eta_2^{\alpha} * O_2(i-1) - \eta_2^{\alpha} * O_2(i-1)) * h^{\alpha} - mem(O_2, c5, i);$

end

for j=1:n

X(j, 1) = A(j);

X(j, 2) = O_1(j);

X(j, 3) = P(j);

X(j, 4) = R(j);

X(j, 5) = O_2(j);

end

T=h:h:TSim;

Output Variables

X $\leftarrow$ arrays of n + 1 real numbers that contain the approximate solutions.

[189]

$$c_0^{(\alpha)} = 1 \quad c_j^{(\alpha)} = (1 - \frac{1+\alpha}{j})c_{j-1}^{(\alpha)}. \tag{3.4.2}$$

Thus we get the numerical solution of the system (3.1.1) by solving the following set of equations with parameters from the two sets S_1, S_2 which are chosen randomly such that $\mathcal{R}_0 > 1$.

$$\begin{aligned}
A(t_k) &= h^\alpha \left(\eta_1^\alpha O_1 - \nu_1^\alpha \frac{A(O_1+O_2)}{(N-P)} + \xi^\alpha R \right) - \sum_{j=1}^{k} c_j^{(\alpha)} A(t_{k-j}) \\
O_1(t_k) &= h^\alpha \left(-\eta_1^\alpha O_1 + \nu_1^\alpha \frac{A(O_1+O_2)}{(N-P)} - \lambda_1^\alpha O_1 \right) - \sum_{j=1}^{k} c_j^{(\alpha)} O_1(t_{k-j}) \\
P(t_k) &= h^\alpha \left(\lambda_1^\alpha O_1 + \lambda_2^\alpha O_2 - r^\alpha P \right) - \sum_{j=1}^{k} c_j^{(\alpha)} P(t_{k-j}) \\
R(t_k) &= h^\alpha \left(r^\alpha P + \eta_2^\alpha O_2 - \nu_2^\alpha R - \xi^\alpha R \right) - \sum_{j=1}^{k} c_j^{(\alpha)} R(t_{k-j}) \\
O_2(t_k) &= h^\alpha \left(\nu_2^\alpha R - \lambda_2^\alpha O_2 - \eta_2^\alpha O_2 \right) - \sum_{j=1}^{k} c_j^{(\alpha)} O_2(t_{k-j})
\end{aligned} \tag{3.4.3}$$

The aforementioned methodology is also presented in Algorithm 1. The resulting equations, input variables, set of parameters, initial conditions and output variables are also mentioned. Numerical results for fractional systems (3.1.1) where α is varying from 0.7 to 1 can be seen in the Figure 3.2 to Figure 3.5. The simulations are shown on two sets of parameters, S_1 has mostly realistic parametric values and S_2 has random parametric values such that $\mathcal{R}_0 > 1$. It is clear from the figures that the models for fractional derivative order α $(0.7 \leq \alpha \leq 1)$ are asymptotically stable. In the previous section, it is theoretically proved that the endemic equilibrium point E^* is locally asymptotically stable if $\mathcal{R}_0 > 1$. Thus the simulations strengthen the theoretical results. The simulations are shown with two different time frames $T_{sim} = 100$ and $T_{sim} = 500$. It can be observed that as the order decreases, the criminal population ($O_1(t)$ and $O_2(t)$) also decreases. The trajectories of all the population classes justify the stability of the proposed model irrespective of the order chosen. The model with parameters from S_1 takes longer to reach the equilibrium point than the model with parameters from S_2. The significant difference between parameters of S_1 and S_2 are the values of η_1, η_2 and λ_2, which represents the rate at which non-incarcerated criminals (first-time offender / repeat offender) are assimilating back into

society and law enforcement rate on recidivists. The set S_1 has significantly lesser values of $\eta_1,\ \eta_2$ and λ_2. This means that society with a lower rate of assimilation back into society and less law enforcement on recidivists will achieve the equilibrium later. Thus, the simulations validate that recidivists should be handled with stricter policies to reduce crime spread.

Figure 3.6 to Figure 3.9 show the comparison between the performance of the basic differential model and fractional model by taking $\alpha = 0.99$ and $\alpha = 0.89$. It is visible from these figures that the fractional order model converges faster to the to the endemic equilibrium point than the basic integer order model. It can also be observed that the fractional order model has richer dynamics than the basic model. The fractional-order model can describe the dynamics in a better way and help more in controlling crime spread. The fractional-order model converges faster than the conventional model The faster convergence of the fractional-order model means that the criminal population will stop growing early in the case of fractional order. It is observed that the fractional order has a significant effect on the dynamic behavior of all the components. Also, it is noticed that when the derivative order α is reduced from 1, the memory effect of the system increases. Therefore the crime spreads slowly with faster convergence to the equilibrium. Moreover, catching criminals in society takes time and depends on the rate of law enforcement in an area. This results in an increase in the non-incarcerated criminals, fast progress of crime and thus an increase in incarcerated criminals.

On the other hand, the experience or knowledge of individuals about the punishment causes non-criminals and non-incarcerated criminals to take different precautions, such as behavioral change, avoiding contact with other criminals and joining rehabilitation programs against crime transmission. This leads to a slow growth of crime among the population. Therefore, from the numerical results in Figure 3.2 to Figure 3.5, we conclude that the order of Caputo's derivative α in the system (3.1.1) can play the role of precautionary measure against crime transmission, punishment of criminals and delay in catching criminals. Moreover, Figure 3.6 to Figure 3.9 infer that the differential equations with fractional order derivatives have rich dynamics and describe criminological systems better than classical integer-order models. It can be concluded that the derivative order can play the role of precaution against crime transmission, and the experience or knowledge of individuals about criminal history.

Table 3.2: Set of parameter values used for showing numerical simulations

Parameter	ν_1	η_1	λ_1	r	ν_2	η_2	λ_2	ξ
Value Set S_1	0.05	0.045	0.6	0.01	0.3	0.03	0.07	0.1
Value Set S_2	0.7	0.4	0.4	0.6	0.6	0.2	0.5	0.7

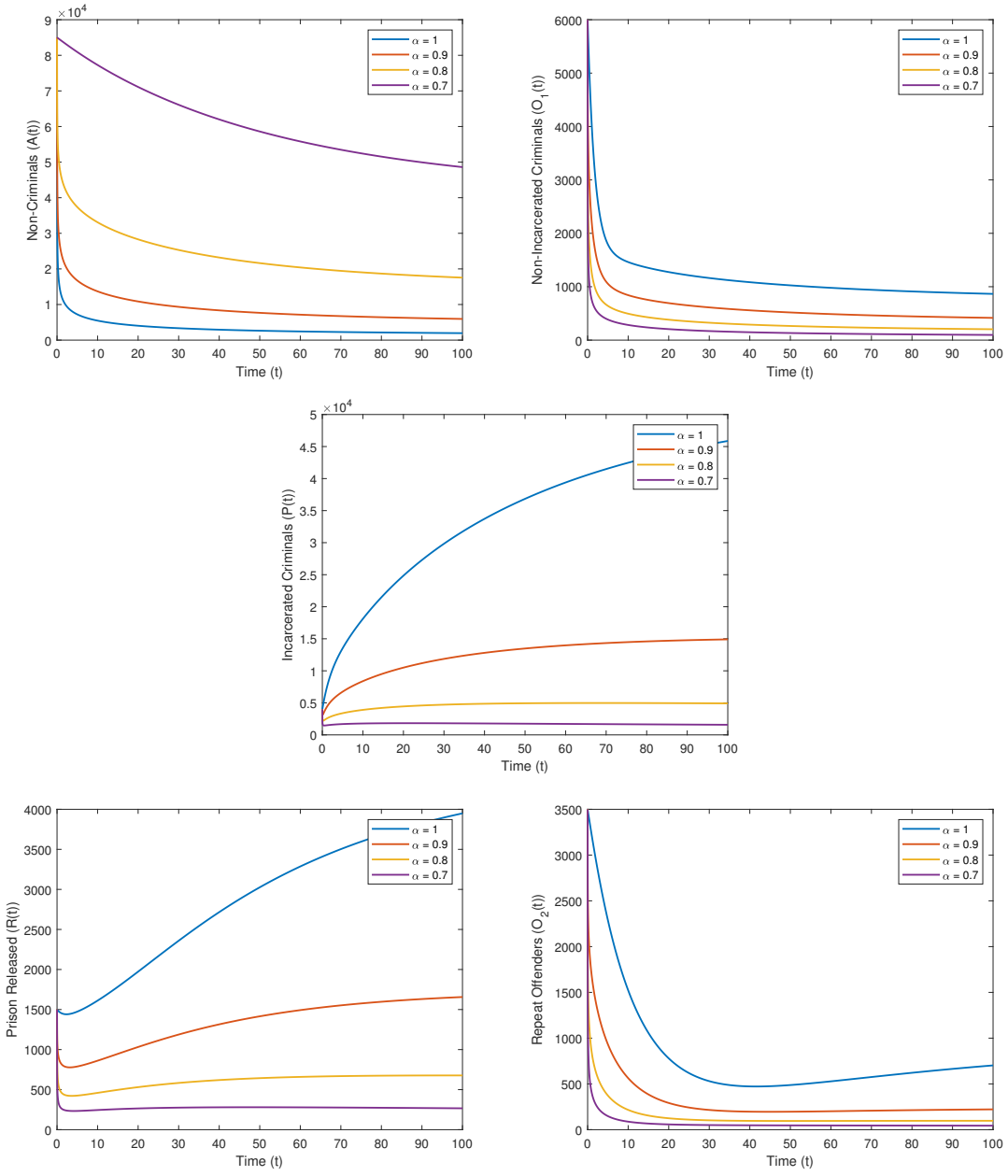

Figure 3.2: Variations of non-criminals A, non-incarcerated criminals O_1, incarcerated criminals P, prison-released population R and repeat offenders O_2 with time $T = 100$ for a set of parameters in S_1 and different order α

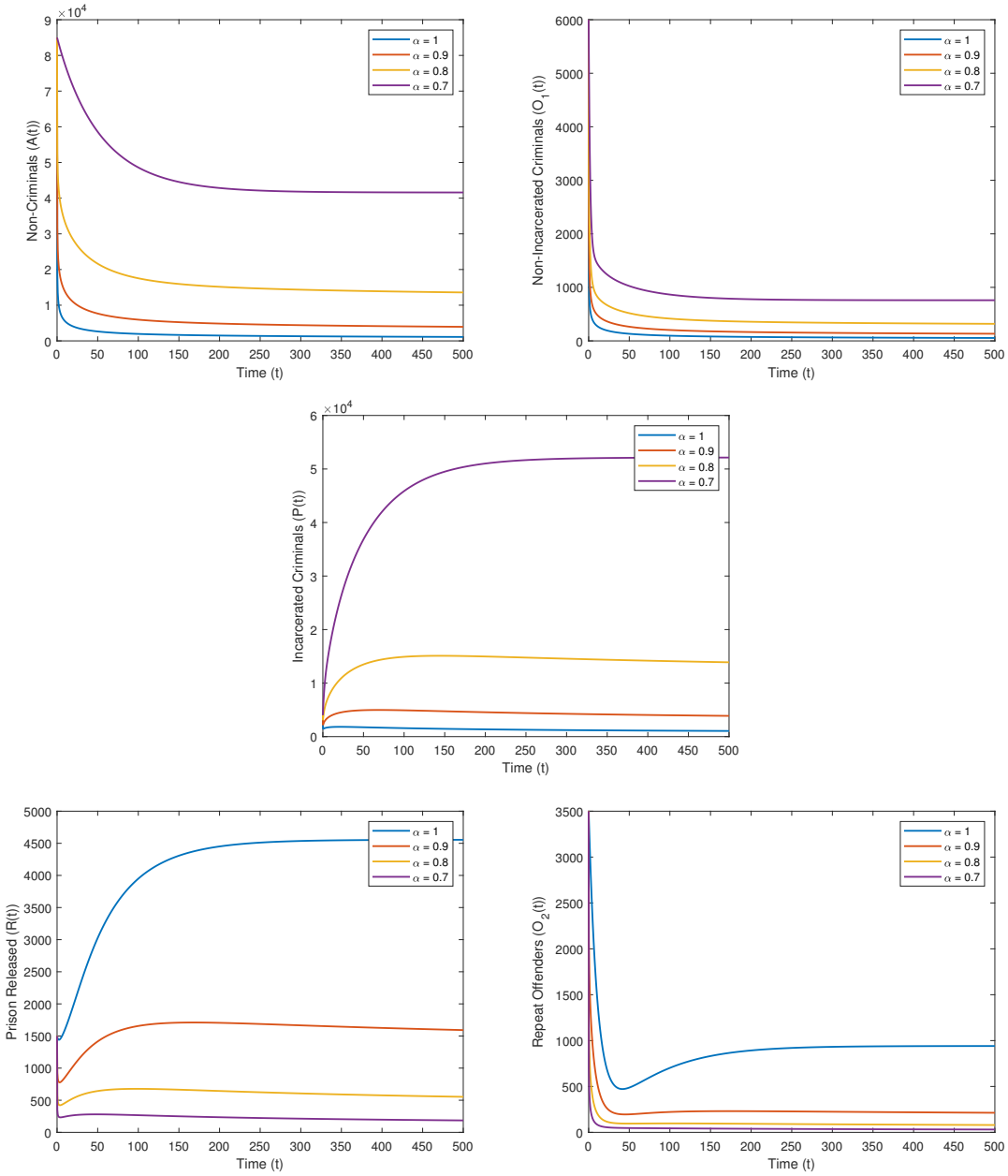

Figure 3.3: Variations of non-criminals A, non-incarcerated criminals O_1, incarcerated criminals P, prison-released population R and repeat offenders O_2 with time $T = 500$ for a set of parameters in S_1 and different order α

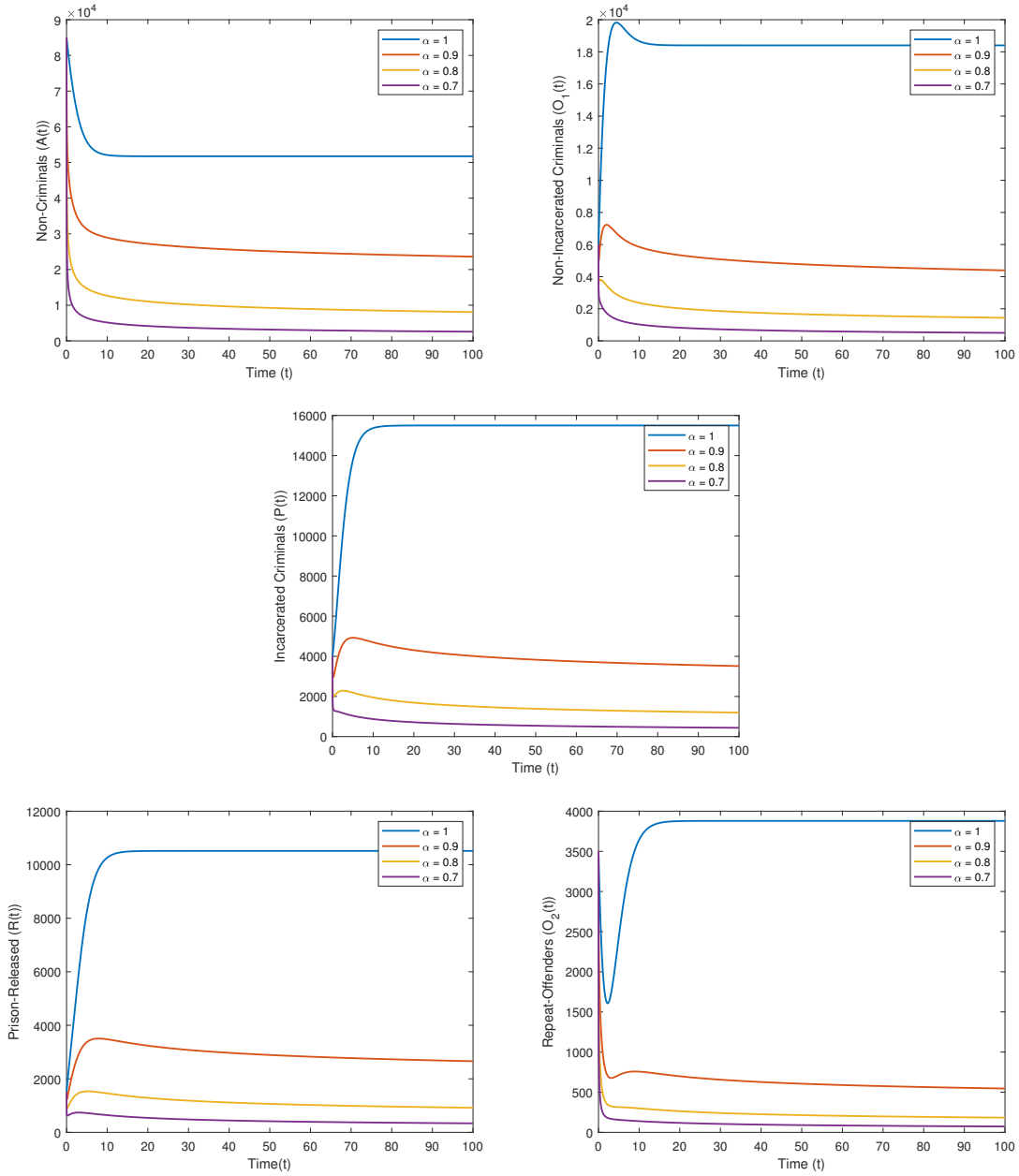

Figure 3.4: Variations of non-criminals A, non-incarcerated criminals O_1, incarcerated criminals P, prison-released population R and repeat offenders O_2 with time $T = 100$ for a set of parameters in set S_2 and different order α

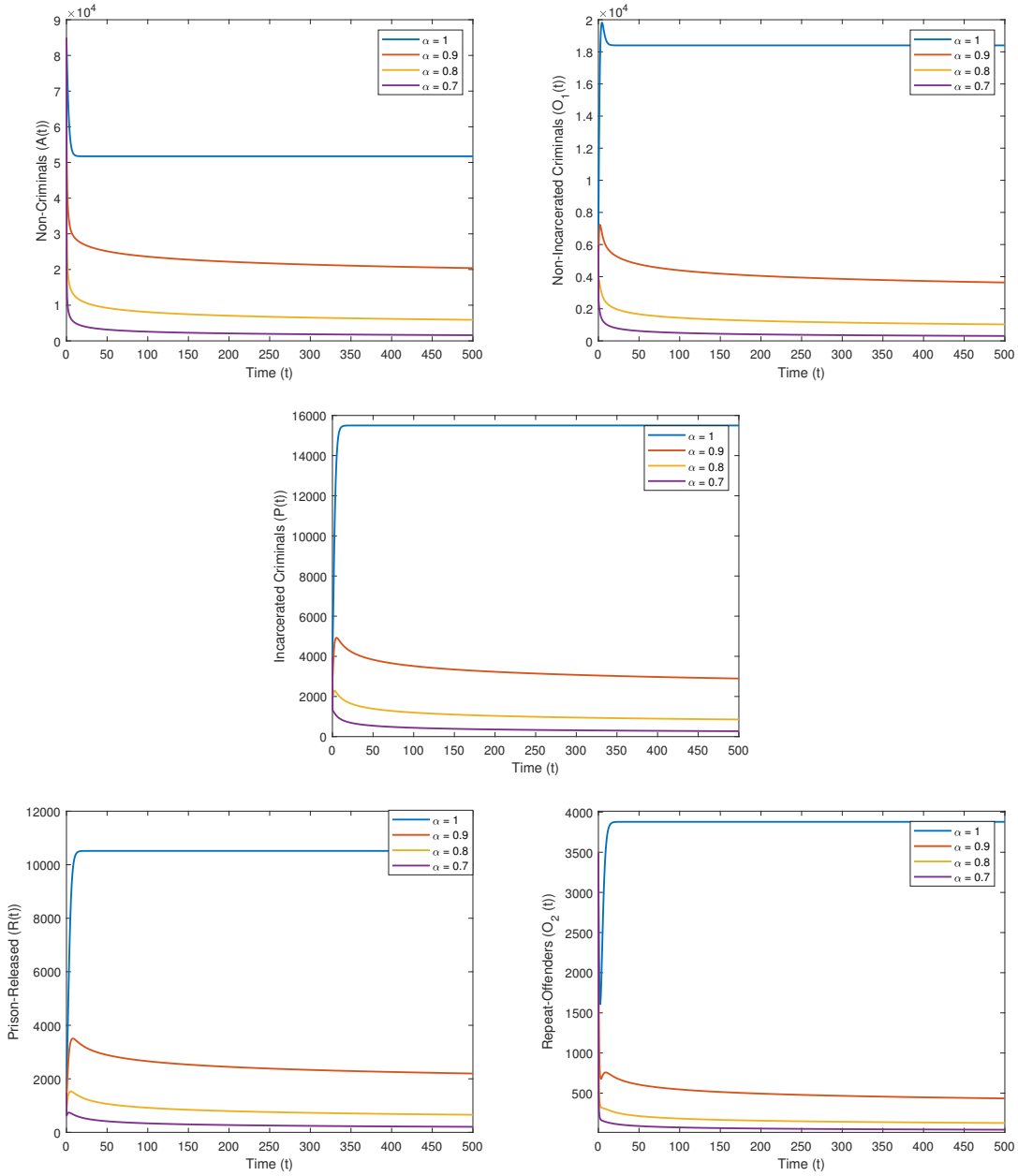

Figure 3.5: Variations of non-criminals A, non-incarcerated criminals O_1, incarcerated criminals P, prison-released population R and repeat Offenders O_2 with time $T = 500$ for a set of parameters in set S_2 and different order α

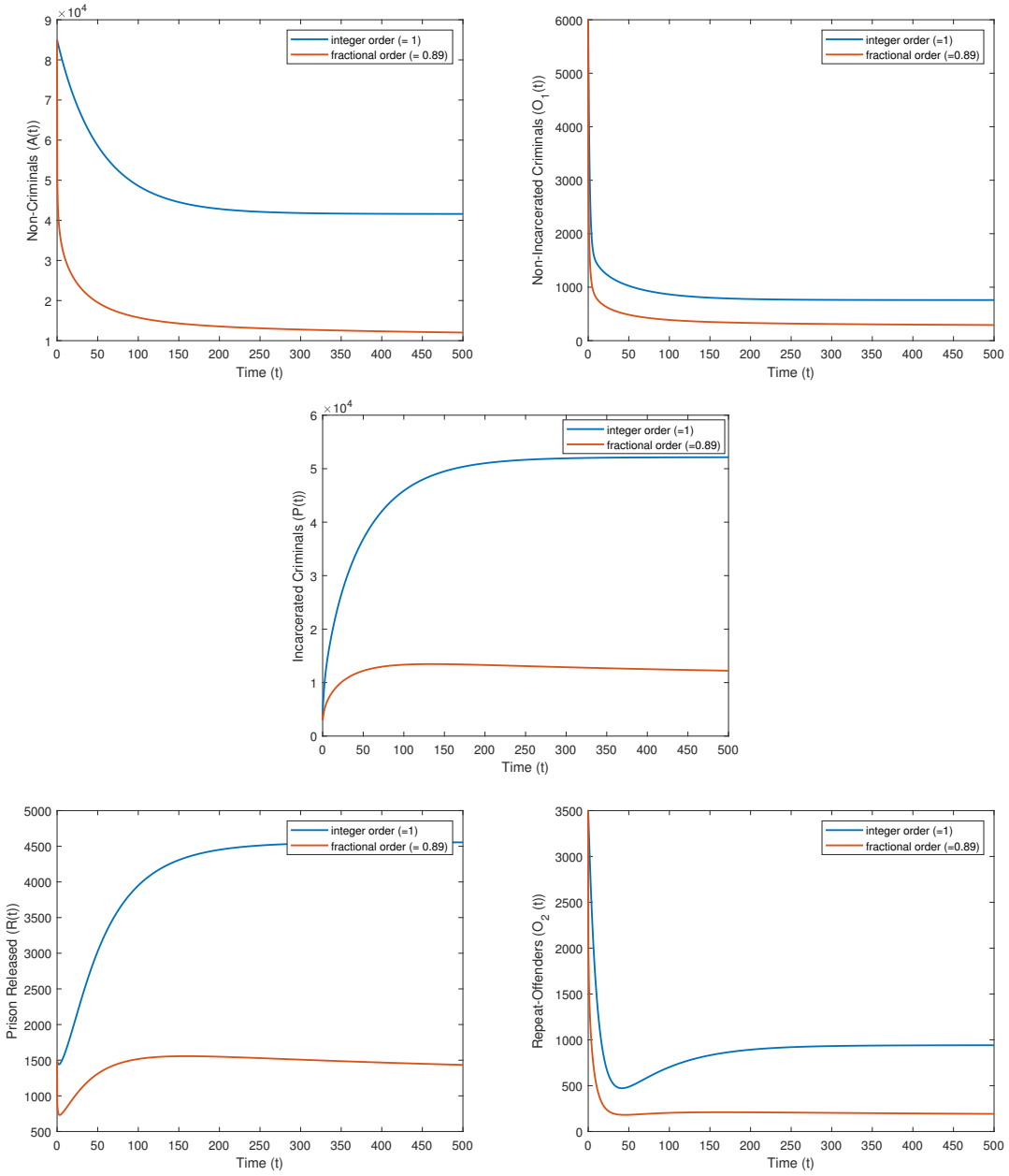

Figure 3.6: Comparison between the basic differential model ($\alpha = 1$) and the fractional dynamics with $\alpha = 0.89$, when parameters are taken from set S_1

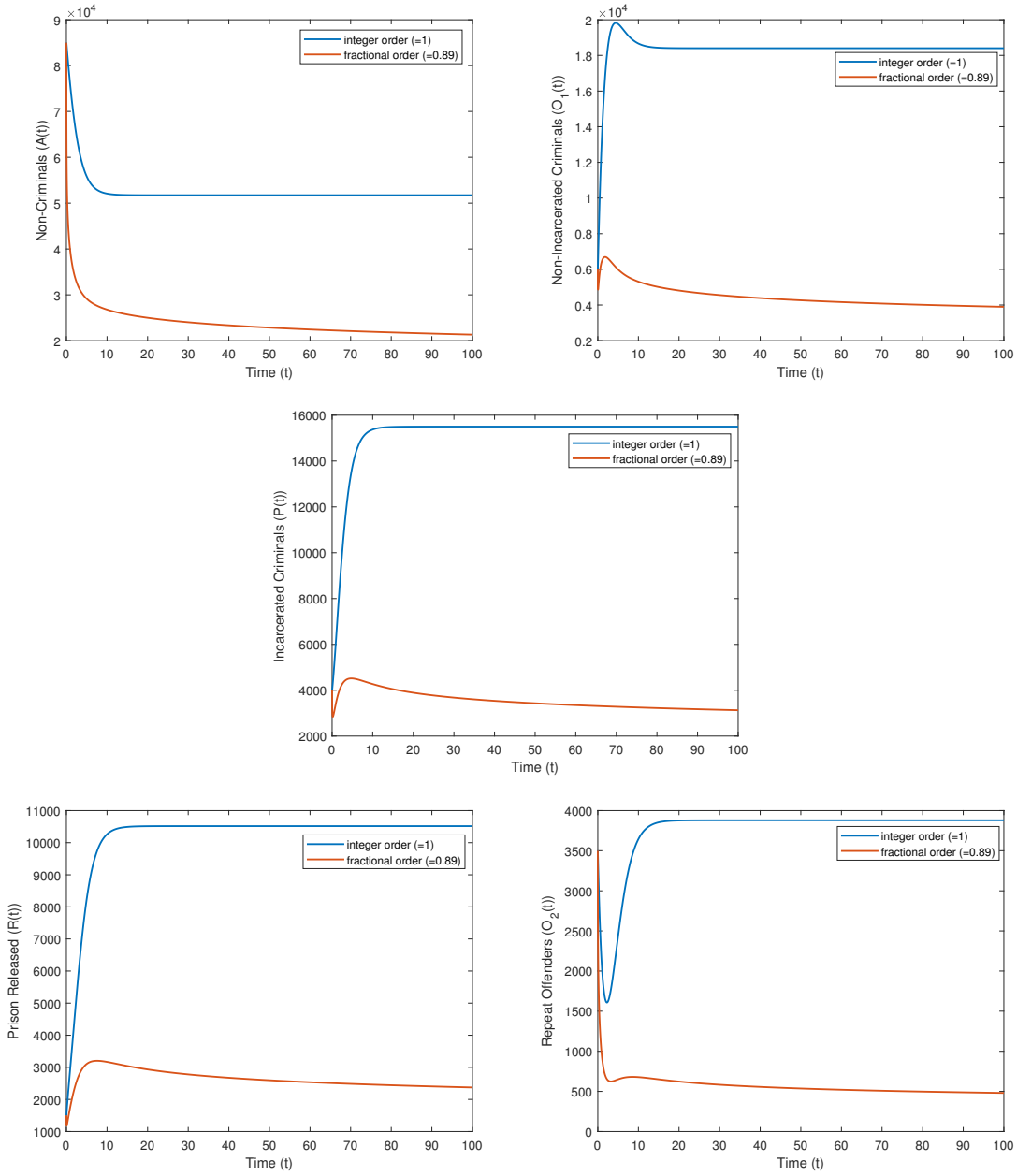

Figure 3.7: Comparison between the basic differential model ($\alpha = 1$) and the fractional dynamics with $\alpha = 0.89$, when parameters are taken from set S_2

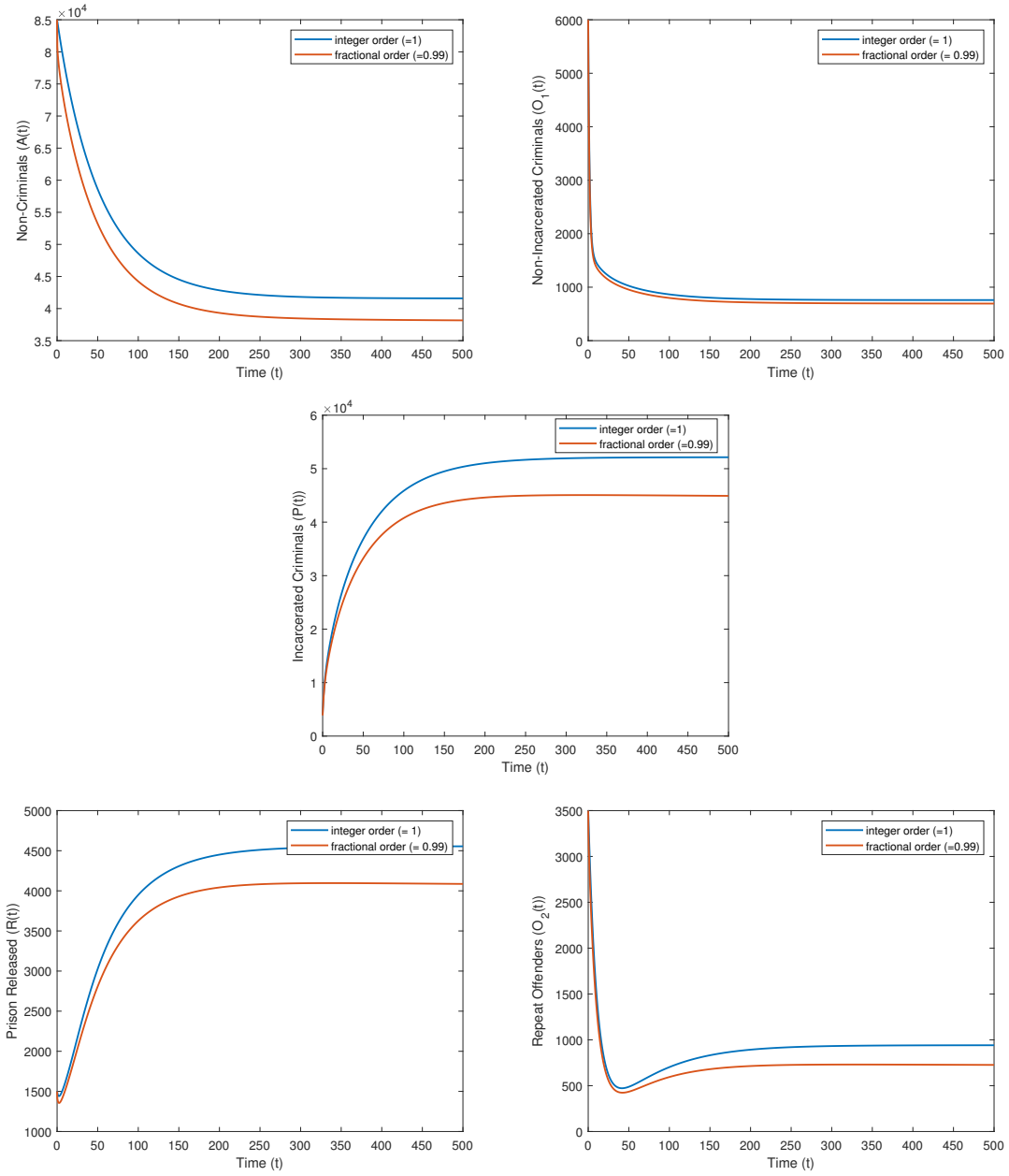

Figure 3.8: Comparison between the classical model ($\alpha = 1$) and the fractional dynamics with $\alpha = 0.99$, when parameters are taken from set S_1

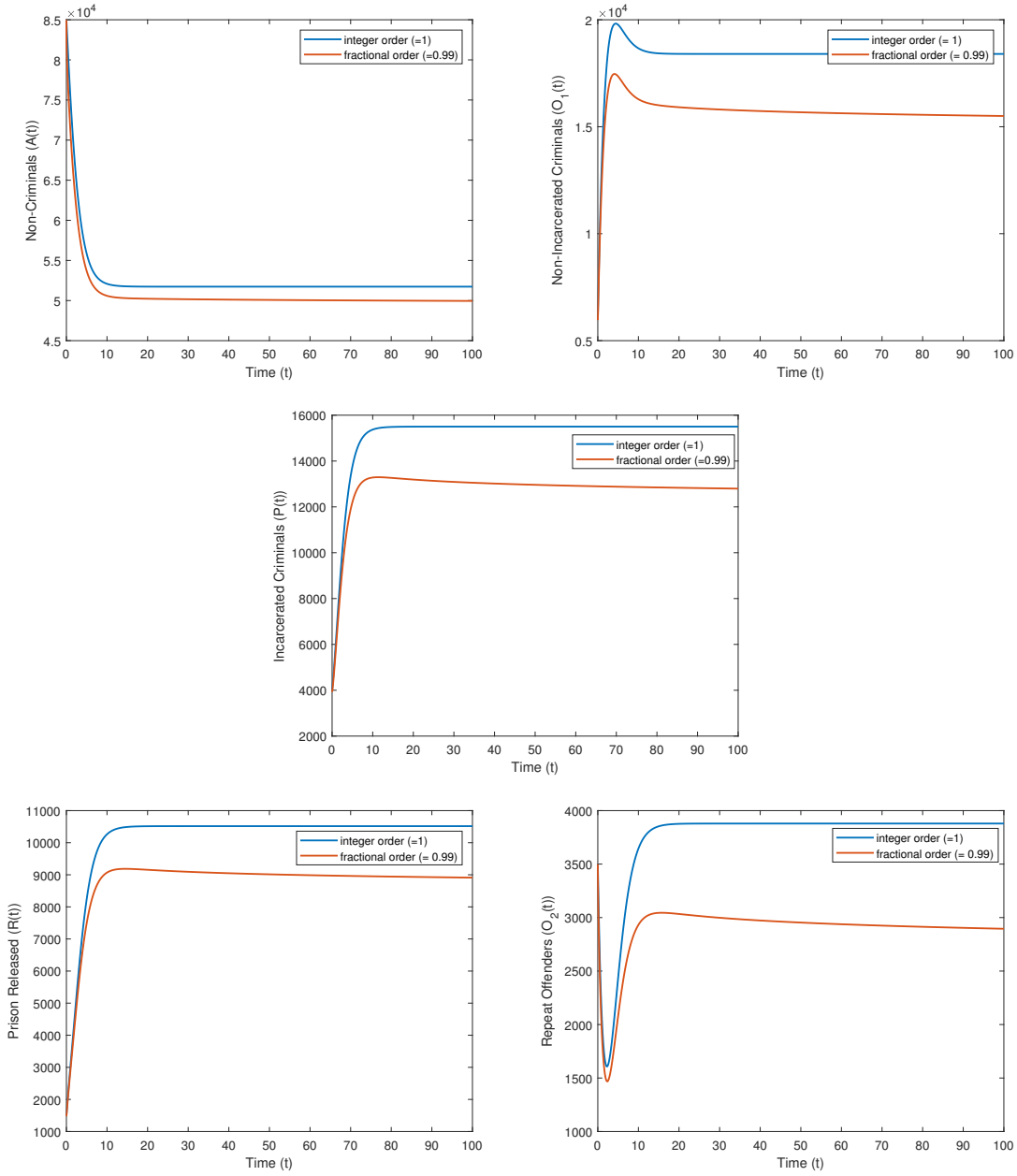

Figure 3.9: Comparison between the classical model ($\alpha = 1$) and the fractional dynamics with $\alpha = 0.99$, when parameters are taken from set S_2

3.5 Effects of Changing Different Parameters

3.5.1 Effect of Increasing Prison Length

It is intriguing to notice that the threshold $\mathcal{R}_0$ and the fractions of criminally active $\frac{A}{N-P}$ and criminally-inactive individuals $\frac{O_1+O_2+R}{N-P}$ are independent of prison-release rate r, hence of prison length $l = 1/r$. However, it can be seen from the second and third equations of the system (3.3.15) that the equilibrium values of all classes A, O_1, O_2, P, R depend on r. As the prison length parameter l increases (r decreases), the equilibrium population of incarcerated criminals increases, while the equilibrium population of other classes decreases irrespective of order α. As we have $\frac{A}{N-P} = \frac{1}{\mathcal{R}_0}$, which implies that flows of A and I are in opposite directions when r increases. Moreover, $O_1 = \frac{\xi^\alpha}{\lambda_1^\alpha}R$ and $O_2 = \frac{\nu_2^\alpha}{(\lambda_2^\alpha+\eta_2^\alpha)}R$ which implies that flows of O_1, O_2 are in same directions when r increases. Hence, considering $R + O_1 + O_2 = kR$ for some $k > 0$ and using $A = \frac{1}{\mathcal{R}_0}(N-P)$ gives the following

$$\frac{1}{\mathcal{R}_0}(N-P) = N - (O_1+O_2+R) - P = N - kR - P \tag{3.5.1}$$

$$\implies \left(1-\frac{1}{\mathcal{R}_0}\right)N = \left(1-\frac{1}{\mathcal{R}_0}\right)P + kR \tag{3.5.2}$$

As $\mathcal{R}_0 > 1$ for endemic equilibrium, the coefficients for variables on the right-hand side of the above equation are positive. Thus, P and R move in the opposite direction as r increases. In addition, the second equation of system (3.3.15), justifies that as r increases, R, O_1, O_2 increases and P decreases. Figure (3.10) shows this dependence for varying prison lengths. In Figure (3.10), one can see that as prison length l increases from 2 to 5, the equilibrium population of prisoners increases, and the rest of the equilibrium population decreases irrespective of order α. It can be concluded that increasing the prison length doesn't have much effect on the threshold condition, on the fractions of criminally active and criminally inactive populations. It leads to a larger prison population along with a reduction of criminally active and inactive individuals. Thus it is advisable not to

increase prison length, and it should be chosen according to the condition of society.

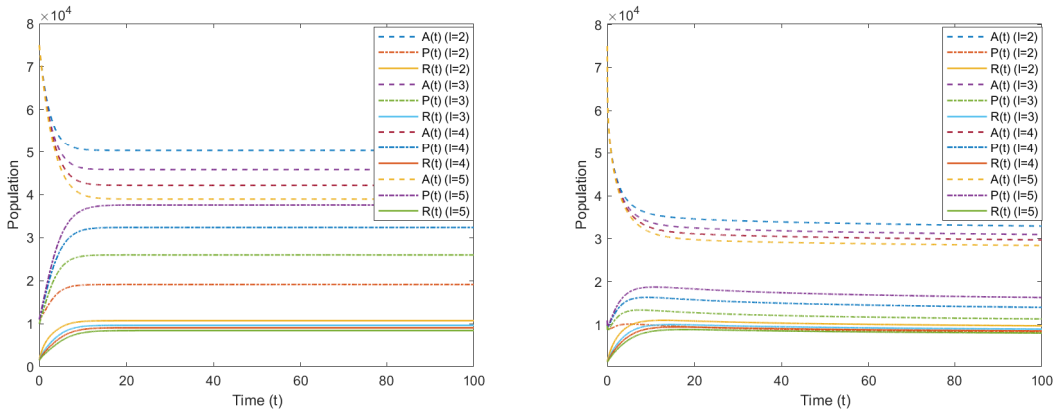

Figure 3.10: Impact of imprisonment or changing prison length ($l = 1/r$) on the criminal population at different states for $\alpha = 1$ (left) and $\alpha = 0.95$ (right)

3.5.2 Impact of Law-Enforcement Rate

It is evident from the expression (3.3.5) for threshold $\mathcal{R}_0$ that to achieve a crime-free society, low crime-indulgence rates (ν_1, ν_2) and high desistance rates (η_1, η_2, ξ) along with high law-enforcement rates (λ_1, λ_2) are required. However, there is a law-enforcement rate term in the numerator of $\mathcal{R}_0$, which means that over-incarceration of first-time offenders is not recommended and optimal values of law-enforcement rate exist. But in the denominator, the law-enforcement rate for recidivists balances the expression and suggests paying more attention to repeat offenders than first-time offenders. Therefore, the required imprisonment level can be evaluated by analyzing this fractional model. As we have

$$\frac{\nu_1^\alpha \nu_2^\alpha \lambda_1^\alpha}{\xi^\alpha(\eta_1^\alpha - \nu_1^\alpha + \lambda_1^\alpha)} - \eta_2^\alpha < \lambda_2^\alpha \tag{3.5.3}$$

Thus, if $\frac{\nu_1^\alpha \nu_2^\alpha \lambda_1^\alpha}{\xi^\alpha(\eta_1^\alpha - \nu_1^\alpha + \lambda_1^\alpha)} < \eta_2^\alpha$, i.e., if the rate of crime indulgence is lesser than the rate of desistance of recidivists then there is no need of imprisonment. Therefore, rehabilitation programs should be conducted effectively for criminals, especially first-time offenders, resulting in low indulgence in criminal activity and hence prevention of crime transmission in society.

3.5.3 Effects of Desistance Parameters

The rates for first-time offenders and repeat offenders of withdrawal from criminal activities without being punished are analyzed in this section. The partial derivatives of $\mathcal{R}_0$ with

respect to η_1 and η_2 are found to be negative as shown in (3.5.4), which means that social interventions, rehabilitation programs for desistance of offenders decrease crime. For majority of judicious parameters, $\left|\frac{\partial \mathcal{R}_0}{\partial \eta_1^\alpha}\right| > \left|\frac{\partial \mathcal{R}_0}{\partial \eta_2^\alpha}\right|$, irrespective of order α. Consequently, first-time offenders require more observation as compared to repeat offenders. So it is required to increase the rate of desistance and decrease the reproduction number, hence decreasing the crime transmission in society. And therefore, punishments and rehabilitation programs should be designed separately for first-time offenders (O_1) and repeat offenders (O_2) with more focus on (O_1) to efficiently control the crime spread due to the assimilation of criminals back into society.

$$\frac{\partial \mathcal{R}_0}{\partial \eta_1^\alpha} = \frac{-\alpha\, \eta_1^{\alpha-1}\nu_1^\alpha}{(\eta_1^\alpha + \lambda_1^\alpha)^2}\left[1 + \frac{\nu_2^\alpha \lambda_1^\alpha}{(\eta_2^\alpha + \lambda_2^\alpha)\xi^\alpha}\right] \quad \frac{\partial \mathcal{R}_0}{\partial \eta_2^\alpha} = \frac{-\alpha\, \eta_2^{\alpha-1}\nu_1^\alpha}{(\eta_1^\alpha + \lambda_1^\alpha)}\left[\frac{\nu_2^\alpha \lambda_1^\alpha}{(\eta_2^\alpha + \lambda_2^\alpha)^2\xi^\alpha}\right] \tag{3.5.4}$$

3.6 Summary

This chapter introduces a mathematical model with in-built memory to study the dynamics of crime transmission using the five stages of the criminal justice system. The basic reproduction parameter $\mathcal{R}_0$ is evaluated with non-locality indulgence, which behaves as a threshold for separating no-crime cases and cases leading to endemic equilibrium. The stability of the fractional order crime transmission model is investigated concerning the values of $\mathcal{R}_0$. The crime-free equilibrium is uniform asymptotically stable for $\mathcal{R}_0 < 1$, and the endemic equilibrium is locally asymptotically stable for $\mathcal{R}_0 > 1$. For $\mathcal{R}_0 \geq 1$, the stability of the positive endemic equilibrium state E^* is investigated. Numerical results are shown to strengthen the results of the proposed model. It is observed that fractional order models converge to the endemic equilibrium faster than the conventional one. When the order of derivative α is reduced from 1, the memory effect of the system increases, and it is observed that crime spreads slowly with a long-time increase in the number of incarcerated criminals. Also, the criminal population and hence the prisoner population decreases with a decrease in fractional order α. Meanwhile, it is observed that increasing the prison length doesn't have much effect on the threshold condition, on the fractions of criminally active and criminally inactive populations. **This work recommends making more strict policies to catch repeat offenders than to catch first-time offenders. It is advised to organize rehabilitation programs for first-time offenders by influencing**

them to prevent engaging in criminal activities and improving their desistance rate for eradicating crime from society. Moreover, the necessary level of imprisonment can be evaluated by scrutinizing the proposed model to reduce the crime prevailing in society.

A part of this chapter is published in the following referred publication:

Sugandha Arora, Trilok Mathur, and Kamlesh Tiwari. "A fractional-order model to study the dynamics of the spread of crime." Journal of Computational and Applied Mathematics 426 (2023): 115102 (I.F- 2.872 , SCI-Q2, Elsevier).

Chapter 4

Air Quality Index Prediction

With the increase in urbanization, industrialization, and traffic in the cities, the air pollutants are increasing and air quality is reducing [191]. To keep a check on the extent of air pollution, US Environment Protection Agency has introduced a parameter called the Air Quality Index (AQI) which tracks the daily effects of air pollutants [192]. AQI is a numerical value between 0 to 500, when the value of AQI is 0, the air quality is adequate and if the value of AQI is 500, then the air quality is hazardous. AQI is calculated by considering major air pollutants $viz.$ Carbon Monoxide (CO), Nitrogen Dioxide (NO_2), Ozone (O_3), Particulate Matter (PM_{10} and $PM_{2.5}$) and Sulphur Dioxide (SO_2). These pollutants are the residual gases and particles emitted from vehicles, industries and due to climate change [193].

Biomass and coal-burning highly increase the levels of Particulate matter (PM_{10} and $PM_{2.5}$) that causes haze in the air. These particles deteriorate the air composition and cause respiratory problems in living beings. Moreover, haze reduces the visibility that further affects the economic sectors such as tourism, and agriculture [194]. The combustion of fossil fuels is carried out in several industries which are the main contributors of SO_2 and NO_2 in the air [195, 196]. Motorized vehicles and combustion of fossil fuels also emit CO, which is another major pollutant responsible for worsening air quality. CO is highly poisonous and can even lead to mortality on long exposure [197]. Another major pollutant is ground-level Ozone O_3, obtained from the combination of two primary pollutants, Nitrogen oxides (NO_x) and Volatile Organic Compounds (VOCs). The 95% of these primary pollutants come from oil, coal, and gasoline combustion in vehicles, industries, power plants, and households; upstream gas and oil production; combustion of residual woods and the evaporated liquid fuels [198]. Exposure to Ozone can significantly affect

human health, cause Asthma, and can lead to pre-mature mortality [199]. In addition, Ozone can adversely affect the vegetation, damage the flowers, and shrubs, and reduce crop productivity. [200, 201].

Air pollution is not a local phenomenon, the current quality of air is dependent on its history. The industrialization has massively impacted the environment especially the air quality [202]. The levels of air pollutants like ground-level Ozone and Particulate Matter are also getting influenced by modifying weather patterns that occurred due to climate change [203, 204]. The change in climate affects the temperature, humidity levels, and wind patterns, which in turn influences the air quality. In addition, the naturally occurring emissions, for example, wind-blown dust, and wildfires, get provoked by climate-driven changes in meteorology that affect air quality. The uncontrolled emission of air pollutants is gradually causing air pollution. Continuous exposure to polluted air is severely affecting human health [205] and leading to the development of lung, heart, and skin diseases. [206]. Thus, forecasting of AQI is required to preserve public health, enable effective policy planning, and promote environmental sustainability by managing and reducing the effects of air pollution.

Several forecasting techniques for AQI are being developed to prevent the serious consequences of air pollution. Based on target objectives, the techniques and approaches of forecasting are being expanded and improved. Traditional AQI forecasting techniques involve statistical techniques such as Auto-regressive Integrated Moving Average (ARIMA) [207, 208], Principal Component Regression (PCR) [209], Multiple Linear Regression (MLR) [210] and Grey models [211, 212]. Fractional calculus is bieng successfully used for air quality prediction [213–215]. Fractional derivative based Kalman filter has been introduced to measure the pollutant emission and hence the air quality [213]. Several variants of fractional Kalman filters have been developed using different fractional order derivatives version for improving the prediction accuracy [214–216]. In these air-quality models, fractional calculus has been incorporated because of its non-local nature. However, these models perform well, but with the high increase in pollution, more accurate methods are required. These models are linear and thus cannot capture the non-linear traits [217, 218]. Even with a large amount of data, not much increase is seen in the accuracy of these models. The performances of the statistical techniques have been improved by developing hybrid techniques [219]. Artificial Intelligence (AI)-based techniques can analyze non-linear data. Thus AI-based models are being developed for time-series forecasting [220, 221], which uses historical data taken at successive equally

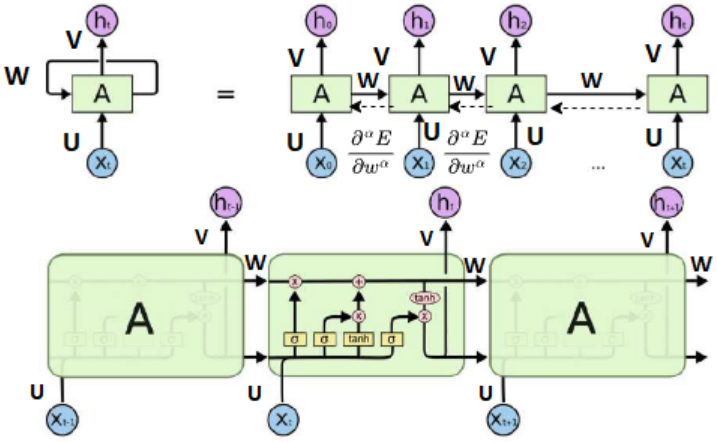

Figure 4.1: RNN Architecture with fractional backpropagation (top) & LSTM architecture (bottom).

spaced points in time to predict future values. With the availability of a sufficient amount of data and computational support, AQI forecasting is being done with a deep neural network [222]. But these methods require to learn large number of parameters. Thus, a simpler and more accurate method is developed in this paper using a Vanilla RNN. The current level of air pollution in any area also depends on AQI status in the past. To capture the history dependency, fractional derivatives have been employed in the backpropagation algorithm to train Vanilla RNN for the prediction of AQI in Indian cities.

In our study, the effect of using fractional derivatives in learning neural networks is analyzed to predict air quality in a few Indian cities. Six of the world's top 10 most polluted cities are from India. Air pollution is observed as the second biggest risk factor causing diseases in India and thus affecting its economy. Thus there is a need to check air pollution in Indian cities. Each city has its unique features like population per square km, temperature, humidity level, climate, vehicles, industries in the region, etc. and thus it is better to study air pollution region-wise. Generally, the air quality in tier I and urban cities is low and it is required to give more attention in such areas. But there is a gradual increase in air pollution in other cities as well across India.

This chapter considers five cities of different tiers for AQI prediction. Bengaluru, Kolkata, and Hyderabad are tier I cities, while Patna and Talcher are tier II and tier III cities respectively. The major air pollutants of Kolkata are also predicted using the proposed approach. The results show that the proposed method achieves minimum error on some fractional order. Also, the obtained results are comparable to the LSTM. This chapter is structured as follows: The next section explains the proposed approach, Section 4.2 discusses the experimental results obtained, followed by concluding remarks in Section 4.3.

4.1 Proposed Approach

In this study, Vanilla RNN is employed to predict the AQI value of a day based on the previous sequential AQI data of five different cities. RNNs are capable of learning the sequential pattern of historical data. Further, the accuracy of the system is improved by incorporating memory into the system using the fractional gradient descent algorithm.

4.1.1 Fractional Gradient Based Backward Propagation Algorithm

This section introduces fractional-order truncated backpropagation through a time algorithm on RNN with 10 neurons in a layer. This backpropagation algorithm considers the truncated depth of the input data and the network state, making the algorithm computationally efficient. For the implementation of the backpropagation algorithm, the mean squared error at an instant is considered which is described as follows:

$$E(s) = \frac{1}{2}\sum_{i\in\Omega}(\Phi(u_i(s)) - x_i(s))^2 = \frac{1}{2}\sum_{i\in\Omega}(e_i(s))^2 \tag{4.1.1}$$

where i is the output neuron, $\Phi(u_i(s))$ and $x_i(s)$ are the actual output and the expected output of the i_{th} neuron at time s and $u_i(s) = \sum_{j\in\Omega} w_{ij}v_j(s)$ at time s where $w_{ij}(s)$ is the weight of a signal from j_{th} neuron to i_{th} and $v_j(s)$ is the output of j_{th} neuron at time s, then the update rule becomes:

$$w_{ij}(s+1) = w_{ij}(s) - \eta\boldsymbol{\nabla}^{\alpha}_{w_{ij}}E(s) \tag{4.1.2}$$

where η is the learning rate and $\boldsymbol{\nabla}^{\alpha}_{w_{ij}}$ represents the factional gradient w.r.t w_{ij}. Now, $\boldsymbol{\nabla}^{\alpha}_{w_{ij}}E(s)$ can be evaluated by applying the approximated chain to the error function. The actual chain rule applicable on fractional derivatives is complicated and involve special mathematical functions, thus several , approximated chain rules has been developed for fractional derivatives. [223–226] The chain rule given by expression (4.1.3) has been obtained by using fractional Taylor's series expansion for differentiable function. Consider a differentiable function, say f then for a small h:

$$f(x+h) = f(x) + \frac{h^{\alpha}}{\Gamma(1+\alpha)}f^{(\alpha)}(x) + \frac{h^{2\alpha}}{\Gamma(2+\alpha)}f^{(2\alpha)}(x) + \frac{h^{3\alpha}}{\Gamma(3+\alpha)}f^{(3\alpha)}(x) + \cdots$$

Then

$$\frac{\Delta f(x)}{h^\alpha} = \frac{1}{\Gamma(1+\alpha)} f^{(\alpha)}(x) + \frac{h^\alpha}{\Gamma(2+\alpha)} f^{(2\alpha)}(x) + \frac{h^{2\alpha}}{\Gamma(3+\alpha)} f^{(3\alpha)}(x) + \cdots$$

Taking limit $h \to 0$, we get

$$lim_{h\to 0} \frac{\Delta f(x)}{h^\alpha} = \frac{1}{\Gamma(1+\alpha)} f^{(\alpha)}(x)$$

Also , $lim_{h\to 0} \frac{\Delta^\alpha f(x)}{h^\alpha} = f^{(\alpha)}(x)$

$$\Rightarrow \Delta^\alpha f(x) \approx \Gamma(1+\alpha)\Delta f(x) \quad 0 < \alpha < 1$$

From above equation we can also say $d^\alpha f(x) \approx \Gamma(1+\alpha) df(x) \quad 0 < \alpha < 1$. Using this result,

$$\begin{aligned} \frac{d^\alpha f(v(x))}{dx^\alpha} &= \frac{d^\alpha f(v(x))}{d^\alpha v} \frac{d^\alpha v}{dx^\alpha} \\ &= \frac{\Gamma(\alpha+1) df(v(x))}{\Gamma(\alpha+1) dv} v_x^{(\alpha)}(x) \\ &= f_v{}'(v).v_x^{(\alpha)} \end{aligned}$$

Hence

$$D_x^\alpha f(v(x)) = D_v^{'} f(v).D_x^\alpha v(x). \tag{4.1.3}$$

After using the above mentioned fractional chain rule, we get

$$\boldsymbol{\nabla}^\alpha_{w_{ji}} E(s) = \frac{\partial E(s)}{\partial e_j(s)} \cdot \frac{\partial e_j(s)}{\partial v_j(s)} \cdot \frac{\partial v_j(s)}{\partial u_i(s)} \cdot \frac{\partial^\alpha u_i(s)}{\partial w_{ji}^\alpha(s)} \tag{4.1.4}$$

Suppose $\dfrac{\partial E(s)}{\partial u_j(s)} = \delta_j(s)$, then

$$\frac{\partial E(s)}{\partial e_j(s)} \cdot \frac{\partial e_j(s)}{\partial v_j(s)} \cdot \frac{\partial v_j(s)}{\partial u_i(s)} = \frac{\partial E(s)}{\partial u_j(s)} \cdot \frac{\partial^\alpha u_i(s)}{\partial w_{ji}^\alpha(s)} = \delta_j(s) \cdot \frac{\partial^\alpha u_i(s)}{\partial w_{ji}^\alpha(s)} \tag{4.1.5}$$

Now, as in this study Caputo's version of fractional derivative (1.1.7) is being used and

${}_0^C D_x^\alpha x^p = \dfrac{\Gamma(p+1)x^{p-\alpha}}{\Gamma(p-\alpha+1)}$, for $p > -1$, then the following holds

$$\frac{\partial^\alpha u_i(s)}{\partial w_{ji}^\alpha(s)} = \frac{w_{ji}^{1-\alpha}(s)v_i(s)}{\Gamma(2-\alpha)} \tag{4.1.6}$$

Thus from Equation (1.1.7), Equation (4.1.5) and Equation (4.1.6) the following final update rule is obtained

$$w_{kj}(s+1) = w_{kj}(s) - \eta \sum_{s=n-h+1}^{n} \delta_k(s) \frac{w_{kj}^{1-\alpha}(s)v_j(s)}{\Gamma(2-\alpha)}. \tag{4.1.7}$$

4.1.2 Data Exploration and Processing

In this study, the continuous AQI data is used to predict future unseen AQI values. For each city, a continuous-time patch of around 1000 data points is used from the AQI dataset. The sample data can be seen in Table 4.1. For constructing the training data, a min-max scaler is used to scale the data values between 0 and 1. The predicted values are also obtained between 0 and 1, which are inverse-transformed later to evaluate the final predicted AQI value.

Table 4.1: Data samples of all cities

Bengaluru						
Date	2019-09-01	2019-09-02	2019-09-03	2019-09-04	2019-09-05	2019-19-06
AQI	61	48	51	51	56	64
Kolkata						
Date	2018-06-16	2018-06-17	2018-06-18	2018-06-19	2018-06-20	2018-06-21
AQI	119	113	107	148	94	100
Hyderabad						
Date	2017-11-01	2017-11-02	2017-11-03	2017-11-04	2017-11-05	2017-11-06
AQI	150	156	158	114	91	80
Patna						
Date	2017-11-05	2017-11-06	2017-11-07	2017-11-08	2017-11-09	2017-11-10
AQI	276	289	286	354	430	439
Talcher						
Date	2018-02-08	2018-02-09	2018-02-10	2018-02-13	2018-02-14	2018-02-15
AQI	311	321	343	343	269	243

4.1.3 Neural Network Architecture and Training

Vanilla RNN is used in the proposed model which has a single-layered architecture with 10 nodes. The fractional gradient-based RNN model is built from scratch. Forward propagation and fractional gradient-based backpropagation as given by Equation (4.1.7) is used for training Vanilla RNN. On the other hand, the LSTM also has a single-layered architecture with 10 nodes, and the integer-order gradient descent algorithm is used to train the model. A window of 10 days (timestamps) is used, which would predict the AQI data for the next (11^{th}) day. Training and testing sets have 600-800 and 100 data values respectively. For the initializing of weights for the models, The most widely adopted Xavier's initialization is used with 0.1 learning rate. This initialization process sets the initial weights by sampling from a Gaussian distribution with zero mean and variance calculated based on the number of inputs and outputs of each layer to avoid the problem of vanishing or exploding gradients. The models corresponding to each city and fractional order are trained for 80 epochs. The Figure 4.1 shows the architecture of the RNN with fractional gradient-based backpropagation. In the diagram, a part of the neural network, **A** accepts input x_t and outputs a value h_t at timestamp t. U, W, and V represent the matrices of weights corresponding to connections joining the input state to the hidden state, one hidden state to the successive hidden state, and the hidden state to the output state respectively. It can be noted that the same set of weights is used for every time step. The gated architecture of LSTM is also shown in Figure 4.1.

4.2 Results and Discussion

This section describes the AQI dataset of five chosen cities, the results obtained using the proposed approach on the AQI data, and the discussion of the comparison between predictions of LSTM and the proposed approach on different fractional orders. The standard evaluation metrics for forecasting models $viz.$ Root Mean Squared Error (RMSE) and Mean Absolute Percentage Error (MAPE) have been employed to assess the performance of the proposed model in the prediction of AQI of different Indian cities and the major pollutants in one of those cities. The lesser the value of RMSE and MAPE, the better the predictor's performance. These errors measure the performance of forecasting, climatology, and regression analysis for verifying the experimental results.

4.2.1 Database Specifications

The AQI dataset of five cities for 2015-2020 is considered which is publicly available at the official portal of the Central Pollution Control Board, Government of India [1]. The dataset consists of daily air quality levels at various stations across multiple cities in India which are obtained by averaging out the hourly value of AQI. Indian cities chosen for the analysis includes Kolkata, Hyderabad, Bengaluru, Patna, and Talcher. Basic information related to these cities:

- **Kolkata** ($22°34'03''$N $88°43'57''$ E), located in West Bengal, is a tier I and the seventh-most populous city of India with third-most populous metropolitan area. The concentration of pollutants such as Sulphur Dioxide and Nitrogen Dioxide remains within the limit but the presence of Particulate Matter in the air is high and is increasing over the years. Due to this air pollution is severe and is causing respiratory ailments like lung cancer.

- **Bengaluru** ($12°58'44''$N $77°35'30''$E) located in Karnataka, is also a tier I, and the third-most populous city of India with fifth-most populous metropolitan area. Bengaluru is also considered as "Silicon Valley of India" because it is the nation's top IT exporter. This IT hub region is the most polluted and is causing several environmental issues. Due to the large population, Bengaluru generates tonnes of solid waste which is polluting the environment. Thus the large population and IT hub of Bengaluru is the major reason for air pollution.

- **Hyderabad** ($17°21'42''$N $78°28'29''$ E) located in Telangana, is also a tier I, and the fourth-most populous city of India with sixth-most populous metropolitan area. Again due to the large population, increased economic activity, and rapid urbanization, tonnes of solid waste are generated and disposal of such waste becomes hazardous and pollutes the environment. The Particulate Matter (PM_{10}) dispersed in the atmosphere causes around 2500 deaths each year.

- **Patna** ($25°36'0''$N $85°6'0''$E) located in Bihar, is a tier II city with a high population. Air pollution is a major issue in this city. The situation in winter becomes even worse due to dense smog, leading to an increase in mortality. Patna was declared as the second most air polluted city in India, in the WHO survey of 2014.

[1] https://cpcb.nic.in/

Table 4.2: Comparison of fractional gradient-based RNN with integer gradient-based RNN and LSTM on the basis of RMSE

Model	Bengaluru	Kolkata	Hyderabad	Patna	Talcher
α =6/9	21.47	31.35	25.35	44.30	14.25
α =7/9	19.36	26.12	**07.41**	34.08	**11.40**
α =8/9	**13.22**	**19.00**	09.75	**23.85**	29.64
α =1	14.78	21.37	08.58	25.44	15.96
α =10/9	24.99	28.50	11.31	38.56	21.09
α =11/9	35.20	21.85	09.95	29.53	24.51
LSTM	**10.78**	**19.00**	**07.02**	24.12	13.11

- **Talcher** ($20°57'0''$ N $85°13'48''$ E) located in Angul district of Orissa, is a tier III city. This is a small city with less population, but Talcher has the country's biggest coalfield with the highest coal reserve of around 52 billion tonnes. The presence of these coal mines leads to air pollution.

The cities of different tiers have been chosen where air pollution is a major issue. To summarise, the cities with a large population or with a high emission rate of air pollutants affecting human health are considered. Around 600 normalized data points for each city have been used for the analysis, which is divided into train and test data in the ratio of 4:1. The model is tested on the data for 100 days for each city.

4.2.2 AQI Prediction Results using Fractional Gradient Learning

The performance of RNN in predicting AQI values of each city using the fractional backpropagation algorithm is analyzed. To assess the performance of the model, RMSE and MAPE are computed. The prediction performance of RNN using the fractional gradient descent algorithm with values of fractional orders in the neighborhood of 1 is compared with the performance of RNN with the traditional integer-order gradient descent algorithm where the order remains 1. The values of fractional order α which are considered are $6/9$, $7/9$, $8/9$, 1, $10/9$, $11/9$ [227]. The results obtained at different orders using the proposed approach can be seen in Table 4.2 and 4.3. The graphs in the Figure 4.2 - Figure 4.6 show the comparison between actual and predicted output for Bengaluru, Kolkata, Hyderabad, Patna and Talcher respectively. In all the graphs, the expected output and the actual output are represented by the orange and blue lines respectively. It can be observed that the least RMSE and MAPE are acquired by Vanilla RNN at some fractional order, either on $7/9$ or $8/9$ for all the cities. The model achieved

Table 4.3: Comparison of fractional gradient-based RNN with integer gradient-based RNN and LSTM on the basis of MAPE (%)

Model	Bengaluru	Kolkata	Hyderabad	Patna	Talcher
α =6/9	14.41	18.21	16.67	14.78	06.62
α =7/9	11.32	11.58	**03.22**	10.64	**04.15**
α =8/9	**06.11**	**07.02**	05.92	**07.43**	16.30
α =1	07.15	09.31	05.23	08.07	06.11
α =10/9	16.60	12.90	05.49	11.51	06.66
α =11/9	22.54	10.50	04.99	12.90	07.90
LSTM	**05.78**	**06.61**	03.45	07.83	**04.11**

minimum RMSE and MAPE of 13.22 and 06.11% respectively at $\alpha = 8/9$ for Bengaluru. Also, the minimum RMSE and MAPE are found to be 19 and 7.02% for Kolkata and 23.85 and 7.43% for Patna at $\alpha = 8/9$. Moreover, the minimum RMSE and MAPE are found to be 7.41 and 3.22% for Hyderabad and 11.40 and 4.15% for Talcher at $\alpha = 7/9$. Thus it can be concluded from the results that the fractional order gradient is more accurate than the integer-order gradient algorithm. Moreover, the proposed model performed best for $\alpha = 0.7$ by achieving the least MAPE of 3.22% for Hyderabad among all the cities.

4.2.3 Results Comparison between Proposed Method and LSTM

The prediction of AQI for the same set of datasets of all cities is done using LSTM as well with the same number of timestamps, nodes, and the same procedure for inputs as for fractional RNN. The obtained results are also shown in Table 4.2 and 4.3. It can be concluded from the table that the performance of the LSTM is comparable to Vanilla RNN with fractional gradient learning. RMSE values for the proposed network are 23.85 & 11.40 which are lesser than 24.12 & 13.11 RMSE achieved by LSTM, corresponding to Talcher and Patna respectively. The RMSE of fractional-based RNN and LSTM is found to be 19 for Kolkata which is equal. Similarly, the MAPE for Hyderabad and Patna are found to be 03.22% and 7.43% respectively by RNN with fractional gradient learning, whereas higher MAPE of 3.45% and 7.83% for Hyderabad and Patna respectively are achieved by LSTM. For Talcher, MAPE is found to be 4.15% corresponding to fractional gradient-based RNN and is found to be 4.11% for LSTM which are almost equivalent. It can be seen that the least MAPE of 3.22% is obtained by fractional gradient-based RNN for Hyderabad as compared to other cities and models. Figure 4.7 shows the comparison between the expected AQI value and the AQI value predicted for all the cities by LSTM.

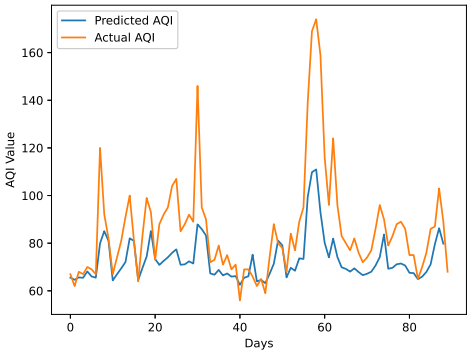

(a) $\alpha = 6/9$

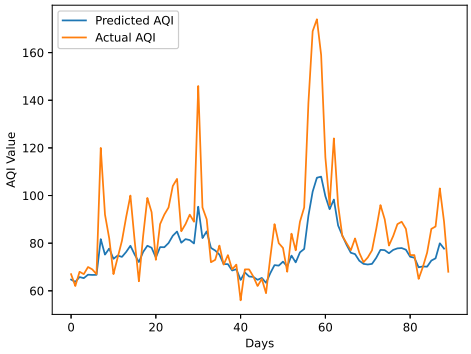

(b) $\alpha = 7/9$

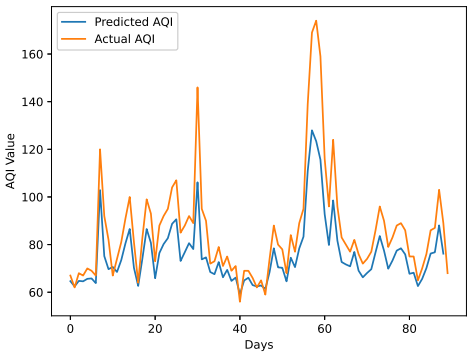

(c) $\alpha = 8/9$

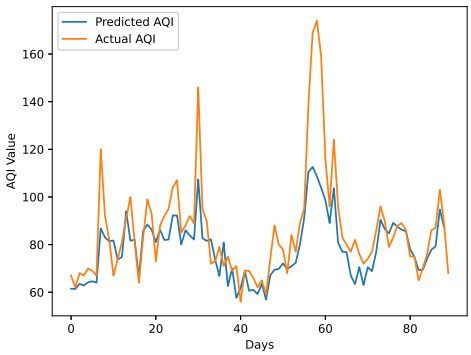

(d) $\alpha = 1$

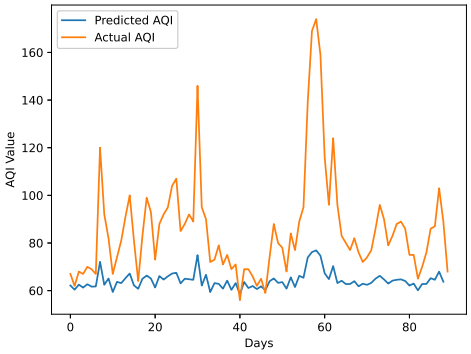

(e) $\alpha = 10/9$

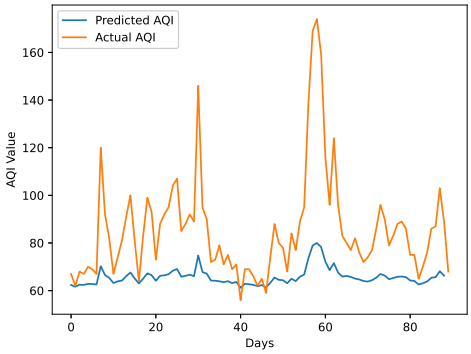

(f) $\alpha = 11/9$

Figure 4.2: Predicted vs actual AQI of Bengaluru city for the period of 100 days from 29-08-2019 to 07-12-2019

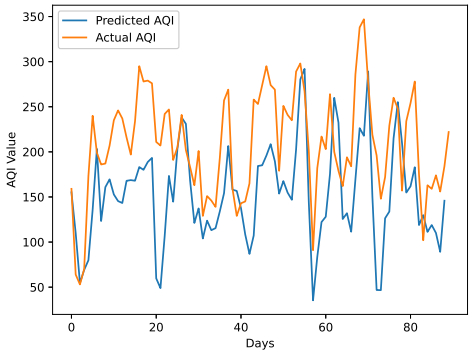

(a) $\alpha = 6/9$

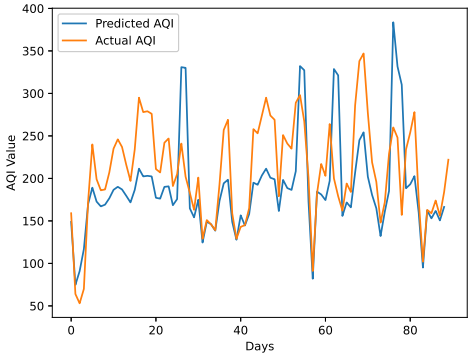

(b) $\alpha = 7/9$

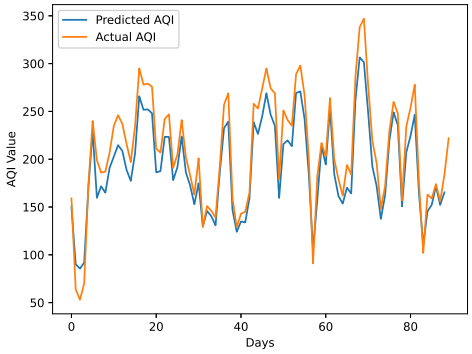

(c) $\alpha = 8/9$

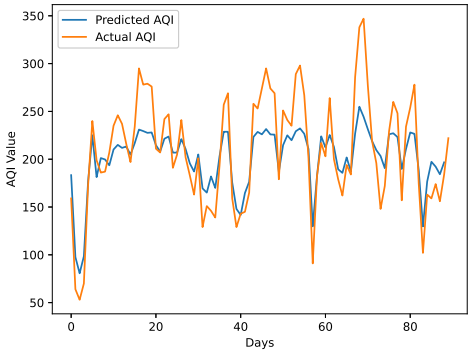

(d) $\alpha = 1$

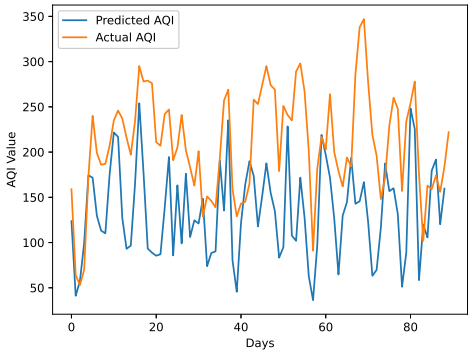

(e) $\alpha = 10/9$

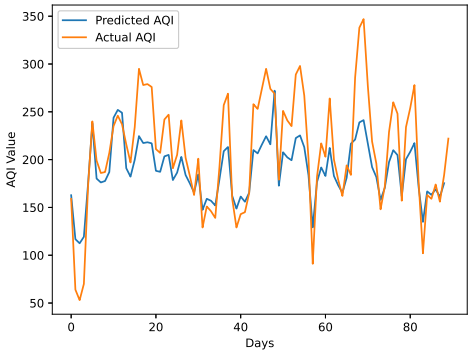

(f) $\alpha = 11/9$

Figure 4.3: Predicted vs actual AQI of Kolkata city for the period of 100 days from 28-10-2019 to 04-02-2020

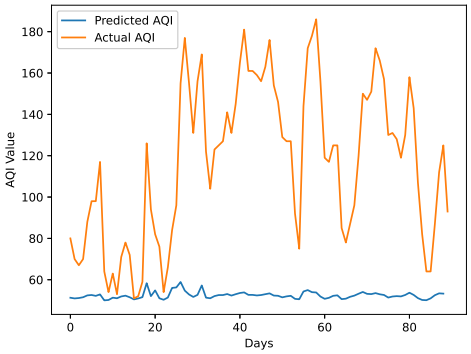

(a) $\alpha = 6/9$

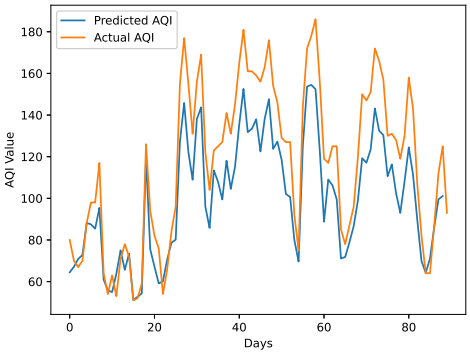

(b) $\alpha = 7/9$

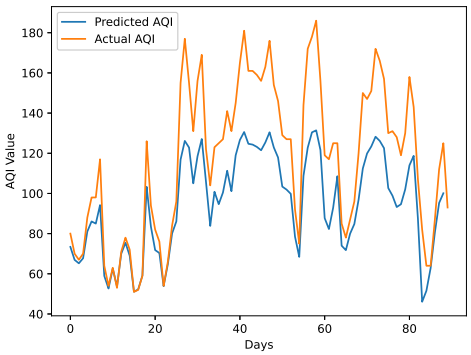

(c) $\alpha = 8/9$

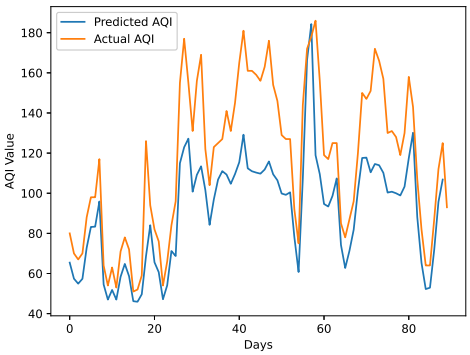

(d) $\alpha = 1$

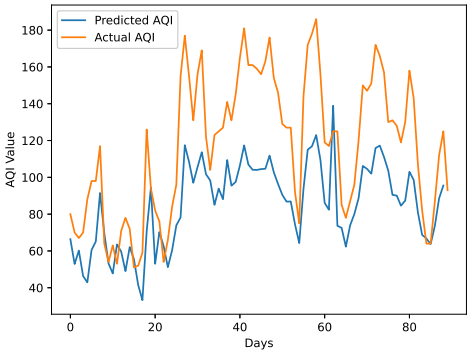

(e) $\alpha = 10/9$

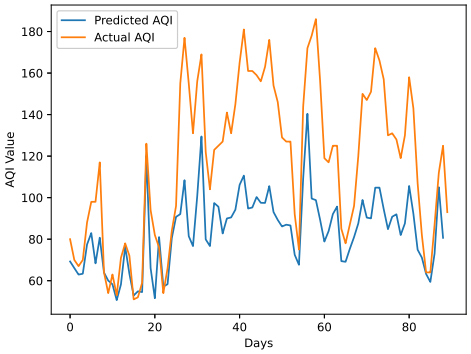

(f) $\alpha = 11/9$

Figure 4.4: Predicted vs actual AQI of Hyderabad city for the period of 100 days from 29-09-2019 to 06-01-2020

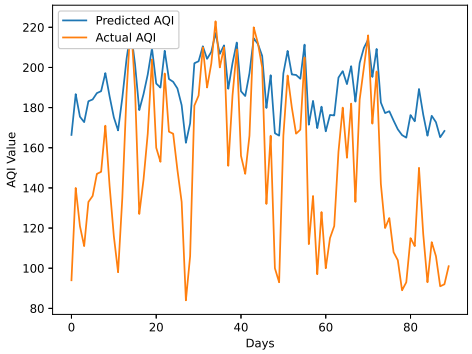

(a) $\alpha = 6/9$

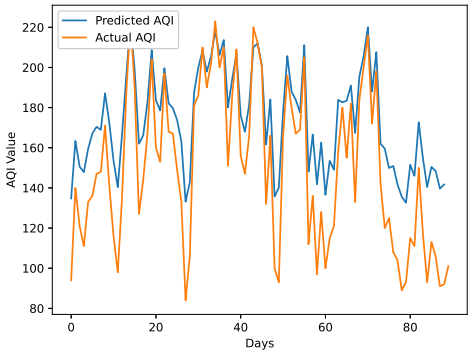

(b) $\alpha = 7/9$

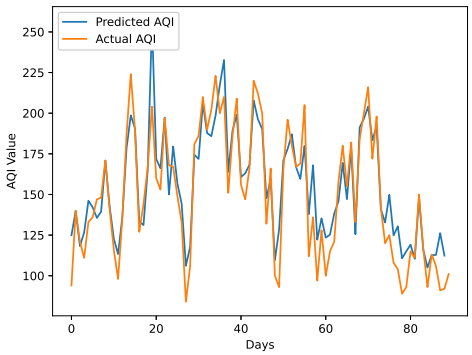

(c) $\alpha = 8/9$

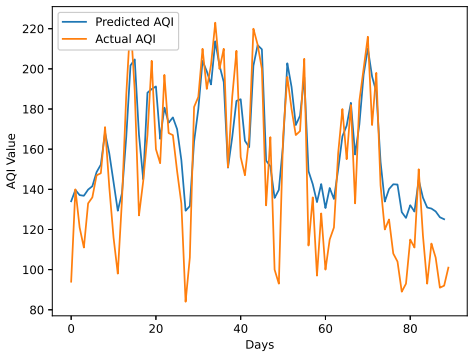

(d) $\alpha = 1$

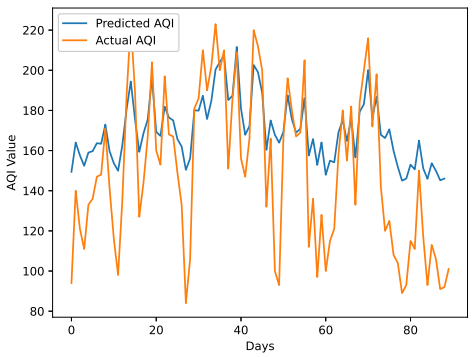

(e) $\alpha = 10/9$

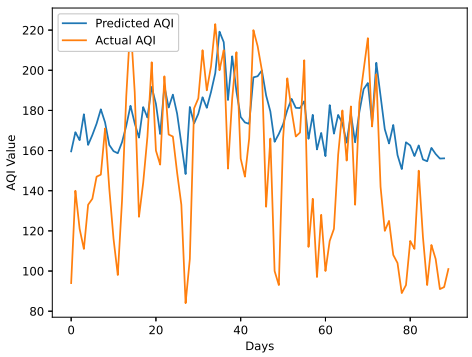

(f) $\alpha = 11/9$

Figure 4.5: Predicted vs actual AQI of Patna city for the period of 100 days from 26-03-2019 to 04-07-2019

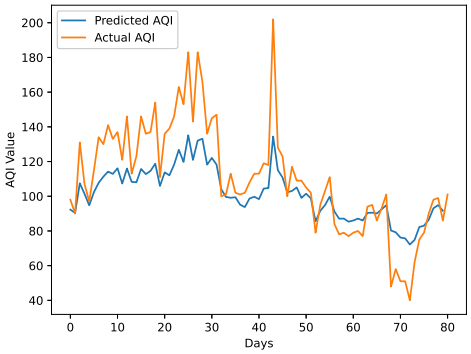

(a) $\alpha = 6/9$

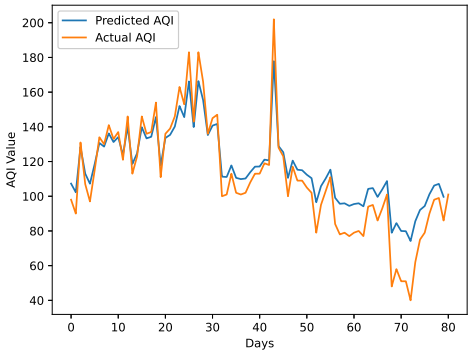

(b) $\alpha = 7/9$

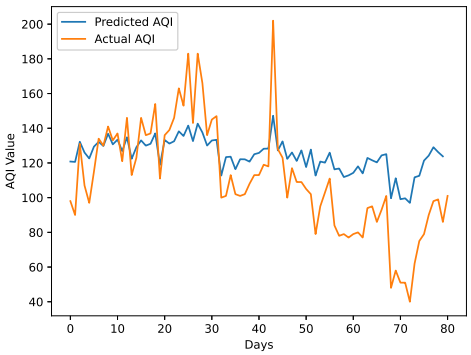

(c) $\alpha = 8/9$

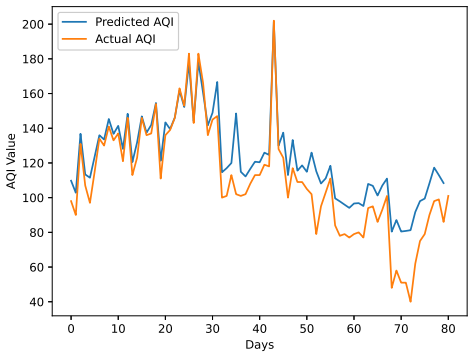

(d) $\alpha = 1$

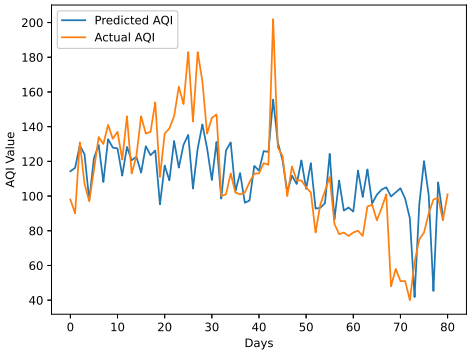

(e) $\alpha = 10/9$

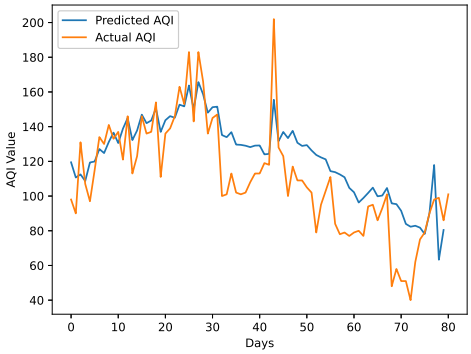

(f) $\alpha = 11/9$

Figure 4.6: Predicted vs actual AQI of Telchar city for the period of 100 days from 01-03-2020 to 08-06-2020

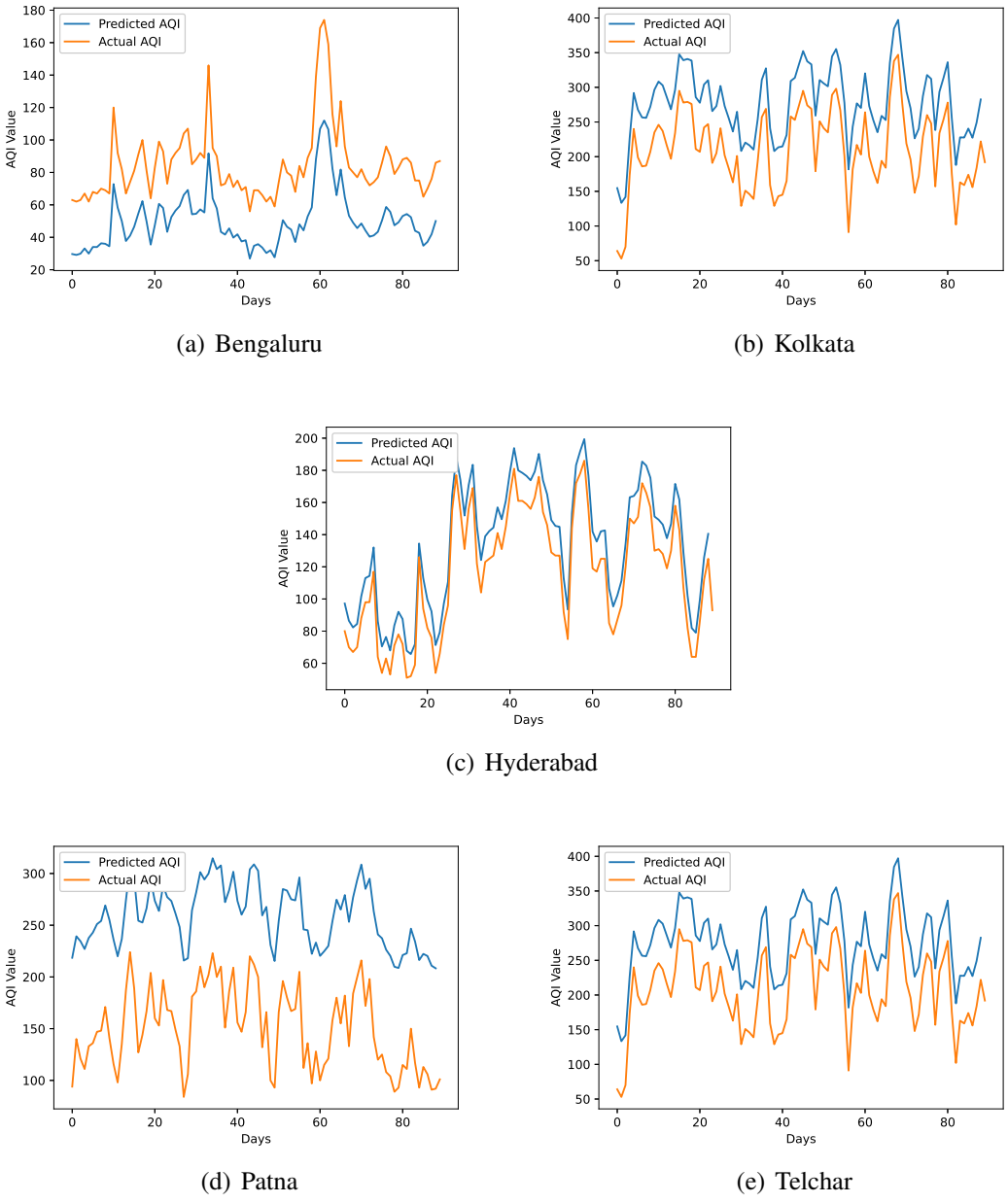

(a) Bengaluru

(b) Kolkata

(c) Hyderabad

(d) Patna

(e) Telchar

Figure 4.7: Predicted vs actual AQI of all cities for the period of 100 days using LSTM

4.2.4 Prediction Results of Major Pollutants in Kolkata

The proposed approach is implemented for the prediction of the concentration of major pollutants- SO_2, CO, and PM_{10}. Here, the considered time is also the same as used in the prediction of the AQI of Kolkata. As we have seen in the above section that the performance of the algorithm is found to be better either for $\alpha = 7/9$ or $8/9$. So we have

Table 4.4: RMSE corresponding to fractional gradient based RNN for different orders in predicting the concentration of different pollutants responsible for air pollution in Kolkata city

Pollutant	**RMSE**			**MAPE (%)**		
	α **=7/9**	α **=8/9**	α **=1**	α **=7/9**	α **=8/9**	α **=1**
SO_2	1.9	**1.62**	1.77	7.00	**5.55**	6.83
CO	0.20	**0.12**	0.15	5.21	**4.20**	4.89
PM_{10}	36.45	**19.25**	33.75	10.95	**6.77**	11.21

considered these two fractional values to compare the results with the integer-order-based learning of Vanilla RNN. The Figure 4.8, Figure 4.9 and Figure 4.10 shows the comparison between expected air pollutant concentrations and actual concentrations in Kolkata. It can be observed from Table 4.4 that minimum RMSE and MAPE for each city are attained at order $\alpha = 8/9$, thus outperforming the traditional integer-order learning for Vanilla RNN. Moreover, the least MAPE of 4.70% is achieved in the prediction of CO and thus, the proposed model is better for predicting the concentrations of CO as compared to other pollutants.

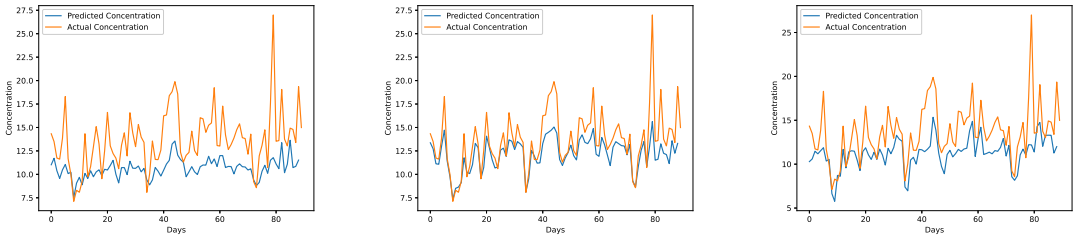

(a) $\alpha = 7/9$ (b) $\alpha = 8/9$ (c) $\alpha = 1$

Figure 4.8: Predicted vs actual Sulphur Dioxide (SO_2) in the air in Kolkata for the period of 100 days from 28-10-2019 to 04-02-2020

4.3 Summary

In this chapter, the fractional-order gradient is used in the backpropagation of error of Vanilla RNN for the AQI prediction of five Indian cities belonging to different tiers. Through the results of the prediction of AQI of multiple cities, it is observed that the minimum error on predictions is achieved at a fractional order. Most cities achieve better results when the order is equal to $8/9$. The architecture of vanilla RNN is much simpler than the structure or functioning of an LSTM, but the predictions made by RNNs with fractional gradient-based backpropagation are comparable and sometimes even better than

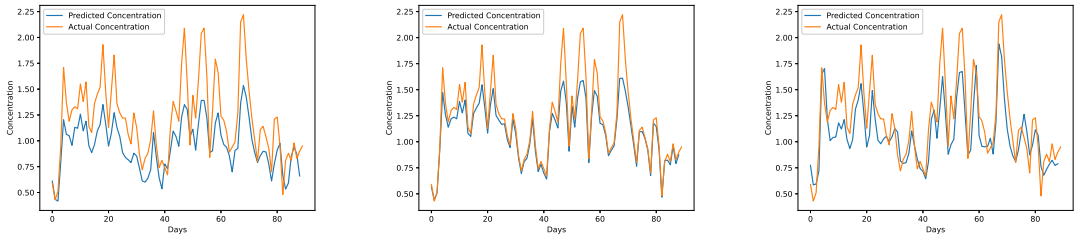

(a) $\alpha = 7/9$ (b) $\alpha = 8/9$ (c) $\alpha = 1$

Figure 4.9: Predicted vs actual Carbon Monoxide (CO) in the air in Kolkata for the period of 100 days from 28-10-2019 to 04-02-2020

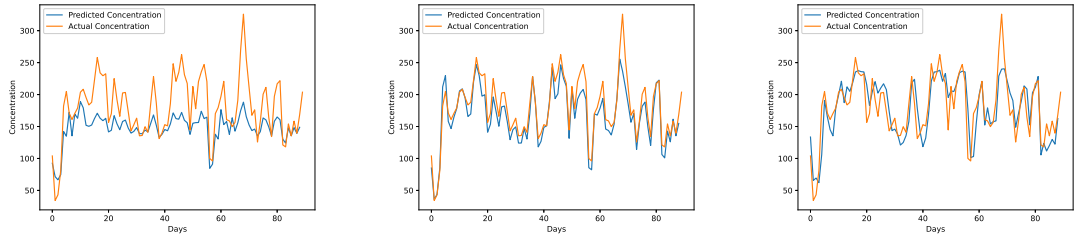

(a) $\alpha = 7/9$ (b) $\alpha = 8/9$ (c) $\alpha = 1$

Figure 4.10: Predicted vs actual Particulate Matter (PM_{10}) in the air in Kolkata for the period of 100 days from 28-10-2019 to 04-02-2020

LSTM with the integer-order gradient descent algorithm. Specifically, the least MAPE value is found for Hyderabad by using fractional gradient-based RNN as compared to other cities and models. Moreover, the proposed approach is used to predict major air pollutants in the tier I city of Kolkata. Here also, it is observed that the least MAPE is achieved during predictions of CO concentrations at a fractional order. Achieving lesser RMSE and MAPE, while using simpler architecture shows the effectiveness of fractional gradient over integer-order gradient descent.

From the results, it can be seen that RMSE is more for Kolkata and Patna. The possible reasons for it can be: 1) Increasing Pollution in Patna, putting it amongst the world's top 10 most polluted cities, and; 2) Continuous growth of Particulate Matter in Kolkata. The memory property of fractional derivatives can be well exploited with deep neural networks for dealing with complex and dynamic data.

This work can be extended by predicting air pollutants in all the cities and subsequently predicting AQI values on that basis. This strategy can detect major air pollutants in a city, and accordingly stringent actions can be taken to prevent further damage. A portfolio of

economic activities can be created considering the air quality of the particular city and also detecting the most affecting gases among them in the future. The order of the derivative is chosen manually in this paper, due to which results are evaluated only on a few values of order. Hence. there is a need to develop an adaptive method that automatically evaluates the optimal order for a particular city or dataset.

A part of this chapter is published in the following referred publication:

Sugandha Arora, Narinderjit Singh Sawaran Singh, Divyanshu Singh, Rishi Rakesh Shrivastava, Trilok Mathur, Kamlesh Tiwari, and Shivi Agarwal. "Air Quality Prediction Using the Fractional Gradient-Based Recurrent Neural Network." Computational intelligence and neuroscience 2022 (2022) (Hindawi).

Chapter 5

Satellite Image Road Segmentation

Remote sensing images acquired through satellites are high-resolution and contain large coverage of the geographical region. These images provide accurate topographical information about the earth's surface [228–230]. Roads can be extracted from these images, which can help in urban planning, emergency rescue, autonomous driving $etc.$ Semantic segmentation is needed to extract roads from such images. It is equivalent to a classification setup that assigns a class of either road or non-road to every pixel of the image. This chapter focuses on extracting all the pixels corresponding to roads.

Traditional automatic road segmentation methods involve the usage of machine learning techniques like Bayesian [231] and heuristic methods [232, 233]. Heuristic methods semantically combine roads and group them using hypothesis and testing paradigm, while the Bayesian approach involves stochastic process models which extract roads by probabilistic modeling [234, 235]. Ambient challenges include shadow, variable road width, complex surroundings, occlusion arising due to traffic and trees $etc.$ pose serious challenges to these methods and significantly reduce their accuracy [236, 237]. Most machine learning algorithms fail to achieve high precision in the road network segmentation due to their inability to handle multi-scale road sections, particularly narrow road segments with substantial width variability [238, 239]. Road extraction models based on road features, automation, problems arising while extraction and the type of methods adopted, are comprehensively reviewed in [240].

To overcome the challenges of road network segmentation, several deep-learning approaches have been developed [249, 261, 284]. Convolutional neural networks (CNN) are popular filters for extracting useful features from an image. A network with multiple layers of CNNs called deep convolutional neural networks (DCNNs) can be devised to

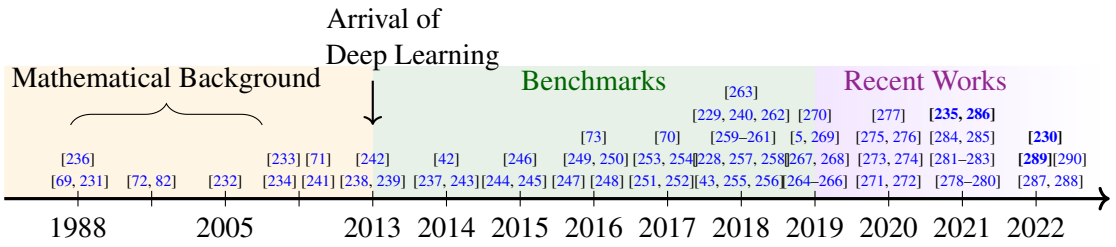

Figure 5.1: Visual representation of references arranged in chronological order

build a hierarchy of features from the multi-scale remote sensing data sets [266, 272]. The mainstream segmentation networks like Fully Convolutional Neural Networks (FCNN) [246], U-Net [244], U-Net++ [262], Deeplabv3 [253], deep residual U-Net [259] *etc* are successfully being used for the road extraction. The FCNNs with skip connection architecture can combine semantic information from deep, coarse layers and appearance information from shallow, fine layers to improve the segmentation performance. This fusion of fine and coarse layers intends to preserve global structure while making local predictions. Further, U-Net [244, 262] uses an end-to-end training approach by concatenating the pair of corresponding cropped feature maps from the encoder and decoder that prevents the loss of information and helps in the precise localization. ResNet [6, 259] uses the past feature maps using skip connections that help to prevent vanishing gradient problems and avoid any loss of information. DenseNet [265] also uses skip connections to get inputs from each preceding layer of a dense block, which increases the input variability and the network performs more accurately.

The architectures of networks mentioned above can efficiently perform the segmentation task, but complex backgrounds and occlusion due to buildings, cars, trees , *etc.*, overlapping, interlacing, and shadowing of the clouds, trees *etc.* in satellite images affects the accuracy of road network extraction. Long-term feature interactions are required to extract roads from the images with complex backgrounds, since such interactions can preserve semantic/appearance information. Thus to improve the forward propagation of the features, it is better to reuse the feature extracted at preceding states. The architecture of some DCNNs such as DenseNet [265], SDUNet [289], CondiNet++ [282] and RoadVecNet [280] have been designed to address the problem of long-term memory and preservation of global and local cues, but without any solid theoretical explanation of memory exploitation. These works extract global and local features separately, while fractional derivative-based methods inherently compute global and local features. FOCNet [5] has been proposed in the literature for image denoising to address the memory issue,

Table 5.1: Comparison of state-of-the-art road segmentation methods with respect to architecture and results on ORD and MRD

	Methods	Architecture	Database	Results
1.	ResUnet: encoder decoder architecture [259] (2018)	U-Net like architecture with residual skip connections	MRD [242]	breaking point=0.9187 and outperformed state-of-the-art methods : U-Net [244], Saito-CNN [247] and Mnih-CNN [241]
2.	D-linkNet : encoder decoder architecture [256] (2018)	pretained ResNet34 as encoder, and decoder of original linkNet with dilated convolutions	DGRD	Achieved best IoU scores 0.6466 and 0.6342 on the validation and the test set resp.
3.	GL-DenseUNet : encoder decoder architecture [257] (2018)	DenseUnet architecture with global attention unit	Google earth images	Outperformed U-Net [244], FCN [246] and DeepLabV3+ [255] with higher F1-scores
4.	End-to-End road centerline extraction using a confidence map [260] (2018)	The model adopted 13 VGG layers to create an encode-decode network architecture.The model generates multiple scale outputs.	MRD [242]	The model achieves 0.92 on completeness metrics and 0.87 on correctness matrics
5.	DenseUNet : encoder and decoder architecture [265] (2019)	UNet with dense blocks	MRD [242]	Outperformed UNet [244], SegNet [251], GL-DenseUNet [257] with F1-score and mIoU of 74.07% and 74.47% resp.
6.	A Two-Step Deep Convolution Neural Network [267] (2019)	Used two continuous Unet: high precision first Unet and then high recall second Unet	MRD [242]	The model achieved significant results in terms of accuracy, precision, Recall and F1-score.
7.	Generative Adversarial Network [279] (2021)	Used GAN based approach with Modified UNet as generative part	MRD [242]	the approach achieved 91.54 precision, 92.92 recall, MCC of 91.13, mIOU of 87.43 and a F1-score of 92.20.
8.	RoadVecNet: encoder and decoder architecture [280] (2021)	Used two encoders, two decoders, basically two U-nets with dense connections	ORD [258] & MRD [242]	Achieved high F1-scores, MCC and mean IoU on both databases
9.	BMDANet: encoder decoder [286] (2021)	with multi-dimensional attention module	ORD [258]	Outperformed S-O-A methods like UNet [244], D-linknet [256] with 0.9363 F1-score and 0.8802 mIoU.
10.	ConDinet++ : encoder and decoder architecture [282] (2022)	Pretrained VGG16 as encoder, feature fusion using conditional dilated convolution blocks in the decoder with the joint loss of cross-entropy and Lovasz loss	MRD [242]	the model outperformed several state-of-the-art with high precision, recall, mIOU and F1-Score
11.	SDUNet: encoder and decoder architecture [289] (2022)	DenseUNet with DULR Module, loss function as sum of binary cross entropy loss and dice coeff loss	MRD [242]	Outperformed state-of-the-art like UNet [244], D-linknet [256] with 0.7410 F1-score & 0.7840 mIoU.

where the network is designed by solving a system of fractional differential equations, and, the global and local features are extracted inherently. Some relevant road segmentation works are compared in Table 5.1 based on architecture and results. Figure 6.1 shows the arrangement of references in chronological order to show how over time, frontiers of mathematical background have developed and the work on the road network segmentation has gained research attention from the community. It can be noted that earlier fractional calculus was an abstract area of research with vigorous calculations and recently with the introduction of new definitions of fractional derivatives, the applications of fractional calculus is being seen in several domains of science and engineering including image processing. It can also be seen that the arrival of deep learning has motivated the growth of automatic road extraction techniques and researchers are engaged in overcoming the challenges through the development of new models.

The automatic way of finding the network parameters treats the system as a black box, which lacks interpretability [291, 292]. Due to this, understanding the conceptual basis, potential advantages, and limitations of methods become difficult [293]. Moreover, tuning the additional parameters when handling different databases is not feasible. If the process of decision-making by the network is known, then this provides the flexibility of adjusting human preferences through parameters. Thus it is recommended to decide these parameters on a mathematical basis. Some recent studies have shown that the forward propagation in DCNNs can be treated as a dynamic system which can further be characterized by a differential equation [69, 70, 263]. The forward propagation of ResNet is shown to be equivalent to the forward Euler numerical discretization of an ordinary differential equation (ODE) in [263]. They also showed that other recent architectures like RevNet [254], and FractalNet [250] can be designed by the discretization of some ordinary/ partial differential equation [271]. The ordinary/partial differential equations systems are local, so only short-term feature interactions are possible, whereas fractional differential systems are non-local and have long-term memory. Numerous dynamic systems have been demonstrated to be better characterized by FODE than ODE [294]. Therefore, designing the road segmentation network using ODE is not enough. We have modeled the propagation of the deep road segmentation network as a dynamic system using fractional differential equations to enhance the memory of the network. Fractional differential equations are non-local and incorporate memory into the system by adding fractional weights to the skip connections between the layers. These fractional weights can be interpreted using the mathematical framework of Grunwald-Letnikov fractional

derivatives [82]. The memory of a dynamic system obeys the power law [42], which means the recent stage will have more weightage than the older ones, and Grunwald Letnikov fractional derivatives also follow the power-law memory property [42, 43].

In this chapter, the road segmentation network is designed by solving a fractional optimal control problem. The forward propagation of the proposed network is constructed by discretizing the system of Grunwald-Letnikov-based FODEs with control variables. As a result, the output of each layer of the proposed network becomes dependent on the weighted sum of features of previous layers at the same level where weights are controlled by fractional order and state of the network. The advantages of using FODE-based dense road segmentation networks over ODE-based dense segmentation networks are: 1) The FODE can describe the power-law memory mode and has been proven effective in preserving memory. 2) The output of each layer of the proposed network depends on the weighted sum of features of previous layers at the same level instead of the concatenation of the features, which reduces the number of learning parameters. The main contributions of the chapter are highlighted below:

1. This chapter proposes a road segmentation network with weighted skip connections which is modeled as a dynamic system using G-L fractional derivative. This work exploits the memory property of fractional derivatives in designing the road extraction network.

2. The proposed fractional derivative-based dense network considers all past feature vectors and reuses them at forward states, but with a lesser number of parameters and with mathematical interpretations behind it. The weighted sum of outputs of the previous layer is computed in place of their concatenation to reduce the number of parameters. Weights corresponding to these skip connections depend on the chosen order of derivative.

3. Experiments are carried out on two open-source databases viz. Massachusetts Road Database (MRD) [242] and Ottawa Road Database (ORD) [258] with different road structures and backgrounds. Results show that the proposed model achieves state-of-the-art performance in terms of recall, F1-score, and mean IoU.

This chapter is structured as follows: Section 5.1 explains the proposed approach, followed by the experimental results obtained in Section 5.2, and the concluding remarks are added in Section 5.3.

Table 5.2: Scalewise architecture details of the proposed road segmentation network

Level	Input Size	Number of layers	Number of Filters
1	512×512	4 (both sides)	64
2	256×256	5 (both sides)	128
3	128×128	7 (both sides)	256
4	64×64	10 (both sides)	512
5	32×32	12	1024

5.1 Proposed Approach

This section describes the proposed methodology from a mathematical perspective. The proposed architecture is designed by solving an optimal control problem comprising fractional differential equations. The fractional optimal problem view of road segmentation is presented in this section. Moreover, the architecture of the network is well explained with the help of mathematical equations.

5.1.1 Fractional Optimal Control View of Road Segmentation

The propagation between the layers of the proposed network is modeled as a dynamic system. The dynamic system is then represented with the help of fractional differential equations with control parameters. The obtained fractional optimal control problem is described here. Consider the following fractional differential system [72] describing the propagation of deep CNN in which the feature trajectory $z(t, s)$ is assumed to be continuous in time and space:

$$\min_{\theta(t)} \int_{\Omega} L(\Phi(z(T, s)), u(s))\, ds$$

s.t.

$$ {}_0D_t^{\alpha} z(t, s) = f(z(t, s), \theta(t)), \;\; z(0, s) = \Psi(I(s)), \;\; t \in [0, T] \tag{5.1.1}$$

where $s \in \Omega$ is the two-dimensional spatial position, $I(s)$ is the input road image, $u(s)$ is the ground truth segmented road image and Φ, Ψ are linear transformation , $e.g.$ convolution. The proposed network is designed by solving the above fractional optimal control problem as the fractional-order differential equation has long-term memory. The problem (5.1.1) aims to find the optimal control $\theta(t)$ such that the objective loss, $i.e.$, dice coefficient loss is minimized [73].

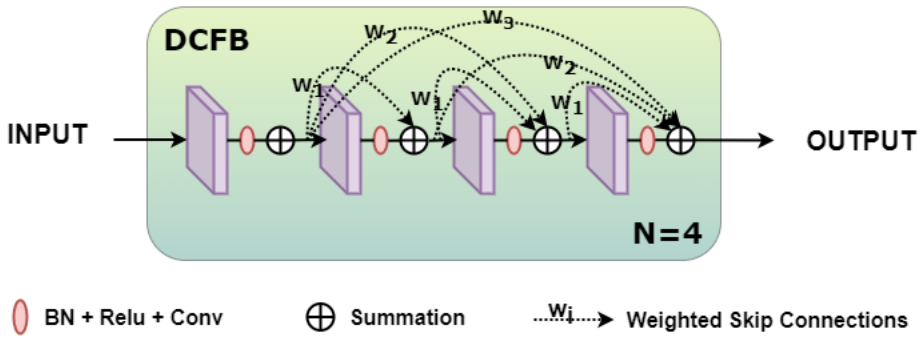

Figure 5.2: Densely Connected Fractional Block (DCFB) with 4 layers

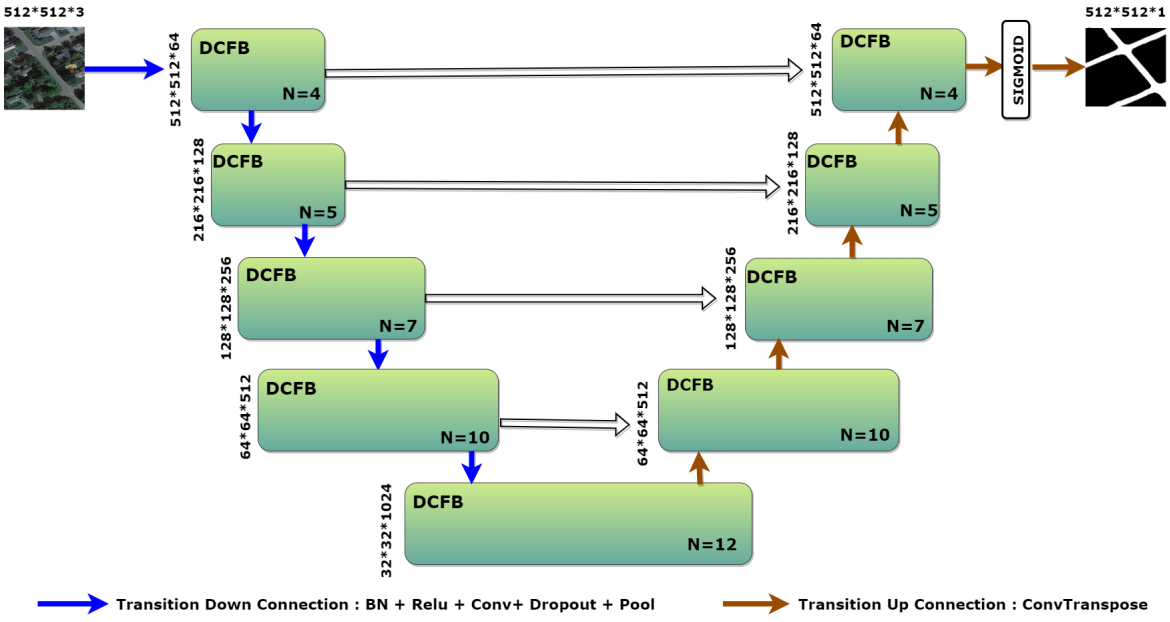

Figure 5.3: Diagram of the proposed architecture for road segmentation

5.1.2 Architecture of the Proposed Road Segmentation Network

The architecture of the proposed model is designed by discretizing the multi-scale system. In each transition, all the features given by the output of the historical states are being used at each state, and thus the features are being used for a long time. Due to the application of fractional derivatives in the evolution process, the network gets embedded with weighted skip connections and those weights are dependent on the fractional order of differentiation and the current state. The order α is positive and less than 1, due to which the weighted sum remains positive and doesn't explode. For discretization, the step size, h is set to be 1. Then definition (1.1.10) takes the following form for order $0 < \alpha < 1$:

Table 5.3: Layerwise architecture details of the proposed road segmentation network

Layer	Description	Kernel Size	Stride Length	Regularizer	Dropout	Pool Size	Pool Stride
Transition Up	Conv2DTranspose	2×2	2	L2	-	-	-
Transition Down	BN+Conv2D	1×1	1	-	-	-	-
	Dropout+MaxPool	-	-	-	0.2	2×2	2
DCFB Layer	BN+Conv2D	3×3	1	-	-	-	-
	Dropout	-	-	-	-	0.2	-

$$ {}_0D_t^{\alpha} z(t,s) \approx \sum_{k=0}^{t} (-1)^k \binom{\alpha}{k} z(t-k,s) \tag{5.1.2} $$

Thus after combining the above expression (5.1.2) with ${}_0D_t^{\alpha} z(t,s) = f(z(t,s),\theta(t))$ of system (5.1.1), we get

$$ z(t,s) = f(z(t,s),\theta(t)) - \sum_{k=1}^{t} (-1)^k \binom{\alpha}{k} z(t-k,s) \tag{5.1.3} $$

$$ z_{t+1} = f(z_t,\theta_t) + \sum_{k=1}^{t} (-1)^{(t-k+1)} \binom{\alpha}{t-k+1} z_k \tag{5.1.4} $$

The proposed network is U-shaped, and thus it has four transitions down and correspondingly four transitions up (four scales). The scale-wise architectural details, $i.e.$, number of layers, filters, and input size at a particular transition are presented in Table 5.2. The following system can describe the multi-scale representation of the evolution process:

$$ {}_0D_t^{\alpha} z(t,s,p_{l_i}) = f(z(t,s,p_{l_i})),\theta_{p_{l_i}}(t)) \tag{5.1.5} $$

$$ {}_0D_t^{\alpha} z(t,s,p_{r_j}) = f(z(t,s,p_{r_j})),\theta_{p_{r_j}}(t)) \tag{5.1.6} $$

for each $i \in [1,5]$, $j \in [1,4]$, $t \in [0,T]$ with the following initial conditions

$$ z(0,s,p_{r_j}) = T_{\uparrow} z(n_{r_{j+1}},s,p_{r_{j+1}}) + z(n_{l_j},s,p_{l_j}), $$

$$ z(0,s,p_{l_1}) = \Psi(I(s)), \quad z(0,s,p_{l_i}) = T_{\downarrow} z(n_{l_{i-1}},s,p_{l_{i-1}}) \tag{5.1.7} $$

where $T_{\downarrow}$ denotes max pooling operation, $T_{\uparrow}$ denotes upsampling, $\theta_{p_{l_i}}$ is convolution kernel at scale i on the left and $\theta_{p_{r_i}}$ is convolution kernel at scale i on the right. Thus the evolution process of the road segmentation network is represented by (5.1.8).

$$z_{t+1}^{p} = \sum_{k=0}^{t} w_k z_k^p + \sigma(\theta_t * (z_t^p))) \tag{5.1.8}$$

where σ is a non-linear unit denoting 'Convolution + Batch normalization[1] + ReLu', z_{t+1}^{p} is the output of t^{th} layer of scale p, $w_k = (-1)^{(t-k+1)}\binom{\alpha}{t-k+1}$, and thus $w_t = \alpha$. The network layers are densely connected with the help of fractional-weighted skip connections. The layer t is connected with $(t-1)^{th}$, $(t-2)^{th}\cdots$ layers via skip connections with weights w_1, w_2.. respectively. The general evolution of the network is represented by (5.1.8). The architecture is built from the Densely Connected Fractional Blocks (DCFBs) shown in Figure 5.2, where BN stands for batch normalization and N stands for number of layers. The layer at each level is addressed as a DCFB layer. The architecture of the model can be seen in Figure 5.3 and the corresponding architectural details related to any layer of the network are presented in Table 5.3. As shown in Figure 5.3, the network is composed of a downsampling path with 4 Transitions Down (TD) shown with blue arrows and an upsampling path with 4 Transitions Up (TU) shown with orange arrows. Black horizontal arrows represent skip connections, the feature maps from the downsampling path are added to the corresponding feature maps in the upsampling path. The propagation in between the layers at left are represented by (5.1.5) and by (5.1.6) for the layers at right with initial conditions given by (5.1.7). If (x_i, y_i) represents the training set where x_i is the input satellite image and y_i is the corresponding ground truth segmented image. So, if $z_T^i(\Theta)$ is the final output and Θ represents the parameters of the network. Thus dice coefficient loss (DCL) for a particular image sample is given by:

$$DCL(z_T^i(\Theta), y_i) = 1 - DC(z_T^i(\Theta), y_i) = \ 1 - \left(\frac{2TP_i}{2TP_i + FP_i + FN_i}\right) \tag{5.1.9}$$

where TP_i, FP_i and FN_i are true positive, false positive and false negative pixels respectively for i^{th} image sample.

The optimized value of network parameters is obtained after solving the above set of fractional differential equations that are representing the evolution process of the proposed network. At each level, the features of each layer are connected with each other with the help of weighted skip connections in accordance with the definition of G-L fractional derivative. This enhances the memory of the system and the features of the present

[1]Process of normalizing the inputs of each layer by adjusting and scaling them to have zero mean and unit variance.

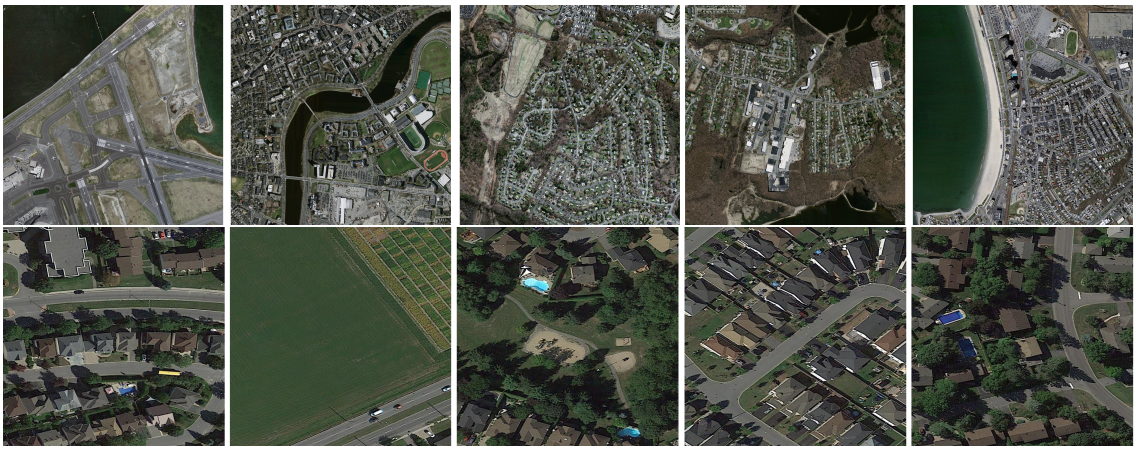

Figure 5.4: Sample database Images. First row MRD, and second row ORD

state become more expressive due to the preservation of the semantic and appearance information of the road images.

5.2 Experimental Results

This section consists of descriptions of the database used, evaluation parameters chosen for assessing the performance of the proposed model, experimental settings, and the results obtained after all the experiments. To show the effectiveness of the proposed model in extracting the roads, experiments are performed on two benchmark databases. An ablation study is done by taking the proposed network with different fractional orders, and the performance of the proposed method is compared with some recent road segmentation networks (with the same hyperparameters).

5.2.1 Database Specifications

Two remote sensing databases $viz.$ MRD [242] and ORD [258] are used to show the performance of the proposed model. Both databases are open-sourced and are being widely used. They have different topographical road maps with variable road widths and complexities. The detailed information of both databases is given below:

1. **Massachusetts Road Database (MRD)** [242]: This database consists of 1171 aerial images with 0.5m spatial resolution of the state of Massachusetts[2]. Images cover a wide variety of urban, suburban, and rural regions. Each image is 1500×1500 pixels covering a total of 2.25 sq km area of Massachusetts with an approximate

[2] [Online]. Available: http://www.cs.toronto.edu/vmnih/data/

road width of 6-9 pixels. The first row of Figure 5.4 displays the sample images of this database.

2. **Ottawa Road Database (ORD)** [258]: This database consists of 20 aerial images of several typical urban areas of the Ottawa state, obtained using Google Earth. The images are of 0.21m spatial resolution per pixel (zoom level 19) with variable size, some being of size 4500×5500 while others being of 1000×2000. This database is challenging as it has highly complex images and covers several urban areas. The second row of Figure 5.4 shows some sample images of this database.

5.2.2 Training/Testing Protocol

The performance of the model is evaluated on two databases. In the case of MRD, 1108 images are used for training, 49 for testing, and 14 for verification. This database split is kept the same as in [289] and other state-of-the-art methods for comparing segmentation results. The training images are further augmented by applying four operations: horizontal/vertical flipping, grid distortion and rotation at 90°. The number of training images becomes five times the original training database split. The model is then trained using the resized 5540 images of size 512×512.

To compare the segmentation results with the state-of-the-art [286], the split of the ORD is set to be as 14 images for training, 3 for validating, and 3 for testing the model. The actual images of ORD are quite large, thus augmentation techniques are applied after dividing the images into segments of size to 512×512. For training the proposed network, the 14 training images are randomly segmented into patches of size 512×512, then the obtained patches are augmented by applying five different operations: horizontal/vertical flipping and rotation at 90°, 180°, and 270°. On average, 280 patches corresponding to each image of the training set are obtained and the model is then trained using 3946 images.

5.2.3 Implementation Details and Experimental Settings

The model is trained from scratch without extra data, a post-processing module, or pre-trained weights. All the experiments are performed on a Linux-based operating system with NVIDIA GeForce GTX 1080 Ti graphic card with graphic memory of 11 GB. The model has ReLu functions, thus it is initialized using the HeNormal initialization method [245]. This initializer randomly draws samples from a truncated normal distribution centered at 0 with a standard deviation equal to $\sqrt{(2/n)}$ where n is the number of input units in the

Table 5.4: Comparison of results obtained by proposed road segmentation network with state-of-the-art methods on MRD

Model	Precision	Recall	mIoU	F1-score
U-Net [244]	0.747	0.721	0.722	0.682
Dlinknet [256]	0.767	0.741	0.737	0.717
HsgNet [268]	0.769	0.752	0.749	0.720
Dense-UNet [289]	0.780	0.731	0.739	0.714
SUNet [289]	0.798	0.736	0.753	0.721
SDUNet [289]	**0.812**	0.757	0.784	0.741
Proposed (α =0.4)	0.698	**0.830**	**0.787**	**0.748**

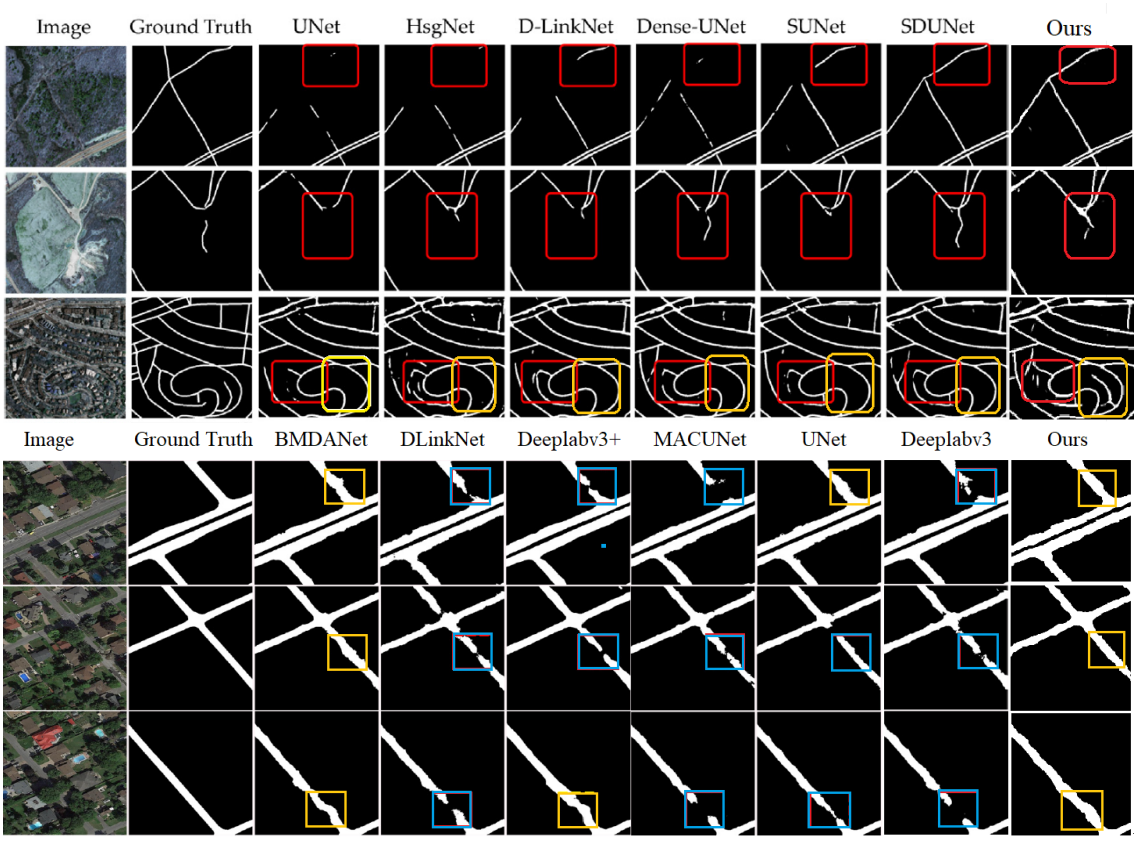

Figure 5.5: Visual results on proposed networks and other existing networks on MRD (top) and ORD (bottom): Yellow and red boxes depict good segmentation results whereas results in the blue boxes are not good for ORD and MRD

Table 5.5: Comparison of results obtained by proposed road segmentation network with state-of-the-art methods on ORD

Model	Precision	Recall	mIoU	F1-score
DeeplabV3 [253]	-	-	0.8362	0.9146
MACUNet [278]	-	-	0.8419	0.9142
DeeplabV3+ [253]	-	-	0.8473	0.9174
D-LinkNet [256]	-	-	0.8360	0.9107
UNet++ [262]	-	-	0.8523	0.9203
BMDANet [286]	-	-	0.8802	0.9363
Proposed (α =0.5)	0.8867	0.9374	**0.9062**	0.9110

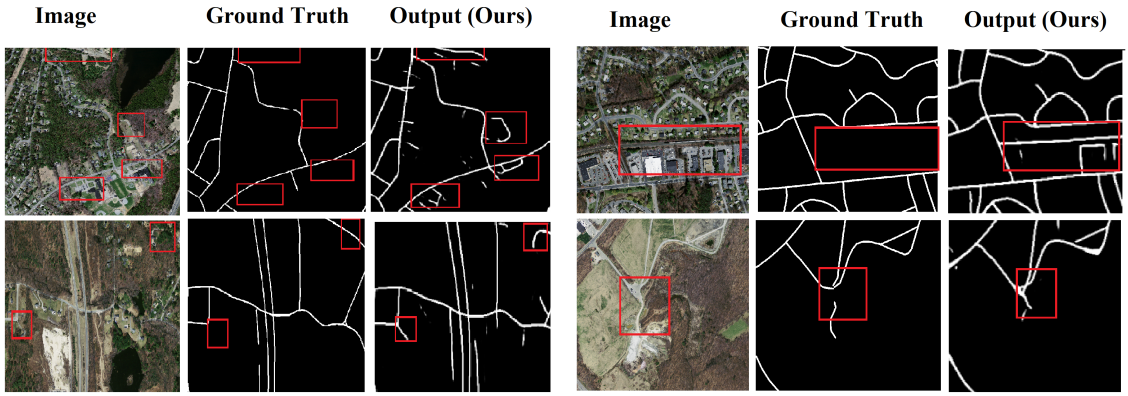

Figure 5.6: Visual results obtained by the proposed network on some mislabeled data of MRD

weight tensor. The Adam optimizer [243] with default settings is used to minimize the loss function and find the optimal control parameters. This optimizer dynamically adjusts weights in an effective manner by incorporating adaptive learning rates and momentum [3]. The learning rate is set to be 0.0001 with a decay of 0.1 after every 20 epoch. The validation set is set for early stopping and the drop-out rate is set to 0.2 to avoid over-fitting. The total number of epochs is set to be 200.

5.2.4 Results and Discussion

To evaluate the road segmentation performance of the proposed network, the ground truth segmented images are compared with the corresponding segmented outputs of the model. We have computed the F1-score, recall, precision, and mean IoU on both databases to assess the quantitative performance. The proposed network is dense, so the

[3] accumulation of a running average of past gradients for dampening the effect of fluctuations in the current gradient direction.

comparison of the quantitative results is made with state-of-the-art road segmentation dense networks. The proposed network ($\alpha = 0.4$) on MRD are compared with the benchmarking segmentation network U-Net [244], Dlinknet [256], HsgNet [268], and dense networks viz. Dense-UNet [289], SUNet [289], and SDUNet [289]. The values of evaluation parameters corresponding to these state-of-the-art methods are extracted from [289]. It can be noted from the Table 5.4 that SDUNet model had achieved the maximum precision, recall, mean IoU and F1-score of 0.812,0.757, 0.784 and 0.741 respectively. The precision of the proposed network is found to be 0.698 which is comparatively lower for MRD due to the extraction of some false regions, but the overall performance is significantly good. The results in the Table 5.4 clearly show that the proposed network achieved 0.830 mean IoU, 0.787 F1-score and recall 0.748 and these metrics are higher than SDUNet [289] and hence than the other aforementioned methods. It can be seen from the visual results in Figure 5.5 that extracted road networks are mostly continuous with very few breaking points even in the presence of complex backgrounds. The third row of images clearly shows the superiorty of our model than other existing models. The presence of weighted skip connections in the proposed dense network has helped in gathering more global information as compared to other dense networks viz. Dense-UNet [289], Dlinknet [256], SDUNet [289].

But the precision of the proposed model is less for MRD as compared to other models. By lower precision, it means that the model returns comparatively more false positives than other models. But due to high recall, the model has a low false negative rate. Thus our model is more capable of extracting the pixels related to roads as compared to other models. But in the MR database, the driveways are of the same color as the roads. Secondly, the MR database contains some errors and imprecision in ground truth where some of the road pixels are mislabeled as non-road pixels due to the occlusion of trees, clouds, and shadows. The mislabeled data affects the pixel classification accuracy [295, 296]. Our model intends to label these road pixels correctly. Thus these two issues lead to an increase in false positives with respect to the ground truth. Hence precision metric is lower in our model. Few samples where road pixels are mislabelled and the corresponding segmentation results obtained by the proposed model are shown in Figure 5.6. The red boxes are drawn over regions of interest. These areas are labeled as non-road in the ground truth. The proposed network is correctly labeling these roads in the boxes.

The quantitative results of the final proposed network ($\alpha = 0.5$) on ORD are compared with other state-of-the-art road segmentation networks viz. Deeplabv3 [253], MACUNet

Table 5.6: Results of the proposed model with different fractional order on MRD and ORD

Model	Precision	Recall	F1-score	Acc	mIoU	Precision	Recall	F1-score	Acc	mIoU
	Database: Massachusetts Road Database					Database: Ottawa Road Database				
α =**0.2**	0.686	0.810	0.741	0.971	0.776	0.836	0.881	0.859	0.962	0.851
α =**0.3**	0.682	0.802	0.737	0.971	0.764	0.829	0.904	0.867	0.963	0.864
α =**0.4**	0.698	**0.830**	**0.748**	**0.978**	**0.787**	0.822	0.926	0.873	0.964	0.876
α =**0.5**	**0.736**	0.764	0.741	0.973	0.772	**0.887**	0.937	**0.911**	**0.976**	**0.906**
α =**0.6**	0.675	0.811	0.735	0.970	0.758	0.829	0.936	0.882	0.966	0.879
α =**0.7**	0.679	0.821	0.721	0.970	0.783	0.868	0.921	0.864	0.971	0.889
α =**0.8**	0.699	0.771	0.729	0.970	0.758	0.833	**0.941**	0.875	0.967	0.882
α =**0.9**	0.657	0.799	0.715	0.968	0.754	0.796	0.951	0.855	0.962	0.874

[278], DeeplabV3+ [253], D-LinkNet [256], UNet++ [262], and BMDANet [286] and the results are reported in the Table 5.5. The values of F1-score and mean IoU corresponding to the aforementioned methods are extracted from [286]. It can be observed from the table that the BMDANet [286] had achieved the maximum values of F1-score and mean IoU as 0.9363 and 0.8802 respectively. The results clearly show that the proposed network achieved a higher mean IoU of 0.9062 as compared to BMDANet [286] and the other mentioned segmentation methods. The proposed method improved the segmentation results of the state-of-the-art for ORD by 3% in terms of mean IoU. The F1-score of the model is found to be 0.9110 which is comparable to other state-of-the-art methods. The model achieved precision and recall of 0.8867 and 0.9374 respectively which depicts a significantly good-performing binary classifier. From the visual results in Figure 5.5 it can be seen that extracted road networks are continuous and the edge information is preserved even in the presence of occlusions like trees and buildings. The effectiveness of non-local fractional derivatives in the proposed network can be observed from the segmented outputs as there is less loss of information.

5.2.5 Ablation Study

The performance of the proposed network depends on the feature extracted and thus on the feature propagation between layers. The features obtained from each layer are being reused at future states with the help of fractional weighted skip connections. Therefore, an ablation study has been done to see the effect of varying the fractional order α on the performance of the model. Experiments are carried out on both databases for $\alpha = 0.2, 0.3, 0.4, 0.5, 0.6, 0.7, 0.8$ and 0.9. To analyze the performance of the network with different fractional weights, we have computed F1-score, recall, precision, pixel-wise

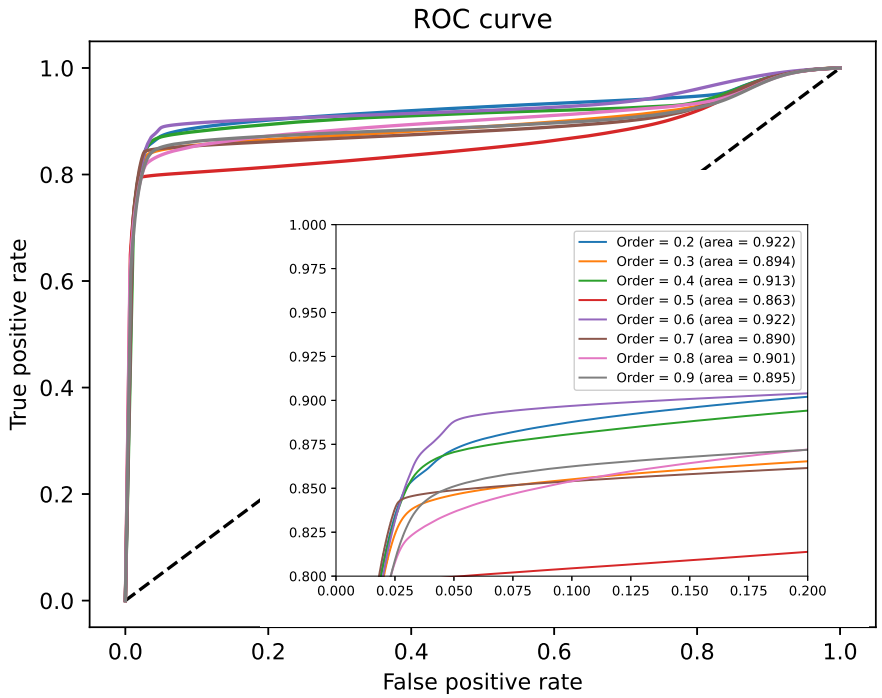

Figure 5.7: ROC plots for MRD at different fractional orders with the zoomed view of the upper left corner of the graphs: Largest area under the curve corresponding to order= 0.6

accuracy (Acc) and mean IoU (mIoU) on the databases. The Table 5.6 shows the obtained results on MRD and ORD. The values of the evaluation parameters for MRD depict that the model performed well for fractional orders $\alpha : 0.2 \leq \alpha \leq 0.7$. It is found that the model achieved the highest precision of 0.736 at fractional order $\alpha = 0.5$ on MRD. However, the model achieved higher recall, F1-score, accuracy and mean IoU of 0.830, 0.748, 0.978 and 0.787 respectively on order $\alpha = 0.4$ for MRD. Furthermore, the model performed better at $\alpha = 0.5$ for ORD with higher precision, F1-score, accuracy, and mean IoU of 0.887, 0.911, 0.976 and 0.906 respectively. The recall value at $\alpha = 0.5$ is found to be 0.937 which is close to the highest recall value of 0.941 attained at $\alpha = 0.8$ for ORD. Receiver Operating Characteristic (ROC) curves shown in Figure 5.7 and Figure 5.8 are also plotted at different fractional orders (hence with different weighted connections) to evaluate the performances of the models. The curves are drawn and the corresponding area under the graphs is also mentioned. It depicts the classification performance of the model at different thresholds for different fractional orders. It is a graph with the false positive rate on the x-axis and the true positive rate on the y-axis. The area under the curve

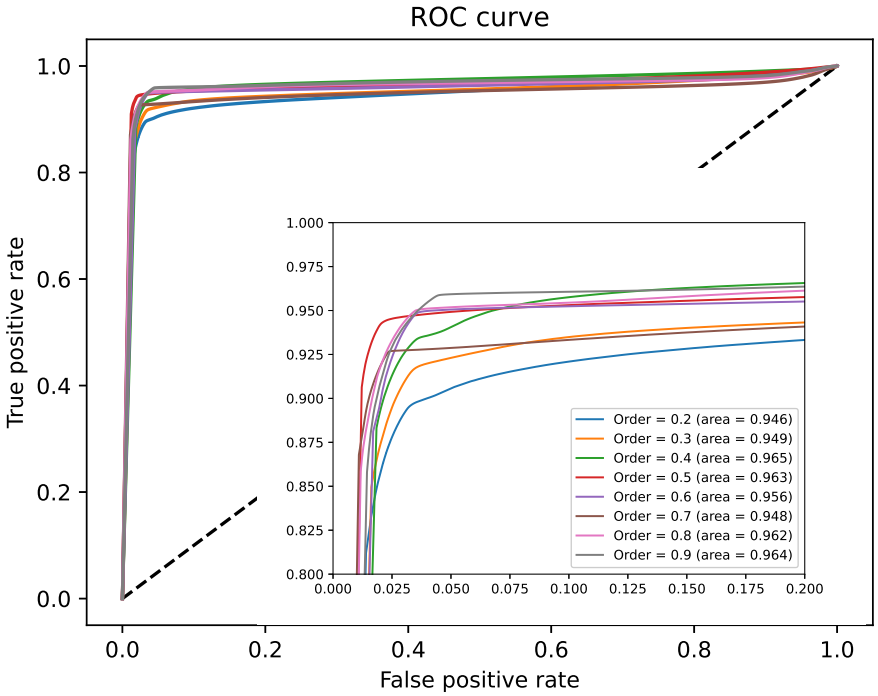

Figure 5.8: ROC plots for ORD at different fractional orders with the zoomed view of the upper left corner of the graphs: Largest area under the curve corresponding to order= 0.4

is computed for each curve which signifies the degree of separability of road and non-road pixels in the database. The more the area under the curves, the better the segmentation (binary classifier). The curve corresponding to order $\alpha = 0.5$ acquires the highest area of 0.965 under it for ORD. Thus all the evaluation metrics are aligned with graphical results for ORD. The curves corresponding to order $\alpha = 0.2, 0.6$ acquires the highest area under them of 0.922 for MRD, but the rest of the evaluation metrics are found to be: precision 0.686, recall 0.810, F1-score 0.741, accuracy 0.971 and mean IoU 0.776 for $\alpha = 0.2$, and precision 0.675, recall 0.811, F1-score 0.735, accuracy 0.970 and mean IoU 0.758 for $\alpha = 0.6$, which are lesser for these orders. The curve corresponding to $\alpha = 0.4$ acquires the second highest area of 0.913 under it with the highest values of other evaluation metrics. Thus the model with order $\alpha = 0.4$ and $\alpha = 0.5$ are used throughout the experiments for MRD and ORD respectively.

5.3 Summary

This chapter proposes a U-shaped dense network with weighted skip connections to segment roads from high-resolution satellite images. The proposed network is designed by solving a fractional optimal control problem. The proposed approach involves the weighted sum of the output of previous layers at a particular transition, unlike basic dense networks where the output of the previous layers is concatenated. Thus the proposed method is computationally efficient. Moreover, the performance of the proposed network is found to be better than other state-of-the-art methods in terms of F1-score and the mean IoU at fractional order 0.4 for MRD and 0.5 for ORD than the state-of-the-art segmentation results. By exploiting the memory property of fractional derivatives, the forward propagation of features is strengthened and lesser loss of information is seen. The results show that the extracted roads are more complete for both databases. Moreover, the model performs better than other state-of-the-art methods on MRD in terms of higher recall, F1-score and mean IoU of 0.830, 0.748 and 0.787 respectively. In addition, the model achieved better mean IoU of 0.9062 that shows an improvement of around 3 % in segmentation results with respect to the state-of-the-art method on ORD.

Two possible areas for improvement are identified: 1) The driveways are the same color as the actual roads, due to which the pixels related to driveways are labeled as roads. This increases the number of false positive pixels. 2) Several trees and their shades falling on the roads cause occlusion. The proposed model captures local and global information simultaneously and is capable of extracting the pixels of roads occluded by the trees. But while solving the issue of occlusion, the model labels some pixels corresponding to trees nearby the roads as road pixels and hence the sharpness of the edges of the roads gets affected. This again increases the false positive pixels. More false negatives affect the segmentation performance of the model hence hampering the precision metric. In the future, these problems can be targeted to obtain continuous and accurate road structures.

A part of this chapter is published in the following referred publication:

Sugandha Arora, Harsh Kumar Suman, Trilok Mathur, Hari Mohan Pandey, and Kamlesh Tiwari. "Fractional derivative based weighted skip connections for satellite image road segmentation." Neural Networks 161 (2023): 142-153 (I.F- 9.657 , SCI-Q1, Elsevier).

Chapter 6

Salient Object Detection

Salient Object Detection is a computer vision task that automatically detects and highlights the most "salient" or visually distinct objects in an image. Salient objects are typically considered objects or regions in an image that captures a viewer's attention and stand out from the surrounding context. This can be determined by various visual cues such as color, texture, shape, and orientation [297]. Salient object detection is used in multiple applications such as image and video summarization [298], visual attention modeling [299], object recognition [300] and tracking [301]. The goal of salient object detection is to identify the regions in an image that are most likely to be of interest to a human observer and to separate these regions from the background or other less important objects in the image.

Salient Object Detection is a challenging task in computer vision for several reasons [302]. First, the intra-class variability, where the same object class can have significant variations in shape, color, and texture, makes it challenging to define a single set of features that can accurately detect salient objects. Second, inter-class similarity is also an issue where different object classes have visual similarities, which makes it difficult to differentiate between them and leads to false positive detections. Third, the salient objects can be partially or fully occluded by other objects, which makes them difficult to detect. Additionally, the presence of clutter in the background can make it difficult to distinguish salient objects from their surroundings. Background complexity of the background adds another dimension where the image may contain multiple objects and textures, making it difficult to distinguish the salient objects from the background. Fourth, illumination and contrast are always a challenge related to the changes in lighting conditions, contrast, and color that can seriously affect the visibility of objects and lead to false detection. Last,

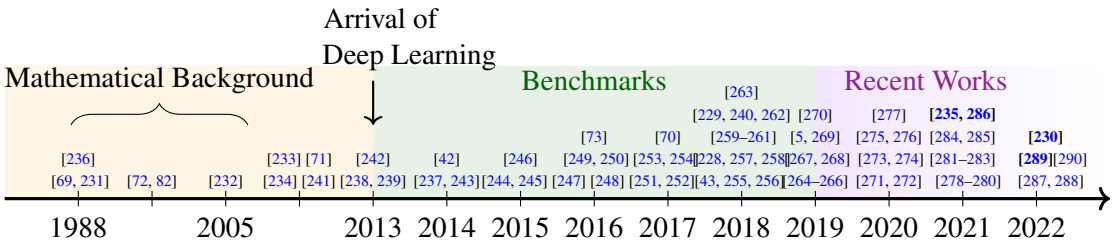

Figure 6.1: Visual representation of references arranged in chronological order

viewpoint and scale variations can significantly affect its salience, making it difficult to design a single algorithm that works for all images [303].

Several deep learning models have been developed to overcome the challenges mentioned above. Multi-level features representing high-level semantic information and low-level fine details are required simultaneously to obtain an accurate salient map. Some of the recent works involving the integration of multi-level features are described as follows. Salient object detection algorithms based on fully convolutional networks [304–306] have multiple convolutional layers and pooling layers that integrate local and global features and thus produce significantly good quality salient maps. Due to the pooling operations, the maps have rich high-level semantic information but with less accurate and rough boundaries. Several other recent works employed skip connections to integrate high-level semantic information and low-level fine details and obtain salient maps with sharper boundaries [14, 307]. Zhang *et al.* [308] designed a network with an attention mechanism in which multi-level contextual information is integrated selectively in a progressive manner. Qin *et al.* [274] proposed a two leveled nested U-structure with residual connections and captured contextual information from multiple levels. Chen *et al.* [309] have developed a model with global information consisting of a backbone network for features extraction and then some modules for aggregating low-level appearance features, high-level semantic features, and global context features. Recently, to improve the performance of the existing encoder-decoder architectures, a masked edge attention module and an object attention module are employed with the encoder and decoder, respectively [310]. Table 6.1 elucidates these and some other recent works.

Most networks mentioned above have an encoder-decoder architecture that uses extracted features through backbone networks. The deep CNNs like AlexNet [65], ResNet [6], ResNeXt [311], and DenseNet [312] are some of the most frequently employed backbone networks. Deep networks like VGG and AlexNet suffer from a vanishing gradient problem that the information can vanish or wash out after passing the features through

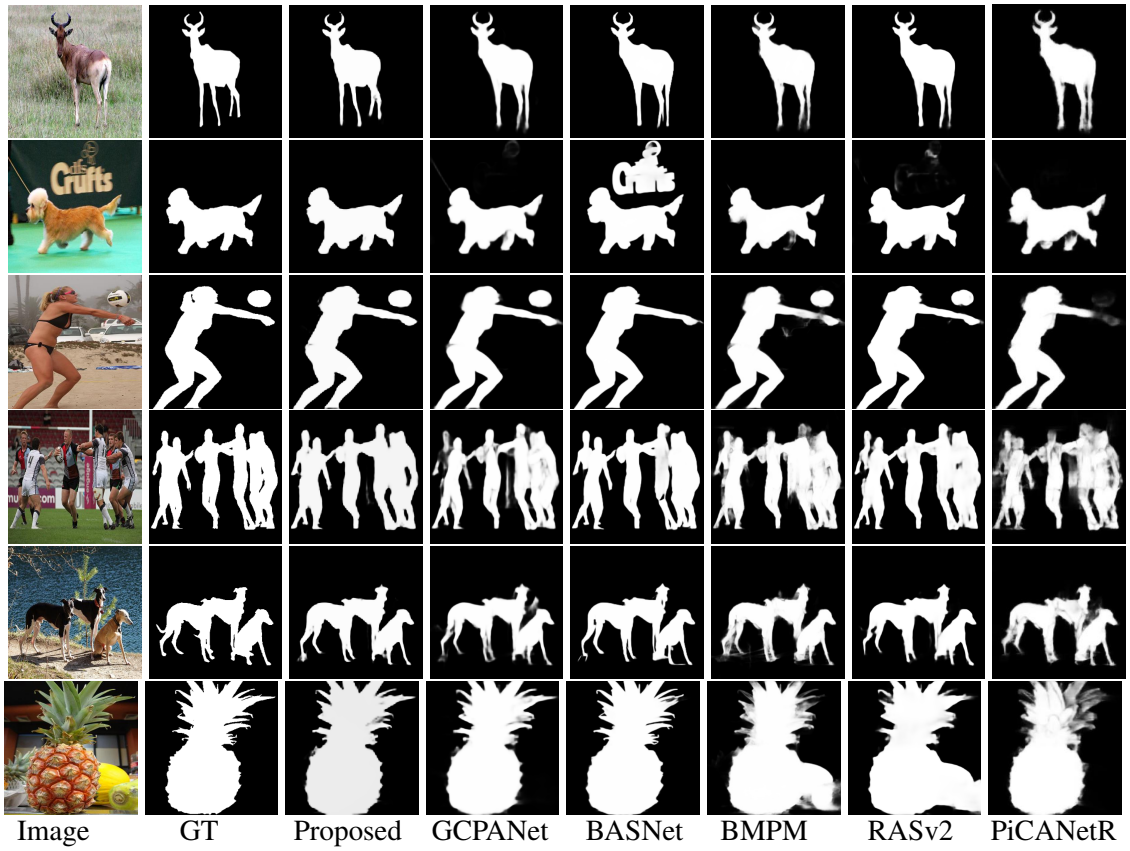

Figure 6.2: Some visual examples and their predictions generated by the proposed network, GCPANet [13], BASNet [14], BMPM [15], RASv2 [16] and PiCANetR [17]

multiple layers [313]. To overcome this issue, networks like ResNet [6], FractalNet [250], ResNeXt [311] and Highway Networks [314] are developed, that pass the information from early to later layers via skip connections. DenseNet [312] was designed to ensure maximum information transfer and to enable the memory of the network by connecting all layers having the same-sized feature maps. But the features are combined through concatenation, which involves using many parameters and there doesn't exist any mathematical framework behind memory exploitation. FOCNet [5] is introduced for image denoising, which densely connects the layers via weighted skip connections and combines their outputs through element-wise summation. This approach is adopted in the previous chapter for enabling long-term feature interactions in the road segmentation network[315]. Long-term memory is required to detect salient objects as long-term feature interactions help preserve mid and high-frequency features and, thus, the fine details in the image. Therefore, long-term feature interactions are expected to help detect salient objects with sharp boundaries.

This chapter has designed a salient object detection network with an encoder-decoder architecture where the encoder part has a residual network with fractional weighted skip connections [5, 315] and the structure of the decoder has feature refinement and aggregation modules inspired by GCPANet [309]. The key contributions of this work are listed below:

1. This chapter proposes a salient object detection network with encoder-decoder architecture equipped with long-term memory. This long-term memory is obtained by densely connecting the layers of the backbone network via fractional weighted skip connections.

2. The network performance is analyzed with different loss functions and fractional orders α $(0 < \alpha \leq 1)$.

3. The performance-based ensembling of models is leveraged corresponding to order α using F-measure. Using multiple learners of the same algorithm diversified the model predictions and developed a better system.

4. The proposed model is evaluated on six benchmark databases with different complexities: $viz.$ HKU-IS [316], PASCAL-S [317], ECSSD [318], DUT-OMRON [319], DUTS-TE [320] and SOD [321]. According to the results, the model exhibits state-of-the-art performance in terms of F-measure and mean absolute error.

The chapter is structured as follows: is explained in Section 6.1 explains the proposed approach, followed by the experimental results obtained and ablation studies in Section 6.2.

6.1 Proposed Approach

This section elaborates the approach adopted for the detection of salient objects. It describes the optimal control view of salient object detection, designing of the proposed network architecture, and the model ensembling technique.

6.1.1 Fractional Optimal Control View of Salient Object Detection

As in the previous chapter, the propagation of features at each layer of the deep CNN can be treated as trajectories of a dynamic system. Subsequently, that dynamic system can be described with the help of differential equations. This approach represents the feature flow in the backbone network, assuming the decoder part to be the nonlinear transformation of the encoder output into a higher dimensional space. In this section, the evolution process

Table 6.1: Summarization of recent state-of-the-art salient object detection methods with respect to architecture and results

S No.	Name of the paper	Method/ Technique/ Architecture	Comparison
1.	BASNet: Boundary-Aware Salient Object Detection (2019) [14]	Densely supervised Encoder-Decoder network and a residual refinement module with hybrid loss function	Outperformed 15 state-of-the-art methods on six benchmark datasets in terms of both region-based and boundary-aware measures
2.	Global Context-Aware Progressive Aggregation Network for Salient Object Detection (2020) [309]	Integrated low-level appearance features, high-level semantic features, and global context features using multiple modules after backbone network	Outperformed 12 state-of-the-art methods on six benchmark datasets
3.	U2-Net: Going deeper with nested U-structure for salient object detection (2020) [274]	1. Two-level nested U-structure- to train a deep network without using backbones from image classification tasks. 2. Residual U-blocks- to capture more contextual information from different scales and increase depth without increasing computational cost.	1. Gives better results for maximal F-measure, MAE, relaxF_β^b, F_β^w and structure measure on ECSSD, HKU-IS and DUT-OMRON datasets when compared to 2020 SOTA models. 2. Faster and smaller model
4.	iNAS: Integral NAS for Device-Aware Salient Object Detection (2021) [322]	1. Flexible device-aware search scheme- to train the model once and find high-performance, low-latency models on multiple devices.	1. Gives better results for maximal F-measure, MAE and structure measure on ECSSD, DUT-O, DUTS-TE, HKU-IS and PASCAL-S datasets. 2. Has better speed than U2-Net and has the best performance-latency balance.
5.	Pyramidal Feature Shrinking for Salient Object Detection (2021) [323]	1. Pyramid Shrinking Decoder- to shrink adjacent features in pairs layer-by-layer. 2. Adjacent Fusion Module- to retain useful information in adjacent feature nodes and reduce noise. 3. Scale-aware Enrichment Module- to pre-process the features extracted and get rich multi-scale features.	1. Gives better results for average F-measure, MAE and E-measure on ECSSD, HKU-IS, PASCAL-S and DUTS-TE datasets. 2. More prominent in multi-object images, complex background images, and images with confusing objects.
6.	Multi-scale Edge-based U-shape Network for Salient Object Detection (2021) [324]	1. U-shape Edge Network modules- to extract useful information for boundary prediction. 2. Additional down-sampling module- to alleviate the location inaccuracy.	1. Gives better results for mean F-measure, MAE, structure measure, E-measure on DUTS-TE, ECSSD, DUT-OMROM and HKU-IS datasets than recent methods. 2. Better at keeping lots of detail with sharp edges and high precision.
7.	Recursive Contour-Saliency Blending Network for Accurate Salient Object Detection (2021) [325]	1. Contour-saliency blending module- to exchange information between contour and saliency 2. Recursive CNN- to increase contour-saliency fusion while keeping the same total trainable parameters. 3. Stage-wise feature extraction module- to pick best features from previous intermediate saliency predictions.	Suppresses wrong predictions better by giving better results across average F-measure, MAE, E-measure, F_β^w on DUT-OMRON, ECSSD, PASCAL-S, HKU-IS and DUTS-TE datasets
8.	TRACER: Extreme Attention Guided Salient Object Tracing Network (2022) [310]	1. The masked edge attention module for the enhancement of the edge features in low-level representations 2. A union attention module for the aggregation of multi-level features 3.Object attention module to reduce the distribution discrepancy between encoder and decoder features 4. Adaptive pixel intensity loss to give optimal attention to the pixels	TRACER improves the performance and computational efficiency in comparison to the existing methods on the DUTS and DUT-OMRON datasets

Table 6.2: Elements of the encoder (ResNet-50 inspired) architecture: Description of image output size, convolution layers, and filters at all scales

Level	Output Size	Layers, Filters	Frequency
Layer1	144×144	7×7, 64, stide=2	
Layer2	72×72	3×3 max pool, stide=2	
1	72×72	$\begin{bmatrix} 1 \times 1, 64 \\ 3 \times 3, 64 \\ 1 \times 1, 256 \end{bmatrix}$	3
2	36×36	$\begin{bmatrix} 1 \times 1, 64 \\ 3 \times 3, 64 \\ 1 \times 1, 256 \end{bmatrix}$	4
3	18×18	$\begin{bmatrix} 1 \times 1, 64 \\ 3 \times 3, 64 \\ 1 \times 1, 256 \end{bmatrix}$	6
4	9×9	$\begin{bmatrix} 1 \times 1, 64 \\ 3 \times 3, 64 \\ 1 \times 1, 256 \end{bmatrix}$	3

of the proposed network is described using fractional differential equations to enhance the process of feature propagation in the backbone network.

Consider the following system Equation (6.1.1) of fractional differential equations [82] that describes the feature propagation in the deep CNN. Here, the feature trajectory is represented by $v(t, s)$, a continuous function in terms of time and space both, $s \in \Omega$ is the two dimensional spatial position, $I(s)$ is the input image, $u(s)$ is the ground truth salient map image and Φ, Ψ are linear transformations, such as convolution.

$$\min_{\theta(t)} \int_{\Omega} L(\Phi(v(T, s)), u(s))\, ds \tag{6.1.1}$$

s.t.

$${}_0D_t^{\alpha} v(t, s) = f(v(t, s), \theta(t)), \;\; v(0, s) = \Psi(I(s)), \;\; t \in [0, T] \tag{6.1.2}$$

The objective is to find the optimal control parameter $\theta(t)$ satisfying equations in the system (6.1.2) such that the loss in Equation (6.1.1) is minimized [73].

6.1.2 Architecture of the Proposed Salient Object Detection Network

The network has an encoder-decoder architecture with a ResNet-50-like [6] structure as the backbone network in the encoder part for feature extraction and has interwoven feature

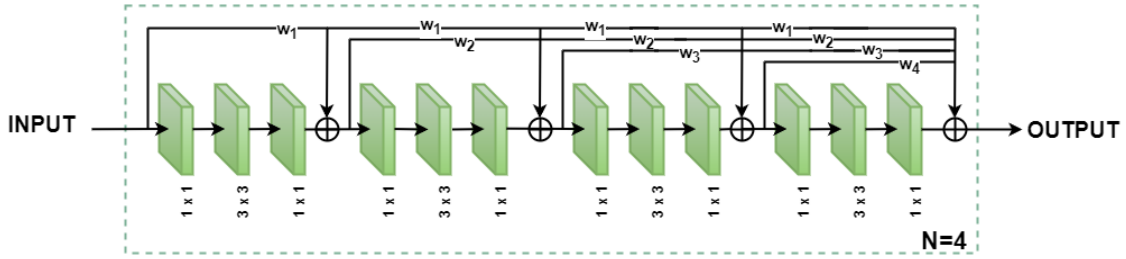

Figure 6.3: Fractional Residual Block (FRB) with four sub-blocks comprising three layers each

aggregation modules with big skip connections in the decoder part to predict the saliency map in a supervised manner. The evolution process in the network is considered a dynamic system. The propagation of features through the sub-blocks of the backbone network is considered as trajectories of the dynamic system and the operations occurring in the decoder part are considered a non-linear function. The evolution process is described using fractional differential equations with optimal control conditions. The sub-blocks at a scale of the encoder are connected to other sub-blocks via fractional weighted skip connections that incorporate long-term memory into the system. These densely connected sub-blocks with weighted skips help preserve global appearance with semantic information. The features extracted from the final layer of the encoder are strengthened using the head attention module and then forwarded to each level of the decoder with the help of the global feature flow module. These strengthened features and the features from each level of the encoder are aggregated with the features of the corresponding level using the feature integration module, and then these aggregated features are refined at each level using the self-refinement module. To improve the optimization process of the network, the minor loss is evaluated at each level of the decoder and then combined with the major loss of the network.

6.1.2.1 Encoder with Fractional Weighed Skips

The ResNet-50-like architecture with a residual connection after every three layers is used in the encoder part. Thus to model the evolution as a dynamic system, each scale/block is divided into sub-blocks of three convolution layers. To sum up, the propagation of features through sub-blocks of the backbone network is modeled as a dynamic system, which is described using a set of fractional differential equations and then the optimal control parameters are evaluated after solving it. The application of fractional derivatives adds weighted skip connections to the backbone network. These weights are dependent on the current sub-block (t) of the network and the order of differentiation. The order α along with fractional weights are positive and less than 1, *i.e.*, $0 < \alpha \leq 1$, and the weighted sum

of features remains positive and does not explode. The following version of the definition 1.1.10 is used in the proposed model where $h = 1$ and t denotes a sub-block of three layers in the network. The evolution process for the multi-scale dynamic system is described below:

$$ {}_0D_t^{\alpha} v(t, s, p_i) = f(v(t, s, p_i)), \theta_{p_i}(t)) \tag{6.1.3} $$

for each $i \in [1, 4]$, $t \in [0, T]$ with the following initial conditions

$$ v(0, s, p_1) = \Psi(I(s)), \quad v(0, s, p_i) = T_{\downarrow} v(\textstyle\sum_{k=1}^{i-1} n_k, s, p_{i-1}) \tag{6.1.4} $$

where $T_{\downarrow}$ denotes max pooling operation, n_k denotes the number of sub-blocks at level k, θ_{p_i} is convolution kernel at level i. Thus the evolution process of the backbone network for the proposed salient map prediction model is represented by Equation (6.1.5).

$$ v_{t+1}^{p_i} = \sum_{k=0}^{t} w_k v_k^{p_i} + \sigma(\theta_t * (v_t^{p_i})) \tag{6.1.5} $$

where σ is a non-linear unit denoting the three consecutive application of 'Convolution + Batch normalization + ReLu' on the output of sub-block t, $v_{t+1}^{p_i}$ is the output of t^{th} sub-block of scale p_i, $w_k = (-1)^{(t-k+1)} \binom{\alpha}{t-k+1}$, and thus $w_t = \alpha$. The structure of a fractional residual block is shown in Figure 6.3. N stands for the number of sub-blocks. The sub-block n is connected with $(n-1)^{th}$, $(n-2)^{th}$ sub-blocks via skip connections with weights w_1, w_2.. respectively. The detailed scale-wise architectural details for the backbone network $viz.$ number of layers, sub-blocks and filters, at a particular level is presented in Table 6.2.

6.1.2.2 Decoder with Refinement and Aggregation Modules

The structure of the decoder part is inspired by GCPANet [309] which has four modules: Head Attention (HA), Feature Integration (FI), Self Refinement (SR) and Global Feature Flow (GFF). HA module helps extract more expressive and selective features by exploiting channel-wise and spatial attention mechanisms. Specifically, the combination of operations like convolution, average-pooling, and ReLu are used for strengthening the features. FI module aggregates the interwoven features of the current layer (f_c) with the features from the same level of the encoder (f_e) and final layer of the encoder (f_d). Specifically, f_c, f_e and f_d are fed through the convolution layer, upsampled and then element-wise multiplied

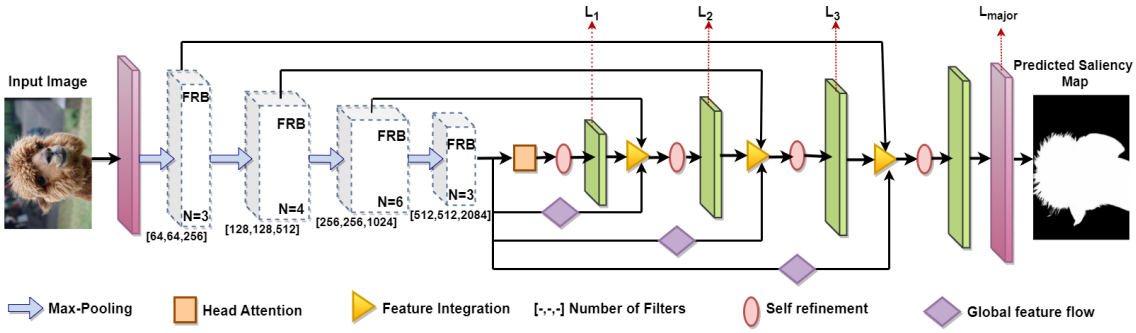

Figure 6.4: Structure of the proposed network for salient object detection

to obtain f_{ce}, f_{ec} and f_{ed} and then these interwoven features are concatenated to obtain the aggregated features. SR module refines the aggregated features obtained after passing through HA and FI modules by multiplying with and adding to features obtained after convolution. GFF module acts as a big skip connection with the combination of non-linear operations like convolution and activation functions. It transfers the multi-level features obtained by the encoder to the FI modules of the decoder.

6.1.2.3 Loss Function

Salient object detection is a binary problem classifying the pixel as belonging to the salient or non-salient category. To train the proposed model, the binary cross-entropy loss is employed as the loss function for comparing the generated saliency map and the ground truth. It can be formulated as

$$L_{BCE} = -\frac{1}{h\,w}\sum_{i=1}^{h}\sum_{j=1}^{w}[G_{ij}\log(p_{ij}) + (1 - G_{ij})\log(1 - p_{ij})] \tag{6.1.6}$$

where $h,\ w$ are the height and width of the input image, $G_{ij} \in \{0, 1\}$ is the ground truth label of the pixel at (i, j) and p_{ij} is the predicted probability of that pixel belonging to the salient category. To optimize the network parameters, the loss is evaluated at three intermediate stages (of the decoder) denoted as L_1, L_2, and L_3, and at the end. Specifically, a 3×3 convolution is applied after each stage to squeeze the channel of the output feature maps to one. Then these maps are up-sampled to the same size as the ground truth using bilinear interpolation and then the sigmoid function is applied to normalize the predicted values into $[0, 1]$. Therefore, the final loss used for training is

$$L = L_{major} + \sum_{i=1}^{3} c_i L_i \tag{6.1.7}$$

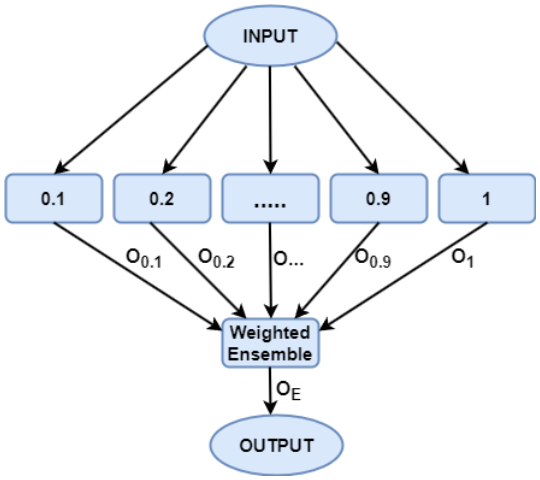

Figure 6.5: Weighted average ensemble model

where c_i denotes the weightage for a loss L_i and L_{major} denotes the final loss of the network. Only L_{major} loss is considered during inference.

Therefore, the proposed salient object detection network is designed by solving the fractional optimal control problem, i.e., evaluating the optimal control parameter $\theta(t)$ that minimizes the loss function L in Equation 6.1.7, subject to conditions in Equation 6.1.3 and Equation 6.1.4. The structure of the proposed network is shown in Figure 6.4. The encoder has four FRBs with N sub-blocks, while the decoder comprises feature refinement and aggregation modules. The feature maps from each FRB are passed to layers of the decoder at the corresponding level via big skip connections for their aggregation. L_1, L_2, L_3 are minor losses and L_{major} is the dominant loss determined at the end.

6.1.3 Weighted Average Ensembling

The most frequently adopted evaluation parameter for binary classification, F-measure is used for the performance-based ensembling of the proposed network. The model with the highest F-measure is given the highest weightage coefficient. Thus, the proposed fractional models with output O_α are ensembled with a weightage coefficient equal to $\xi_\alpha = F^{avg}_{\beta,\alpha}$, that represents the average F-measure corresponding to order α. The Formula used for ensembling is given by (6.1.8). O_E represents the final output of the model. Figure 6.5 shows the model ensemble method for obtaining the final model.

$$O_E = \frac{\xi_{0.1} O_{0.1} + \xi_{0.2}\, O_{0.2} + \xi_{0.3}\, O_{0.3} + \cdots \xi_{1.0}\, O_{1.0}}{\xi_{0.1} + \xi_{0.2} + \xi_{0.3} + \cdots \xi_{1.0}} \tag{6.1.8}$$

6.2 Experimental Results

In this section, databases, implementation details, and training/testing strategies are described. Further, the results are evaluated on these databases to show the effectiveness of the proposed technique.

6.2.1 Database Specifications

The performance of proposed approach is evaluated on six benchmark databases for salient object detection viz.ECSSD [318], HKU-IS [316], PASCAL-S [317] , DUT-OMRON [319], DUTS-TE [320] and SOD [321]. A brief description of these databases is given below.

- **ECSSD [318]** consists of 1000 natural images with complex structures and meaningful semantics.
- **HKU-IS** [316] contains 4,477 images. Most of the images have low contrast and multiple salient objects with common pixels.
- **PASCAL-S** [317] consists of 850 natural images derived from the PASCAL VOC dataset. Many images have cluttered backgrounds and complex foreground objects.
- **DUT-OMRON** [319] includes 5168 high resolution images. Images have multiple salient objects with relatively cluttered backgrounds and complex structures.
- **DUTS** [320] is the largest salient object detection benchmark database with a training partition of 10,553 images, referred as the DUTS-TR set, and a testing partition of 5,019 images, referred to as DUTS-TE set.
- **SOD** [321] is originally designed for image segmentation. The images are of low contrast and have multiple salient objects touching the boundary of the image.

6.2.2 Training/Testing Protocol

The model's performance is evaluated on six benchmark databases mentioned above and trained on the DUTS-TR database. The training data is augmented by horizontal/vertical flipping, random contrast, and blurring to increase the generalization capability of the model. Each image is resized to 320×320 and then a patch of size 288×288 is randomly cropped and used for training. Each testing image is also resized to 320 before predicting their saliency map.

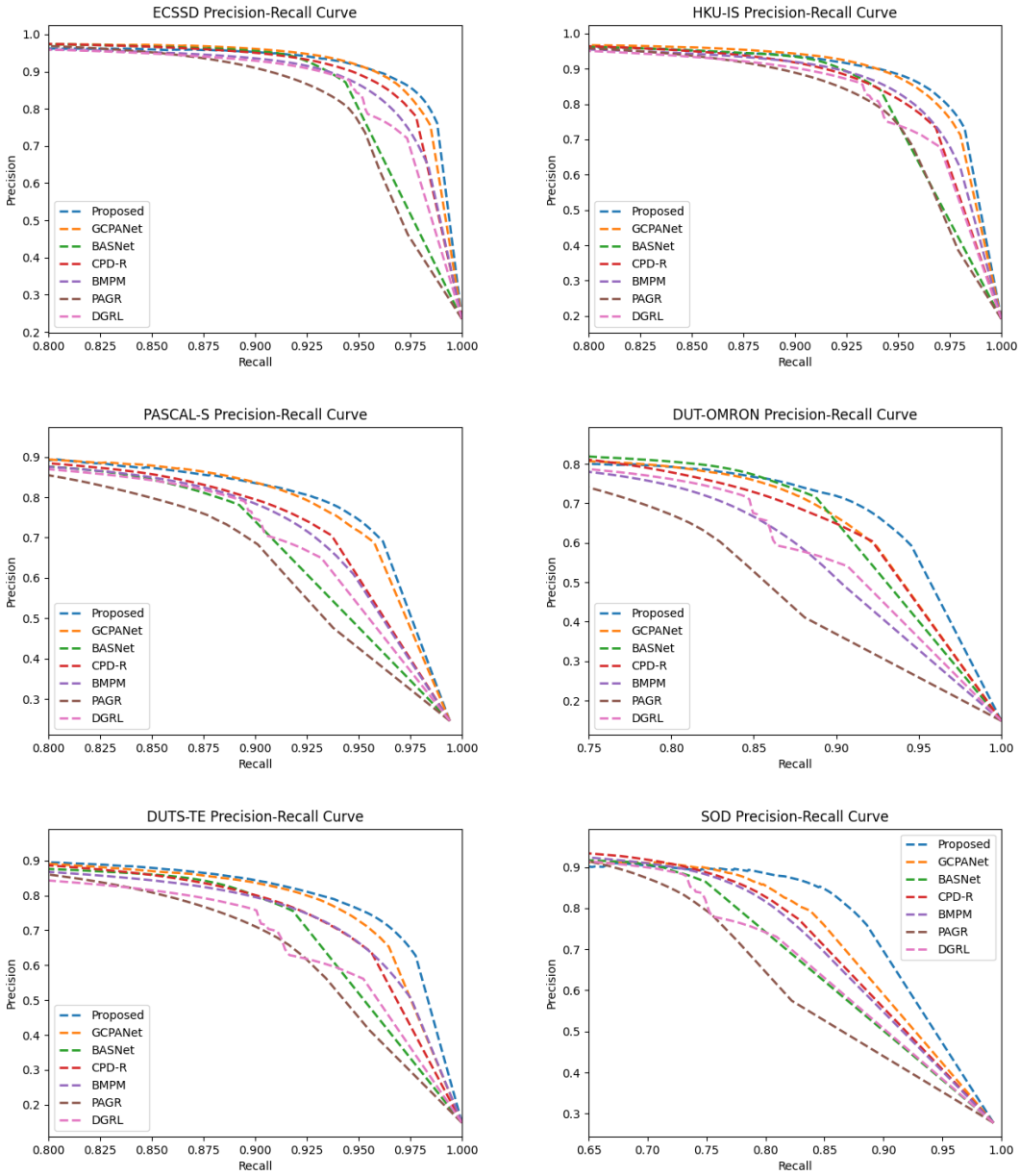

Figure 6.6: Precision-recall curves for all databases showing comparison of the proposed approach with other state-of-the-art models

6.2.3 Implementation Details and Experimental Settings

The backbone network consists of ResNet-50 [6] with dense fractional-weighted connections where the weights for the skips are derived from G-L fractional derivative. The pre-trained weights of ResNet-50 on ImageNet [326] are used for initializing the backbone networks corresponding to all fractional orders. Mini-batch Stochastic gradient descent (SGD) algorithm[1] is applied to optimize the proposed network with a batch size of 64, weight decay of $5e-4$, and momentum of 0.9. The maximum learning rates for the backbone network and the rest of the network are set to be 0.005 and 0.5 respectively, which are further adjusted by applying warm-up and linear decay strategies. The total number of epochs is set to be 50. The model is implemented in PyTorch framework on a Linux-based operating system with the NVIDIA A100-PCIE graphic card with graphic memory of 40 GB.

6.2.4 Results and Discussion

The results obtained by the proposed network are ensembled to obtain the final results, which are compared with following other state-of-the-art saliency map generation methods: Amulet [327], C2SNet [328], RADF [329], RANet[16] DGRL [330], PAGR [308], R3Net [331], BMPM [15], PiCANet [17], CPD-R [332], BASNet[14] and GCPANet [309]. For fair comparisons, the provided saliency maps or the maps generated using their official implementations are used to compute the quantitative parameters further.

Quantitative Comparison. The models are compared based on three evaluation metrics $viz.$ mean absolute error (MAE), max F-measure (F_β^{max}) and averaged F-measure (F_β^{avg}) with $\beta^2 = 0.3$. The proposed model's performance is better than the other methods in terms of either of the parameters on all the databases. Specifically, the model achieved state-of-the-art performance on DUTS and SOD with significant improvement in all three parameters, on HKU-IS and PASCAL-S with higher F_β^{max} and lower MAE, on DUT-OMRON with lesser MAE and ECSSD with same F_β^{avg}. The rest of the parameters are also comparable to other models. Table 6.3 compares the proposed method with these existing models by displaying the values of all evaluation metrics on six considered databases. The comparison of the proposed model with other state-of-the-art models is also drawn via precision-Recall curves. The area under these curves depicts the classifying ability of the model. More be the area under the curve, better be the system. The zoomed

[1]It is a variant of gradient descent algorithm that updates weights after looking at a small batch of the training set.

Table 6.3: Comparison of performance with other saliency detection methods based on the values of MAE, the maximum and mean F-measure on six benchmark databases: Best results are highlighted with bold text

Models	ECSSD			HKU-IS			PASCAL-S			DUT-OMRON			DUTS-TE			SOD		
	$\mathbf{F}_{avg}$	$\mathbf{F}_{max}$	**MAE**	$\mathbf{F}_{avg}$	$\mathbf{F}_{max}$	**MAE**	$\mathbf{F}_{avg}$	$\mathbf{F}_{max}$	**MAE**	$\mathbf{F}_{avg}$	$\mathbf{F}_{max}$	**MAE**	$\mathbf{F}_{avg}$	$\mathbf{F}_{max}$	**MAE**	$\mathbf{F}_{avg}$	$\mathbf{F}_{max}$	**MAE**
Amulet [327]	0.868	0.915	0.059	0.843	0.899	0.050	0.771	0.841	0.098	0.647	0.743	0.098	0.678	0.778	0.085	0.756	0.803	0.139
C2SNet [328]	0.865	0.911	0.053	0.851	0.898	0.046	0.775	0.848	0.080	0.682	0.759	0.072	0.717	0.811	0.062	0.763	0.819	0.121
RADF [329]	0.864	0.912	0.064	0.860	0.903	0.052	0.764	0.832	0.104	0.709	0.785	0.071	0.712	0.811	0.073	0.761	0.822	0.136
RANet [16]	0.891	0.920	0.055	0.880	0.912	0.045	0.766	0.830	0.102	0.710	0.785	0.063	0.792	0.831	0.060	0.809	0.847	0.122
DGRL [330]	0.903	0.925	0.043	0.882	0.914	0.038	0.814	0.860	0.075	0.709	0.779	0.063	0.794	0.828	0.051	0.808	0.844	0.104
PAGR [308]	0.894	0.926	0.061	0.887	0.919	0.047	0.808	0.858	0.093	0.711	0.771	0.071	0.784	0.854	0.056	0.755	0.836	0.145
R3Net[331]	0.913	0.934	0.041	0.894	0.915	0.035	0.805	0.846	0.095	0.748	0.795	0.076	0.787	0.833	0.057	0.789	0.837	0.129
BMPM [15]	0.884	0.929	0.044	0.889	0.920	0.039	0.814	0.857	0.073	0.734	0.775	0.063	0.790	0.852	0.049	0.808	0.852	0.105
PiCANetR[17]	0.886	0.935	0.046	0.870	0.919	0.043	0.804	0.863	0.075	0.717	0.803	0.065	0.795	0.860	0.051	0.811	0.853	0.102
CPD-R [332]	0.913	0.936	0.039	0.896	0.924	0.034	**0.831**	0.864	0.072	0.747	0.797	0.056	0.805	0.865	0.043	0.810	0.857	0.110
BASNet [14]	0.879	0.943	0.037	0.898	0.928	0.032	0.781	0.857	0.076	**0.756**	0.805	0.057	0.791	0.859	0.048	0.809	0.849	0.112
GCPANet[309]	0.916	**0.949**	**0.035**	**0.899**	**0.938**	**0.031**	0.811	0.876	0.066	0.744	0.812	**0.056**	0.809	0.888	**0.038**	0.826	0.872	**0.089**
Proposed	**0.917**	0.947	**0.035**	0.896	0.935	**0.031**	0.829	**0.882**	**0.065**	0.746	**0.823**	**0.056**	**0.812**	**0.890**	0.041	**0.828**	**0.876**	0.091

view of the top right corner of the graphs is shown in Figure 6.6 for clear comparison. It can be observed from the figure that the curves corresponding to the proposed model have the highest area under them for the majority of the databases.

Qualitative Comparison. Some saliency maps obtained by the proposed model and other state-of-the-art methods are compared in Figure 6.2. It can be observed from the figure that the proposed model can perform better even in challenging scenarios such as cluttered background (row2 and row 4), multiple salient objects (row3 and row 5), low contrast difference between salient objects and background (row 1), and foreground/background disturbances (row 1 and row 3). The proposed model chooses the correct salient objects and produces more complete salient maps due to the simultaneous aggregation of local and local features.

6.2.5 Ablation Study

In this section, the effectiveness of key components of the proposed model is analyzed. The ablation study comprises two parts: architecture ablation and loss function ablation. The ablation study is performed on all six databases.

6.2.5.1 Loss Function Ablation

To determine the most suitable loss function for the proposed model, experiments are conducted for the architecture obtained at $\alpha = 1$. The results are evaluated on all the databases. The following loss functions and their combinations are considered: binary cross-entropy (BCE), focal, structural similarity (SSIM), and intersection over union (IOU). Results in Table 6.4 justify the reason behind choosing the binary-cross entropy loss. It can be observed from the metrics that the network trained with BCE loss performed better on the majority of the databases.

6.2.5.2 Architecture Ablation

The performance of any salient object detection network depends upon the feature extracted and their propagation between the layers at each level. The proposed network reuses the features obtained from previous layers at the present state with the help of fractional-weighted skip connections. Different factional orders give different arrays of weights for the skip connections in the backbone network. At $\alpha = 1$, the backbone network becomes almost equivalent to the ResNet-50 architecture [6]. To evaluate the effectiveness of the proposed network, the results are reported for the architectures corresponding to the different values of fractional order α $(0 < \alpha \leq 1)$ for all the databases with BCE loss

Table 6.4: Ablation study on different architectures and loss functions: Best results with different losses and the same architecture and vice-versa are highlighted

	Configurations	ECSSD			HKU-IS			PASCAL-S			DUTS-OMRON			DUTS-TE			SOD		
		F_β^{avg}	F_β^{max}	MAE	F_β^{avg}	F_β^{max}	MAE	F_β^{avg}	F_β^{max}	MAE	F_β^{avg}	F_β^{max}	MAE	F_β^{avg}	F_β^{max}	MAE	F_β^{avg}	F_β^{max}	MAE
Loss	**BCE** (α=1)	**0.910**	0.937	**0.039**	**0.891**	0.927	**0.034**	**0.829**	**0.871**	**0.065**	0.732	0.787	0.061	**0.807**	**0.871**	0.043	**0.810**	0.850	**0.091**
	Focal (α=1)	0.796	0.901	0.081	0.807	0.890	0.074	0.686	0.836	0.109	0.619	0.747	0.105	0.645	0.809	0.087	0.688	0.824	0.127
	Focal+ IOU + SSIM (α=1)	0.875	**0.941**	0.040	0.888	0.926	0.034	0.762	0.863	0.072	0.749	0.799	**0.057**	0.797	0.869	**0.042**	0.736	0.841	0.101
	BCE + IOU + SSIM (α=1)	0.862	0.933	0.042	0.889	**0.928**	0.034	0.757	0.861	0.074	**0.752**	**0.804**	0.059	0.796	0.869	0.043	0.758	**0.860**	0.096
Architecture	BCE (α=**0.9**)	0.910	0.936	0.040	0.891	0.928	0.033	0.828	0.869	0.068	0.738	0.791	0.057	0.809	0.872	0.042	0.806	0.851	0.102
	BCE (**α=0.8**)	0.909	0.935	0.038	0.892	0.928	0.033	0.828	0.871	0.065	0.740	0.797	0.056	**0.812**	0.873	**0.041**	0.810	0.855	0.097
	BCE(**α=0.7**)	0.909	0.935	0.038	0.891	0.928	0.033	0.828	0.869	0.066	**0.744**	**0.802**	0.058	0.807	0.869	0.042	0.816	**0.864**	0.093
	BCE(**α=0.6**)	0.913	0.939	0.039	0.891	0.927	0.033	0.826	0.871	0.067	0.742	0.798	**0.055**	0.811	**0.874**	0.042	0.805	0.852	0.099
	BCE(**α=0.5**)	0.912	0.937	**0.038**	0.891	0.927	0.033	0.823	0.865	0.069	0.742	0.798	0.060	0.801	0.866	0.045	**0.821**	0.857	0.094
	BCE(**α=0.4**)	**0.913**	**0.940**	0.039	**0.894**	**0.930**	**0.032**	0.827	0.869	0.068	0.743	0.801	0.057	0.808	0.872	0.042	0.817	0.859	0.097
	BCE(**α=0.3**)	0.909	0.936	0.040	0.892	0.929	0.033	0.821	0.864	0.069	0.741	0.799	0.058	0.802	0.866	0.044	0.814	0.859	0.100
	BCE(**α=0.2**)	0.907	0.936	0.042	0.889	0.927	0.034	0.825	**0.872**	0.070	0.738	0.800	0.060	0.796	0.863	0.046	0.806	0.849	0.103
	BCE(**α=0.1**)	0.897	0.929	0.046	0.873	0.916	0.040	0.798	0.848	0.083	0.727	0.795	0.065	0.766	0.842	0.055	0.793	0.842	0.112
	BCE + IOU + SSIM (α=**0.9**)	0.866	0.937	0.041	0.889	0.928	0.033	0.760	0.862	0.073	0.754	0.805	0.057	0.798	0.869	0.043	0.751	0.857	0.097
	BCE + IOU + SSIM (α=**0.8**)	0.863	0.935	0.040	**0.890**	**0.929**	**0.033**	0.760	0.865	0.072	0.754	0.806	0.058	0.798	0.870	0.043	0.743	0.854	0.097
	BCE + IOU + SSIM (α=**0.7**)	0.864	.937	0.040	0.889	0.928	0.033	0.754	0.861	0.072	0.755	0.807	0.057	0.797	0.870	0.043	0.754	0.862	0.096
	BCE + IOU + SSIM (α=**0.6**)	0.866	0.940	0.040	0.889	0.928	0.034	0.757	0.862	0.074	0.750	0.807	0.061	0.793	0.869	0.045	0.751	0.863	**0.094**
	BCE + IOU + SSIM (α=**0.5**)	0.870	0.938	0.039	0.888	0.927	0.033	0.764	0.858	0.072	**0.757**	0.804	**0.054**	0.800	0.871	0.041	0.748	0.850	0.095
	BCE + IOU + SSIM (α=**0.4**)	0.873	0.942	0.038	0.890	0.928	0.034	**0.767**	**0.868**	**0.072**	0.756	0.805	0.056	**0.806**	**0.875**	**0.041**	0.757	0.858	0.099
	BCE + IOU + SSIM (α=**0.3**)	**0.875**	**0.942**	**0.038**	0.889	0.928	0.034	0.761	0.862	0.075	0.756	**0.812**	0.058	0.796	0.868	0.046	0.751	0.860	0.095
	BCE + IOU + SSIM (α=**0.2**)	0.869	0.938	0.041	0.888	0.926	0.035	0.765	0.859	0.076	0.752	0.808	0.059	0.792	0.865	0.045	**0.759**	**0.866**	0.100
	BCE + IOU + SSIM (α=**0.1**)	0.859	0.930	0.045	0.876	0.919	0.039	0.752	0.854	0.0829	0.739	0.803	0.066	0.770	0.854	0.052	0.746	0.854	0.102

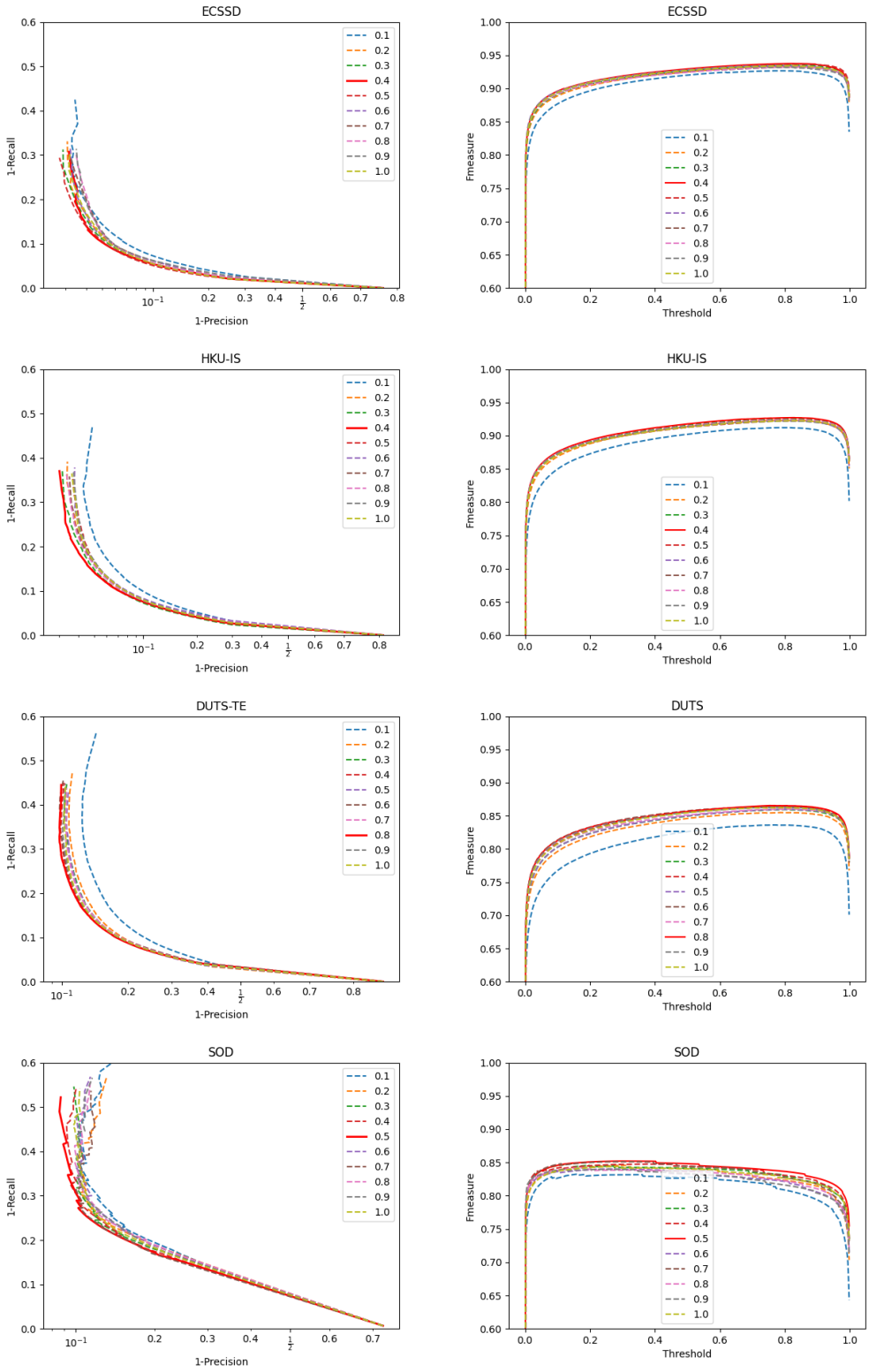

Figure 6.7: Precision-Recall curves and Fmeasure-Threshold curves for four databases corresponding to different fractional orders in column 1 and column 2, respectively: Red curve in each graph depicts the performance of the best model

and the 'BCE+SSIM+IOU' loss. A system's memory gets enhanced at fractional orders, as seen from Table 6.4 results. It can be observed that irrespective of the loss function used, the best results are obtained at a fractional order and not at $\alpha = 1$. From the values of the evaluation parameters, the network with 'BCE+SSIM+IOU' loss performed the best at $\alpha = 0.3$ for ECSSD and SOD, at $\alpha = 0.4$ for PASCAL and DUTS-TE, at $\alpha = 0.5$ and $\alpha = 0.3$ for DUTS-OMRON, and at $\alpha = 0.8$ for HKU-IS. The network with BCE loss performed the best at $\alpha = 0.4$ for ECSSD and HKU-IS, at $\alpha = 0.5$ for SOD, at $\alpha = 0.7$ for DUTS-OMRON, $\alpha = 0.8$ for DUTS-TE, and PASCAL at $\alpha = 1, 0.8$. The Precision-Recall and F-measure curves with BCE loss are shown in Figure 6.7 are also drawn to validate the quantitative results of the final model. '1-Precision' and '1-Recall' are plotted for each fractional order. The areas below these graphs depict errors in the system. Thus, the lesser the area under the curve, the better the system. The model with the best metrics for a database is plotted in red.

6.3 Summary

In this chapter, a salient object detection network with an encoder-decoder architecture equipped with feature aggregation paths and modules is designed by exploiting the memory property of fractional derivatives. In the encoder, weighted skip connections are added for combining the output of previous layers through summation and passing the features to subsequent layers, increasing the input variability and accuracy of the system. Thus the proposed model is computationally efficient even with dense connections. The decoder has feature aggregation, self-refinement, and attention modules for obtaining the more expressive and selective features that assist in learning the relationship between multiple salient objects. The network's performance is evaluated at multiple values of fractional order $\alpha < 1$. It is observed that the model is achieving its best performance on a database at different values of fractional order α. The models are aggregated based on F-measure values obtained for a system corresponding to α for diversifying the model predictions. The results show that the salient maps are produced with clear boundaries. The model performs well even in the presence of low contrast and cluttered background and accurately generates the salient maps from the images with multiple objects. Moreover, the proposed network's performance is found to be better than the other state-of-the-art methods on all six databases in terms of either F-measure or MAE. Therefore, it can be concluded that the feature propagation through layers has strengthened, leading to uniform performance

across all databases and improvement in the model's generalization capability. The results show that the model performs well even in the presence of low contrast and cluttered background and accurately generates the salient maps from the images with multiple objects.

There is a scope for improvement in two areas: 1) The boundaries of salient maps are sometimes not sharp enough. The proposed model simultaneously captures local and global information with the capability of understanding the relation between multiple salient objects and extracting objects from the background with low contrast difference. However, while solving the above issues, the model labels some background pixels as pixels belonging to the salient object. Hence, the sharpness of the boundaries of the salient objects gets affected. This affects the saliency map generation accuracy of the model. 2) The salient objects comprising very fine structures are inaccurately generated. The pixels corresponding to objects with thin structures are difficult to extract. The example showing this issue can be seen in row 6 of Figure 6.2. The thin sharp branches are not precisely extracted. In the future, these problems can be targeted to obtain saliency maps with sharper boundaries.

A part of this chapter is communicated as follows :

Sugandha Arora, Trilok Mathur and Kamlesh Tiwari. "Feature Aggregation for Salient Object Detection Using Fractional Weighted Skip Connections." (Communicated).

Chapter 7

Palmprint-based Human Recognition System

Biometric authentication utilizes an individual's behavior and biological characteristics for automated recognition. Biometric modalities such as face [333], palmprint [334], fingerprint[335], iris [336], teeth [337], footprint [338], knuckle print [339], etc have been successfully applied for human authentication. Each biometric trait has different advantages, due to which modality is chosen based on the application. Palmprint has unique and stable features like ridges and stripes, which make the authentication system more reliable and efficient [340]. Moreover, the palmprint images can be extracted with and without any contact with the sensor/camera, making extracting data for palmprint-based authentication easier. Palmprint biometrics is used in various applications, including border control, access control, and time and attendance tracking.

Like any biometric technology, palmprint-based human authentication faces several challenges affecting its accuracy and reliability [341]. First, the quality of the palmprint image can significantly impact the accuracy of the authentication system. The images' improper illumination, motion blur, and low resolution make feature extraction difficult [20]. Second, the non-uniformity in the features of the palm, as the shape and texture of the palm can vary significantly from person to person, makes it challenging to develop a universal model that can accurately identify all individuals [342]. Third, the presence of jewellery, gloves, or other objects that cover the palm can cause occlusion and reduce the accuracy of the authentication system [343]. Fourth, the skin on the palm can change with time due to the appearance of wrinkles and cuts caused by some injury. Such changes in the palmprint patterns can impact the accuracy of the authentication system, mainly if

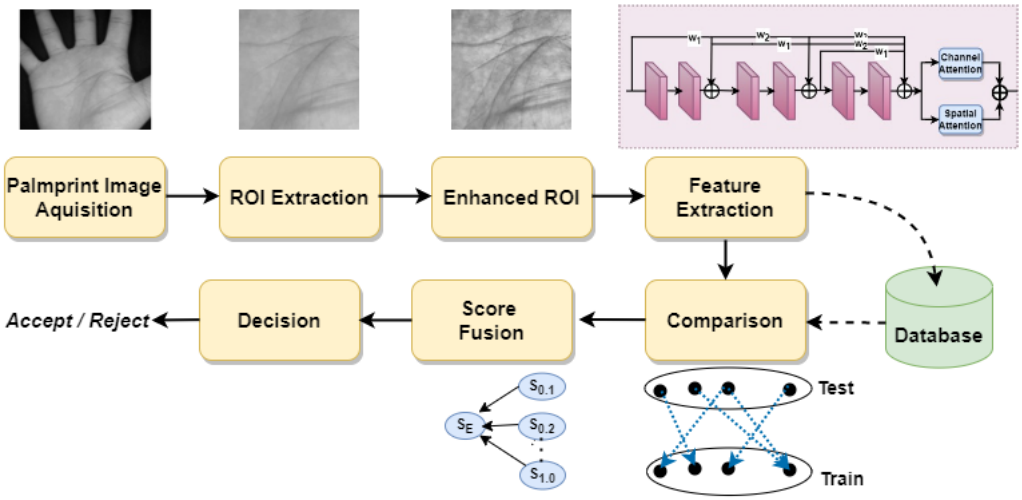

Figure 7.1: Block Diagram showing the stages of the proposed palmprint recognition system

the system is developed using older images of the individual [344]. Lastly, developing a robust and accurate palmprint recognition algorithm requires significant computational resources, making it challenging to implement palmprint-based authentication systems on low-power devices or in resource-constrained environments.

To overcome the above-mentioned challenges, several palmprint recognition systems have been developed. Some of the effective methods are based on handcrafted features [345] and traditional machine learning algorithms [346, 347]. Manual extraction of features was found to be more erroneous and traditional machine learning methods were also unable to handle image variations [348, 349]. The most advanced techniques include coding-based methods, local pattern descriptors, and deep learning approaches. Coding-based methods compute a biometric template by applying filters to the image and encoding the results. Then, the resulting biometric templates are compared globally based on their Hamming distance [350]. The PalmCode [351], binary Orientation Co-Occurrence Vector method [352], Double-Orientation Code [353], and Robust Line Orientation Code [354] are some of the most frequently used coding-based methods. Due to their global-matching procedure, these methods perform well on partially constrained databases but face difficulty dealing with local variations like rotation and translation [355]. Several recent approaches focus on local texture patterns that perform well on unconstrained data with variations. Some of those techniques are Scale-Invariant Feature Transform (SIFT) [356], Local Directional Patterns (LDP) [357], Local Binary Patterns (LBP) [357], Histograms of Oriented Gradients (HOG) [358], and Local Tetra Patterns (LTrP) [359] descriptors. These are texture-based techniques that first encode pixel intensity values,

then blockwise compute the histograms of the encodings, and then concatenate these blockwise histograms to obtain the feature vectors. The obtained feature vectors represent the corresponding biometric templates which are compared using different distance metrics (Euclidean or chi-squared distance). The LDP [357], LBP [357], and LTrP [359] are widely adopted and highly accurate local texture descriptors for touchless palmprint recognition. However, its computations involve handcrafted feature extraction procedures requiring manual parameter tuning. While overcoming these drawbacks, several deep-learning-based palmprint recognition systems are developed due to their ability to natively process input images and adapt to samples captured with heterogeneous devices. Deep learning-based methods are successfully being used to extract features; hence, deep CNNs are applicable for image classification, object detection, and several other tasks. Deep CNNs are used for palmprint recognition and give state-of-the-art results [341]. These algorithms can learn complex and non-linear relationships between the palmprint features and the individual's identity, leading to high recognition accuracy.

The performance of a recognition system depends upon the quality of features extracted. Deep neural networks use multiple layers to extract higher-level features progressively. With the increase in depth of the networks, the problem of vanishing gradient and information loss arises. Many recent works such as ResNets [6], FractalNet [250], DenseNet [312], and many others, have addressed this issue. The drawbacks of these networks are mentioned in the earlier chapters. The approach used in the previous two chapters of adding weighted skip connections is adopted here for developing a recognition system. Adding weighted skip connections: 1) enables deeper networks for better feature extraction; 2) solves the vanishing gradient problem; 3) incorporates long-term memory with a mathematical framework; and 4) improves the network's generalization ability, leading to the extraction of more expressive features. The obtained feature vectors can be improved by further refinement and adding explicit constraints on their distribution to make them significantly separable. A fractional-derivative-based feature extraction network integrated with a dual attention mechanism is designed to address this. The key contributions of this work are described below:

1. This chapter proposes a palmprint-based authentication system that extracts features from FrDPalmNet, a novel fractional-derivative-based residual network embedded with dual attention modules. The feature extraction process is modeled as a dynamic system using the G-L fractional derivative. The fractional derivative incorporates long-term memory into the system to extract more expressive features, that are

further refined in a dual way, $i.e.$, channel-wise and position-wise.

2. The trainable weights of FrDPalmNet are optimized by using large-margin cosine loss [360] with focal loss [146]. This increases the inter-class variations and intra-class similarities between the features and helps learn more discriminative features.

3. The predictions of FrDPalmNet for each α are aggregated using a weighted average ensemble method based on the system's error rate. Using multiple learners of the same algorithm diversified the model predictions and developed a better recognition system.

4. The effectiveness of adopting the proposed palmprint recognition system is evaluated on three widely used publicly available palmprint image databases viz. CASIA [18] , IIT Delhi Touchless [19] and Tongji Contactless Palmprint Database [20]. All these databases are acquired in an unconstrained environment.

The rest of the chapter is structured as follows: Section 7.1 describes the proposed approach, $i.e.$, pre-processing, architecture designing, loss function, matching strategy, and model ensembling. The detailed analysis of experimental results is done in the Section 7.2.

7.1 Proposed Approach

This section provides a detailed description of the proposed palmprint recognition approach. The four main components of the proposed approach *viz.* pre-processing of Region of Interest (ROI) palmprint images, feature extraction, matching the extracted features and evaluating the scores, and score fusion via ensembling. The original palmprint images have cluttered backgrounds and some unnecessary parts of the hands like wrists and fingers, other than the palms. The method given by Zhang *et. al.* [351] is adopted to extract the required portion of the palms from the images. It binarizes the image and then separates the palm from the background. Then, the gaps between the fingers are used as reference points to get the y-axis of the coordinate system. The point at which the line perpendicular to the line joining these reference points is referred to as the origin of the coordinate system. A sub-image is extracted from the central part of the image based on the coordinate system. The histogram equalization technique is used to enhance the extracted ROI images. For feature extraction, FrDPalmNet is proposed which has layers with fractional weighted skip connections and dual attention modules are applied at each level. The large-margin cosine loss and focal loss are applied in FrDPalmNet for effective learning. Ten variants

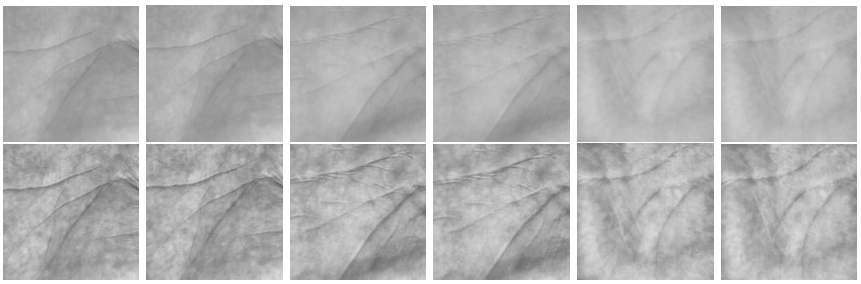

Figure 7.2: Samples of palmprint ROIs in row 1 with corresponding enhanced images in row 2

of FrDPalmNet depending on different fractional orders ($0 < \alpha \leq 1$) are considered. The features of test images are matched with the features of training images. The score files corresponding to each fractional order are fused to obtain the final ensembled score file. All the components of the proposed approach are described in the following subsections.

7.1.1 Pre-processing

The extracted ROI images are enhanced by adaptively equalizing their histograms. It means that the most frequent intensity values are effectively spread out, $i.e.$, the intensity range of the ROI images is stretched out. CLAHE (contrast limited adaptive histogram equalization) variant of adaptive histogram equalization is employed, which locally improves the contrast in an image while preventing noise amplification. ROI images are divided into small tiles of size 4×4 each and then the histogram is equalized in these small tiles separately. Before applying CLAHE, pixels in any histogram bin that exceeds the chosen contrast limit ($= 2$), are clipped and uniformly distributed to other histogram bins. This enhancement technique highlights the edges and reduces any blurry effect due to light reflection during palmprint image acquisition. The enhanced output image becomes more suitable for deep feature extraction and matching. Figure 7.2 shows that images enhanced with CLAHE have prominent principal lines and ridges.

7.1.2 Architecture of FrDPalmNet

The proposed network has four residual blocks with fractional-weighted skip connections and dual attention assistance after each block. Each fractional residual block has multiple sub-blocks. The sub-blocks at a scale of the network are connected to other sub-blocks via fractional weighted skip connections that incorporate long-term memory into the system. The features extracted from the final layer of a fractional residual block are pooled and then strengthened using the dual attention modules. The evolution process in the network is modeled as a dynamic system. The propagation of features through the sub-blocks

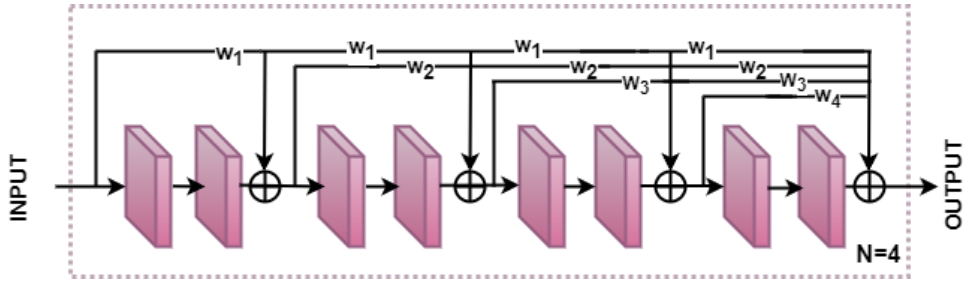

Figure 7.3: Fractional Residual Block (FRB) with $N = 4$ sub-blocks comprising two layers each

of the network are considered as trajectories of the dynamic system and the operations occurring in the dual attention modules are considered as a non-linear function. The feature propagation through sub-blocks is described using fractional differential equations with optimal control conditions. Large-margin cosine loss followed by focal loss is applied to improve the optimization process of the network. The major components of the network are described below with supporting mathematical explanations for memory exploitation.

7.1.2.1 Fractional Residual Blocks (FRB)

The ResNet-34-like architecture with residual connection after every two layers is used for feature extraction. For modeling the evolution process of the network as a dynamic system, each scale/block is divided into sub-blocks of two convolution layers. To sum up, the propagation of features through sub-blocks of the network is modeled as a dynamic system, which is described using a set of fractional differential equations, and then the optimal control parameters are evaluated after solving it. The application of fractional derivatives adds weighted skip connections to the residual blocks of the network. These weights depend on the network's current sub-block (t) and the differentiation order. The order α and fractional weights are positive and less than 1, *i.e.*, $0 < \alpha \leq 1$, and the weighted sum of features remains positive and does not explode. Fractional Residual Block with four sub-blocks comprising two layers each is shown in Figure 7.3. N stands for the number of sub-blocks. The sub-block n is connected with $(n-1)^{th}$, $(n-2)^{th}$ sub-blocks via skip connections with weights w_1, w_2.. respectively.

7.1.2.2 Dual Attention Module

Since the ROI of palmprint images has noise due to improper illumination, motion blur, and low resolution, it leads to distorted features and affects the system's accuracy. To improve the discriminating ability of the palmprint-based authentication system, the local features are adaptively integrated with their global dependencies based on a self-

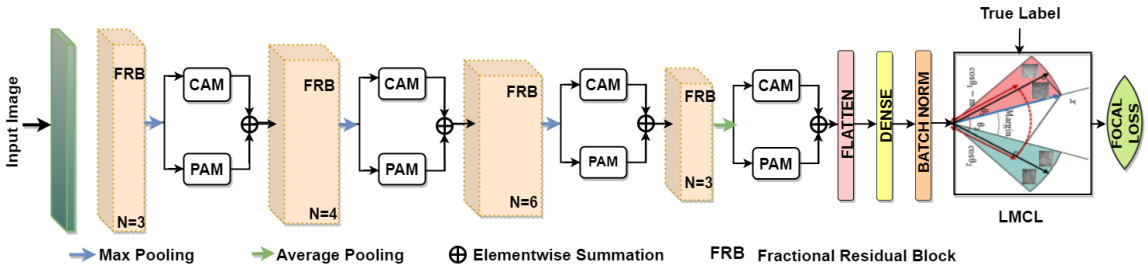

Figure 7.4: Structure of the proposed FrDPalmNet for palmprint feature extraction

attention mechanism. The attention modules automatically select the region from the image responsible for maximum contribution in accurate matching. The dual attention module applies position attention and channel attention mechanisms after the final layer of the FRB. The Position Attention Module (PAM) aggregates semantically similar pixels in the spatial domain of the input feature map. It is applied to the entire input feature map based on pixel values without consideration of the spatial positions of the pixel. The Channel Attention Module (CAM) captures the channel-wise relationship of features obtained from the FRB. Both modules are spatially invariant. The outputs of both modules are then combined to improve feature representation, resulting in more precise matching results.

- **Channel Attention Module (CAM).** The different channel maps corresponding to high level features are class-specific and their semantic information are interdependent to each other. To capture this channel-wise relationship, it is required to differentiate between essential features and redundant information. This improves the representation of features and stability of the network. Therefore, ECA-Net [361] is used as a channel attention module after every FRB to specifically model the interdependencies between the channel maps. Its implementation involves the usage of a one-dimensional convolution of size $F(=5)$ that requires just six trainable parameters. The CAM is applied on the feature $E_m^{(i)}$ extracted from FRB at level m with weights given by $A_m^{(1)}$, is denoted by $A_{CAM}(E_m^{(i)}; A_m^{(1)})$. Mathematically, the channel-wise highlighted feature $F_{m,1}^{(i)}$ at level m is given by the following

$$F_{m,1}^{(i)} = E_m^{(i)} \otimes A_{CAM}(E_m^{(i)}; A_m^{(1)}) \tag{7.1.1}$$

where $\otimes$ represents matrix multiplication.

- **Position Attention Module (PAM).** The palmprint images have diverse features like ridges, principal lines, and wrinkles spread from one end of the image to another. PAM [362] captures the spatial semantic regularities in the palmprints. Assume $E_m^{(i)}$ be the output of the FRB at level m that is passed to PAM for focusing on spatial dependencies. The PAM is applied on the feature $E_m^{(i)}$ extracted from FRB at level m with weights given by $A_m^{(2)}$, is denoted by $A_{PAM}(E_m^{(i)}; A_m^{(2)})$. Mathematically, the spatially enhanced feature $F_{m,2}^{(i)}$ at level m is given by the following

$$F_{m,2}^{(i)} = E_m^{(i)} \otimes A_{PAM}(E_m^{(i)}; A_m^{(2)}) + E_m^{(i)}. \tag{7.1.2}$$

  where $\otimes$ represents matrix multiplication.

- **Feature Combination.** The outputs from CAM and PAM after each FRB are aggregated to get the spatially and channel-wise highlighted feature. The features vectors are summed up element-wise to get the final feature. Mathematically, the final feature $C_m^{(i)}$ is given by

$$C_m^{(i)} = F_{m,1}^{(i)} \oplus F_{m,2}^{(i)} \tag{7.1.3}$$

  where $\oplus$ denotes element-wise summation, $F_{m,1}^{(i)}$ and $F_{m,2}^{(i)}$ are features extracted from CAM and PAM respectively, applied after FRB at level m. These attention modules are applied four times in the network. The output of the fourth dual attention module C_4 is flattened to get a one-dimensional vector followed by applying a fully connected and batch normalization layer to get the embedding $P^{(i)}$ of size 512×1 for the input palmprint image $I^{(i)}$.

7.1.2.3 Loss Function

Large-Margin cosine Loss (LMCL) is employed to increase the feature discrimination power of the network. Its formulation involves combining the Softmax function with a cosine similarity transformation. It adds an angular margin to the conventional Softmax loss, ensuring that the embeddings of different classes are more distinguishable. This is achieved by increasing the angular distance between the embedding of the correct class and the embeddings of other classes. The norm of the feature vectors is fixed to be s, and θ is the angle between the feature vector and the corresponding weight vector obtained after applying L_2 normalization/euclidean normalization. Palmprint recognition is a binary

classification problem as the images matched are genuine or imposter matches. The motive is to increase the margin between imposter matches and decrease the margin between genuine matches. If θ_i denotes the angle between the weight vector and the learned feature vector for an image belonging to class i, then the conditions followed by these feature vectors are given as

$$C_1 : \cos\theta_1 - m > \cos\theta_2 \tag{7.1.4}$$

$$C_2 : \cos\theta_2 - m > \cos\theta_1 \tag{7.1.5}$$

The conditions C_1 and C_2 are satisfied to match within class S_1 and S_2 respectively. The term $\cos\theta_i - m < \cos\theta_j$ with margin $m > 0$ makes the classification more stringent. Using these margin constraints, the LMCL function is expressed as

$$L_{lmc} = \frac{1}{N}\sum_i -\log\frac{e^{s(\cos(\theta_{y_i},i)-m)}}{e^{s(\cos(\theta_{y_i},i)-m)} + \sum_{j\neq y_i} e^{s\cos(\theta_j,i)}} \tag{7.1.6}$$

where, $\cos(\theta_j, i) = W_j^T O^{(i)}$ and W_j is the weight vector for the class i. The output of LMCL, a vector of class probabilities, is fed to the Focal Loss (FL) [146] for facilitating backpropagation. Mathematically, it is expressed as

$$FL(p, y) = -(1 - p_y)^\gamma log(p_y) \tag{7.1.7}$$

where γ is a hyperparameter focused on hard negative examples. After combining the FRBs, dual attention modules, and the loss function, we get the final feature extraction models corresponding to different fractional order α. The proposed deep feature extraction network FrDPalmNet is designed by solving the following fractional optimal control problem :

$$\min_{\theta(t)} \sum_{y=1}^{M} FL(p, y),$$

subject to,

$$\begin{aligned} {}_0D_t^\alpha v(t, s, p_i) &= f(v(t, s, p_i)), \theta_{p_i}(t)) \\ \text{s.t. } v(0, s, p_i) &= \mathcal{A}_d(T_\downarrow v(\textstyle\sum_{k=1}^{i-1} n_k, s, p_{i-1})), \\ v(0, s, p_1) &= \Psi(I(s)),\ i \in [1, 4],\ \ t \in [0, T] \end{aligned} \tag{7.1.8}$$

Table 7.1: Description and comparison of the considered palmprint databases

Database	Hand State	Sessions	Session Interval	Number of Palms	Samples per palm	Gallery Samples	Probe Samples	Total Samples
CASIA [18]	Fixed	1	-	602	8-10	2408	2831	5239
IIT-D [19]	Fixed	1	-	460	5-6	1841	760	2600
Tongji [20]	Free	2	61 days	600	20	6000	6000	12000

where $\mathcal{A}_d$ denotes dual attention, $T_{\downarrow}$ denotes max pooling operation, n_k denotes the number of sub-blocks at level k, θ_{p_i} is convolution kernel at level i. Thus the evolution process of the proposed feature extraction model is represented by (7.1.9).

$$v_{t+1}^{p_i} = \sum_{k=0}^{t} w_k v_k^{p_i} + \sigma(\theta_t * (v_t^{p_i}))) \tag{7.1.9}$$

, where σ is a non-linear unit denoting the twice consecutive application of 'Convolution + Batch normalization + ReLu' on the output of sub-block t, $v_{t+1}^{p_i}$, is the output of t^{th} sub-block of scale p_i, $w_k = (-1)^{(t-k+1)}\binom{\alpha}{t-k+1}$, and thus $w_t = \alpha$. The p network is shown in Figure 7.4, built from four FRBs shown in Figure 7.3 with N sub-blocks.

7.1.3 Matching Strategy

The features of the palmprint database are extracted from the models corresponding to each α. The features of test images are matched to train images and the matching score is evaluated for each pair. The score files corresponding to each α are S_α. The score file is further analyzed and evaluation metrics are computed for each database.

7.1.4 Weighted Average Ensembling

The verification performance of the authentication system is majorly dependent on EER. The model with the highest EER is given the least weightage coefficient. Thus the proposed fractional models are ensembled with a weightage coefficient equal to $\beta_\alpha = \frac{1}{EER_\alpha}$. The Formula used for ensembling is given by (7.1.10). S_E represents the final matching score of the model.

$$S_E = \frac{\beta_{0.1} S_{0.1} + \beta_{0.2}\, S_{0.2} + \beta_{0.3}\, S_{0.3} + \cdots \beta_{1.0}\, S_{1.0}}{\beta_{0.1} + \beta_{0.2} + \beta_{0.3} + \cdots \beta_{1.0}} \tag{7.1.10}$$

7.2 Experimental Results

In this section, databases are introduced, and implementation details and matching strategies are described. Further, the results are evaluated on these databases to show the effectiveness of the proposed system.

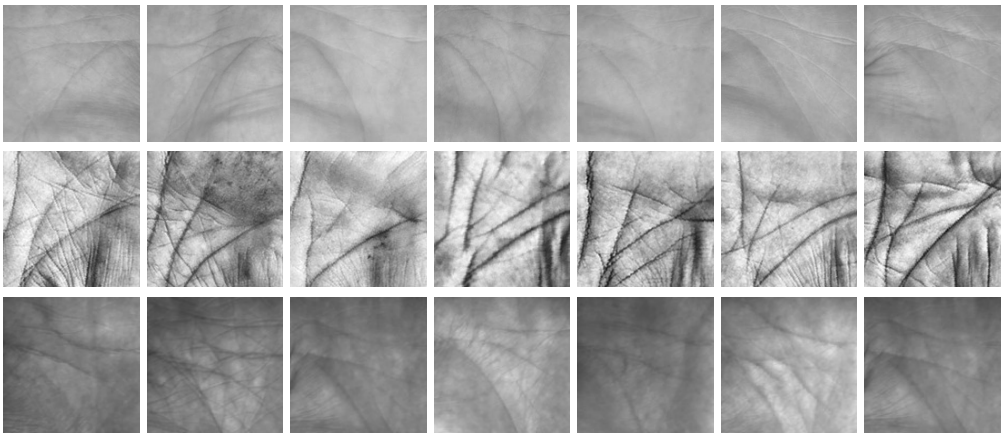

Figure 7.5: Sample ROIs of the palmprint databases: First, second and third row shows the images from CASIA [18], IIT-D [19] and Tongji [20] databases respectively

7.2.1 Database Specifications

The proposed approach is evaluated on the three most widely-used and publicly-available palmprint databases, namely, CASIA Palmprint Image Database [18], IIT Delhi Touchless Palmprint Database [19] and Tongji Contactless Palmprint Database [20]. Every database considers a person's left and right palms as two different subjects. All the databases are acquired using contactless devices. The Tongji Contactless Palmprint database images are extracted by freely placing the hand in an enclosed box, having controlled illumination without any contact with the surface. The rest of the databases are acquired by placing the hand on a fixed surface in an enclosed box having controlled brightness. The Region of interest (ROI) from these palmprint images is extracted using the well-approved technique proposed in [351]. The databases are briefly described below and in Table 7.1. The sample ROI images are shown in the Figure 7.5.

- **CASIA Palmprint Image Database [18]** The CASIA palmprint database from the Chinese Academy of Sciences, Institute of Automation consists of 5239 images collected from the palms of 301 individuals. Around Eight images from each subject's palm are collected in a single session without any restriction on posture and position of the palm. The original images are in bitmap ($*$.bmp) format with dimensions 640×480. The extracted ROI images are of dimension 128×128.

- **IIT Delhi Touchless Palmprint Database [19]** This database consists of 2600 palmprint images acquired from both palms of 230 students and staff of IIT Delhi from June 2006- July 2007. Five-Six images from each palm were captured in

varying poses. The original images are in bitmap ($*$.bmp) format with dimensions 800×600. The extracted ROI images are of dimension 150×150.

- **Tongji Contactless Palmprint Database [20]** This is a large-scale database consisting of 12000 palmprint images. It is collected by Tongji University from both the palms of 300 subjects in two sessions with the gap of 2 months. 275 subjects are from the age group of 20 to 30 years and the rest are from the 30 to 50-year age group. Ten images from each subject's palm are collected in each session. The original images are of dimensions 800×600. The extracted ROI images are of dimension 128×128.

Table 7.2: Recognition performance of FrDPalmNet shown with state-of-the-art results from PalmHashNet [4] on the considered databases

Model	CASIA				IIT-D				Tongji			
	CRR	**EER**	**DI**	**Acc**	**CRR**	**EER**	**DI**	**Acc**	**CRR**	**EER**	**DI**	**Acc**
PalmHashNet	**100**	**0.031**	**4.71**	**99.98**	**99.42**	0.39	**3.94**	99.62	97.8	**0.53**	2.82	97.65
Proposed	99.55	0.34	3.82	99.74	99.34	**0.24**	3.80	**99.78**	**98.73**	0.64	**3.28**	**99.38**

7.2.2 Training/Testing Protocol

All the databases used for experiments are non-uniform, and there is no fixed partition of training and testing images. The most frequently followed partition in the existing literature is adopted to evaluate the recognition performance. The training partition contains the gallery images used for training the model, and the testing partition contains query images, which are matched with the gallery images for identification. If the match is between images of the same subject, then that is termed a genuine match otherwise it is an imposter match. Each subject of the CASIA palmprint database has around eight or ten images, thus train partition has four images associated with each subject, and the rest of the images are added to the test partition. Each subject of the IIT-D palmprint database has around five or six images, thus test partition has one or two images associated with each subject. The Tongji contactless palmprint database is acquired in two sessions. Each subject has ten images in each session. The images collected from one session are added to the train partition and second-session images are added to the test partition.

The acquired palmprint images are non-uniform, have occlusion and variations in illumination, etc. To make the network resilient to such non-uniformities, the training partitions of the databases are augmented using Python Augmentor [363]. The images

are transformed by applying random zoom, rotation, contrast, brightness, and horizontal flipping. These five processes are performed on each image of the training partition, making the final training size six times. The final training portion of CASIA, IIT-D, and Tongji databases consisted of 14448, 11046, and 36000, respectively.

7.2.3 Implementation Details and Experimental Settings

A Linux-based operating system with the NVIDIA A100-PCIE graphic card having graphic memory of 40 GB is used to implement the model in the PyTorch framework. LMCL loss with margin $m = 0.35$ and norm $s = 300$ and focal loss with $\gamma = 2$ is employed for training the network. Adam optimizer is used for weight updation with weight decay of $5e - 4$, the initial learning rate of 3^{-4} which is adjusted after every 20 epochs with linear decay of 0.1. The model is trained for 100 epochs with a batch size of 64.

7.2.4 Results and Discussion

The proposed network FrDPalmNet extracts the feature embeddings of training and test images. To evaluate the palmprint recognition performance of the proposed system, the feature embeddings for the test and training images are compared, and Euclidean distance is evaluated between them. Those distances are treated as scores; on that basis, the system's accuracy, CRR, EER, and DI are computed on all three databases. The final proposed recognition system is developed from the ensemble of FrDPalmNet for each α. The final proposed system's results on all databases and their comparison with the state-of-the-art network PalmHashNet [4] are shown in Table 7.2. The accuracies of the proposed system are 99.4%, 99.78% and 99.38% on CASIA, IIT-D, and Tongji respectively. Moreover, the EERs of the proposed system are 0.34%, 0.24%, and 0.64% on CASIA, IIT-D, and Tongji respectively. Thus the system has accuracy above 99% and EER below 1% on all the databases which justifies the great verification performance of the authentication system. The genuine and imposter score histogram is plotted in the second column of Figure 7.6 showing the performance of the proposed approach on all three databases. The peaks for genuine and imposter scores in the score histogram for all the databases are well separable. The best imposter score and a genuine score of all the images are plotted on the graphs in the first column of Figure 7.6. It can be observed that the proposed system has a clear separation between the values. More separability implies a better recognition system. The value of the parameter DI denotes class separability. The proposed system achieved DI of 3.82, 3.80 and 3.28 on CASIA, IIT-D and Tongji respectively. The proposed system has better verification performance than the PalmHashNet with higher accuracy, higher DI,

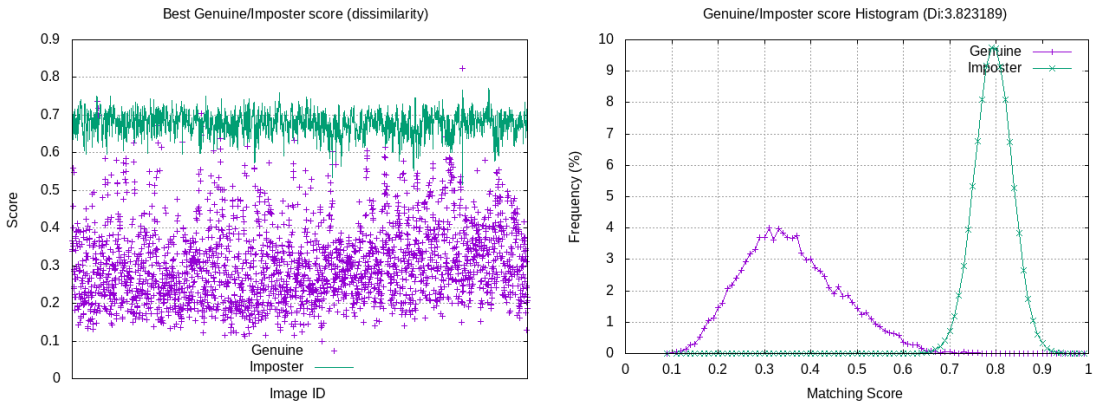

a) CASIA

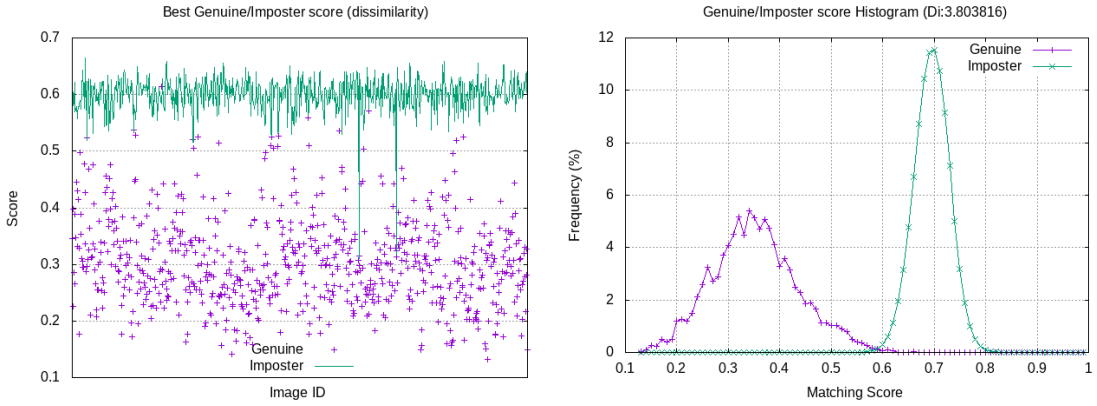

b) IIT-D

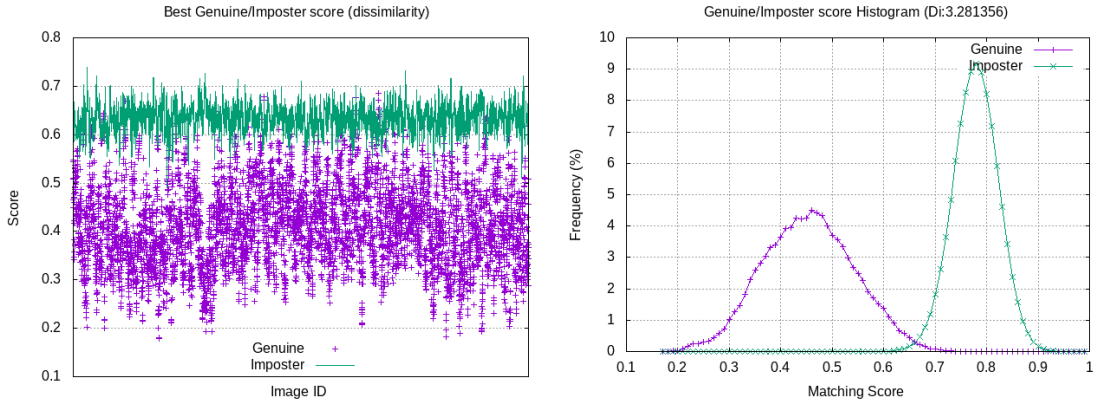

c) Tongji

Figure 7.6: **First column:** Best genuine and imposter scores for every image in the database; **Second column:** Histogram of genuine and imposter scores

Table 7.3: EERs (%) of palmprint verification using proposed approach (FrDPalmNet) and other benchmarking methods on the considered databases

Feature Extraction Method	CASIA	IIT-D	Tongji
Feature extraction using Karhunen–Loeve transform [364]	0.55	7.72	
Column Sampling based Discrete Supervised Hashing (COSDISH) [354]	0.81	7.44	
L_1 norm sparse multiscale competitive code with Gaussian filters [365]	0.48	-	-
Local Line binary Directional Patterns (LLDP) [357]	-	4.07	-
Adversarial Metric Learning [359]	-	1.73	1.21
Feature extraction using Local Micro-structure Tetra Pattern (LMTrP) [366]	-	0.87	-
PalmHashNet with modified Softmax loss [4]	**0.03**	0.39	**0.53**
Proposed FrDPalmNet	0.34	**0.24**	0.64

Table 7.4: CRR (%) of the proposed recognition system (FrDPalmNet) and other benchmarking methods on the considered databases

Feature Extraction Method	CASIA	IIT-D	Tongji
Difference of Block Means [367]	94.17	99.02	-
Adversial Metric Learning [359]	-	99.02	97.17
Deep CNN for discriminative feature representation (DDR) [368]	97.06	97.25	-
Column Sampling based Discrete Supervised Hashing (COSDISH) [354]	-	-	96.38
Hashing network with structural similarity metric [369]	-	-	97.65
PalmHashNet with modified Softmax loss [4]	**100**	**99.42**	97.8
ProposedFrDPalmNet	99.55	99.34	**98.73**

and comparable EER of 99.38, 3.28 and 0.64 respectively for the Tongji database. On the other hand, PalmHashNet has accuracy, DI, and EER of 97.6, 0.53, and 2.82 respectively on Tongji. The proposed achieved accuracy and EER of 99.78% and 0.24% respectively on the IIT-D database, while PalmHashNet has accuracy and EER of 99.62% and 0.39% respectively. Clearly, the proposed system is a better palmprint verification system on the IIT-D palmprint database. On the CASIA database, the proposed approach has achieved comparable accuracy of 99.74% with PalmHashNet.

The Rank-1 identification rates (CRR) for the proposed approach are 99.55% and 99.34% ($> 99\%$) for CASIA and IIT-D. The identification performance is comparable to the state-of-the-art model for CASIA and IIT-D, while the identification rate is 98.73% for the Tongji database, better than the state-of-the-art. The verification and identification results of the proposed approach are compared with various existing palmprint recognition techniques. It can be seen from Table 7.3 that the proposed approach performs best in terms of EER when tested on the IIT-D Touchless palmprint database. Table 7.4 shows that the proposed approach performs best in terms of rank-1 identification rate (CRR) when tested on the Tongji database. Therefore, it can be said that the proposed approach performs well with comparable performance with the other state-of-the-art techniques

Table 7.5: Comparison of the proposed method for different fractional orders and their ensemble based on CRR, EER, DI, and Accuracy (Acc)

Network	CRR	EER	DI	Acc	CRR	EER	DI	Acc	CRR	EER	DI	Acc
	CASIA				IIT-D				Tongji			
$\alpha = 0.1$	98.90	0.57	3.58	99.53	98.03	1.22	3.27	98.86	94.13	2.27	2.73	97.85
$\alpha = 0.2$	99.17	0.57	*3.65*	*99.54*	98.42	0.96	3.36	99.14	94.17	2.00	2.84	98.05
$\alpha = 0.3$	99.10	0.60	3.52	99.42	98.42	0.85	3.36	99.20	95.98	1.46	2.96	98.56
$\alpha = 0.4$	99.02	0.66	3.45	99.42	97.76	0.92	3.46	9.17	96.37	1.56	2.96	98.49
$\alpha = 0.5$	99.17	***0.55***	***3.65***	***99.54***	98.42	0.82	3.46	99.28	96.83	1.40	3.06	98.67
$\alpha = 0.6$	99.10	0.62	3.53	99.44	98.16	0.82	3.52	99.29	97.10	***1.25***	3.06	***98.79***
$\alpha = 0.7$	98.83	0.70	3.61	99.43	***98.95***	***0.53***	***3.54***	***99.57***	97.63	1.36	3.03	98.69
$\alpha = 0.8$	99.24	0.57	3.63	99.50	98.42	0.89	3.39	99.19	***97.70***	1.30	***3.09***	98.77
$\alpha = 0.9$	98.94	0.60	3.48	99.43	98.16	0.66	3.41	99.36	97.18	1.38	3.06	98.69
$\alpha = 1$	***99.28***	0.68	3.51	99.40	98.42	0.85	3.41	99.20	97.32	1.46	3.01	98.59
Ensembled	**99.55**	**0.34**	**3.82**	**99.74**	**99.34**	**0.24**	**3.80**	**99.78**	**98.73**	**0.64**	**3.28**	**99.38**

proposed in the literature.

7.2.5 Ablation Study

The performance of the proposed recognition system depends upon the quality of features extracted and thus on the process of feature propagation. The feature from a layer of the network is propagated to multiple layers via weighted skip connections and those weights are dependent on the fractional order α. Thus ablation study is performed on order α to search for the optimal weights leading to the extraction of superior features that would improve the palmprint recognition performance. The features are extracted from the FrDPalmNet at $\alpha = 0.1, 0.2, 0.3, \cdots, 1.0$ on all three databases. Rank-1 identification rate (CRR), EER, DI and accuracy are computed for analyzing the performance of the models. At $\alpha = 1$, the weight of just the previous connection becomes equal to one and the rest of the weights become zero. Thus the network obtained at $\alpha = 1$ is equivalent to plain ResNet34 integrated with dual attention.

Table 7.5 shows the results obtained at different α. The best results at some α are represented by bold and italic font for each database. At $\alpha = 1$, the values of CRR, EER, DI and accuracy are 0.68%, 3.51 and 99.40% for CASIA, 98.42%, 0.85%, 3.41 and 99.20% for IIT-D, and 99.28%, 97.32%, 1.46%, 3.01 and 98.59% for Tongji, respectively. The results at some fractional orders α are better than those at $\alpha = 1$ for all three databases. The best CRR for CASIA is 99.28% obtained at $\alpha = 1$. But the best EER, DI and accuracy are 0.55%, 3.65 and 99.54% respectively, obtained at $\alpha = 0.5$. The best CRR, DI, EER and accuracy are 98.95% 0.53% 3.54 and 99.57% respectively obtained at $\alpha = 0.7$ for IIT-D. The best CRR and DI are 97.70% and 3.09 respectively, obtained at $\alpha = 0.8$, while

the best EER and accuracy are 1.25% and 98.79% respectively obtained at $\alpha = 0.6$ for Tongji.

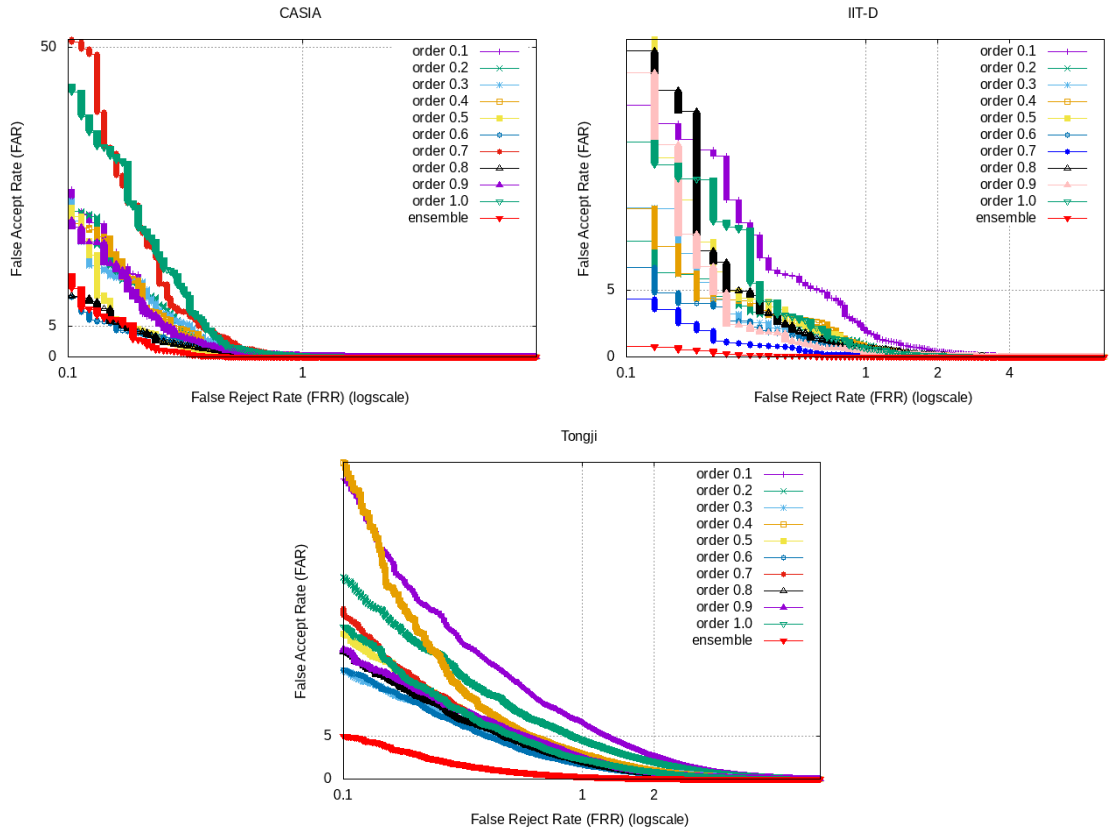

Figure 7.7: ROC Curves of the proposed approach at each α and final proposed ensemble system: Red curve depicts the final proposed system

The ROC curves for each database corresponding to each α are plotted in log-scale as shown in Figure 7.7. The log scaling focuses on a more meaningful lower side of the curve. The area under the ROC curve depicts the degree of separability between the classes. Lesser be the area under the curve, the better the system. The blue ROC curve in each graph representing the performance for CASIA, IIT-D and Tongji at $\alpha = 0.6$, $\alpha = 0.7$ and $\alpha = 0.7$ respectively, has the least area amongst all the models for different α. The same can be validated from the values of evaluation parameters as well in Table 7.5. It can be seen that the models are performing well for all databases on different fractional orders. Thus the dissimilarity scores of the features of a database obtained from the models for different α are ensembled using the weighted average method based on the EER parameter to focus on better verification performance of the system. After ensembling the models for all α, the best results are obtained for all the databases. The red ROC curve for each

database represents the performance of the ensemble model.

7.3 Summary

In this chapter, a palmprint-based human authentication system is developed using the proposed network FrDPalmNet that generates highly discriminative and expressive features. FrDPalmNet is designed using the theory of fractional optimal control which mitigated the issue of short-term memory of the existing integer-order derivative-based networks. The outputs of the layers of the fractional residual blocks (FRB) of this network are integrated using weighted summation, unlike other dense networks which involve concatenation of outputs. Thus the propagation of features is enhanced resulting in the preservation of information with lesser computation cost. The features after each FRB is strengthened using dual attention modules. Further, LMCL with focal loss is used to train the model for feature extraction and obtain the embeddings with high intra-class similarity and inter-class separability. The three major elements of FrDPalmNet: FRBs, dual attention modules, and LMCL with focal loss, helps in the determination of high-accuracy features. The feature vectors generated using FrDPalmNet for each α are matched with all gallery images and the genuine/imposter scores are determined. CRR, EER, DI, and accuracy are computed to analyze the systems' performance. The score files are aggregated based on EER values obtained for a system corresponding to α. The decision is made using multiple learners of the same algorithm for diversifying the model predictions. The proposed approach is validated on CASIA, IIT-D, and Tongji palmprint databases for thorough evaluation. The proposed system achieved comparable and sometimes even better results than the other methods existing in the literature. Moreover, the system showed more uniform accuracy results on heterogeneous databases. Specifically, the system achieved an accuracy of above 99% and EER below 1% on all considered databases. The rank-1 identification rate is 98.73% for Tongji outperforming the state-of-the-art and above 99% for CASIA and IIT-D. The consistent results of the proposed system demonstrate the efficiency and feasibility of its application on other heterogeneous databases captured using different devices.

A part of this chapter is communicated as follows:

Sugandha Arora, Trilok Mathur and Kamlesh Tiwari. "FrDPalmNet: Dual Attention Mechanism and Residual Blocks with Fractional Weighted Skips for Palmprint-based Human Authentication System." (Communicated).

Chapter 8

Conclusion and Future Scope

This thesis presents novel approaches to investigate the effectiveness of fractional differentiation. The potential applications of fractional calculus in science, engineering, finance, and social science are exponentially growing with time. This research uses fractional calculus to model crime transmission, train neural networks, and design memory-inherent deep neural networks through a concrete mathematical framework. It is observed that the memory property of fractional derivatives is well exploited in considered domains, by allowing the modeling and analysis of the complex systems that exhibit long-term dependence and non-linear behavior. This process of memory incorporation brings explainability and interpretability into the system, enhancing transparency and trustworthiness and enabling a better understanding of the process. The comparative analysis with the existing literature reveals that the findings are better than those of prior work reported in the literature. The conclusions inferred for each application area, followed by the future scope of this research work, are discussed in the next section.

8.1 Conclusions of the Work

8.1.1 Crime Transmission Modeling

Unlike existing crime transmission differential models, the proposed fractional model helps investigate the historic and simultaneous effects of imprisonment, recidivism, contagion, history of criminals, and jurisdiction on crime transmission. The basic reproduction parameter $\mathcal{R}_0$ is evaluated with non-locality indulgence, which behaves as a threshold for representing the number of citizens a criminal can influence to indulge in crime. This work recommends stricter policies to catch repeat offenders than first-time offenders. It is

also advised to organize rehabilitation programs for first-time offenders by influencing them to prevent criminal activities and improve their desistance rate for eradicating crime transmission from society. Meanwhile, it is observed that increasing the prison length doesn't have much effect on the threshold condition, on the fractions of criminally active and criminally inactive populations. The fractional order α can be a precautionary measure against crime transmission, punishment of criminals and delay in catching criminals by computing the necessary level of imprisonment by scrutinizing the proposed model to reduce the crime prevailing in society.

8.1.2 AQI Forecasting

The fractional-order gradient-based backpropagation algorithm is utilized to train Vanilla RNN for the AQI prediction of five Indian cities. The proposed approach is used to predict major air pollutants in tier I city, Kolkata. The results of the prediction of AQI of multiple cities and the prediction of air pollutants show that the minimum error on predictions is achieved using fractional order derivative. Most cities achieve better results when the order is equal to $8/9$. The architecture of vanilla RNN is much simpler than the structure/functioning of an LSTM, but the predictions made by RNNs with fractional gradient-based backpropagation are comparable and sometimes even better than LSTM with the integer-order gradient descent algorithm. With simpler architecture, achieving lesser RMSE and MAPE shows the effectiveness of fractional gradient over integer-order gradient descent. Hence, the memory property of fractional derivatives can be well exploited with deep neural networks for dealing with more complex and dynamic data.

8.1.3 Satellite Image Road Segmentation

A dense network with weighted skip connections is proposed to segment roads from high-resolution satellite images. Weights corresponding to the skip connections are determined using Grunwald-Letnikov fractional derivative. Fractional derivatives being non-local, incorporates memory into the system, combining local and global features. This introduces interpretability to the memory exploitation of the network. The proposed network involves the weighted sum of the output of previous layers at a particular transition, unlike basic dense networks where the output of the previous layers is concatenated. Thus the proposed method is computationally efficient. Experiments are performed on two open-source, widely-used benchmark databases $viz.$ Massachusetts Road database (MRD) and Ottawa Road database (ORD). These datasets represent different road topography and network structure, including varying road widths and complexities. Moreover, the performance of

the proposed network is found to be better than other state-of-the-art methods in terms of F1-score and the mean IoU at fractional order 0.4 for MRD and at 0.5 for ORD than the state-of-the-art segmentation results. The results show that the extracted roads are more complete for both databases. Moreover, the model has performed better than other state-of-the-art methods on MRD in terms of higher recall, F1-score, and mean IoU of 0.830, 0.748, and 0.787, respectively. In addition, the model achieved a better mean IoU of 0.9062 that shows an improvement of around 3 % in segmentation results with respect to the state-of-the-art method on ORD. Therefore, it can be concluded that the forward propagation of features has strengthened and lesser loss of information is seen.

8.1.4 Salient Object Detection

A salient object detection network is designed with a densely connected encoder having fractional derivative-based weighted skip connections and a decoder with multiple modules. The weighted skip connections add memory to the system, which prevents the dilution of features due to the increasing network depth. The weighted skip connections and multiple decoder modules has assisted in obtaining the discriminative features required for learning the relationship between multiple salient objects. The network's performance is evaluated at multiple values of fractional order $\alpha < 1$. It is observed that the model is achieving its best performance on a database at different values of fractional order α. The models are aggregated based on F-measure values obtained for a system corresponding to α for diversifying the model predictions. The results show that the salient maps are produced with clear boundaries. The model performs well even in the presence of low contrast and cluttered background and accurately generates the salient maps from the images with multiple objects. Moreover, the proposed network performs better than the other state-of-the-art methods on all six databases with either a higher F-measure or lower MAE. Therefore, it can be concluded that the feature propagation through layers has strengthened, leading to uniform performance across all databases and improvement in the model's generalization capability.

8.1.5 Palmprint Recognition System

A palmprint-based human authentication system is developed using the proposed network FrDPalmNet that generates embeddings with high intra-class similarity and inter-class separability. FrDPalmNet is designed using the theory of fractional optimal control, which

mitigated the issue of short-term memory of the existing integer-order derivative-based networks. The feature vectors generated using FrDPalmNet for each α are matched with all gallery images and the genuine/imposter scores are determined. CRR, EER, DI, and accuracy are computed to analyze the systems' performance. The score files are aggregated based on EER values obtained for a system corresponding to α. The decision is made using multiple learners of the same algorithm, diversifying the model predictions. The proposed approach is validated on CASIA, IIT-D, and Tongji palmprint databases for a thorough evaluation. The proposed system achieved comparable and sometimes even better results than the other methods existing in the literature. Moreover, the system showed uniform accuracy results across all databases. Specifically, the system achieved an accuracy of above 99% and EER below 1% on all considered databases. The rank-1 identification rate is 98.73% for Tongji outperforming the state-of-the-art and above 99% for CASIA and IIT-D. The proposed system's uniform results demonstrate the efficiency and feasibility of its application on other heterogeneous databases acquired using different devices.

8.2 Future Scope of Research

The future scope for the above-mentioned fields is presented in this section. The findings of this research provide valuable insights and contribute to the existing body of knowledge in the field. Based on the observations made in the presented work, the following research prospects arise :

8.2.1 Crime Transmission Modeling

1. **Development of Higher-dimensional Models:** in the actual scenario, a recidivist can commit crimes and be convicted multiple times. To address this with non-locality inherence, the models considering more population sub-classes can be developed by considering more factors affecting crime growth in societies to model crime dynamics accurately.

2. **Criminal Data Validation:** The approaches must be developed for validating the theoretical results through actual criminal data.

8.2.2 AQI Forecasting

1. **Detection of Major Pollutants:** This work can be extended by predicting other air pollutants in the cities and subsequently AQI values can also be predicted. This strategy can detect major air pollutants in a city, and stringent actions can be

taken to prevent further damage. A portfolio of economic activities can be created considering the air quality of the particular city and also detecting the most affecting gases among them in the future.

2. **Complex Architectures:** The current work aims to analyze fractional derivatives' effectiveness in the backpropagation algorithm for training basic ANNs which can be extended to the application on complex architectures.

3. **Generalization of other CNN optimizers :** The stochastic gradient descent algorithm is generalized to a fractional version and applied in time-series forecasting. This can be extended to applying fractional versions of Adam, AdaGrad, RMSProp, and other derivative-based training algorithms.

8.2.3 Satellite Image Road Segmentation

1. **Availability of Large Databases:** The currently available satellite image road databases are smaller, which is insufficient to develop highly accurate models robust to environmental factors such as shadows, occlusions, and varying road widths. Therefore, there is a need to acquire large-sized databases in heterogeneous conditions.

2. **Multi-spectral Data Analysis:** Incorporating multi-spectral data into road segmentation can help improve road detection accuracy, especially in challenging environments, such as urban areas with high building densities. Future research could focus on developing algorithms that effectively use multispectral data for road segmentation.

3. **Application to New Domains:** Road segmentation in satellite images is primarily applied to urban areas, but there are still many other domains where road segmentation could have applications. For instance, road segmentation could be applied to agricultural areas to improve crop yield prediction. Therefore, data should be made available accordingly.

8.2.4 Salient Object Detection

1. **Benchmark Datasets and Evaluation Metrics:** The availability of diverse and challenging benchmark databases and appropriate evaluation metrics is crucial for fair and comprehensive evaluation of salient object detection algorithms. Continuously

developing and maintaining benchmark databases and promoting standardized evaluation protocols will facilitate objective comparisons and drive further advancements in the field.

2. **Real-Time Detection:** This work can be extended to the detection of objects in real-time. The algorithms should be developed on real-time data to apply salient object detection techniques in robotics and autonomous vehicles.

8.2.5 Palmprint Recognition System

1. **Acquisition of Large Databases:** The benchmark databases available for experimentation are smaller than the actual biometric databases for real-world scenarios. Therefore, there is a need to collect a large database for experimentation.

2. **Different Biometric Modalities:** In this work, the human authentication system is developed using palmprint databases. It can be extended to developing systems based on other biometric modalities: Iris, fingerprint, knuckle print, teeth, and forehead.

3. **Multi-modal Systems:** Biometric authentication systems can be classified as Uni-modal or Multi-modal based on the number of modalities considered. Uni-modal systems use only one biometric trait while multi-modal systems use two or more biometric traits together for authentication. However, combining different biometric traits into one system requires fusion which can be done at the sensor, feature, matching score, or decision level. In this work, a recognition technique is proposed for uni-modal systems. It can be extended by combining multiple modalities for recognition.

Comprehensively, some approaches must be explored to apply evolutionary optimization algorithms like PSO, genetic algorithm, or other heuristic algorithms to develop an adaptive method that automatically evaluates the optimal fractional order for a particular model or database. Subsequently, fractional calculus will be an even more powerful tool for modeling and analyzing complex systems in various fields. Its applications are still being explored and are likely to find new avenues.

References

[1] Syed Abbas, Jai Prakash Tripathi, and Aanam Neha. Dynamical analysis of a model of social behavior: Criminal vs non-criminal population. *Chaos, Solitons & Fractals*, 98:121–129, 2017.

[2] Komal Bansal, Trilok Mathur, Narinderjit Singh Sawaran Singh, and Shivi Agarwal. Analysis of illegal drug transmission model using fractional delay differential equations. *AIMS Mathematics*, 7(10):18173–18193, 2022.

[3] Akhil Kumar Srivastav, Mini Ghosh, and Peeyush Chandra. Modeling dynamics of the spread of crime in a society. *Stochastic Analysis and Applications*, 37(6): 991–1011, 2019.

[4] Geetika Arora, Sumit Kalra, Ashutosh Bhatia, and Kamlesh Tiwari. PalmHashNet: Palmprint hashing network for indexing large databases to boost identification. *IEEE Access*, 9:145912–145928, 2021.

[5] Xixi Jia, Sanyang Liu, Xiangchu Feng, and Lei Zhang. FOCNet: A fractional optimal control network for image denoising. In *Proceedings of the IEEE/CVF Conference on Computer Vision and Pattern Recognition*, pages 6054–6063, 2019.

[6] Kaiming He, Xiangyu Zhang, Shaoqing Ren, and Jian Sun. Deep residual learning for image recognition. In *Proceedings of the IEEE Conference on Computer Vision and Pattern Recognition*, pages 770–778, 2016.

[7] Kocherlakota Satya Pritam, Sugandha Arora, Trilok Mathur, and Shivi Agarwal. Underlying dynamics of crime transmission with memory. *Chaos, Solitons & Fractals*, 146:110838, 2021.

[8] Komal Bansal, Sugandha Arora, Kocherlakota Satya Pritam, Trilok Mathur, and

Shivi Agarwal. Dynamics of crime transmission using fractional-order differential equations. *Fractals*, 30(01):2250012, 2022.

[9] Salim Lahmiri. Glioma detection based on multi-fractal features of segmented brain MRI by particle swarm optimization techniques. *Biomedical Signal Processing and Control*, 31:148–155, 2017.

[10] Yichao Zhang, Silvia L Pintea, and Jan C Van Gemert. Video acceleration magnification. In *Proceedings of the IEEE Conference on Computer Vision and Pattern Recognition*, pages 529–537, 2017.

[11] Shoichiro Takeda, Kazuki Okami, Dan Mikami, Megumi Isogai, and Hideaki Kimata. Jerk-aware video acceleration magnification. In *Proceedings of the IEEE Conference on Computer Vision and Pattern Recognition*, pages 1769–1777, 2018.

[12] Shoichiro Takeda, Yasunori Akagi, Kazuki Okami, Megumi Isogai, and Hideaki Kimata. Video magnification in the wild using fractional anisotropy in temporal distribution. In *Proceedings of the IEEE Conference on Computer Vision and Pattern Recognition*, pages 1614–1622, 2019.

[13] Ming-Ming Cheng, Niloy J Mitra, Xiaolei Huang, Philip HS Torr, and Shi-Min Hu. Global contrast based salient region detection. *IEEE Transactions on Pattern Analysis and Machine Intelligence*, 37(3):569–582, 2014.

[14] Xuebin Qin, Zichen Zhang, Chenyang Huang, Chao Gao, Masood Dehghan, and Martin Jagersand. BASNet: Boundary-aware salient object detection. In *Proceedings of the IEEE/CVF Conference on Computer Vision and Pattern Recognition*, pages 7479–7489, 2019.

[15] Lu Zhang, Ju Dai, Huchuan Lu, You He, and Gang Wang. A bi-directional message passing model for salient object detection. In *Proceedings of the IEEE Conference on Computer Vision and Pattern Recognition*, pages 1741–1750, 2018.

[16] Shuhan Chen, Xiuli Tan, Ben Wang, and Xuelong Hu. Reverse attention for salient object detection. In *Proceedings of the European Conference on Computer Vision*, pages 234–250, 2018.

[17] Nian Liu, Junwei Han, and Ming-Hsuan Yang. PiCANet: Learning pixel-wise contextual attention for saliency detection. In *Proceedings of the IEEE Conference on Computer Vision and Pattern Recognition*, pages 3089–3098, 2018.

[18] Zhenan Sun, Tieniu Tan, Yunhong Wang, and Stan Z Li. Ordinal palmprint representation for personal identification. In *Proceedings of the IEEE Conference on Computer Vision and Pattern Recognition*, pages 279–284, 2005.

[19] Ajay Kumar. Incorporating cohort information for reliable palmprint authentication. In *Proceedings of the 6th Indian Conference on Computer Vision, Graphics & Image Processing*, pages 583–590. IEEE, 2008.

[20] Lin Zhang, Lida Li, Anqi Yang, Ying Shen, and Meng Yang. Towards contactless palmprint recognition: A novel device, a new benchmark, and a collaborative representation based identification approach. *Pattern Recognition*, 69:199–212, 2017.

[21] Igor Podlubny. Fractional-order systems and fractional-order controllers. *Institute of Experimental Physics, Slovak Academy of Sciences, Kosice*, 12(3):1–18, 1994.

[22] Nicole Heymans and J-C Bauwens. Fractal rheological models and fractional differential equations for viscoelastic behavior. *Rheologica Acta*, 33(3):210–219, 1994.

[23] Lei Song, Shiyun Xu, and Jianying Yang. Dynamical models of happiness with fractional order. *Communications in Nonlinear Science and Numerical Simulation*, 15(3):616–628, 2010.

[24] Ralf Metzler and Joseph Klafter. The random walk's guide to anomalous diffusion: A fractional dynamics approach. *Physics Reports*, 339(1):1–77, 2000.

[25] Bruce Ian Henry and Susan L Wearne. Existence of turing instabilities in a two-species fractional reaction-diffusion system. *SIAM Journal on Applied Mathematics*, 62(3):870–887, 2002.

[26] Giulio Cottone, Mario Di Paola, and Roberta Santoro. A novel exact representation of stationary colored Gaussian processes (fractional differential approach). *Journal of Physics A: Mathematical and Theoretical*, 43(8):085002, 2010.

[27] Nobumasa Sugimoto. Burgers equation with a fractional derivative; hereditary effects on nonlinear acoustic waves. *Journal of Fluid Mechanics*, 225:631–653, 1991.

[28] Nader Engheia. On the role of fractional calculus in electromagnetic theory. *IEEE Antennas and Propagation Magazine*, 39(4):35–46, 1997.

[29] Francesco Mainardi. Fractional relaxation-oscillation and fractional diffusion-wave phenomena. *Chaos, Solitons & Fractals*, 7(9):1461–1477, 1996.

[30] Mitsunojo Ichise, Yutaka Nagayanagi, and Tsugio Kojima. An analog simulation of non-integer order transfer functions for analysis of electrode processes. *Journal of Electroanalytical Chemistry and Interfacial Electrochemistry*, 33(2):253–265, 1971.

[31] Edgar Reyes-Melo, Jorge Martinez-Vega, Carlos Guerrero-Salazar, and Ubaldo Ortiz-Mendez. Application of fractional calculus to the modeling of dielectric relaxation phenomena in polymeric materials. *Journal of Applied Polymer Science*, 98(2):923–935, 2005.

[32] Hong Guang Sun, Wen Chen, and Yang Quan Chen. Variable-order fractional differential operators in anomalous diffusion modeling. *Physica A: Statistical Mechanics and its Applications*, 388(21):4586–4592, 2009.

[33] Peter J Torvik and Ronald L Bagley. On the appearance of the fractional derivative in the behavior of real materials. *Journal of Applied Mechanics*, 51(2):294–298, 1984.

[34] Richard L Magin. Fractional calculus models of complex dynamics in biological tissues. *Computers & Mathematics with Applications*, 59(5):1586–1593, 2010.

[35] Alvaro Cartea and Diego del Castillo-Negrete. Fractional diffusion models of option prices in markets with jumps. *Physica A: Statistical Mechanics and its Applications*, 374(2):749–763, 2007.

[36] Wen Chen, Hong Guang Sun, Xiaodi Zhang, and Dean Korošak. Anomalous diffusion modeling by fractal and fractional derivatives. *Computers & Mathematics with Applications*, 59(5):1754–1758, 2010.

[37] Ahmed MA El-Sayed, SZ Rida, and Anas AM Arafa. On the solutions of time-fractional bacterial chemotaxis in a diffusion gradient chamber. *International Journal of Nonlinear Science*, 7(4):485–492, 2009.

[38] Qi Yang, Dali Chen, Tiebiao Zhao, and Yang Quan Chen. Fractional calculus in image processing: A review. *Fractional Calculus and Applied Analysis*, 19(5): 1222–1249, 2016.

[39] Hu Wang, Yongguang Yu, Guoguang Wen, Shuo Zhang, and Junzhi Yu. Global stability analysis of fractional-order Hopfield neural networks with time delay. *Neurocomputing*, 154:15–23, 2015.

[40] Kenneth S Miller and Bertram Ross. *An introduction to the fractional calculus and fractional differential equations*. Wiley, 1993.

[41] Michele Caputo. Linear models of dissipation whose q is almost frequency independent—ii. *Geophysical Journal International*, 13(5):529–539, 1967.

[42] Mark Edelman. Fractional maps as maps with power-law memory. In *Nonlinear Dynamics and Complexity*, pages 79–120. Springer, 2014.

[43] Mark Edelman. Universality in systems with power-law memory and fractional dynamics. *Chaotic, Fractional, and Complex Dynamics: New Insights and Perspectives*, pages 147–171, 2018.

[44] Muhammad Farman, Ali Akgül, Saud Fahad Aldosary, Kottakkaran Sooppy Nisar, and Aqeel Ahmad. Fractional order model for complex Layla and Majnun love story with chaotic behavior. *Alexandria Engineering Journal*, 61(9):6725–6738, 2022.

[45] Carlos A Valentim Jr, Naila A Oliveira, José A Rabi, and Sergio A David. Can fractional calculus help improve tumor growth models? *Journal of Computational and Applied Mathematics*, 379:112964, 2020.

[46] Martin Burger, Luis Caffarelli, and Peter A Markowich. Partial differential equation models in the socio-economic sciences. *Philosophical Transactions of the Royal Society A: Mathematical, Physical and Engineering Sciences*, 372(2028):20130406, 2014.

[47] Ndolane Sene. SIR epidemic model with Mittag–Leffler fractional derivative. *Chaos, Solitons & Fractals*, 137:109833, 2020.

[48] Kai Velten. *Mathematical modeling and simulation: Introduction for scientists and engineers*. John Wiley & Sons, 2009.

[49] Yan Li, Yang Quan Chen, and Igor Podlubny. Stability of fractional-order nonlinear dynamic systems: Lyapunov direct method and generalized Mittag–Leffler stability. *Computers & Mathematics with Applications*, 59(5):1810–1821, 2010.

[50] Denis Matignon. Stability results for fractional differential equations with applications to control processing. In *Computational Engineering in Systems Applications*, volume 2, pages 963–968. Citeseer, 1996.

[51] Ahmed E Sayed, Ahmed MA El-Sayed, and Hala AA El-Saka. On some Routh–Hurwitz conditions for fractional order differential equations and their applications in Lorenz, Rössler, Chua and Chen systems. *Physics Letters A*, 358(1):1–4, 2006.

[52] Ahmed Sayed E, Ahmed MA El-Sayed, and Hala AA El-Saka. Equilibrium points, stability and numerical solutions of fractional-order predator–prey and rabies models. *Journal of Mathematical Analysis and Applications*, 325(1):542–553, 2007.

[53] Hadi Delavari, Dumitru Baleanu, and Jalil Sadati. Stability analysis of Caputo fractional-order nonlinear systems revisited. *Nonlinear Dynamics*, 67(4):2433–2439, 2012.

[54] Lotfi A Zadeh. Foreword: Fuzzy logic. *Journal of Intelligent Information Systems*, 2(4):309–310, 1993.

[55] Wen Jiang, De-Shuang Huang, and Shenghong Li. Random walk-based solution to triple level stochastic point location problem. *IEEE Transactions on Cybernetics*, 46(6):1438–1451, 2015.

[56] Zhan-Li Sun, De-Shuang Huang, and Yiu-Ming Cheun. Extracting nonlinear features for multispectral images by FCMC and KPCA. *Digital Signal Processing*, 15(4):331–346, 2005.

[57] Bo Li, De-Shuang Huang, Chao Wang, and Kun-Hong Liu. Feature extraction using constrained maximum variance mapping. *Pattern Recognition*, 41(11):3287–3294, 2008.

[58] Li Shang, De-Shuang Huang, Chun-Hou Zheng, and Zhan-Li Sun. Noise removal using a novel non-negative sparse coding shrinkage technique. *Neurocomputing*, 69 (7-9):874–877, 2006.

[59] David E Rumelhart, Geoffrey E Hinton, and Ronald J Williams. Learning representations by back-propagating errors. *Cognitive Modeling*, 5(3):1, 1988.

[60] Andreas Zell. *Simulation of neural networks*, volume 1. Addison-Wesley Bonn, 1994.

[61] Shun-Ichi Amari. Learning patterns and pattern sequences by self-organizing nets of threshold elements. *IEEE Transactions on Computers*, 100(11):1197–1206, 1972.

[62] Mark A Kramer. Autoassociative neural networks. *Computers & Chemical Engineering*, 16(4):313–328, 1992.

[63] Klaus Greff, Rupesh K Srivastava, Jan Koutník, Bas R Steunebrink, and Jürgen Schmidhuber. LSTM: A search space odyssey. *IEEE Transactions on Neural Networks and Learning Systems*, 28(10):2222–2232, 2016.

[64] Yann LeCun, Léon Bottou, Yoshua Bengio, and Patrick Haffner. Gradient-based learning applied to document recognition. *Proceedings of the IEEE*, 86(11):2278–2324, 1998.

[65] Alex Krizhevsky, Ilya Sutskever, and Geoffrey E Hinton. Imagenet classification with deep convolutional neural networks. *Communications of the ACM*, 60(6): 84–90, 2017.

[66] Karen Simonyan and Andrew Zisserman. Very deep convolutional neural networks for large-scale image recognition. In *Proceedings of the International Conference on Learning Representations*, pages 25–27, 2013.

[67] Xiao-Feng Wang, De-Shuang Huang, and Huan Xu. An efficient local Chan–Vese model for image segmentation. *Pattern Recognition*, 43(3):603–618, 2010.

[68] David Marr. *Vision: A computational investigation into the human representation and processing of visual information*. W.H. Freeman and Company, 1982.

[69] Fernando J Pineda. Dynamics and architecture for neural computation. *Journal of Complexity*, 4(3):216–245, 1988.

[70] E Weinan. A proposal on machine learning via dynamical systems. *Communications in Mathematics and Statistics*, 1(5):1–11, 2017.

[71] Jack Macki and Aaron Strauss. *Introduction to optimal control theory*. Springer Science & Business Media, 2012.

[72] Igor Podlubny. Fractional-order systems and $PI^{\lambda} D^{\mu}$-controllers. *IEEE Transactions on Automatic Control*, 44(1):208–214, 1999.

[73] Hegagi M Ali, Fernando Lobo Pereira, and Sílvio MA Gama. A new approach to the Pontryagin maximum principle for nonlinear fractional optimal control problems. *Mathematical Methods in the Applied Sciences*, 39(13):3640–3649, 2016.

[74] Qianxiao Li, Long Chen, Cheng Tai, et al. Maximum principle based algorithms for deep learning. *Journal of Machine Learning Research*, 18:1–29, 2018.

[75] Yarens J Cruz, Marcelino Rivas, Ramón Quiza, Rodolfo E Haber, Fernando Castaño, and Alberto Villalonga. A two-step machine learning approach for dynamic model selection: A case study on a micro milling process. *Computers in Industry*, 143: 103764, 2022.

[76] Randi Hjalmarsson and Matthew J Lindquist. Like godfather, like son exploring the intergenerational nature of crime. *Journal of Human Resources*, 47(2):550–582, 2012.

[77] Sytske Besemer. *Intergenerational transmission of criminal and violent behaviour*. Sidestone Press, 2012.

[78] Mark L Howe and Lauren M Knott. The fallibility of memory in judicial processes: Lessons from the past and their modern consequences. *Memory*, 23(5):633–656, 2015.

[79] David McMillon, Carl P Simon, and Jeffrey Morenoff. Modeling the underlying dynamics of the spread of crime. *PloS one*, 9(4):e88923, 2014.

[80] Shoou-Jiun Wang, Rajan Batta, and Christopher M Rump. Stability of a crime level equilibrium. *Socio-Economic Planning Sciences*, 39(3):229–244, 2005.

[81] Martin B Short, P Jeffrey Brantingham, and Maria R D'orsogna. Cooperation and punishment in an adversarial game: How defectors pave the way to a peaceful society. *Physical Review E*, 82(6):066114, 2010.

[82] Igor Podlubny. *Fractional Differential Equations, Mathematics in Science and Engineering*, volume 198. Academic press New York, 1999.

[83] Yi Fei Pu, Zhang Yi, and Ji Liu Zhou. Fractional Hopfield neural networks: Fractional dynamic associative recurrent neural networks. *IEEE Transactions on Neural Networks and Learning Systems*, 28(10):2319–2333, 2016.

[84] Jian Wang, Yanqing Wen, Yida Gou, Zhenyun Ye, and Hua Chen. Fractional-order gradient descent learning of BP neural networks with Caputo derivative. *Neural Networks*, 89:19–30, 2017.

[85] Shujaat Khan, Jawwad Ahmad, Imran Naseem, and Muhammad Moinuddin. A novel fractional gradient-based learning algorithm for recurrent neural networks. *Circuits, Systems, and Signal Processing*, 37(2):593–612, 2018.

[86] X Chen. Application of fractional calculus in back propagation neural networks [Ph.D Thesis]. *Nanjing Forestry University, Nanjing, Jiangsu*, 2013.

[87] Yi Fei Pu, Ji Liu Zhou, Yi Zhang, Ni Zhang, Guo Huang, and Patrick Siarry. Fractional extreme value adaptive training method: Fractional steepest descent approach. *IEEE Transactions on Neural Networks and Learning Systems*, 26(4): 653–662, 2013.

[88] Yuquan Chen, Qing Gao, Yiheng Wei, and Yong Wang. Study on fractional order gradient methods. *Applied Mathematics and Computation*, 314:310–321, 2017.

[89] Beijing Chen, Ming Yu, Qingtang Su, Hiuk Jae Shim, and Yun-Qing Shi. Fractional quaternion Zernike moments for robust color image copy-move forgery detection. *IEEE Access*, 6:56637–56646, 2018.

[90] Shujaat Khan, Imran Naseem, Muhammad Ammar Malik, Roberto Togneri, and Mohammed Bennamoun. A fractional gradient descent-based RBF neural network. *Circuits, Systems, and Signal Processing*, 37(12):5311–5332, 2018.

[91] Chunhui Bao, Yi Fei Pu, and Yi Zhang. Fractional-order deep backpropagation neural network. *Computational Intelligence and Neuroscience*, 2018:1–10, 2018.

[92] Dian Sheng, Yiheng Wei, Yuquan Chen, and Yong Wang. Convolutional neural networks with fractional order gradient method. *Neurocomputing*, 408:42–50, 2020.

[93] Anil K Shukla, Rajesh K Pandey, and Ram Bilas Pachori. A fractional filter based efficient algorithm for retinal blood vessel segmentation. *Biomedical Signal Processing and Control*, 59:101883, 2020.

[94] Anil K Shukla, Rajesh K Pandey, Swati Yadav, and Ram Bilas Pachori. Generalized fractional filter-based algorithm for image denoising. *Circuits, Systems, and Signal Processing*, 39(1):363–390, 2020.

[95] Kanwarpreet Kaur, Neeru Jindal, and Kulbir Singh. Fractional Fourier transform based Riesz fractional derivative approach for edge detection and its application in image enhancement. *Signal Processing*, 180:107852, 2021.

[96] Kanwarpreet Kaur, Neeru Jindal, and Kulbir Singh. Fractional derivative based unsharp masking approach for enhancement of digital images. *Multimedia Tools and Applications*, 80(3):3645–3679, 2021.

[97] A Oustaloup, B Mathieu, and P Melchior. Robust edge detector of noninteger order: The CRONE detector. *8th CongrÂes de CytomÃetrie en Flux et d'Analyse d'lmage*, 1991.

[98] A Oustaloup, B Mathieu, and P Melchior. Edge detection using non-integer derivation. In *IEEE European Conference on Circuit Theory and Design*, pages 3–6, 1991.

[99] Pedram Ghamisi, Micael S Couceiro, and Jon Atli Benediktsson. Extending the fractional order Darwinian particle swarm optimization to segmentation of hyperspectral images. In *Image and Signal Processing for Remote Sensing XVIII*, volume 8537, page 85370F. International Society for Optics and Photonics, 2012.

[100] Pedram Ghamisi, Micael S Couceiro, Fernando ML Martins, and Jon Atli Benediktsson. Multilevel image segmentation based on fractional-order Darwinian particle swarm optimization. *IEEE Transactions on Geoscience and Remote sensing*, 52(5): 2382–2394, 2013.

[101] Pedram Ghamisi, Micael S Couceiro, Mathieu Fauvel, and Jon Atli Benediktsson. Integration of segmentation techniques for classification of hyperspectral images. *IEEE Geoscience and Remote Sensing Letters*, 11(1):342–346, 2013.

[102] Dalia Yousri, Mohamed Abd Elaziz, and Seyedali Mirjalili. Fractional-order calculus-based flower pollination algorithm with local search for global optimization and image segmentation. *Knowledge-Based Systems*, 197:105889, 2020.

[103] Amir Hossein Gandomi, Xin-She Yang, and Amir Hossein Alavi. Cuckoo Search Algorithm: A metaheuristic approach to solve structural optimization problems. *Engineering with Computers*, 29(1):17–35, 2013.

[104] Seyedali Mirjalili, Seyed Mohammad Mirjalili, and Andrew Lewis. Grey wolf optimizer. *Advances in Engineering Software*, 69:46–61, 2014.

[105] Seyedali Mirjalili, Amir H Gandomi, Seyedeh Zahra Mirjalili, Shahrzad Saremi, Hossam Faris, and Seyed Mohammad Mirjalili. Salp Swarm Algorithm: A bio-inspired optimizer for engineering design problems. *Advances in Engineering Software*, 114:163–191, 2017.

[106] JE Solís-Pérez, José Francisco Gómez-Aguilar, Ricardo Fabricio Escobar-Jiménez, and Juan Reyes-Reyes. Blood vessel detection based on fractional Hessian matrix with non-singular Mittag–Leffler Gaussian kernel. *Biomedical Signal Processing and Control*, 54:101584, 2019.

[107] Attila Budai, Rüdiger Bock, Andreas Maier, Joachim Hornegger, and Georg Michelson. Robust vessel segmentation in fundus images. *International Journal of Biomedical Imaging*, 2013, 2013.

[108] Adam Hoover, Valentina Kouznetsova, and Michael Goldbaum. Locating blood vessels in retinal images by piecewise threshold probing of a matched filter response. *IEEE Transactions on Medical Imaging*, 19(3):203–210, 2000.

[109] Joes Staal, Michael D Abràmoff, Meindert Niemeijer, Max A Viergever, and Bram Van Ginneken. Ridge-based vessel segmentation in color images of the retina. *IEEE Transactions on Medical Imaging*, 23(4):501–509, 2004.

[110] Hugo Aguirre-Ramos, Juan Gabriel Avina-Cervantes, Ivan Cruz-Aceves, José Ruiz-Pinales, and Sergio Ledesma. Blood vessel segmentation in retinal fundus images

using Gabor filters, fractional derivatives, and expectation maximization. *Applied Mathematics and Computation*, 339:568–587, 2018.

[111] Zemin Ren. Adaptive active contour model driven by fractional order fitting energy. *Signal Processing*, 117:138–150, 2015.

[112] Tony F Chan and Luminita A Vese. Active contours without edges. *IEEE Transactions on Image Processing*, 10(2):266–277, 2001.

[113] Chunming Li, Chiu-Yen Kao, John C Gore, and Zhaohua Ding. Implicit active contours driven by local binary fitting energy. In *Proceedings of the IEEE Conference on Computer Vision and Pattern Recognition*, pages 1–7. IEEE, 2007.

[114] Kaihua Zhang, Lei Zhang, Kin-Man Lam, and David Zhang. A level set approach to image segmentation with intensity inhomogeneity. *IEEE Transactions on Cybernetics*, 46(2):546–557, 2015.

[115] Bo Chen, Shan Huang, Zhengrong Liang, Wensheng Chen, and Binbin Pan. A fractional order derivative based active contour model for inhomogeneous image segmentation. *Applied Mathematical Modelling*, 65:120–136, 2019.

[116] Kaihua Zhang, Lei Zhang, Huihui Song, and Wengang Zhou. Active contours with selective local or global segmentation: A new formulation and level set method. *Image and Vision Computing*, 28(4):668–676, 2010.

[117] Nobuyuki Otsu. A threshold selection method from gray-level histograms. *IEEE Transactions on Systems, Man, and Cybernetics*, 9(1):62–66, 1979.

[118] Pedram Ghamisi, Micael S Couceiro, JóN Atli Benediktsson, and Nuno MF Ferreira. An efficient method for segmentation of images based on fractional calculus and natural selection. *Expert Systems with Applications*, 39(16):12407–12417, 2012.

[119] Dan Tian, Dingyu Xue, Dali Cheri, and Shenshen Sun. A fractional-order regulatory CV model for brain MR image segmentation. In *Proceedings of the 25th Chinese Control and Decision Conference*, pages 37–40. IEEE, 2013.

[120] Phenlan Lin, Po W Huang, Poying Huang, and Hui C Hsu. Alveolar bone-loss area localization in periodontitis radiographs based on threshold segmentation with a hybrid feature fused of intensity and the H-value of fractional Brownian motion model. *Computer Methods and Programs in Biomedicine*, 121(3):117–126, 2015.

[121] Jason Tillett, TM Rao, Ferat Sahin, and Raghuveer Rao. Darwinian particle swarm optimization. In *Proceedings of the 2nd Indian International Conference on Artificial Intelligence*, pages 1474—-1487, 2005.

[122] Micael S Couceiro, NM Ferreira, and JA Tenreiro Machado. Fractional order Darwinian particle swarm optimization. In *3rd Symposium on Fractional Signals and Systems*, pages 127–136, 2011.

[123] Francisco das Chagas Fontenele Marques Junior, Thelmo Pontes de Araujo, José Vigno Moura Sousa, Nator Junior Carvalho da Costa, Rodrigo Teixeira Melo, Alano Martins Pinto, and Arata Andrade Saraiva. Recognition of simple handwritten polynomials using segmentation with fractional calculus and convolutional neural networks. In *8th Brazilian Conference on Intelligent Systems*, pages 245–250. IEEE, 2019.

[124] Jian Bai and Xiang-Chu Feng. Fractional-order anisotropic diffusion for image denoising. *IEEE Transactions on Image Processing*, 16(10):2492–2502, 2007.

[125] Ashish Vaswani, Noam Shazeer, Niki Parmar, Jakob Uszkoreit, Llion Jones, Aidan N Gomez, Łukasz Kaiser, and Illia Polosukhin. Attention is all you need. *Advances in Neural Information Processing Systems*, 30, 2017.

[126] Wenhui Wang, Hangbo Bao, Li Dong, Johan Bjorck, Zhiliang Peng, Qiang Liu, Kriti Aggarwal, Owais Khan Mohammed, Saksham Singhal, Subhojit Som, et al. Image as a foreign language: BEiT pretraining for vision and vision-language tasks. In *Proceedings of the IEEE/CVF Conference on Computer Vision and Pattern Recognition*, pages 19175–19186, 2023.

[127] Jitesh Jain, Jiachen Li, Mang Tik Chiu, Ali Hassani, Nikita Orlov, and Humphrey Shi. OneFormer: One transformer to rule universal image segmentation. In *Proceedings of the IEEE/CVF Conference on Computer Vision and Pattern Recognition*, pages 2989–2998, 2023.

[128] Jian Guan, X-L Chen, Yong Huang, and You He. Adaptive fractional Fourier transform-based detection algorithm for moving target in heavy sea clutter. *IET Radar, Sonar & Navigation*, 6(5):389–401, 2012.

[129] You He, Jian Guan, Ying Ning Peng, et al. Automatic radar detection and CFAR processing. Beijing: Tsinghua University Press, 1999.

[130] Xiaohan Yu, Xiaolong Chen, Yong Huang, and Jian Guan. Sparse fractional Fourier transform and its applications in radar moving target detection. In *International Conference on Radar (RADAR)*, pages 1–5. IEEE, 2018.

[131] Avinash Ratre and Vinod Pankajakshan. Tucker visual search-based hybrid tracking model and fractional Kohonen self-organizing map for anomaly localization and detection in surveillance videos. *The Imaging Science Journal*, 66(4):195–210, 2018.

[132] Xing Hu, Shiqiang Hu, Yingping Huang, Huanlong Zhang, and Hanbing Wu. Video anomaly detection using deep incremental slow feature analysis network. *IET Computer Vision*, 10(4):258–267, 2016.

[133] Sindhia Lingaswamy and Dhananjay Kumar. An efficient moving object detection and tracking system based on fractional derivative. *Multimedia Tools and Applications*, 79(13):8519–8537, 2020.

[134] Vincent Christlein, Christian Riess, Johannes Jordan, Corinna Riess, and Elli Angelopoulou. An evaluation of popular copy-move forgery detection approaches. *IEEE Transactions on Information Forensics and Security*, 7(6):1841–1854, 2012.

[135] Davide Cozzolino, Giovanni Poggi, and Luisa Verdoliva. Efficient dense-field copy–move forgery detection. *IEEE Transactions on Information Forensics and Security*, 10(11):2284–2297, 2015.

[136] Xiuli Bi, Chi-Man Pun, and Xiao-Chen Yuan. Adaptive polar based filtering method for image copy-move forgery detection. In *Trustcom/BigDataSE/ISPA*, pages 952–956. IEEE, 2016.

[137] Mohsen Zandi, Ahmad Mahmoudi-Aznaveh, and Alireza Talebpour. Iterative copy-move forgery detection based on a new interest point detector. *IEEE Transactions on Information Forensics and Security*, 11(11):2499–2512, 2016.

[138] Xiuli Bi and Chi-Man Pun. Fast copy-move forgery detection using local bidirectional coherency error refinement. *Pattern Recognition*, 81:161–175, 2018.

[139] Shengheng Liu, Tao Shan, Ran Tao, Yimin D Zhang, Guo Zhang, Feng Zhang, and Yue Wang. Sparse discrete fractional Fourier transform and its applications. *IEEE Transactions on Signal Processing*, 62(24):6582–6595, 2014.

[140] K S Raghunandan, Palaiahnakote Shivakumara, Hamid A Jalab, Rabha W Ibrahim, G Hemantha Kumar, Umapada Pal, and Tong Lu. Riesz fractional based model for enhancing license plate detection and recognition. *IEEE Transactions on Circuits and Systems for Video Technology*, 28(9):2276–2288, 2017.

[141] Dimosthenis Karatzas, Lluis Gomez-Bigorda, Anguelos Nicolaou, Suman Ghosh, Andrew Bagdanov, Masakazu Iwamura, Jiri Matas, Lukas Neumann, Vijay Ramaseshan Chandrasekhar, Shijian Lu, Faisal Shafait, Seiichi Uchida, and Ernest Valveny. ICDAR competition on robust reading. In *13th International Conference on Document Analysis and Recognition*, pages 1156–1160. IEEE, 2015.

[142] Chien-Yao Wang, Alexey Bochkovskiy, and Hong-Yuan Mark Liao. Scaled-YOLOv4: Scaling cross stage partial network. In *Proceedings of the IEEE/CVF Conference on Computer Vision and Pattern Recognition*, pages 13029–13038, 2021.

[143] Tsung-Yi Lin, Michael Maire, Serge Belongie, James Hays, Pietro Perona, Deva Ramanan, Piotr Dollár, and C Lawrence Zitnick. Microsoft COCO: Common objects in context. In *European Conference on Computer Vision*, pages 740–755. Springer, 2014.

[144] Zixuan Xu, Banghuai Li, Ye Yuan, and Anhong Dang. Beta R-CNN: Looking into pedestrian detection from another perspective. *Advances in Neural Information Processing Systems*, 33:19953–19963, 2020.

[145] Joseph Redmon, Santosh Divvala, Ross Girshick, and Ali Farhadi. You only look once: Unified, real-time object detection. In *Proceedings of the IEEE Conference on Computer Vision and Pattern Recognition*, pages 779–788, 2016.

[146] Tsung-Yi Lin, Priya Goyal, Ross Girshick, Kaiming He, and Piotr Dollár. Focal loss for dense object detection. In *Proceedings of the IEEE International Conference on Computer Vision*, pages 2980–2988, 2017.

[147] Ross Girshick. Fast R-CNN. In *Proceedings of the IEEE International Conference on Computer Vision*, pages 1440–1448, 2015.

[148] Jian-Xun Mi, De-Shuang Huang, Bing Wang, and Xingjie Zhu. The nearest-farthest subspace classification for face recognition. *Neurocomputing*, 113:241–250, 2013.

[149] Zhong-Qiu Zhao, De-Shuang Huang, and Wei Jia. Palmprint recognition with 2DPCA+ PCA based on modular neural networks. *Neurocomputing*, 71(1-3): 448–454, 2007.

[150] Yun-Hao Yuan, Quan-Sen Sun, and Hong-Wei Ge. Fractional-order embedding canonical correlation analysis and its applications to multi-view dimensionality reduction and recognition. *Pattern Recognition*, 47(3):1411–1424, 2014.

[151] Dhirendra Kumar and Naveen K Nishchal. Three-dimensional object recognition using joint fractional Fourier transform correlators with the help of digital Fresnel holography. *Optik*, 126(20):2690–2695, 2015.

[152] Jun Liu, Songcan Chen, and Xiaoyang Tan. Fractional order singular value decomposition representation for face recognition. *Pattern Recognition*, 41(1):378–395, 2008.

[153] Chengjun Liu. Gabor-based kernel PCA with fractional power polynomial models for face recognition. *IEEE Transactions on Pattern Analysis and Machine Intelligence*, 26(5):572–581, 2004.

[154] Jun-Bao Li. Gabor filter based optical image recognition using fractional power polynomial model based common discriminant locality preserving projection with kernels. *Optics and Lasers in Engineering*, 50(9):1281–1286, 2012.

[155] Xiao-Yuan Jing, Hau-San Wong, and David Zhang. Face recognition based on discriminant fractional Fourier feature extraction. *Pattern Recognition Letters*, 27 (13):1465–1471, 2006.

[156] P Jonathon Phillips, Harry Wechsler, Jeffery Huang, and Patrick J Rauss. The FERET database and evaluation procedure for face-recognition algorithms. *Image and Vision Computing*, 16(5):295–306, 1998.

[157] Terence Sim, Simon Baker, and Maan Bsat. The CMU Pose, Illumination, and Expression (PIE) database. In *Proceedings of 5th IEEE International Conference on Automatic Face Gesture Recognition*, pages 53–58. IEEE, 2002.

[158] Ferdinando S Samaria and Andy C Harter. Parameterisation of a stochastic model for human face identification. In *Proceedings of IEEE Workshop on Applications of Computer Vision*, pages 138–142. IEEE, 1994.

[159] AM Martinez and R Benavente. *The AR Face Database: CVC Technical Report 24*. 1998.

[160] Peter N. Belhumeur, Joao P Hespanha, and David J. Kriegman. Eigenfaces vs. fisherfaces: Recognition using class specific linear projection. *IEEE Transactions on Pattern Analysis and Machine Intelligence*, 19(7):711–720, 1997.

[161] AT&T Laboratories Cambridge. The database of faces, 2002. URL http://www.cl.cam.ac.uk/research/dtg/attarchive/facedatabase.html.

[162] Sameer A Nene, Shree K Nayar, Hiroshi Murase, et al. Columbia Object Image Library (COIL-100), 1996.

[163] Rachid Benouini, Imad Batioua, Khalid Zenkouar, Azeddine Zahi, Said Najah, and Hassan Qjidaa. Fractional-order orthogonal Chebyshev moments and moment invariants for image representation and pattern recognition. *Pattern Recognition*, 86:332–343, 2019.

[164] Mario Döller and Harald Kosch. The MPEG-7 multimedia database system (MPEG-7 MMDB). *Journal of Systems and Software*, 81(9):1559–1580, 2008.

[165] Parminder Kaur, Husanbir Singh Pannu, and Avleen Kaur Malhi. Plant disease recognition using fractional-order Zernike moments and SVM classifier. *Neural Computing and Applications*, 31(12):8749–8768, 2019.

[166] Lin Hu and Jian Cui. Digital image recognition based on fractional-order-PCA-SVM coupling algorithm. *Measurement*, 145:150–159, 2019.

[167] Bin Xiao, Linping Li, Yu Li, Weisheng Li, and Guoyin Wang. Image analysis by fractional-order orthogonal moments. *Information Sciences*, 382:135–149, 2017.

[168] Xiaohua Zhai, Alexander Kolesnikov, Neil Houlsby, and Lucas Beyer. Scaling vision transformers. In *Proceedings of the IEEE/CVF Conference on Computer Vision and Pattern Recognition*, pages 12104–12113, 2022.

[169] Hugo Touvron, Andrea Vedaldi, Matthijs Douze, and Hervé Jégou. Fixing the train-test resolution discrepancy. *Advances in Neural Information Processing Systems*, 32, 2019.

[170] Mauro Costantini, Iris Meco, and Antonio Paradiso. Do inequality, unemployment and deterrence affect crime over the long run? *Regional Studies*, 52(4):558–571, 2018.

[171] John A Gardiner. Research models in law enforcement and criminal justice. *Law & Society Review*, 6(2):223–230, 1971.

[172] James Q Wilson and George L Kelling. Broken windows. *Atlantic Monthly*, 249(3): 29–38, 1982.

[173] Alex R Piquero, David P Farrington, and Alfred Blumstein. *Key issues in criminal career research: New analyses of the Cambridge Study in Delinquent Development*. Cambridge University Press, 2007.

[174] Steven N Durlauf and Daniel S Nagin. Imprisonment and crime: Can both be reduced? *Criminology & Public Policy*, 10(1):13–54, 2011.

[175] Patricia Brantingham, Uwe Glässer, Piper Jackson, and Mona Vajihollahi. Modeling criminal activity in urban landscapes. In *Mathematical Methods in Counterterrorism*, pages 9–31. Springer, 2009.

[176] Marcus Felson. What every mathematician should know about modelling crime. *European Journal of Applied Mathematics*, 21(4-5):275–281, 2010.

[177] KA Jane White, Eduard Campillo-Funollet, Farai Nyabadza, Davide Cusseddu, Christian Kasumo, Nancy Matendechere Imbusi, Victor Ogesa Juma, Ammon J Meir, and Theresia Marijani. Towards understanding crime dynamics in a heterogeneous environment: A mathematical approach. *Journal of Interdisciplinary Mathematics*, pages 1–21, 2021.

[178] Joanna Sooknanan, Balswaroop Bhatt, and Donna MG Comissiong. Another way of thinking: A review of mathematical models of crime. *Math Today*, 131, 2013.

[179] David JB Lloyd and Hayley O'Farrell. On localised hotspots of an urban crime model. *Physica D: Nonlinear Phenomena*, 253:23–39, 2013.

[180] Martin B Short, Andrea L Bertozzi, and P Jeffrey Brantingham. Nonlinear patterns in urban crime: Hotspots, bifurcations, and suppression. *SIAM Journal on Applied Dynamical Systems*, 9(2):462–483, 2010.

[181] Yasaman Dehghani Abbasi, Martin Short, Arunesh Sinha, Nicole Sintov, Chao Zhang, and Milind Tambe. Human adversaries in opportunistic crime security games: Evaluating competing bounded rationality models. In *Proceedings of the 3rd Annual Conference on Advances in Cognitive Systems*, page 2, 2015.

[182] Edward L Glaeser, Bruce Sacerdote, and Jose A Scheinkman. Crime and social interactions. *The Quarterly Journal of Economics*, 111(2):507–548, 1996.

[183] Andrew Alfred Lacey and Michael Tsardakas. A mathematical model of serious and minor criminal activity. *European Journal of Applied Mathematics*, 27(3): 403–421, 2016.

[184] Martin B Short et al. A statistical model of criminal behavior. *Mathematical Models and Methods in Applied Sciences*, 18:1249–1267, 2008.

[185] Nelson Baloian, Col Enrique Bassaletti, Mario Fernández, Oscar Figueroa, Pablo Fuentes, Raúl Manasevich, Marcos Orchard, Sergio Peñafiel, José A Pino, and Mario Vergara. Crime prediction using patterns and context. In *21st International Conference on Computer Supported Cooperative Work in Design*, pages 2–9. IEEE, 2017.

[186] Maria R D'Orsogna and Matjaž Perc. Statistical physics of crime: A review. *Physics of Life Reviews*, 12:1–21, 2015.

[187] Bijan Berenji, Tom Chou, and Maria R D'Orsogna. Recidivism and rehabilitation of criminal offenders: A carrot and stick evolutionary game. *PLoS One*, 9(1):e85531, 2014.

[188] Aristides Dokoumetzidis, Richard Magin, and Panos Macheras. A commentary on fractionalization of multi-compartmental models. *Journal of Pharmacokinetics and Pharmacodynamics*, 37(2):203–207, 2010.

[189] Ivo Petráš. Chaos in the fractional-order Volta's system: Modeling and simulation. *Nonlinear Dynamics*, 57(1):157–170, 2009.

[190] Ivo Petráš. Modeling and numerical analysis of fractional-order Bloch equations. *Computers & Mathematics with Applications*, 61(2):341–356, 2011.

[191] Jun Ma, Yuexiong Ding, Jack CP Cheng, Feifeng Jiang, Yi Tan, Vincent JL Gan, and Zhiwei Wan. Identification of high impact factors of air quality on a national scale using big data and machine learning techniques. *Journal of Cleaner Production*, 244:118955, 2020.

[192] Gaganjot Kaur Kang, Jerry Zeyu Gao, Sen Chiao, Shengqiang Lu, and Gang Xie. Air quality prediction: Big data and machine learning approaches. *International Journal of Environmental Science and Development*, 9(1):8–16, 2018.

[193] Lu Bai, Jianzhou Wang, Xuejiao Ma, and Haiyan Lu. Air pollution forecasts: An overview. *International Journal of Environmental Research and Public Health*, 15 (4):780, 2018.

[194] Wei Feng and Hang Yuan. Haze pollution and economic fluctuations: An empirical analysis of chinese cities. *Cleaner Environmental Systems*, 2:100010, 2021.

[195] Seshibe Makgato and Evans M N Chirwa. Recent developments in reduction of sulphur emissions from selected Waterberg coal samples used in South African power plants. *Journal of Cleaner Production*, 276:123192, 2020.

[196] Manzhu Yu and Qian Liu. Deep learning-based downscaling of tropospheric nitrogen dioxide using ground-level and satellite observations. *Science of The Total Environment*, 773:145145, 2021.

[197] Kai Chen, Susanne Breitner, Kathrin Wolf, Massimo Stafoggia, Francesco Sera, Ana M Vicedo-Cabrera, Yuming Guo, Shilu Tong, Eric Lavigne, Patricia Matus, et al. Ambient carbon monoxide and daily mortality: A global time-series study in 337 cities. *The Lancet Planetary Health*, 5(4):e191–e199, 2021.

[198] Hua Lu, Min Xie, Xiaoran Liu, Bojun Liu, Minzhi Jiang, Yanghua Gao, and Xiaoli Zhao. Adjusting prediction of ozone concentration based on CMAQ model and machine learning methods in Sichuan-Chongqing region, China. *Atmospheric Pollution Research*, 12(6):101066, 2021.

[199] Pierre Sicard, Elena Paoletti, Evgenios Agathokleous, Valda Araminienė, Chiara Proietti, Fatimatou Coulibaly, and Alessandra De Marco. Ozone weekend effect in cities: Deep insights for urban air pollution control. *Environmental Research*, 191: 110193, 2020.

[200] Arideep Mukherjee, Durgesh Singh Yadav, Shashi Bhushan Agrawal, and Madhoolika Agrawal. Ozone a persistent challenge to food security in India: Current status and policy implications. *Current Opinion in Environmental Science & Health*, 19: 100220, 2021.

[201] Tony Fischer. Wheat yield losses in India due to ozone and aerosol pollution and their alleviation: A critical review. *Outlook on Agriculture*, 48(3):181–189, 2019.

[202] Ann L Power, Richard K Tennant, Richard T Jones, Ya Tang, Jie Du, Annie T Worsley, and John Love. Monitoring impacts of urbanisation and industrialisation on air quality in the Anthropocene using urban pond sediments. *Frontiers in Earth Science*, 6:131, 2018.

[203] Giang Tran Huong Nguyen, Hikari Shimadera, Katsushige Uranishi, Tomohito Matsuo, and Akira Kondo. Numerical assessment of $PM_{2.5}$ and O_3 air quality in continental Southeast Asia: Impacts of potential future climate change. *Atmospheric Environment*, 215:116901, 2019.

[204] Arlene M Fiore, Vaishali Naik, and Eric M Leibensperger. Air quality and climate connections. *Journal of the Air & Waste Management Association*, 65(6):645–685, 2015.

[205] Gennaro D'Amato, Carlos E Baena-Cagnani, Lorenzo Cecchi, Isabella Annesi-Maesano, Carlos Nunes, Ignacio Ansotegui, Maria D'Amato, Gennaro Liccardi, Matteo Sofia, and Walter G Canonica. Climate change, air pollution and extreme events leading to increasing prevalence of allergic respiratory diseases. *Multidisciplinary Respiratory Medicine*, 8(1):1–9, 2013.

[206] R Sivarethinamohan, S Sujatha, Shanmuga Priya, S Sankaran, Abdul Gafoor, and Zunaithur Rahman. Impact of air pollution in health and socio-economic aspects:Review on future approach. *Materials Today: Proceedings*, 37:2725–2729, 2021.

[207] PJ García Nieto, F Sánchez Lasheras, E García-Gonzalo, and FJ de Cos Juez. PM_{10} concentration forecasting in the metropolitan area of Oviedo (Northern Spain) using models based on SVM, MLP, VARMA and ARIMA: A case study. *Science of the Total Environment*, 621:753–761, 2018.

[208] Lanyi Zhang, Jane Lin, Rongzu Qiu, Xisheng Hu, Huihui Zhang, Qingyao Chen, Huamei Tan, Danting Lin, and Jiankai Wang. Trend analysis and forecast of $PM_{2.5}$ in Fuzhou, China using the ARIMA model. *Ecological Indicators*, 95:702–710, 2018.

[209] Anikender Kumar and Pramila Goyal. Forecasting of air quality in Delhi using principal component regression technique. *Atmospheric Pollution Research*, 2(4): 436–444, 2011.

[210] Shuaib Lwasa, Frank Mugagga, Bolanle Wahab, David Simon, John Connors, and Corrie Griffith. Urban and peri-urban agriculture and forestry: Transcending poverty alleviation to climate change mitigation and adaptation. *Urban Climate*, 7:92–106, 2014.

[211] Lifeng Wu, Xiaohui Gao, Yanli Xiao, Sifeng Liu, and Yingjie Yang. Using Grey Holt-Winters model to predict the air quality index for cities in China. *Natural Hazards*, 88(2):1003–1012, 2017.

[212] Lifeng Wu, Nu Li, and Yingjie Yang. Prediction of air quality indicators for the Beijing-Tianjin-Hebei region. *Journal of Cleaner Production*, 196:682–687, 2018.

[213] Lifeng Wu, Sifeng Liu, Ligen Yao, Shuli Yan, and Dinglin Liu. Grey system model with the fractional order accumulation. *Communications in Nonlinear Science and Numerical Simulation*, 18(7):1775–1785, 2013.

[214] Santanu Metia, Seth Daniel Oduro, Hiep Nguyen Duc, and Quang Ha. Inverse air-pollutant emission and prediction using extended fractional Kalman filtering. *IEEE Journal of Selected Topics in Applied Earth Observations and Remote Sensing*, 9 (5):2051–2063, 2016.

[215] Yonghui Sun, Xiaopeng Wu, Jinde Cao, Zhinong Wei, and Guoqiang Sun. Fractional extended Kalman filtering for non-linear fractional system with lévy noises. *IET Control Theory & Applications*, 11(3):349–358, 2017.

[216] Yessy Vita Oktaviana, Erna Apriliani, and Didik Khusnul Arif. Fractional Kalman filter to estimate the concentration of air pollution. *Journal of Physics: Conference Series*, 1008:012008, 2018.

[217] Wendong Yang, Jianzhou Wang, Tong Niu, and Pei Du. A hybrid forecasting system based on a dual decomposition strategy and multi-objective optimization for electricity price forecasting. *Applied Energy*, 235:1205–1225, 2019.

[218] Wendong Yang, Jianzhou Wang, Haiyan Lu, Tong Niu, and Pei Du. Hybrid wind energy forecasting and analysis system based on divide and conquer scheme: A case study in China. *Journal of Cleaner Production*, 222:942–959, 2019.

[219] Jianzhou Wang, Pei Du, Yan Hao, Xin Ma, Tong Niu, and Wendong Yang. An innovative hybrid model based on outlier detection and correction algorithm and heuristic intelligent optimization algorithm for daily air quality index forecasting. *Journal of Environmental Management*, 255:109855, 2020.

[220] Wen-jing Niu and Zhong-kai Feng. Evaluating the performances of several artificial intelligence methods in forecasting daily streamflow time series for sustainable water resources management. *Sustainable Cities and Society*, 64:102562, 2021.

[221] Nikita Singh, Sugandha Arora, Trilok Mathur, Shivi Agarwal, and Kamlesh Tiwari. Stock price prediction using fractional gradient-based long short term memory. *Journal of Physics: Conference Series*, 1969:012038, 2021.

[222] Ramadoss Janarthanan, Pachaivannan Partheeban, Krishnan Somasundaram, and P Navin Elamparithi. A deep learning approach for prediction of air quality index in a metropolitan city. *Sustainable Cities and Society*, 67:102720, 2021.

[223] Guy Jumarie. Modified Riemann-Liouville derivative and fractional Taylor's series of non-differentiable functions further results. *Computers & Mathematics with Applications*, 51(9-10):1367–1376, 2006.

[224] Guy Jumarie. Table of some basic fractional calculus formulae derived from a Modified Riemann-Liouville derivative for non-differentiable functions. *Applied Mathematics Letters*, 22(3):378–385, 2009.

[225] Guy Jumarie. An approach via fractional analysis to non-linearity induced by coarse-graining in space. *Nonlinear Analysis: Real World Applications*, 11(1): 535–546, 2010.

[226] Guy Jumarie. On the derivative chain-rules in fractional calculus via fractional difference and their application to systems modelling. *Open Physics*, 11(6):617–633, 2013.

[227] Dian Sheng, Yiheng Wei, Yuquan Chen, and Yong Wang. Convolutional neural networks with fractional order gradient method. *Neurocomputing*, 408:42–50, 2020.

[228] Guilherme Pina Cardim, Erivaldo Antônio da Silva, Mauricio Araújo Dias, Ignácio Bravo, and Alfredo Gardel. Statistical evaluation and analysis of road extraction methodologies using a unique dataset from remote sensing. *Remote Sensing*, 10(4): 620, 2018.

[229] Ramesh Kestur, Shariq Farooq, Rameen Abdal, Emad Mehraj, Omkar Subbaramajois Narasipura, and Meenavathi Mudigere. UFCN: A fully convolutional neural network for road extraction in RGB imagery acquired by remote sensing from an unmanned aerial vehicle. *Journal of Applied Remote Sensing*, 12(1):016020, 2018.

[230] Himanshu Verma, Yogendra Sharma, and Sumanta Pasari. Synthetic aperture Radar interferometry to measure earthquake-related deformation: A case study from Nepal. In *Disaster Management in the Complex Himalayan Terrains*, pages 133–140. Springer, 2022.

[231] Meir Barzohar and David B Cooper. Automatic finding of main roads in aerial images by using geometric-stochastic models and estimation. *IEEE Transactions on Pattern Analysis and Machine Intelligence*, 18(7):707–721, 1996.

[232] Stefan Hinz. Automatic road extraction in urban scenes and beyond. *International Archives of Photogrammetry and Remote Sensing*, 35(Part B3):349–355, 2004.

[233] Aleksey Boyko and Thomas Funkhouser. Extracting roads from dense point clouds in large scale urban environment. *ISPRS Journal of Photogrammetry and Remote Sensing*, 66(6):S2–S12, 2011.

[234] Yanqing Wang, Yuan Tian, Xianqing Tai, and Lixia Shu. Extraction of main urban roads from high resolution satellite images by machine learning. In *Asian Conference on Computer Vision*, pages 236–245. Springer, 2006.

[235] Pramod Kumar Soni, Navin Rajpal, and Rajesh Mehta. Road centerline extraction from VHR images using SVM and multi-scale maximum response filter. *Journal of the Indian Society of Remote Sensing*, 49(7):1519–1532, 2021.

[236] Donald Geman and Bruno Jedynak. An active testing model for tracking roads in satellite images. *IEEE Transactions on Pattern Analysis and Machine Intelligence*, 18(1):1–14, 1996.

[237] Ali Akbar Matkan, Mohammad Hajeb, and Saeed Sadeghian. Road extraction from lidar data using support vector machine classification. *Photogrammetric Engineering & Remote Sensing*, 80(5):409–422, 2014.

[238] Pankaj Pratap Singh and Rahul Dev Garg. Automatic road extraction from high resolution satellite image using adaptive global thresholding and morphological operations. *Journal of the Indian Society of Remote Sensing*, 41(3):631–640, 2013.

[239] Gang Fu, Hongrui Zhao, Cong Li, and Limei Shi. Road detection from optical remote sensing imagery using circular projection matching and tracking strategy. *Journal of the Indian Society of Remote Sensing*, 41(4):819–831, 2013.

[240] Pramod Kumar Soni, Navin Rajpal, and Rajesh Mehta. A comparison of road network extraction from high resolution images. In *International Conference on Secure Cyber Computing and Communication*, pages 525–531. IEEE, 2018.

[241] Volodymyr Mnih and Geoffrey E Hinton. Learning to detect roads in high-resolution aerial images. In *European Conference on Computer Vision*, pages 210–223. Springer, 2010.

[242] Volodymyr Mnih. *Machine learning for aerial image labeling*. University of Toronto (Canada), 2013.

[243] Diederik P Kingma and Jimmy Ba. Adam: A method for stochastic optimization. In *Proceedings of the 3rd International Conference on Learning Representations*, volume 1, 2014.

[244] Olaf Ronneberger, Philipp Fischer, and Thomas Brox. U-Net: Convolutional networks for biomedical image segmentation. In *International Conference on Medical image Computing and Computer-assisted Intervention*, pages 234–241. Springer, 2015.

[245] Kaiming He, Xiangyu Zhang, Shaoqing Ren, and Jian Sun. Delving deep into rectifiers: Surpassinghuman-level performance on ImageNet classification. In *Proceedings of the IEEE International Conference on Computer Vision*, pages 1026–1034, 2015.

[246] Jonathan Long, Evan Shelhamer, and Trevor Darrell. Fully convolutional networks for semantic segmentation. In *Proceedings of the IEEE Conference on Computer Vision and Pattern Recognition*, pages 3431–3440, 2015.

[247] Shunta Saito, Takayoshi Yamashita, and Yoshimitsu Aoki. Multiple object extraction from aerial imagery with convolutional neural networks. *Electronic Imaging*, 2016(10):1–9, 2016.

[248] Zilong Zhong, Jonathan Li, Weihong Cui, and Han Jiang. Fully convolutional networks for building and road extraction: Preliminary results. In *International Geoscience and Remote Sensing Symposium*, pages 1591–1594. IEEE, 2016.

[249] Weixing Wang, Nan Yang, Yi Zhang, Fengping Wang, Ting Cao, and Patrik Eklund. A review of road extraction from remote sensing images. *Journal of Traffic and Transportation Engineering*, 3(3):271–282, 2016.

[250] Gustav Larsson, Michael Maire, and Gregory Shakhnarovich. FractalNet: Ultra-deep neural networks without residuals. In *Proceedings of the 4th International Conference on Learning Representations*, 2016.

[251] Vijay Badrinarayanan, Alex Kendall, and Roberto Cipolla. SegNet: A deep convolutional encoder-decoder architecture for image segmentation. *IEEE Transactions on Pattern Analysis and Machine Intelligence*, 39(12):2481–2495, 2017.

[252] Yanan Wei, Zulin Wang, and Mai Xu. Road structure refined CNN for road extraction in aerial image. *IEEE Geoscience and Remote Sensing Letters*, 14(5): 709–713, 2017.

[253] Liang-Chieh Chen, George Papandreou, Florian Schroff, and Hartwig Adam. Rethinking atrous convolution for semantic image segmentation. *arXiv preprint arXiv:1706.05587*, 2017.

[254] Aidan N Gomez, Mengye Ren, Raquel Urtasun, and Roger B Grosse. The reversible residual network: Backpropagation without storing activations. *Advances in Neural Information Processing Systems*, 30, 2017.

[255] Liang-Chieh Chen, Yukun Zhu, George Papandreou, Florian Schroff, and Hartwig Adam. Encoder-decoder with atrous separable convolution for semantic image segmentation. In *Proceedings of the European Conference on Computer Vision*, pages 801–818, 2018.

[256] Lichen Zhou, Chuang Zhang, and Ming Wu. D-LinkNet: LinkNet with pretrained encoder and dilated convolution for high resolution satellite imagery road extraction. In *Proceedings of the IEEE Conference on Computer Vision and Pattern Recognition Workshops*, pages 182–186, 2018.

[257] Yongyang Xu, Zhong Xie, Yaxing Feng, and Zhanlong Chen. Road extraction from high-resolution remote sensing imagery using deep learning. *Remote Sensing*, 10 (9):1461, 2018.

[258] Yahui Liu, Jian Yao, Xiaohu Lu, Menghan Xia, Xingbo Wang, and Yuan Liu. RoadNet: Learning to comprehensively analyze road networks in complex urban scenes from high-resolution remotely sensed images. *IEEE Transactions on Geoscience and Remote Sensing*, 57(4):2043–2056, 2018.

[259] Zhengxin Zhang, Qingjie Liu, and Yunhong Wang. Road extraction by deep residual U-Net. *IEEE Geoscience and Remote Sensing Letters*, 15(5):749–753, 2018.

[260] Wei Yujun, Hu Xiangyun, and Gong Jinqi. End-to-end road centerline extraction via learning a confidence map. In *10th IAPR Workshop on Pattern Recognition in Remote Sensing*, pages 1–5. IEEE, 2018.

[261] Alexander Buslaev, Selim Seferbekov, Vladimir Iglovikov, and Alexey Shvets. Fully convolutional network for automatic road extraction from satellite imagery. In *Computer Vision and Pattern Recognition Workshops*, pages 207–210. IEEE, 2018.

[262] Zongwei Zhou, Md Mahfuzur Rahman Siddiquee, Nima Tajbakhsh, and Jianming Liang. UNet++: A nested U-Net architecture for medical image segmentation. In *Deep learning in Medical Image Analysis and Multimodal Learning for Clinical Decision Support*, pages 3–11. Springer, 2018.

[263] Yiping Lu, Aoxiao Zhong, Quanzheng Li, and Bin Dong. Beyond finite layer neural networks: Bridging deep architectures and numerical differential equations. In *International Conference on Machine Learning*, pages 3276–3285. PMLR, 2018.

[264] Bruno Artacho and Andreas Savakis. Waterfall atrous spatial pooling architecture for efficient semantic segmentation. *Sensors*, 19(24):5361, 2019.

[265] Jiang Xin, Xinchang Zhang, Zhiqiang Zhang, and Wu Fang. Road extraction of high-resolution remote sensing images derived from DenseUNet. *Remote Sensing*, 11(21):2499, 2019.

[266] Ye Li, Lele Xu, Jun Rao, Lili Guo, Zhen Yan, and Shan Jin. A Y-Net deep learning method for road segmentation using high-resolution visible remote sensing images. *Remote Sensing Letters*, 10(4):381–390, 2019.

[267] Priya Singh and Ratnakar Dash. A two-step deep convolution neural network for road extraction from aerial images. In *6th International Conference on Signal Processing and Integrated Networks*, pages 660–664. IEEE, 2019.

[268] Yan Xie, Fang Miao, Kai Zhou, and Jing Peng. HsgNet: A road extraction network based on global perception of high-order spatial information. *ISPRS International Journal of Geo-Information*, 8(12):571, 2019.

[269] Jee-Young Sun, Seung-Wook Kim, Sang-Won Lee, Ye-Won Kim, and Sung-Jea Ko. Reverse and boundary attention network for road segmentation. In *Proceedings of the IEEE/CVF International Conference on Computer Vision Workshops*, pages 0–0, 2019.

[270] Man Yuan, Zhi Liu, and Fan Wang. Using the wide-range attention U-Net for road segmentation. *Remote Sensing Letters*, 10(5):506–515, 2019.

[271] Lars Ruthotto and Eldad Haber. Deep neural networks motivated by partial differential equations. *Journal of Mathematical Imaging and Vision*, 62(3):352–364, 2020.

[272] Abolfazl Abdollahi, Biswajeet Pradhan, Nagesh Shukla, Subrata Chakraborty, and Abdullah Alamri. Deep learning approaches applied to remote sensing datasets for road extraction: A state-of-the-art review. *Remote Sensing*, 12(9):1444, 2020.

[273] Huimin Huang, Lanfen Lin, Ruofeng Tong, Hongjie Hu, Qiaowei Zhang, Yutaro Iwamoto, Xianhua Han, Yen-Wei Chen, and Jian Wu. UNet 3+: A full-scale connected unet for medical image segmentation. In *Proceedings of IEEE International Conference on Acoustics, Speech and Signal Processing*, pages 1055–1059. IEEE, 2020.

[274] Xuebin Qin, Zichen Zhang, Chenyang Huang, Masood Dehghan, Osmar R Zaiane, and Martin Jagersand. U2-Net: Going deeper with nested U-structure for salient object detection. *Pattern Recognition*, 106:107404, 2020.

[275] Abolfazl Abdollahi, Biswajeet Pradhan, and Abdullah Alamri. VNet: An end-to-end fully convolutional neural network for road extraction from high-resolution remote sensing data. *IEEE Access*, 8:179424–179436, 2020.

[276] Meng Lan, Yipeng Zhang, Lefei Zhang, and Bo Du. Global context based automatic road segmentation via dilated convolutional neural network. *Information Sciences*, 535:156–171, 2020.

[277] Pourya Shamsolmoali, Masoumeh Zareapoor, Huiyu Zhou, Ruili Wang, and Jie Yang. Road segmentation for remote sensing images using adversarial spatial pyramid networks. *IEEE Transactions on Geoscience and Remote Sensing*, 59(6): 4673–4688, 2020.

[278] Rui Li, Shunyi Zheng, Chenxi Duan, Jianlin Su, and Ce Zhang. Multistage attention ResU-Net for semantic segmentation of fine-resolution remote sensing images. *IEEE Geoscience and Remote Sensing Letters*, 19:1–5, 2021.

[279] Abolfazl Abdollahi, Biswajeet Pradhan, Gaurav Sharma, Khairul Nizam Abdul Maulud, and Abdullah Alamri. Improving road semantic segmentation using generative adversarial network. *IEEE Access*, 9:64381–64392, 2021.

[280] Abolfazl Abdollahi, Biswajeet Pradhan, and Abdullah Alamri. RoadVecNet: A new approach for simultaneous road network segmentation and vectorization from aerial and Google Earth imagery in a complex urban set-up. *GIScience & Remote Sensing*, 58(7):1151–1174, 2021.

[281] Abolfazl Abdollahi and Biswajeet Pradhan. Integrated technique of segmentation and classification methods with connected components analysis for road extraction from orthophoto images. *Expert Systems with Applications*, 176:114908, 2021.

[282] Ke Yang, Jizheng Yi, Aibin Chen, Jiaqi Liu, and Wenjie Chen. ConDinet++: Full-scale fusion network based on conditional dilated convolution to extract roads from remote sensing images. *IEEE Geoscience and Remote Sensing Letters*, 19:1–5, 2021.

[283] Lefei Zhang, Meng Lan, Jing Zhang, and Dacheng Tao. Stagewise unsupervised domain adaptation with adversarial self-training for road segmentation of remote-sensing images. *IEEE Transactions on Geoscience and Remote Sensing*, 60:1–13, 2021.

[284] Zengguo Sun, Hui Geng, Zheng Lu, Rafał Scherer, and Marcin Woźniak. Review of road segmentation for SAR images. *Remote Sensing*, 13(5):1011, 2021.

[285] Cheng Ding, Liguo Weng, Min Xia, and Haifeng Lin. Non-local feature search network for building and road segmentation of remote sensing image. *ISPRS International Journal of Geo-Information*, 10(4):245, 2021.

[286] Sijun Dong and Zhengchao Chen. Block multi-dimensional attention for road segmentation in remote sensing imagery. *IEEE Geoscience and Remote Sensing Letters*, 19:1–5, 2021.

[287] Zheng Zhang, Chunle Miao, Chang'an Liu, and Qing Tian. DCS-TransUperNet: Road segmentation network based on CSwin transformer with dual resolution. *Applied Sciences*, 12(7):3511, 2022.

[288] Shi Gong, Huan Zhou, Feng Xue, Cong Fang, Yiqun Li, and Yu Zhou. FastRoadSeg: Fast monocular road segmentation network. *IEEE Transactions on Intelligent Transportation Systems*, 2022.

[289] Mengxing Yang, Yuan Yuan, and Ganchao Liu. SDUNet: Road extraction via spatial enhanced and densely connected UNet. *Pattern Recognition*, 126:108549, 2022.

[290] Sugandha Arora, Trilok Mathur, Shivi Agarwal, Kamlesh Tiwari, and Phalguni Gupta. Applications of fractional calculus in computer vision: A survey. *Neurocomputing*, 489:407–428, 2022.

[291] Vanessa Buhrmester, David Münch, and Michael Arens. Analysis of explainers of black box deep neural networks for computer vision: A survey. *Machine Learning and Knowledge Extraction*, 3(4):966–989, 2021.

[292] Ravid Shwartz-Ziv and Naftali Tishby. Opening the black box of deep neural networks via information. *Entropy*, 23(10):1360, 2017.

[293] Yi-han Sheu. Illuminating the black box: Interpreting deep neural network models for psychiatric research. *Frontiers in Psychiatry*, 11:551299, 2020.

[294] Riccardo Caponetto. *Fractional order systems: Modeling and control applications*, volume 72. World Scientific, 2010.

[295] Mark J Carlotto. Effect of errors in ground truth on classification accuracy. *International Journal of Remote Sensing*, 30(18):4831–4849, 2009.

[296] Alina E Maas, Franz Rottensteiner, and Christian Heipke. A label noise tolerant random forest for the classification of remote sensing data based on outdated maps for training. *Computer Vision and Image Understanding*, 188:102782, 2019.

[297] Ali Borji, Ming-Ming Cheng, Qibin Hou, Huaizu Jiang, and Jia Li. Salient object detection: A survey. *Computational Visual Media*, 5:117–150, 2019.

[298] Fan Zhang, Bo Du, and Liangpei Zhang. Saliency-guided unsupervised feature learning for scene classification. *IEEE Transactions on Geoscience and Remote Sensing*, 53(4):2175–2184, 2014.

[299] Derrick Parkhurst, Klinton Law, and Ernst Niebur. Modeling the role of salience in the allocation of overt visual attention. *Vision Research*, 42(1):107–123, 2002.

[300] Ghazal Rouhafzay and Ana-Maria Cretu. Object recognition from haptic glance at visually salient locations. *IEEE Transactions on Instrumentation and Measurement*, 69(3):672–682, 2019.

[301] Seunghoon Hong, Tackgeun You, Suha Kwak, and Bohyung Han. Online tracking by learning discriminative saliency map with convolutional neural network. In *International Conference on Machine Learning*, pages 597–606. PMLR, 2015.

[302] Dingwen Zhang, Huazhu Fu, Junwei Han, Ali Borji, and Xuelong Li. A review of co-saliency detection algorithms: Fundamentals, applications, and challenges. *ACM Transactions on Intelligent Systems and Technology*, 9(4):1–31, 2018.

[303] Wenguan Wang, Qiuxia Lai, Huazhu Fu, Jianbing Shen, Haibin Ling, and Ruigang Yang. Salient object detection in the deep learning era: An in-depth survey. *IEEE Transactions on Pattern Analysis and Machine Intelligence*, 44(6):3239–3259, 2021.

[304] Nian Liu and Junwei Han. DHSNet: Deep hierarchical saliency network for salient object detection. In *Proceedings of the IEEE Conference on Computer Vision and Pattern Recognition*, pages 678–686, 2016.

[305] Zhiming Luo, Akshaya Mishra, Andrew Achkar, Justin Eichel, Shaozi Li, and Pierre-Marc Jodoin. Non-local deep features for salient object detection. In *Proceedings of the IEEE Conference on Computer Vision and Pattern Recognition*, pages 6609–6617, 2017.

[306] Linzhao Wang, Lijun Wang, Huchuan Lu, Pingping Zhang, and Xiang Ruan. Salient object detection with recurrent fully convolutional networks. *IEEE Transactions on Pattern Analysis and Machine Intelligence*, 41(7):1734–1746, 2018.

[307] Qibin Hou, Ming-Ming Cheng, Xiaowei Hu, Ali Borji, Zhuowen Tu, and Philip HS Torr. Deeply supervised salient object detection with short connections. In *Proceedings of the IEEE Conference on Computer Vision and Pattern Recognition*, pages 3203–3212, 2017.

[308] Xiaoning Zhang, Tiantian Wang, Jinqing Qi, Huchuan Lu, and Gang Wang. Progressive attention guided recurrent network for salient object detection. In *Proceedings of the IEEE Conference on Computer Vision and Pattern Recognition*, pages 714–722, 2018.

[309] Zuyao Chen, Qianqian Xu, Runmin Cong, and Qingming Huang. Global context-aware progressive aggregation network for salient object detection. In *Proceedings of the AAAI Conference on Artificial Intelligence*, volume 34, pages 10599–10606, 2020.

[310] Min Seok Lee, WooSeok Shin, and Sung Won Han. TRACER: Extreme attention guided salient object tracing network. In *Proceedings of the AAAI Conference on Artificial Intelligence*, volume 36, pages 12993–12994, 2022.

[311] Saining Xie, Ross Girshick, Piotr Dollár, Zhuowen Tu, and Kaiming He. Aggregated residual transformations for deep neural networks. In *Proceedings of the IEEE Conference on Computer Vision and Pattern Recognition*, pages 1492–1500, 2017.

[312] Gao Huang, Zhuang Liu, Laurens Van Der Maaten, and Kilian Q Weinberger. Densely connected convolutional networks. In *Proceedings of the IEEE Conference on Computer Vision and Pattern Recognition*, pages 4700–4708, 2017.

[313] Xavier Glorot and Yoshua Bengio. Understanding the difficulty of training deep feedforward neural networks. In *Proceedings of the 13th International Conference on Artificial Intelligence and Statistics*, pages 249–256. PMLR, 2010.

[314] Rupesh K Srivastava, Klaus Greff, and Jürgen Schmidhuber. Training very deep networks. *Advances in Neural Information Processing Systems*, 28, 2015.

[315] Sugandha Arora, Harsh Kumar Suman, Trilok Mathur, Hari Mohan Pandey, and Kamlesh Tiwari. Fractional derivative based weighted skip connections for satellite image road segmentation. *Neural Networks*, 161:142–153, 2023.

[316] Guanbin Li and Yizhou Yu. Visual saliency based on multiscale deep features. In *Proceedings of the IEEE Conference on Computer Vision and Pattern Recognition*, pages 5455–5463, 2015.

[317] Yin Li, Xiaodi Hou, Christof Koch, James M Rehg, and Alan L Yuille. The secrets of salient object segmentation. In *Proceedings of the IEEE Conference on Computer Vision and Pattern Recognition*, pages 280–287, 2014.

[318] Qiong Yan, Li Xu, Jianping Shi, and Jiaya Jia. Hierarchical saliency detection. In *Proceedings of the IEEE Conference on Computer Vision and Pattern Recognition*, pages 1155–1162, 2013.

[319] Chuan Yang, Lihe Zhang, Huchuan Lu, Xiang Ruan, and Ming-Hsuan Yang. Saliency detection via graph-based manifold ranking. In *Proceedings of the IEEE Conference on Computer Vision and Pattern Recognition*, pages 3166–3173, 2013.

[320] Lijun Wang, Huchuan Lu, Yifan Wang, Mengyang Feng, Dong Wang, Baocai Yin, and Xiang Ruan. Learning to detect salient objects with image-level supervision. In *Proceedings of the IEEE Conference on Computer Vision and Pattern Recognition*, pages 136–145, 2017.

[321] Vida Movahedi and James H Elder. Design and perceptual validation of performance measures for salient object segmentation. In *Proceedings of the IEEE Conference on Computer Vision and Pattern Recognition Workshops*, pages 49–56. IEEE, 2010.

[322] Yu-Chao Gu, Shang-Hua Gao, Xu-Sheng Cao, Peng Du, Shao-Ping Lu, and Ming-Ming Cheng. iNAS: Integral NAS for device-aware salient object detection. pages 4934–4944, 2021.

[323] Mingcan Ma, Changqun Xia, and Jia Li. Pyramidal feature shrinking for salient object detection. In *Proceedings of the AAAI Conference on Artificial Intelligence*, volume 35, pages 2311–2318, 2021.

[324] Han Sun, Yetong Bian, Ningzhong Liu, and Huiyu Zhou. Multi-scale edge-based U-shape network for salient object detection. In *Proceedings of Trends in Artificial Intelligence: 18th Pacific Rim International Conference on Artificial Intelligence*, volume 18, pages 501–514. Springer, 2021.

[325] Yun Yi Ke and Takahiro Tsubono. Recursive contour-saliency blending network for accurate salient object detection. In *Proceedings of the IEEE/CVF Winter Conference on Applications of Computer Vision*, pages 2940–2950, 2022.

[326] Jia Deng, Wei Dong, Richard Socher, Li-Jia Li, Kai Li, and Li Fei-Fei. Imagenet: A large-scale hierarchical image database. In *Proceedings of the IEEE Conference on Computer Vision and Pattern Recognition*, pages 248–255. Ieee, 2009.

[327] Pingping Zhang, Dong Wang, Huchuan Lu, Hongyu Wang, and Xiang Ruan. Amulet: Aggregating multi-level convolutional features for salient object detection. In *Proceedings of the IEEE International Conference on Computer Vision*, pages 202–211, 2017.

[328] Xin Li, Fan Yang, Hong Cheng, Wei Liu, and Dinggang Shen. Contour knowledge transfer for salient object detection. In *Proceedings of the European Conference on Computer Vision*, pages 355–370, 2018.

[329] Xiaowei Hu, Lei Zhu, Jing Qin, Chi-Wing Fu, and Pheng-Ann Heng. Recurrently aggregating deep features for salient object detection. In *Proceedings of the AAAI Conference on Artificial Intelligence*, volume 32, 2018.

[330] Tiantian Wang, Lihe Zhang, Shuo Wang, Huchuan Lu, Gang Yang, Xiang Ruan, and Ali Borji. Detect globally, refine locally: A novel approach to saliency detection. In *Proceedings of the IEEE Conference on Computer Vision and Pattern Recognition*, pages 3127–3135, 2018.

[331] Zijun Deng, Xiaowei Hu, Lei Zhu, Xuemiao Xu, Jing Qin, Guoqiang Han, and Pheng-Ann Heng. R3Net: Recurrent residual refinement network for saliency detection. In *Proceedings of the 27th International Joint Conference on Artificial Intelligence*, pages 684–690. AAAI Press, 2018.

[332] Zhe Wu, Li Su, and Qingming Huang. Cascaded partial decoder for fast and accurate salient object detection. In *Proceedings of the IEEE/CVF Conference on Computer Vision and Pattern Recognition*, pages 3907–3916, 2019.

[333] Florian Schroff, Dmitry Kalenichenko, and James Philbin. FaceNet: A unified embedding for face recognition and clustering. In *Proceedings of the IEEE Conference on Computer Vision and Pattern Recognition*, pages 815–823, 2015.

[334] Huikai Shao, Dexing Zhong, Xuefeng Du, Shaoyi Du, and Raymond NJ Veldhuis. Few-shot learning for palmprint recognition via meta-siamese network. *IEEE Transactions on Instrumentation and Measurement*, 70:1–12, 2021.

[335] Phalguni Gupta, Kamlesh Tiwari, and Geetika Arora. Fingerprint indexing schemes–a survey. *Neurocomputing*, 335:352–365, 2019.

[336] Moktari Mostofa, Salman Mohamadi, Jeremy Dawson, and Nasser M Nasrabadi. Deep GAN-based cross-spectral cross-resolution iris recognition. *IEEE Transactions on Biometrics, Behavior, and Identity Science*, 3(4):443–463, 2021.

[337] Amit Pandia, Geetika Arora, Archit Jain, Rohit Bharadwaj, Ashutosh Bhatia, and Kamlesh Tiwari. Dteeth: Teeth-photo based human authentication for mobile devices. In *International Joint Conference on Biometrics*, pages 1–8. IEEE, 2022.

[338] Shakila Basheer, Kapil Kumar Nagwanshi, Surbhi Bhatia, Sipi Dubey, and GR Sinha. FESD: An approach for biometric human footprint matching using fuzzy ensemble learning. *IEEE Access*, 9:26641–26663, 2021.

[339] Aditya Nigam, Kamlesh Tiwari, and Phalguni Gupta. Multiple texture information fusion for finger-knuckle-print authentication system. *Neurocomputing*, 188:190–205, 2016.

[340] David Zhang, Wangmeng Zuo, and Feng Yue. A comparative study of palmprint recognition algorithms. *ACM Computing Surveys*, 44(1):1–37, 2012.

[341] Dexing Zhong, Xuefeng Du, and Kuncai Zhong. Decade progress of palmprint recognition: A brief survey. *Neurocomputing*, 328:16–28, 2019.

[342] Zhenhua Guo, Lei Zhang, David Zhang, and Xuanqin Mou. Hierarchical multiscale LBP for face and palmprint recognition. In *Proceedings of IEEE International Conference on Image Processing*, pages 4521–4524. IEEE, 2010.

[343] Deepti Tamrakar and Pritee Khanna. Occlusion invariant palmprint recognition with ULBP histograms. *Procedia Computer Science*, 54:491–500, 2015.

[344] Andreas Lanitis. A survey of the effects of aging on biometric identity verification. *International Journal of Biometrics*, 2(1):34–52, 2010.

[345] Dapeng Zhang and Wei Shu. Two novel characteristics in palmprint verification: Datum point invariance and line feature matching. *Pattern Recognition*, 32(4): 691–702, 1999.

[346] Pengfei Yu, Pengcheng Yu, and Dan Xu. Comparison of PCA, LDA and GDA for palmprint verification. In *Proceedings of International Conference on Information, Networking and Automation*, volume 1, pages 148–152. IEEE, 2010.

[347] Tee Connie, Andrew Teoh, Michael Goh, and David Ngo. Palmprint recognition with PCA and ICA. In *Proceedings of Image and Vision Computing*, pages 227–232, 2003.

[348] De-Shuang Huang, Wei Jia, and David Zhang. Palmprint verification based on principal lines. *Pattern Recognition*, 41(4):1316–1328, 2008.

[349] Xiangqian Wu, David Zhang, and Kuanquan Wang. Palm line extraction and matching for personal authentication. *IEEE Transactions on Systems, Man, and Cybernetics-Part A: Systems and Humans*, 36(5):978–987, 2006.

[350] Angelo Genovese, Vincenzo Piuri, Fabio Scotti, et al. *Touchless palmprint recognition systems*, volume 60. Springer, 2014.

[351] David Zhang, Wai-Kin Kong, Jane You, and Michael Wong. Online palmprint identification. *IEEE Transactions on Pattern Analysis and Machine Intelligence*, 25 (9):1041–1050, 2003.

[352] Zhenhua Guo, David Zhang, Lei Zhang, and Wangmeng Zuo. Palmprint verification using binary orientation co-occurrence vector. *Pattern Recognition Letters*, 30(13): 1219–1227, 2009.

[353] Lunke Fei, Yong Xu, Wenliang Tang, and David Zhang. Double-orientation code and nonlinear matching scheme for palmprint recognition. *Pattern Recognition*, 49: 89–101, 2016.

[354] Wei Jia, De-Shuang Huang, and David Zhang. Palmprint verification based on robust line orientation code. *Pattern Recognition*, 41(5):1504–1513, 2008.

[355] Yong Xu, Lunke Fei, Jie Wen, and David Zhang. Discriminative and robust competitive code for palmprint recognition. *IEEE Transactions on Systems, Man, and Cybernetics: Systems*, 48(2):232–241, 2016.

[356] Xiangqian Wu, Qiushi Zhao, and Wei Bu. A SIFT-based contactless palmprint verification approach using iterative RANSAC and local palmprint descriptors. *Pattern Recognition*, 47(10):3314–3326, 2014.

[357] Yue-Tong Luo, Lan-Ying Zhao, Bob Zhang, Wei Jia, Feng Xue, Jing-Ting Lu, Yi-Hai Zhu, and Bing-Qing Xu. Local line directional pattern for palmprint recognition. *Pattern Recognition*, 50:26–44, 2016.

[358] Wei Jia, Rong-Xiang Hu, Ying-Ke Lei, Yang Zhao, and Jie Gui. Histogram of oriented lines for palmprint recognition. *IEEE Transactions on Systems, Man, and Cybernetics: Systems*, 44(3):385–395, 2013.

[359] Jinsong Zhu, Dexing Zhong, and Kai Luo. Boosting unconstrained palmprint recognition with adversarial metric learning. *IEEE Transactions on Biometrics, Behavior, and Identity Science*, 2(4):388–398, 2020.

[360] Hao Wang, Yitong Wang, Zheng Zhou, Xing Ji, Dihong Gong, Jingchao Zhou, Zhifeng Li, and Wei Liu. CosFace: Large margin cosine loss for deep face recognition. In *Proceedings of the IEEE Conference on Computer Vision and Pattern Recognition*, pages 5265–5274, 2018.

[361] Qilong Wang, Banggu Wu, Pengfei Zhu, Peihua Li, Wangmeng Zuo, and Qinghua Hu. ECA-Net: Efficient channel attention for deep convolutional neural networks. In *Proceedings of the IEEE/CVF Conference on Computer Vision and Pattern Recognition*, pages 11534–11542, 2020.

[362] Jun Fu, Jing Liu, Haijie Tian, Yong Li, Yongjun Bao, Zhiwei Fang, and Hanqing Lu. Dual attention network for scene segmentation. In *Proceedings of the IEEE/CVF Conference on Computer Vision and Pattern Recognition*, pages 3146–3154, 2019.

[363] Marcus D Bloice, Peter M Roth, and Andreas Holzinger. Biomedical image augmentation using Augmentor. *Bioinformatics*, 35(21):4522–4524, 2019.

[364] Guangming Lu, David Zhang, and Kuanquan Wang. Palmprint recognition using eigenpalms features. *Pattern Recognition Letters*, 24(9-10):1463–1467, 2003.

[365] Wangmeng Zuo, Zhouchen Lin, Zhenhua Guo, and David Zhang. The multiscale competitive code via sparse representation for palmprint verification. In *Proceedings of the IEEE Conference on Computer Vision and Pattern Recognition*, pages 2265–2272. IEEE, 2010.

[366] Gen Li and Jaihie Kim. Palmprint recognition with local micro-structure tetra pattern. *Pattern Recognition*, 61:29–46, 2017.

[367] Jumma Almaghtuf, Fouad Khelifi, and Ahmed Bouridane. Fast and efficient difference of block means code for palmprint recognition. *Machine Vision and Applications*, 31:1–10, 2020.

[368] Shuping Zhao and Bob Zhang. Deep discriminative representation for generic palmprint recognition. *Pattern Recognition*, 98:107071, 2020.

[369] Chengcheng Liu, Dexing Zhong, and Huikai Shao. Few-shot palmprint recognition based on similarity metric hashing network. *Neurocomputing*, 456:540–549, 2021.

List of Publications

1. **Arora, Sugandha**., Mathur, Trilok., & Tiwari, Kamlesh. (2023) "A fractional-order model to study the dynamics of the spread of crime", *Journal of Computational and Applied Mathematics*, 115102. (I.F- 2.872 , SCI-Q2)
(https://doi.org/10.1016/j.cam.2023.115102)

2. **Arora, Sugandha**., Suman, Harsh Kumar., Mathur, Trilok., Pandey, Hari Mohan., & Tiwari, Kamlesh. (2023) "Fractional derivative-based weighted skip connections for satellite image road segmentation", *Neural Networks*, 161, 142–153. (I.F- 9.657 , SCI-Q1)
(https://doi.org/10.1016/j.neunet.2023.01.031)

3. **Arora, Sugandha**., Mathur, Trilok., Agarwal, Shivi., Tiwari, Kamlesh., & Gupta, Phalguni. (2022) "Applications of fractional calculus in computer vision: A survey", *Neurocomputing*, 489, 407–428. (I.F- 5.779 , SCI-Q1)
(https://doi.org/10.1016/j.neucom.2021.10.122)

4. **Arora, Sugandha**., Sawaran Singh, Narinderjit., Singh, Divyanshu., Rakesh Shrivastava, Rishi., Mathur, Trilok., Tiwari, Kamlesh., & Agarwal, Shivi. (2022) "Air quality prediction using the fractional gradient-based recurrent neural network", *Computational Intelligence and Neuroscience*, 2022.
(https://doi.org/10.1155/2022/9755422)

5. Bansal, Komal., **Arora, Sugandha**., Pritam, Kocherlakota Satya., Mathur, Trilok., & Agarwal, Shivi. (2022) "Dynamics of crime transmission using fractional-order differential equations", *Fractals*, 30 (01), 2250012. (I.F- 4.555 , SCI-Q1)
(https://doi.org/10.1142/S0218348X22500128)

6. Pritam, Kocherlakota Satya., **Arora, Sugandha**., Mathur, Trilok., & Agarwal, Shivi. (2021) "Underlying dynamics of crime transmission with memory", *Chaos, Solitons & Fractals*, 146, 110838. (I.F- 9.922 , SCI-Q1)
(https://doi.org/10.1016/j.chaos.2021.110838)

7. Singh, Nikita., **Arora, Sugandha**., Mathur, Trilok., Agarwal, Shivi., & Tiwari, Kamlesh. (2021) "Stock price prediction using fractional gradient-based long short-term memory", *Journal of physics: Conference series*, 1969 (1), 012038. (I.F-0.547, Scopus-Q4)
(https://doi.org/10.1088/1742-6596/1969/1/012038)

8. **Arora, Sugandha**., Mathur, Trilok., & Tiwari, Kamlesh. "Feature Aggregation for Salient Object Detection Using Fractional Weighted Skip Connections", *(Communicated)*

9. **Arora, Sugandha**., Mathur, Trilok., & Tiwari, Kamlesh. "FrDPalmNet: Dual Attention Mechanism and Residual Blocks with Fractional Weighted Skips for Palmprint-based Human Authentication System", *(Communicated)*

Conferences / Workshops

1. TEQIP-III sponsored two days Faculty Development Programme, "Research Methodology and Latex" held at Rajasthan Technical University, Kota, 2018.
2. Seven days workshop on "Academic Writing" organized by the Department of Humanities and social sciences of BITS Pilani held at BITS Pilani, Pilani Campus in 2019.
3. Seven days Indo-french workshop on "Theory and Simulation of Hyperbolic PDEs arising in Mathematical Biology and Fluid Flow", organized by the Department of Mathematics, Bits Pilani, Pilani Campus during 05-11 January 2019.
4. International Conference and course on "Orthogonal Polynomials, Special Functions and Computer Algebra: Applications in Engineering" in association with CIMPA, France, during 05-07 March 2019.
5. Short Term Training Programme (STTP) on "Fractional Calculus Applications in Control, Computing, Signal & Image Processing (Theory & Implementation)" organized by RAIT, Mumbai during 02-07 December 2019.
6. Short-term course entitled "Optimization Theory, Methods and Applications" organized by the Department of Mathematics, IIT Roorkee during 18-20 Aug 2020.
7. Presented in International Conference on "Intelligent Robotics, Mechatronics and Automation Systems", organized by VIT Chennai on 26-27 March 2021.
8. Workshop on "Artificial Intelligence Application for Electro-Optical (EO) Sensors", organized jointly by BITS Pilani and IRDE Dehradun during 04 February 2022.
9. A Faculty Development Programme, "Mathematical Models for Machine Learning and its Applications", organized by NIT Warangal and Faculty of Science & Technology, ICFAI, Hyderabad during 11-20 July 2022.
10. Presented in International Conference on "Mathematical Modelling and Simulation in Physical Sciences" organized by the Department of Mathematics and Department of Physics, S. V. National Institute of Technology (SVNIT), Surat, during 23-24 June, 2023.

Biography of the Candidate

Ms. Sugandha received her B.Sc. (Honours) and M.Sc. degree in Mathematics from the University of Delhi, India. She was declared successful in Joint CSIR-UGC Test for Junior Research Fellowship and Eligibility for Lectureship (NET) under the Eligibility for Lectureship category and qualified for GATE in the subject Mathematical Sciences. In 2018, she joined as a full-time Ph.D. scholar in the Department of Mathematics at Birla Institute of Technology and Science (BITS) Pilani, India under the supervision of Prof. Trilok Mathur and Prof. Kamlesh Tiwari. Her research interests are related to the applications of Fractional Calculus. She's working on Fractional-differential modeling, Deep learning, Biometrics, and Computer Vision. She has served as a teaching assistant for the mathematics courses at BITS Pilani, Pilani Campus. More about her research contributions can be found at https://www.researchgate.net/profile/Sugandha-Arora-2. Contact her at p20180024@pilani.bits-pilani.ac.in.

Biography of the Supervisor

Prof. Trilok Mathur is an Associate Professor at the Department of Mathematics, Birla Institute of Technology and Science, Pilani, INDIA since July 2008. He has also worked as Lecturer at Banasthali University, INDIA from 2005 to 2008. He has done his Ph.D. in 2005, from the Department of Mathematics, University of Rajasthan, Jaipur, INDIA in the area of "Special Functions and Fractional Calculus". He has published more than 40 research papers and articles in various refereed journals of international repute and presented his work at many international conferences in India and abroad. His main research interests are the Theory and Applications of Fractional Calculus, Complex Analysis, Multivariable Decision Techniques, Data Envelopment Analysis, and Fuzzy Logic. He visited many universities of international repute like the University of Malaya, Malaysia; Imperial College, London, UK; Ivan Franko National University, Lviv, Ukraine; Leshan Normal University, China; VSB Technical University of Ostrava, Czech Republic to present his research work. He is a member of IAENG, the Indian Mathematical Society (IMS), SSFA, Rajasthan Ganita Parishad (RGP), and many international and national bodies. More on his research contributions can be found at https://www.researchgate.net/profile/Trilok-Mathur. Contact him at tmathur@pilani.bits-pilani.ac.in.

Biography of the Co-Supervisor

Prof. Kamlesh Tiwari is an Associate Professor in the Department of Computer Science and Information Systems at Birla Institute of Technology and Science Pilani, Pilani campus. He earned his Ph.D. from the Department of Computer Science and Engineering of the Indian Institute of Technology Kanpur. His research interests include Machine Learning, Deep Learning, Artificial Intelligence, Computer Vision, Multimodal Biometrics (Fingerprint, Face, Palmprint, Knuckleprint, Forehead crease, teeth photo, and Footprint), and Security. He is a Co-Founder of CogniX Technologies which provides cutting-edge solutions to revolutionize motion analysis for tracking, detection, and feature matching. He has published over 80 research articles in journals, conferences, and book chapters. He regularly organizes workshops on deep learning and machine learning. He is an IEEE and Signal Processing Society (SPS) member. He is an APPCAIR-affiliated faculty and heads the mapmyIndia AI-ML lab. He is a co-in charge of the Advanced Data Analytics & Parallel Technologies Lab at BITS Pilani and an active member of the Multimedia & HCI Laboratory. More on his research contributions can be found at www.ktiwari.in. His email address is kamlesh.tiwari@pilani.bits-pilani.ac.in.